Synthesis, Structure and Magnetism of Mixed-Anion Solids

Robert D. J. Smyth

A thesis submitted in part fulfilment of the requirements for the degree of

Doctor of Philosophy at the University of Oxford

St Catherine's College

University of Oxford

September 2023



Abstract

Synthesis, Structure and Magnetism of Mixed-Anion Solids

DPhil Thesis Robert D. J. Smyth September 2023

This thesis investigates the structure-property relationships in the series of mixed-anion solids $Ae_2MO_2X_2Ch_2$ (*Ae* = Sr, Ba; *M* = Co, Ni; *X* = Cu, Ag; *Ch* = S, Se), $Ae_{3-x}Ae'_xFe_2O_5Cu_2Ch_2$ (*Ae* = Ba, Sr, Ca; *Ch* = S, Se), and $Sr_2NiO_2Cl_2$.

A spin-state crossover in the solid solution $Sr_2NiO_2Cu_2(Se_{1-x}S_x)_2$ has been observed as a function of composition, with two-dimensional magnetic correlations observed for one sample of high S-content before all sign of magnetic scattering is lost which is accompanied by a clear structural signal suggesting a change from high- to low-spin.

The novel, lithiated $Ae_2CoO_2X_{2-x}Li_xCh_2$ (*Ae* = Sr, Ba; *X* = Cu, Ag; *Ch* = S, Se) phases have been synthesised and have similar magnetic ordering to that seen in their non-lithiated analogues. These materials have localised Co^{2+} moments greater than the spin-only predicted 3 μ_B, suggesting a large orbital contribution to the moment which is discussed further within the chapter.

$Ba_{3-x}Sr_xFe_2O_5Cu_2Ch_2$ (*x* = 1, 2; *Ch* = S, Se) and $BaCa_2Fe_2O_5Cu_2S_2$ both show distinct cation ordering between a larger 12-coordinate site and 8-coordinate site and order antiferromagnetically with moments tilted away from the basal plane as opposed to within the plane when there is only one alkaline earth metal present.

Declaration

The work described in this thesis was carried out in the Inorganic Chemistry Laboratory, South Parks Road, Oxford from October 2020 to September 2023 under the supervision of Prof. Simon J. Clarke. Unless stated otherwise, all work described is my own and has not been submitted for any degree at this or any other university.

Robert David James Smyth

September 2023

Acknowledgements

First and foremost, my greatest thanks is to Professor Simon Clarke. Since I joined the group in my 4th year of undergraduate studies, he has been a well of ideas, enthusiasm and guidance in everything I have done in the group and he has continually gone above and beyond what I expected from a supervisor and I will be forever thankful to him for giving me the opportunity to work in the group.

I have been extremely fortunate that working in the group has almost become like hanging out with best friends. Special thanks have to go to the other members of the "core four". Brad – Thanks for 7 years of memories at Catz and being the other member of dumb and dumb. Mahmoud – Thanks for all the warzone nights, table tennis and football and Penny – Thanks for all the cooking advice, clay masks and gossip and I'm sure no matter where you end up, I'll see you in 10!

Another special thanks to my fellow BuLi boy, Souvik Giri who has become one of my closest friends since he joined the group. It has been a pleasure to duel you on the table tennis table, drown our samples with *n*-BuLi and almost completing the "Oxford pub-crawl" together!

I thank Dr. Simon Cassidy for instrumental help and teaching me TOPAS, especially the analysis of neutron diffraction data. I thank Dr Viktoria Falkowski for all the pub trips and games nights, Dr Xabier Martinez de Irujo-Labalde for being mi hermano and visits to "the Portuguese" and I thank Dr Nicola Kelly for all the funny stories and enthusiasm she has brought to the group.

I would also like to thank all the other members of the group who have added to my experience in the group and made it a wonderful place to work – Shunsuke for his boundless enthusiasm, Lexy for making me trek to the top of Grenoble against my will and for all the baked goodies she brings in for the lab, Mila for bringing in Ata for lab adventures, Katie for being our LEAF champion, Lemuel for being the groups #1 Spotify artist and also thanks to previous masters students Ben, Billy, Emily, Fergus as well as this year's cohort; Henry, Saumitra, Adam and especially Jamie (J) for all the sports discussion.

I would like to thank all of those who collaborated with me throughout my thesis, without which it would have been a lot less interesting and impactful; Pascal Manuel, Fabio Orlandi, Dmitry Khalyavin (WISH), Craig Bull (PEARL) and Ivan Da Silva (GEM) for help with neutron experiments, Yoshihiro Tsujimoto (NIMS, Japan), for providing me with a sample of $Sr_2NiO_2Cl_2$ which required high-pressure, James Murrell for help with conductivity and Eric Yang for help with Raman spectroscopy.

I must also thank my closest friends; Will, Bjarne and CC for all the house antics over the last few years, Danny who has become a brother to me, for keeping me on the straight and narrow and enabling me to be the best version of myself. Bradley for all the pool and snooker evenings and of course the "GP" club, for keeping my weekends full of fun and laughter. You are all the best.

Finally, and most importantly, I thank my family for all their support throughout the years and especially to Claire – Ceci est pour toi.

Publications

DPhil work

Smyth, R. D., Wilson, J. A. D., Manuel, P., & Clarke, S. J. (**2021**). Synthesis, structure, magnetism and cation ordering in $Ba_{3-x}Sr_xFe_2O_5Cu_2Ch_2$ (x = 0, 1, 2; *Ch* = S, Se) and $BaCa_2Fe_2O_5Cu_2S_2$. *Journal of Solid-State Chemistry*, *307*, 122841. https://doi.org/10.1016/J.JSSC.2021.122841

Smyth, R. D., Blandy, J. N., Yu, Z., Liu, S., Topping, C. V., Cassidy, S. J., Smura, C. F., Woodruff, D. N., Manuel, P., Bull, C. L., Funnell, N. P., Ridley, C. J., McGrady, J. E., & Clarke, S. J. (**2022**). High- versus Low-Spin Ni^{2+} in Elongated Octahedral Environments: $Sr_2NiO_2Cu_2Se_2$, $Sr_2NiO_2Cu_2S_2$, and $Sr_2NiO_2Cu_2(Se_{1-x}S_x)_2$. *Chemistry of Materials*, *34*(21), 9503–9516. https://doi.org/10.1021/acs.chemmater.2c02002

Smyth, R. D., Khalyavin, D., Tsujimoto, Y., Yamaura, K., & Clarke, S. J. (**2023**). Magnetic ordering in the layered oxyhalide $Sr_2NiO_2Cl_2$. *Solid State Sciences*, *144*, 1293–2558. https://doi.org/10.1016/j.solidstatesciences.2023.107297

Part II work

Sheath, B. C., **Smyth, R. D**., Xu, X., Cassidy, S. J., Batuk, M., Hadermann, J., & Clarke, S. J. Exploring structural distortions and magnetic ordering in the Ae_2FeO_3CuCh (*Ae* = Ca, Sr; *Ch* = S, Se) family of compounds. *Manuscript in preparation*.

Contents

1 Introduction **1**
1.1 Solid-state chemistry 1
1.2 Oxide and non-oxide solids 3
1.3 Mixed-anion solids 5
1.3.1 Oxide chalcogenides 5
1.3.1.1 The Ae_2MO_3CuCh & $Ae_3Fe_2O_5Cu_2Ch_2$ structure types 6
1.3.1.2 The $Ae_2MO_2X_2Ch_2$ structure type 9
1.3.1.3 The ZrSiCuAs structure 14
1.3.2 Oxide halides 16
1.3.2.1 $Sr_2NiO_2Cl_2$ and Sr_2NiO_3Cl 16
1.4 Magnetic behaviour of solids 18
1.4.1 Paramagnetism 18
1.4.1.1 Curie paramagnetism 18
1.4.1.2 Curie-Weiss paramagnetism 20
1.4.1.3 Pauli paramagnetism 21
1.4.2 Ferromagnetism 22
1.4.3 Antiferromagnetism 23
1.4.4 Diamagnetism 25
1.4.5 Metamagnetism 25
1.4.6 Spin-glass materials 26
1.5 Models of magnetic exchange 27
1.5.1 Superexchange 27
1.5.2 Double exchange 30
1.6 Topochemical alterations 31
1.7 Aims of this thesis 33
2 Experimental techniques **35**
2.1 Synthetic methods 35
2.1.1 Solid-state synthesis 35
2.1.2 Argon filled glovebox 37
2.1.3 Preparation of starting material 38
2.1.3.1 *Ae*O (*Ae* = Ba, Sr, Ca) 38
2.1.3.2 *Ae*S (*Ae* = Ba, Sr) 39
2.1.3.3 Sublimation of Sr metal 41
2.1.3.4 SrSe 42
2.1.3.5 Cu_2O 42
2.1.4 Soft chemistry 43
2.2 Characterisation techniques 46
2.2.1 Diffraction 46
2.2.1.1 X-ray diffraction 47
2.2.1.2 Neutron diffraction 51
2.2.1.3 Limits of X-ray diffraction compared to neutron diffraction 54
2.2.2 X-ray diffractometers 55
2.2.2.1 Bruker d8 Advance ECO 57

2.2.2.2 PANalytical Empyrean 58
2.2.2.3 The I11 beamline at Diamond Light Source 58
2.2.3 Neutron diffractometers 61
2.2.3.1 The WISH diffractometer at ISIS 61
2.2.3.2 The PEARL diffractometer at ISIS 61
2.2.3.3 The GEM diffractometer at ISIS 62
2.2.4 Structural refinement 63
2.2.5 Electron microscopy and diffraction 66
2.2.6 X-ray absorption near-edge spectroscopy (XANES) 68
2.2.6.1 The B18 beamline at the Diamond Light Source 69
2.2.7 SQUID magnetometry 70
2.2.7.1 DC susceptibility measurements 71
2.2.8 Resistivity 73
2.2.9 Raman spectroscopy 76
2.2.10 Bond valence calculations 78
3 Structure-property relationships in Ni-containing mixed-anion solids 79
3.1 Introduction 79
3.2 Synthesis and characterisation of the solid solution $Sr_2NiO_2Cu_2(Se_{1-x}S_x)_2$ 84
3.2.1 Synthesis of $Sr_2NiO_2Cu_2(Se_{1-x}S_x)_2$ $0 \leq x \leq 0.5$ 84
3.2.2 Synthesis of $Sr_2NiO_2Cu_2(Se_{1-x}S_x)_2$ $0.625 < x \leq 0.875$ 85
3.2.3 Room temperature powder X-ray diffraction 86
3.2.4 Room temperature powder neutron diffraction 88
3.2.5 Variable temperature SPXRD 91
3.2.6 Magnetometry 92
3.2.7 Traversing the spin-state crossover in $Sr_2NiO_2Cu_2(Se_{1-x}S_x)_2$ using PND 93
3.2.8 Variable temperature PND. 102
3.2.9 Computational results for $Sr_2MO_2Cu_2Ch_2$ (M = Co, Ni, Cu, Zn ; Ch = S, Se) 104
3.2.10 Structural response of $Sr_2NiO_2Cu_2Se_2$ to pressure 107
3.2.11 SEM / EDX 114
3.2.12 Resistivity 118
3.3 Synthesis and characterisation of $Sr_2NiO_2Cl_2$ 120
3.3.1 Synthesis of $Sr_2NiO_2Cl_2$ 120
3.3.2 Room temperature PXRD and PND 121
3.3.3 Variable temperature powder X-ray diffraction 126
3.3.4 Magnetometry 128
3.3.5 Variable temperature PND to probe magnetic ordering 129
3.4 Discussion 134
3.5 Conclusion 141
4 Soft chemistry of cobalt containing oxide chalcogenides 144
4.1 Introduction 144
4.2 Li / Cu exchange in $Sr_2CoO_2Cu_2Ch_2$ (Ch = S, Se) 147
4.2.1 Synthesis and cycling 147
4.2.2 PXRD / PND 149
4.2.3 Variable temperature SPXRD 158
4.2.4 Magnetometry 160
4.2.5 Low temperature PND to probe magnetic ordering 163
4.2.6 XANES 166

4.3 Li / Ag exchange in $Ae_2CoO_2Ag_2Se_2$ (*Ae* = Sr, Ba) 168
4.3.1 Synthesis and cycling 168
4.3.2 PXRD / PND 169
4.3.3 Magnetometry 177
4.3.4 Low temperature PND to probe magnetic ordering 179
4.3.5 XANES measurements 181
4.4 Discussion / Conclusion 183
5 Synthesis and characterisation of $Ae_{3-x}Ae'_xFe_2O_5Cu_2Ch_2$ (*Ae*/Ae' = Ba, Sr, Ca; *Ch* = S, Se) 189
5.1 Introduction 189
5.2 Synthesis 192
5.3 Results & Discussion 193
5.3.1 Room temperature PXRD / PND 193
5.3.2 Cation ordering 204
5.3.3 Low temperature PND to probe magnetic ordering 206
5.3.4 Magnetometry 211
5.4 Conclusion 214
6 Future work / conclusions 215
6.1 Future work 215
6.1.1 Introduction 215
6.1.2 Synthesis of CeAgOSe and CeOSe 217
6.1.3 Room temperature powder X-ray diffraction 218
6.1.4 Raman spectroscopy 219
6.1.5 XANES 220
6.1.6 EDX 222
6.2 Conclusion 224
References 230
Appendix A Computation of $Sr_2MO_2Cu_2Ch_2$ (*M* = Co, Ni, Cu, Zn; *Ch* = S, Se) i
A.1 Full computational procedure i
A.2 Sensitivity of the spin-state to *U* v
Appendix B Ni-*Ch* / Ni-O ratio as a function of temperature in $Sr_2NiO_2Cu_2Ch_2$ (*Ch* = S, Se) vii
Appendix C Previous report of $Sr_2NiO_2Cl_2$ viii
C.1 Comparison of structural parameters viii
C.2 Comparison of magnetometry viii
Appendix D Reactivity of $Sr_2CoO_2Cu_2Te_2$ to *n*-BuLi ix
Appendix E Further magnetometry of $Ae_2CoO_2X_2Ch_2$ x
E.1 *M* vs *T* plots x
E.2 *M* vs *H* plots xi
References xiii

Chapter 1

1 Introduction

1.1 Solid-state chemistry

Solid-state chemistry, as its name suggests, involves crystalline solids which normally have long-range periodic order. The development of X-ray crystallography by W.H. and W.L. Bragg in the early 20th century[1] allowed for these crystalline structures to be investigated more thoroughly than ever before, greatly accelerating advancements in the field and for the first time, allowing for relationships between the structure and properties of solid state compounds to be developed.

Despite large, favourable thermodynamic driving forces for solid-state reactions, solids are generally unreactive due to the low mobility of ions within the solid-state, meaning that high temperatures are required to give the particles at the grain boundaries enough energy to overcome this thermal activation barrier (e.g. the acid-base reaction of SiO_2 and CaO respectively, to form $CaSiO_3$ ($\Delta H_{f(298)} \approx$ - 90 kJ mol^{-1} i.e., should occur spontaneously from the Gibbs free energy equation $\Delta G = \Delta H - T\Delta S$, where G is the Gibbs energy, ΔH is the change in enthalpy and ΔS is the change in entropy, but requires in excess of 1000 °C for a reaction to occur). Because of these reaction conditions, traditional solid-state syntheses at high temperatures tend to give the thermodynamic product of the reaction. More recently, it has been shown that lower temperature syntheses using soft-chemical techniques has

revealed that there are an abundance of metastable, kinetic phases accessible in the solid state, leading to the fine-tuning of a compound's properties and optimisation for application in the real world.

Despite the now large amount of research done into both thermodynamic and kinetic reactions of various compositions, it is still relatively difficult to predict the outcome of certain reaction conditions and therefore, even more difficult to predict their properties. It is often trial and error which is based on historical results that leads to new discoveries in solid-state chemistry and this speculative approach to synthesis is readily adopted within this thesis whereby the same structure types as investigated in previous studies are adopted within this new work using different isovalent or aliovalent substitutions.

In this thesis, the synthesis of mixed-anion solids along with topochemical (i.e., some preservation of structural fragments) reactions are investigated which allow a developing understanding of structure-property relationships in this class of material. Before the results section, this introduction will look into the background chemistry related to the various structures, kinetic approaches and various types of magnetism relevant to mixed-anion solids to help with understanding the conclusions deduced from this work. The experimental section will also help with the theory behind the solid-state along with the various techniques and instruments used throughout the thesis during the characterisation of the synthesised solids.

1.2 Oxide and non-oxide solids

Due to the oxidising nature of the atmosphere, the most stable products of conventional solid-state ceramic synthesis are the oxides. Due to their relative ease of preparation, the field of metal oxides is now rich and well-studied. However, for this same reason, non-oxide solids lagged behind due to the difficulties involved in their synthesis. Non-oxide materials tend to oxidise at the elevated temperatures used in solid-state synthesis, which hindered progress in the field, but advancement in synthetic techniques, mainly being able to work in an inert atmosphere by use of a glovebox (see section 2.1.2) greatly enhanced the ease in which these often-metastable phases could be synthesised.

How different anions can affect the structure and properties of a solid are most easily seen in structures such as TiO_2 and TiS_2. TiO_2 is a white powder with the rutile structure and is an insulator, whereas TiS_2 is a gold-coloured powder with the CdI_2 structure and is a semiconductor. Sulfur is less electronegative than oxygen and hence its more diffuse 3*p* orbitals have better orbital energy overlap with the titanium 3*d* orbitals, this results in broader bands and a smaller band gap i.e., semiconducting behaviour. Both of these compounds are shown in Figure 1.1.

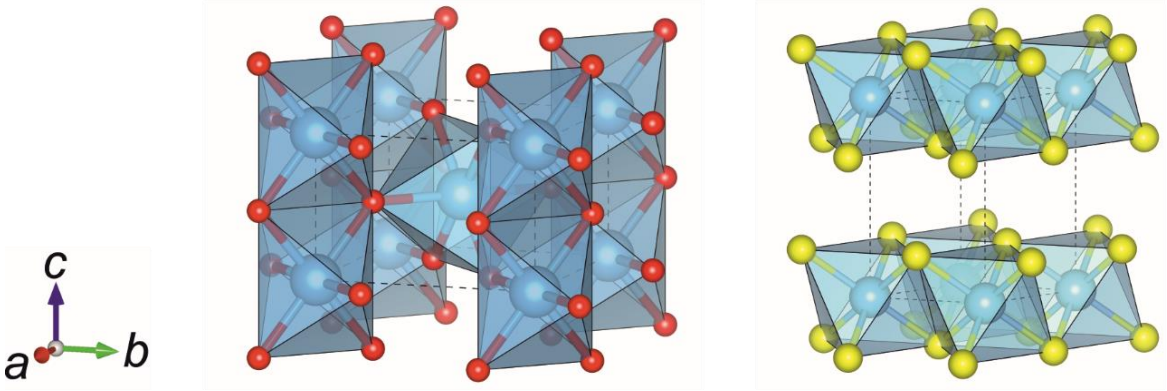


Figure 1.1 The structure of TiO_2 (left) and TiS_2 type (right).

The most striking difference between the two is the layered structure of TiS_2. This is typical of chalcogenide solids whereby the layers are held together by weak Van der Waals interactions due to ionic polarisation effects induced by the presence of chalcogen within the solid. Hence the repulsion between cations can be effectively screened by the polarisable anions when they are in an asymmetric environment.[2]

As synthetic techniques advance, increasingly more non-oxide materials are being studied and this has led to a range of compounds with interesting properties of commercial use. Three of note are GaAs, GaN and MgB_2. GaAs is used in solar panels[3] where the additional contribution to the bandgap from the electronegativity difference between Ga and As leads to a larger bandgap (1.35 V) than that of Si (1.17 V), GaN has an even larger gap close to the visible / uv edge due to the greater electronegativity of N and is used in blue lasers and light emitting diodes[4] and finally, MgB_2 is a commercially viable high temperature superconductor with a critical temperature, T_C, of 39 K and has the potential to be used in M.R.I scanners.[5]

1.3 Mixed-anion solids

As non-oxide solids become increasingly common-place within the solid-state arena, the focus has now expanded to mixed-anion solids. The oxide nitrides and oxide halides (see section 1.3.2) have been the main focus of these mixed-anion compounds to date but oxide chalcogenides (see section 1.3.1) are becoming of interest[6,7] due to the vast array of compounds within this class that show exciting properties that are yet to be understood. These will be explored in the following sections. One example of an oxide nitride with commercial use is the series of compounds $Ta_{3-x}Zr_xO_xN_{5-x}$ which has use as an inert inorganic pigment[8] which may help with the transition away from pigments containing toxic metals such as antimony and arsenic.

1.3.1 Oxide chalcogenides

Oxide chalcogenides are mixed-anion solids which contain both oxygen and either sulfur, selenium or tellurium. Because all these elements are in the same periodic group, substitution of one by another does not alter the oxidation state of the other elements within the compound and hence it would be thought these changes would be straightforward. However, this is found not to be the case mainly due to the properties of the anions. The chalcogenides (S^{2-}, Se^{2-}, Te^{2-}) have ionic radii of 1.84 Å, 1.98 Å and 2.21 Å respectively whereas O^{2-} has an ionic radius of 1.40 Å.[9] The larger, more polarisable chalcogens have a chemical preference to bond to softer, more polarising, cations such as copper and silver whereas oxygen prefers to bond to harder cations such as the earlier first-row transition metals. This leads to anion segregation, whereby the oxide anions reside in one layer and the chalcogenide anions in another layer to fulfil their spatial and chemical requirements.

The difference between sulfur and selenium is a subtler one. Due to the *d*-block contraction, selenium is similar in size to sulfur and they have valence orbitals of similar energies meaning that they can normally occupy the same crystallographic site within the same structure. This is exploited in chapter 3 whereby the solid solution $Sr_2NiO_2Cu_2(Se_{1-x}S_x)_2$ is synthesised, revealing a "high-to-low-spin" transition on increasing sulfur content. An example of an oxide chalcogenide with useful properties is BiCuOSe which can be used in the range of 300-600 ℃ and has a thermoelectric figure of merit value of 1.4 at 650 ℃ which makes it the best *p*-type thermoelectric material that is free of lead or tellurium.[10] The oxide chalcogenides explored in this these are expanded on in sections 1.3.1.1 and 1.3.1.2.

1.3.1.1 The Ae_2MO_3CuCh & $Ae_3Fe_2O_5Cu_2Ch_2$ structure types

The Ae_2MO_3CuCh structure type was first discovered by Zhu and Hor in 1997.[11] It was reported as the Sr_2CuGaO_3S structure[12] and reported for Sr_2MO_3CuS (M = Cr,[11] Mn,[13] Fe,[11] Ga[12] and In[11]). This structure type crystallises in the *P*4/*mmm* space group and is characterised by anti-PbO type $[Cu_2Ch_2]^{2-}$ layers and a small trivalent metal ion such as Fe^{3+} in a square-pyramidal configuration within the oxide layer. The four vertices on the basal plane of the square pyramid are shared with neighbouring pyramids. These two anionic layers are separated by an alkaline earth metal cation which is commonly Sr^{2+}. There are two possible sites for the alkaline earth metal ion to reside; a 9-coordinate site bonded solely to oxygen or an 8-coordinate site bonding to four oxygens and four chalcogens.

The $Ae_3Fe_2O_5Cu_2Ch_2$ structure type was first reported in the same paper by Zhu and Hor in 1997 for $Sr_3Fe_2O_5Cu_2S_2$.[11] This structure type crystallises in the *I*4/*mmm* space group and has some similarities with the Ae_2MO_3CuCh structure type. It too has anti-PbO type $[Cu_2Ch_2]^{2-}$ layers and Fe^{3+} cations in a square-pyramidal geometry. The main difference

between these two structure types resides in the oxide layer. The oxide layer in the $Ae_3Fe_2O_5Cu_2Ch_2$ structure type contains a double layer of FeO_5 pyramids where they are fused together by an apical O, the Ae_2MO_3CuCh structure has an additional SrO slab inserted between its pyramids to separate the layers of pyramids. Again, there are two different sized sites for the Ae^{2+} cation to reside. However, in the $Ae_3Fe_2O_5Cu_2Ch_2$ structure, the larger site is a 12-coordinate cubo-octahedron bonding to 12 oxygens, whereas the smaller site is an 8-coordinate square anti-prism bonding to four oxygens and four chalcogens. Both of these structures are shown visually in Figure 1.2.

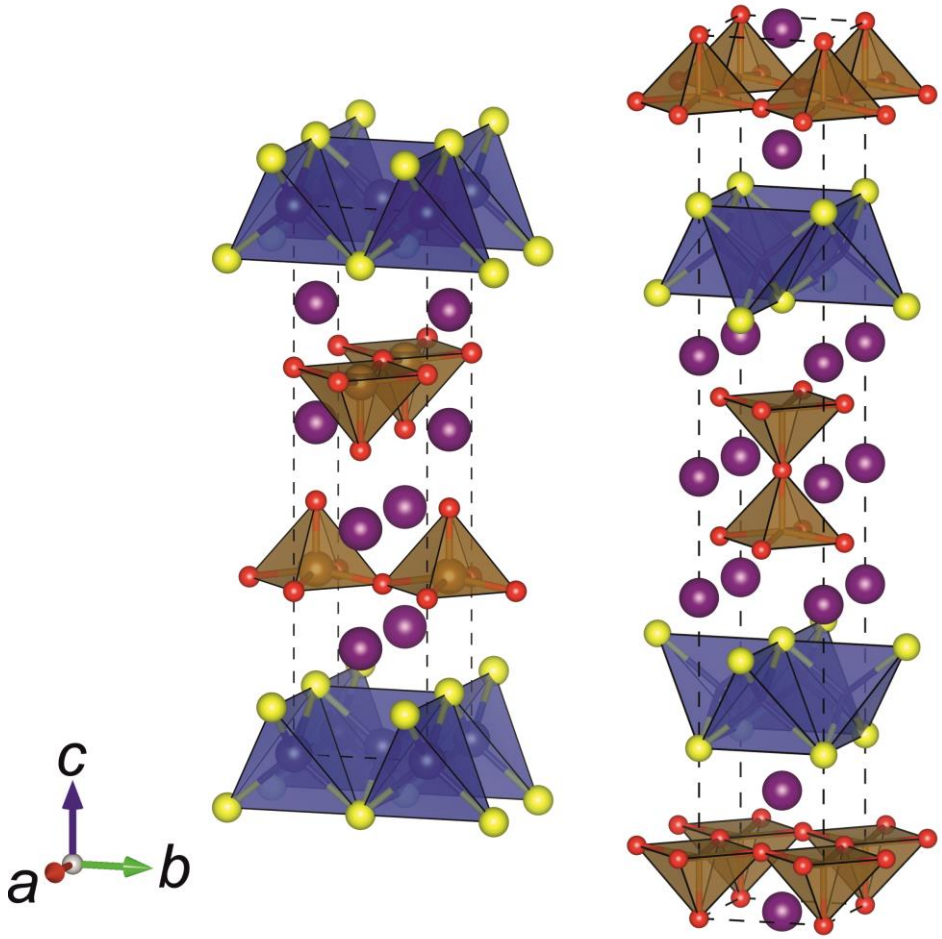


Figure 1.2 The Ae_2MO_3CuCh structure type (left) which crystallises in the *P*4/*nmm* space group and the $Ae_3Fe_2O_5Cu_2Ch_2$ structure type (right) which crystallises in the *I*4/*mmm* space group.

The size disparity in the Ae^{2+} sites in the $Ae_3Fe_2O_5Cu_2Ch_2$ structure type compared to the Ae_2MO_3CuCh structure type led to the possibility of cation ordering whereby the larger site has the site preference of [$Ba^{2+} > Sr^{2+} > Ca^{2+}$][9] with the inverse trend observed for the smaller site. Cation ordering within this class of compound was discovered by Bradley Sheath on attempting to synthesise members of the solid solution $(Ca_xSr_{1-x})_2FeO_3CuCh$.[14] During an attempted synthesis of $CaSrFeO_3CuSe$ it was noted that CaO was a major impurity; equation 1.1 shows the reaction that was deduced to have occurred by Sheath:

$$2\ CaSrFeO_3CuSe \rightarrow CaSr_2Fe_2O_5Cu_2Se_2 + CaO \qquad (1.1)$$

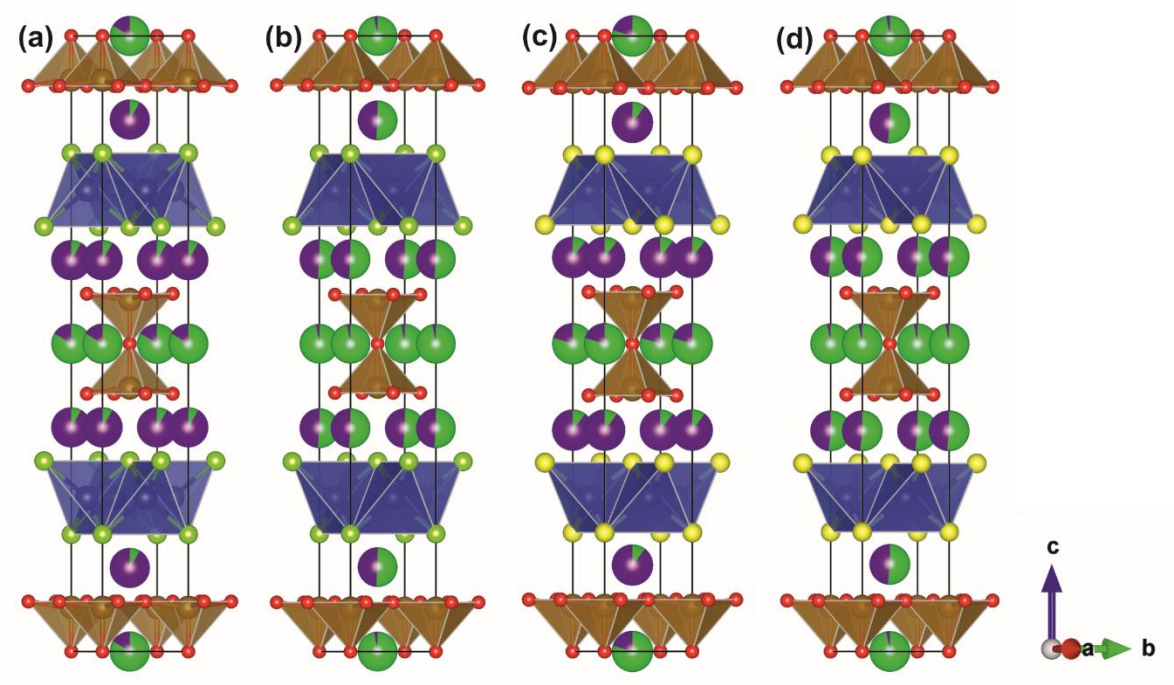


Figure 1.3 The fractional occupancies of the alkaline earth metal sites by Ca^{2+} (purple) and Sr^{2+} (green) of **(a)** $Ca_2SrFe_2O_5Cu_2Se_2$ **(b)** $CaSr_2Fe_2O_5Cu_2Se_2$ **(c)** $Ca_2SrFe_2O_5Cu_2S_2$ and **(d)** $CaSr_2Fe_2O_5Cu_2S_2$.[14]

The inability to realise this solid solution despite the existence of both end members i.e., Sr_2FeO_3CuCh (*Ch* = S, Se) and Ca_2FeO_3CuCh (*Ch* = S, Se) was attributed to the aforementioned sizes of the Ae^{2+} site within each structure type. The fact that the $Ae_3Fe_2O_5Cu_2Ch_2$ structure type has a 12-coordinate and 9-coordinate site as opposed to a 9

and 8-coordinate site means that it can more readily accommodate 2 different sized cations via a high degree of cation ordering as can be seen in Figure 1.3.

1.3.1.2 The $Ae_2MO_2X_2Ch_2$ structure type

Layered oxide chalcogenides of composition $Ae_2MO_2X_2Ch_2$ (*Ae* = Sr, Ba; *M* = Mn, Co, Ni, Cu, Zn; *X* = Cu, Ag and *Ch* = S, Se)[7,15–21] were also first described by Zhu and Hor in 1997.[17] This series adopts a crystal structure similar to that first described for $Sr_2Mn_3Sb_2O_2$[22] that crystallises in the *I*4/*mmm* space group as shown in Figure 1.4. It contains alternating layers of anti-fluorite type X_2Ch_2 layers with square planar MO_2 sheets sandwiched by Ae^{2+} cations.

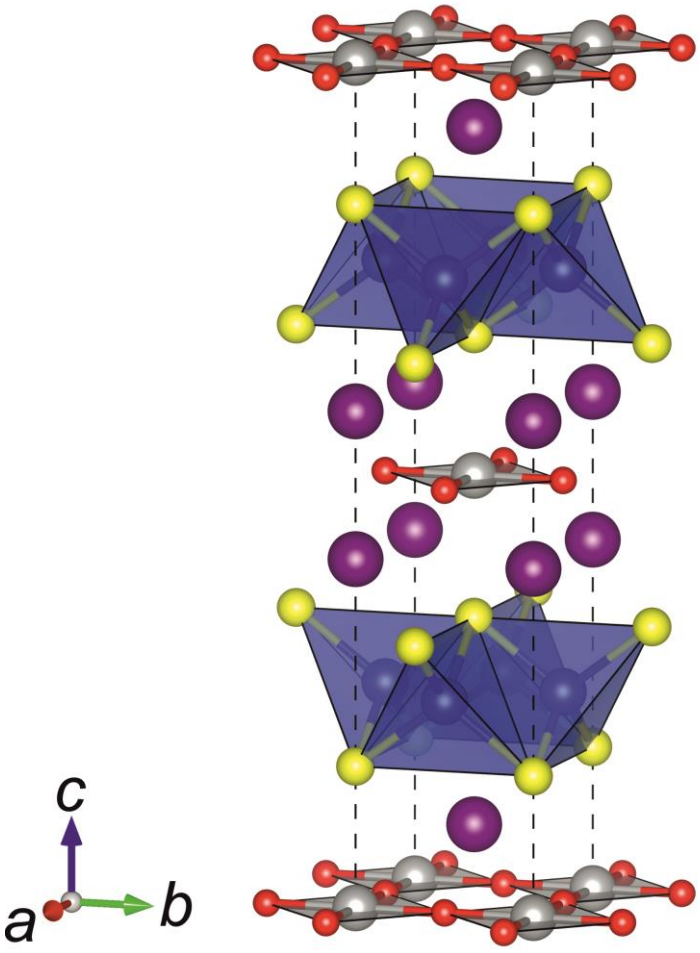


Figure 1.4 The $Ae_2MO_2Cu_2Ch_2$ structure type.

These "single-layer" oxide compounds contain transition metals in a distorted, elongated, octahedral environment, often in a lower oxidation state than is usual for pure oxide materials, and this has the potential to give way to interesting electronic and magnetic properties. The degree of elongation "built in" to the structure is comparable to that found for 1st order Jahn-Teller active 1st row cations.[23,24]

This structure type is part of a wider homologous series of compounds $(Ae_{n+1}M_nO_{3n-1})(X_{2m}Ch_{m+1})$ which has been heavily studied within the Clarke group.[7,23,25–27] In the next few sections, different members of this series will be introduced.

$m \geq 1$, $n = 1$

The triple-oxide-layer compound (m = 3, n = 1) is only known for $Sr_4Mn_{3-\delta}O_{8-\gamma}Cu_2Ch_2$ (*Ch* = S, Se) and its barium analogues and was first discovered by Zhu and Hor in 2000.[13] In these compounds, the anti-fluorite type Cu_2Ch_2 layers alternate with triple perovskite $(MnO_2)(SrO)(MnO_{1.5})(SrO)(MnO_2)$ layers with the anion deficient $MnO_{1.5}$ layer being able to be topochemically reduced using NaH or oxidised using XeF_2.[28]

The double-layer-oxide compound (m = 2, n = 1) is known for $Sr_3Sc_2O_5Cu_2S_2$ and $Ae_3Fe_2O_5X_2Ch_2$ (where *Ae* = Sr, Ba; *X* = Cu, Ag and *Ch* = S, Se)(see section 1.3.1.1).[11,15,29,30] In these compounds, the anti-fluorite type Cu_2Ch_2 layers alternate with double perovskite $(MO_2)(SrO)(MO_2)$-type layers with the central cation in a square pyramidal coordination and in a formal oxidation state of +3. $Sr_3Sc_2O_5Cu_2S_2$ is a *p*-type transparent conductor with a large band gap of 3.1 eV and high electrical conductivity with possible uses in optoelectronics.[31,32] Studies on widegap materials for these uses is one of the most important current fields in materials science.

***m* = 1, *n* = 1**

The single layer oxide compound (m = 1, n = 1) $Ae_2MO_2X_2Ch_2$ is known for *Ae* = Sr, Ba; *M* = Mn, Co, Ni, Cu, Zn; *X* = Cu, Ag and *Ch* = S, Se. Interestingly, compounds with $[Ag_2S_2]^{2-}$ layers do not seem to be able to be synthesised using typical high-temperature routes which is most likely due to steric arguments as sulfide is relatively small and so to accommodate the oxide slabs, the AgS_4 tetrahedron needs to be very distorted. Corresponding $[Ag_2Se_2]^{2-}$ compounds which could not be formed using ceramic syntheses have been synthesised using high pressure[33] as well as compounds with even larger $[Ag_2Te_2]^{2-}$ layers,[34] suggesting that high-pressure may be a useful medium to synthesise these less stable targets. It follows that this versatile series of oxide chalcogenides is extremely compositionally flexible resulting in a rich array of compounds with interesting properties. There is also the possibility of intrinsic deficiencies in the coinage metal occupancy, most notable in the *M* = Mn series due to the Mn +2 / +3 mixed oxidation state which is prevalent in mixed-anion compounds similar to the +3 / +4 mixed valence seen in the pure oxides. In the series $Ae_2MnO_2X_{2-\delta}Se_2$ (*Ae* = Sr, Ba; *X* = Cu, Ag),[35–37] the Ba analogues are closer to complete stoichiometry (i.e., smaller δ) than their Sr counterparts implying that they have a lower oxidation state induced by the longer Mn-O bond. Changing the *M*-O bond within the crystal structure can be a powerful tool to change the properties of a material as will be explored in chapter 3 looking at the spin-state crossover in $Sr_2NiO_2Cu_2(Se_{1-x}S_x)_2$.[38]

It is for *M* = Mn and Co that the majority of these phases are found, with $Sr_2MO_2Cu_2S_2$, $Sr_2MO_2Cu_2Se_2$, $Sr_2MO_2Ag_2Se_2$, $Ba_2MO_2Cu_2Se_2$, and $Ba_2MO_2Ag_2Se_2$ and $Ba_2CoO_2Cu_2S_2$ all having been previously reported.[16,17,35,37,39] Due to the lower 3rd ionisation of Fe, it is more easily oxidised than Mn and Co and higher oxidation states have higher affinities for larger

coordination numbers and as shown in Figure 1.5, it prefers to form compounds with the *m* = 2 structure type.

The story is a bit more complicated when *M* = Ni and Cu. These phases have been reported for $Sr_2MO_2Cu_2S_2$, $Sr_2MO_2Cu_2Se_2$ and $Ba_2MO_2Cu_2Se_2$.[15,35,40] The sulfides however are metastable and require an alternative, low-temperature synthetic approach and even then, cannot yield pure products; owing to the relative ease of target decomposition, The Ba analogues also cannot be produced phase pure or stoichiometrically with $Ba_2CuO_2Cu_2Se_2$ being intrinsically deficient in O. More recently, this family of compounds have been expanded using high-pressure in the aforementioned $Ae_2NiO_2Ag_2Se_2$ (*Ae* = Sr, Ba), whereby using elevated pressure during synthesis seems to alleviate the steric challenges of having the size mismatch between the MO_2 sublattice and larger coinage metal $[Ag_2Se_2]^{2-}$ layers.[33]

For *M* = Zn, only $Sr_2ZnO_2Cu_2Ch_2$ (*Ch* = S, Se) may be formed as phase-pure products with $Ba_2ZnO_2X_2Se_2$ (*X* = Cu, Ag) made as a majority phase. Unlike their counterparts with un-filled *d*-orbitals, these d^{10} compounds tend to be coloured band gap insulators as opposed to the dull black powders found for the $d \neq 10$ compounds which are magnetic Mott-Hubbard-type insulators.[41,42]

This single layer oxide compound can also be extended into oxide pnictides. The oxide arsenide, $Sr_2CrO_2Cr_2As_2$, which was first synthesised by Jiang et al., in 2015[43] has recently been expanded on by Xu et al., to include the Ba analogue.[24,44] Powder neutron diffraction has shown both analogues to have checkerboard type antiferromagnetic ordering in the arsenide layer, with T_N for the Sr analogue being 600 K and the Ba analogue 465 K. The Cr sublattice within the oxide layer also order antiferromagnetically at 330 K for $Sr_2CrO_2Cr_2As_2$ and 230 K for $Ba_2CrO_2Cr_2As_2$.

Soft chemistry is also possible in this class of material. For example, the oxidative deintercalation of Cu from $SrMnO_2Cu_{1.5}S_2$ with I_2 results in a modulated crystal structure of $Sr_2MnO_2Cu_{1.3}S_2$.[19] The Te analogue $Sr_2MnO_2Cu_{1.82}Te_2$ has no long-range magnetic ordering, but a Warren peak in the low temperature neutron diffractogram is indicative of short-range magnetic ordering.[26] Topochemical oxidation of this phase using I_2 allows a phase of composition $Sr_2MnO_2Cu_{1.58}Te_2$ to be accessed which has a Mn^{2+}/Mn^{3+} valence ratio close enough to 1:1 for long range magnetic ordering to be "turned on" with magnetic moments ferromagnetically coupled in the plane but antiferromagnetically coupled in the stacking direction. Furthermore, similar treatment of $Sr_2CoO_2Ag_2Se_2$ leads $Sr_2CoO_2Ag_{1.5(2)}Se_2$ which has a ferromagnetic-like transition at ≈ 70 K, with a large spin-glass element that freezes below ≈ 30 K.[40]

Across the first-row transition metals, towards the end of the series the +2 state becomes more favourable, especially for Ni and Cu. Most of the soft chemistry performed on these compounds tends to be oxidative deintercalation and so it owes that most of the soft chemistry in these structure types is centred around the Mn and Co analogues due to their ability to be more easily oxidised above +2.

$m = 1, n > 1$

The single oxide compounds with thicker chalcogenide blocks (m = 1, n = 2, 3) is only known for when M = Mn and Ch = S. In 2003, a compound of composition $Sr_4MnO_4Cu_5S_5$ was synthesised with an average n of 1.5.[45] Here, single layers with thickness Cu_2S_2 alternate with double-thickness Cu_3S_3 layers. Since then, two compounds have been synthesised with fully double thickness chalcogenide layers, $Sr_2MnO_2Cu_4S_3$ and fully triple thickness chalcogenide layers, $Sr_2MnO_2Cu_6S_4$.[25] In all these compounds there are copper vacancies to

compensate for charge balance of the mixed Mn valence which has an average of +2.5. These vacancies are disordered at room temperature due to the high mobility of the Cu ions which is a common phenomenon in layered oxide chalcogenides, but vacancy ordering is observed on cooling. $Sr_2MnO_2Cu_{3.5}S_2$ can have as many as 3 different ordering schemes depending on the cooling rate used. As described later in section 1.4.5, these compounds display metamagnetism.

The relationship between the building blocks in the homologous series $(Ae_{n+1}M_nO_{3n-1})(X_{2m}Ch_{m+1})$ is shown pictorially in Figure 1.5. Note that the anti-fluorite coinage metal chalcogenide block can also be made up of pnictides and other first-row transition metals such as $[Cr_2As_2]^{2-}$ layers seen in $Sr_2CrO_2Cr_2As_2$.

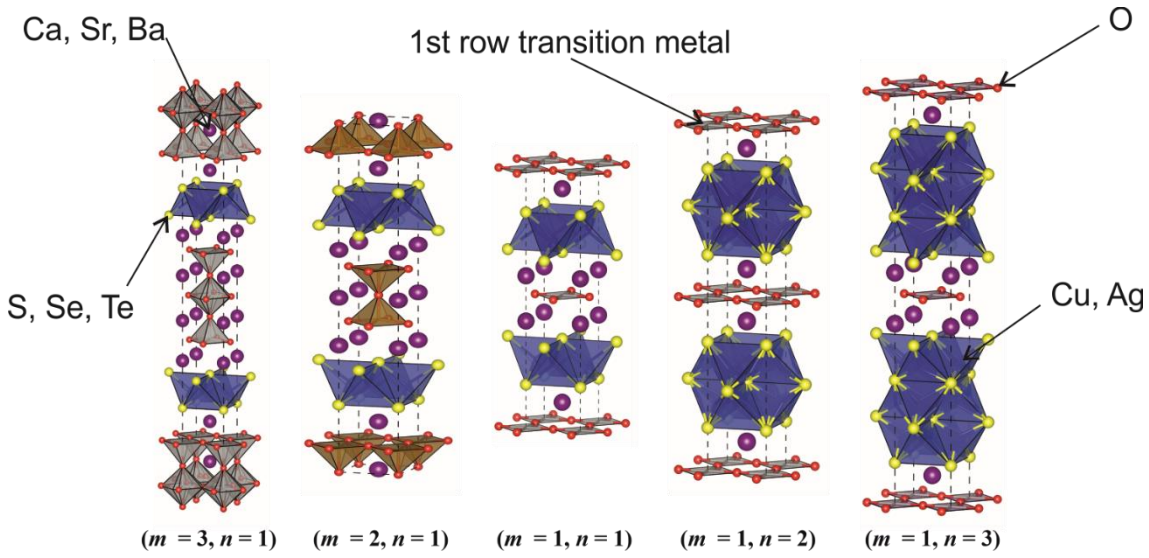


Figure 1.5 The homologous series $(Ae_{n+1}M_nO_{3n-1})(X_{2m}Ch_{m+1})$.

1.3.1.3 The ZrSiCuAs structure

The ZrSiCuAs structure is an extremely versatile one with an array of already known compositions.[46–49] It can be thought of as the "filled" PbFCl structure and crystallises in the tetragonal *P*4/*nmm* space group. This is the structure of the oxide chalcogenide CeAgOSe

which is briefly commented on at the end of this thesis with its structure shown in Figure 1.6. It has PbO-type CeO layers with the Ce^{3+} cation in a distorted square anti-prismatic site and coordinated to 4 oxide and 4 selennide anions and is stacked alternately with anti-PbO-type AgSe layers whereby the Ag^{+} cations are tetrahedrally coordinated to 4 selenide ions. Materials with this structure type have already shown to be promising materials with real life application with their properties enhanced by the presence of two anions i.e., oxide chalcogenide or oxide pnictide, such as transparent conductors[50] or the recently topical iron oxide arsenide high temperature superconductors.[51]

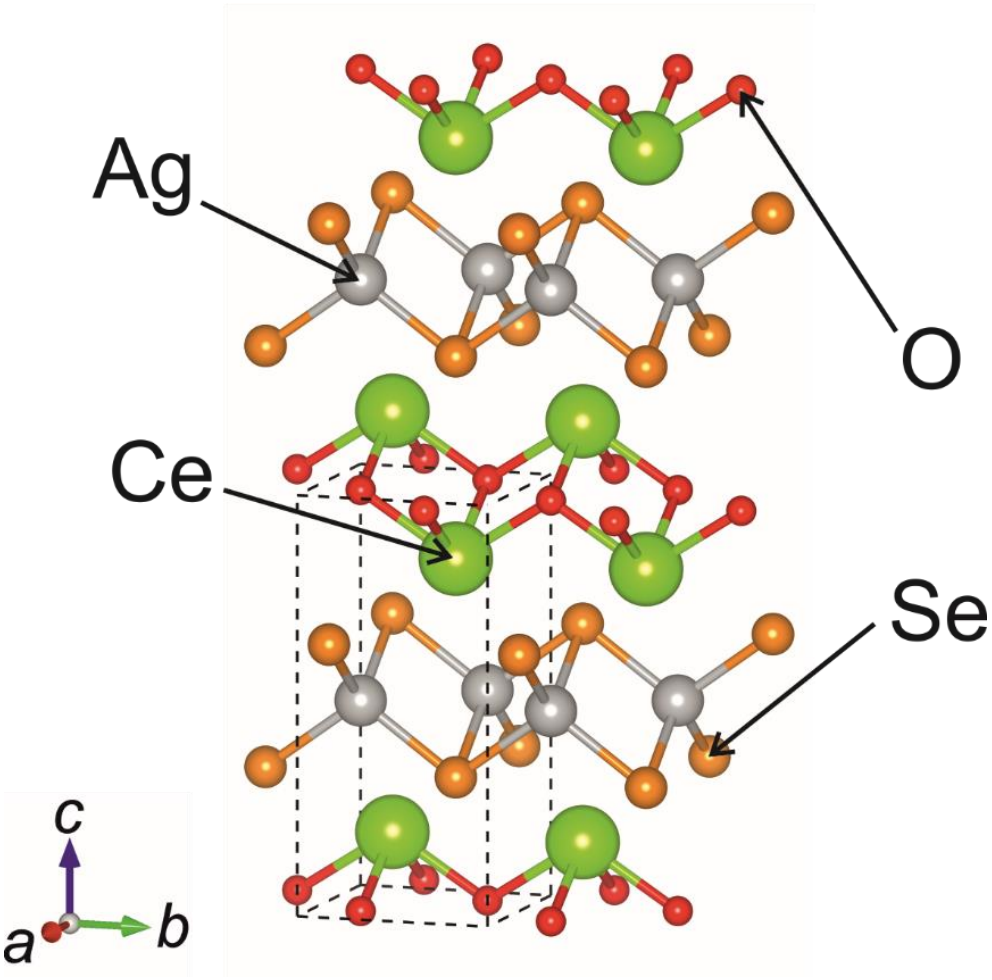


Figure 1.6 The structure of CeAgOSe.

1.3.2 Oxide halides

The oxide halides are much more studied than oxide chalcogenides with many known examples in the literature.[52] The same anion segregation is observed in oxide halides leading to layered structures except for the oxide fluorides where both O^{2-} and F^{-} are small. In these compounds it is common to see a random distribution of anions throughout the lattice on the same crystallographic site i.e., no long-range ordering of anions.

More recently, fluorination of disordered rocksalt cathodes such as $Li_{1.9}Mn_{0.95}O_{2.05}F_{0.95}$ in Li-ion batteries has led to reduced oxide oxidation at high voltage and therefore more reversible redox reactions,[53] presumably due to lowering the Mn oxidation state and hence more of the oxidative redox is on Mn. The discovery of a series of high T_C superconductors, $Sr_{2-x}A_xCuO_2F_{2+\delta}$ (A = Ca, Ba), especially $Sr_{1.4}Ba_{0.6}CuO_2F_{2+\delta}$ with a critical temperature, T_C, of 64 K has resulted in a renewed interest in oxide halide precursors and their structurally related analogues.[54] In the next section, the structures of the oxide halides, $SrNiO_2Cl_2$, which is focussed on in chapter 3 along with the closely related Sr_2NiO_3Cl are discussed.

1.3.2.1 $Sr_2NiO_2Cl_2$ and Sr_2NiO_3Cl

$Sr_2NiO_2Cl_2$ was first synthesised by Tsujimoto et al., in 2014[55] using a high-pressure synthesis and is closely related to the $Ae_2MO_2X_2Ch_2$ structure type described in section 1.3.1.2. The square planar NiO_2 sheets in this compound alternate with double rocksalt Sr_2Cl_2 layers as opposed to the $ThCr_2Si_2$-type $Ae_2X_2Ch_2$ layers in the $Ae_2MO_2X_2Ch_2$ structure and hence the structures are related by formally removing all the coinage metal from $Ae_2MO_2X_2Ch_2$ and substituting the chalcogen ions by chlorine ions. The temperature dependence of the magnetic susceptibility showed a gradual drop with a cusp at ≈ 210 K

which was identified as the Néel temperature suggesting that this oxide halide displays long-range antiferromagnetic ordering. This is investigated further in chapter 3 using powder neutron diffraction to investigate these findings.

The substitution of one Cl in $Sr_2NiO_2Cl_2$ by O yields a new compound, Sr_2NiO_3Cl.[56] This compound was also first synthesised by Tsujimoto et al., in 2013 and was the first example of incorporation of oxygen and halogen anions in trivalent centred perovskites. Sr_2NiO_3Cl adopts a tetragonal structure and crystallises in the *P*4/*nmm* space group as a result of a lowering in symmetry from the fluoride analogue, Sr_2NiO_3F which itself crystallises in *I*4/*mmm* due to O/Cl ordering.[56] This structure is closely related to the Ae_2MO_3CuCh structure described in section 1.3.1.1, with the key difference being the presence or not of the coinage metal ion, reinforcing the relationship and close interplay between the structures. Both of these structures are shown visually in Figure 1.7. Sr_2NiO_3Cl has a broad maxima, characteristic of low-dimensional antiferromagnets, in the temperature dependence of its magnetic susceptibility with a Néel temperature, T_N, of 33 K.[57]

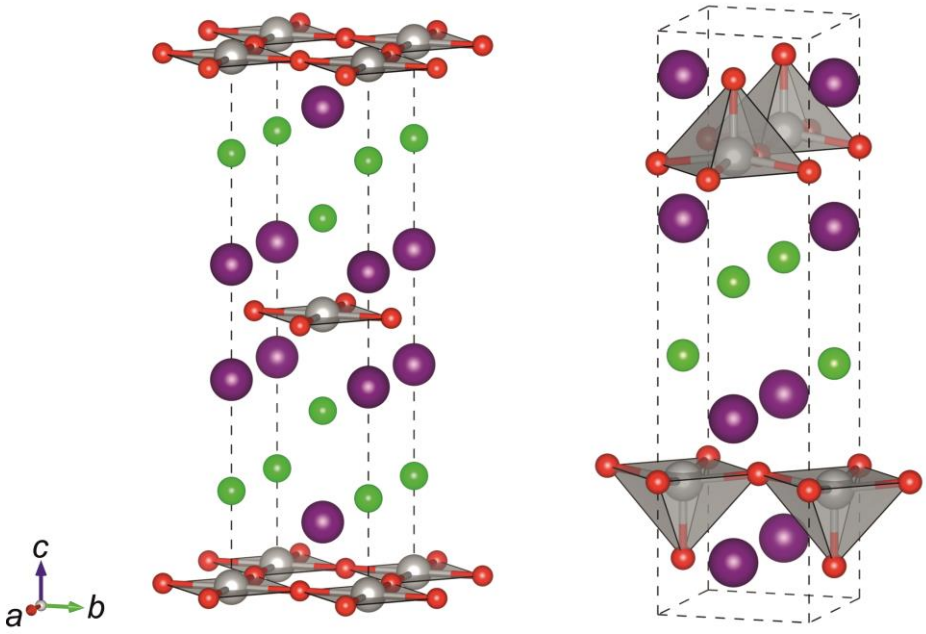


Figure 1.7 The $Sr_2NiO_2Cl_2$ structure (left) and the Sr_2NiO_3Cl structure type (right) .

1.4 Magnetic behaviour of solids

1.4.1 Paramagnetism

Paramagnetism is displayed in systems which contain unpaired electrons (S ≠ 0). It arises from the fact that unpaired electrons contain net electronic angular momentum. The orbital motion of the electrons produce a magnetic moment perpendicular to the plane of motion in addition to an intrinsic moment related to the electron's spin. These can act independently, or they can couple via spin-orbit coupling. In an applied magnetic field, the spins will align with the field in order to lower the system's energy. There are 3 main types of paramagnetism which are discussed in the following 3 sections.

1.4.1.1 Curie paramagnetism

The simplest model of paramagnetism is by applying Curie's law. This assumes that the metal centres within a solid do not interact and that the moments do not vary with temperature. In the Curie law, there is an inverse relationship between the magnetic susceptibility, which is a measure of how magnetised a material will become in an applied field (which for a paramagnet is a linear dependence), and temperature which is shown in equation 1.2.

$$\chi_{\mathrm{mol}} = \frac{C}{T} = \frac{N_{\mathrm{A}}\mu_{\mathrm{eff}}^2\mu_{\mathrm{B}}^2}{3k_{\mathrm{B}}T} \qquad (1.2)$$

Here, N_{A} is Avogadro's constant, k_{B} is Boltzmann's constant, T is the temperature, μ_{B} is the Bohr magneton, μ_{eff} is the effective magnetic moment and C is the Curie constant. Once this is known, the effective magnetic moment can be approximated to equation 1.3.

$$\mu_{\text{eff}} = 2.84\sqrt{C} \tag{1.3}$$

The magnetic properties of unpaired electrons are comprised of 2 components, the orbital angular momentum, **L**, and the spin angular momentum, **S**, to give a total angular momentum, **J**, however this breaks down for f^6 ions such as Eu^{3+} owing to low energy *J* states being thermally populated.

$$\mathbf{J} = \mathbf{L} + \mathbf{S} \tag{1.4}$$

The total angular momentum is related to the effective magnetic moment via the Landé formula shown in equation 1.5 where g is the electron spin *g*-factor which is shown in equation 1.6.

$$\mu_{\text{eff}} = g\sqrt{J(J+1)} \tag{1.5}$$

$$g = 1 + \frac{J(J+1) + S(S+1) - L(L+1)}{2J(J+1)} \tag{1.6}$$

The ligand field present around the first-row transition metals described within this thesis lifts the degeneracy of the 3*d* orbitals which leads to the orbital angular momentum most usually being completely quenched and so the magnetic moment can be closely approximated by the spin-only approximation shown in equation 1.7 but note there can also be deviations from this formula such as in the case of Co^{2+} which normally has a large orbital contribution to the magnetic moment which is investigated in chapter 4.

$$\mu_{\text{so}} = g_{\text{so}}\sqrt{S(S+1)} \tag{1.7}$$

In the spin-only approximation $L = 0$ and hence $J = S$. Substitution into equation 1.6 results in the magneto-gyric ratio for the electron that links the spin angular momentum to the magnetic moment becoming equal to 2.

Combining equations 1.3 and 1.6 results in:

$$\mathrm{C} \approx \frac{S(S+1)}{2} \tag{1.8}$$

Therefore we can use the Curie constant to calculate the number of unpaired electrons (2*S*) which is extracted from the gradient of a plot of χ^{-1} against temperature.

1.4.1.2 Curie-Weiss paramagnetism

In the complex solids described within this thesis, the interaction between the magnetic moments localised on the metal centres cannot be ignored. Instead, the Curie-Weiss law is adopted, $\chi_{mol} = C/(T-\theta)$, which is shown in full in equation 1.9.

$$\chi_{\mathrm{mol}} = \frac{N_{\mathrm{A}}\mu_0}{3k_{\mathrm{B}}(T-\theta)}(\mu_{\mathrm{eff}})^2 \tag{1.9}$$

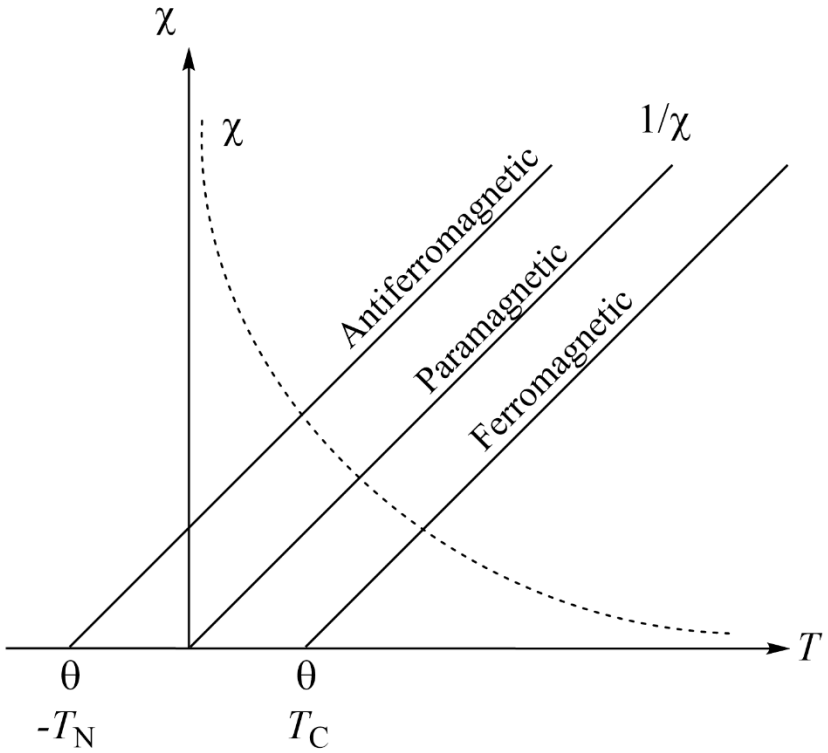


Figure 1.8 χ^{-1} against temperature for a Curie-Weiss antiferromagnet, paramagnet and ferromagnet.

Here, N_A is Avogadro's constant, k_B is Boltzmann's constant, T is the temperature, μ_0 is the vacuum permeability, μ_{eff} is the effective magnetic moment and θ is a measure of the mean strength of the coupling between the metal centres. If θ is greater than 0, then the interactions are net ferromagnetic and if θ is less than 0 then the interactions are net antiferromagnetic, this is shown visually in Figure 1.8.

This coupling can then lead to long-range magnetic order in ferromagnets and antiferromagnets where the Curie temperature, T_C, or the Néel temperature T_N should occur at the value of θ. When θ vastly exceeds the observed ordering transition in the magnetisation versus temperature plot, it may be taken as a good indicator of frustration. In general, the order of paramagnetism is $1 – 100 \times 10^{-4}$ emu mol^{-1}.

1.4.1.3 Pauli paramagnetism

Pauli paramagnetism is a special case of paramagnetism which occurs when the electrons are delocalised throughout the system such as in a metal. When no field is applied then the conduction band has both its spin up and spin down band equally occupied. However, when a field is applied, this degeneracy is lost, and the spin state co-aligned with the applied field becomes lower in energy and the spin state anti-aligned becomes higher in energy. This results in higher occupation of the spin state aligned with the magnetic field and a net magnetisation occurs, this can be seen schematically in Figure 1.9.

Pauli paramagnetism is independent of temperature and because it arises from a small number of electrons close to the Fermi level, E_F, the effect is small and of the order 1 to 100 $\times 10^{-7}$ emu mol^{-1}, much smaller than for localised-moment paramagnetism.

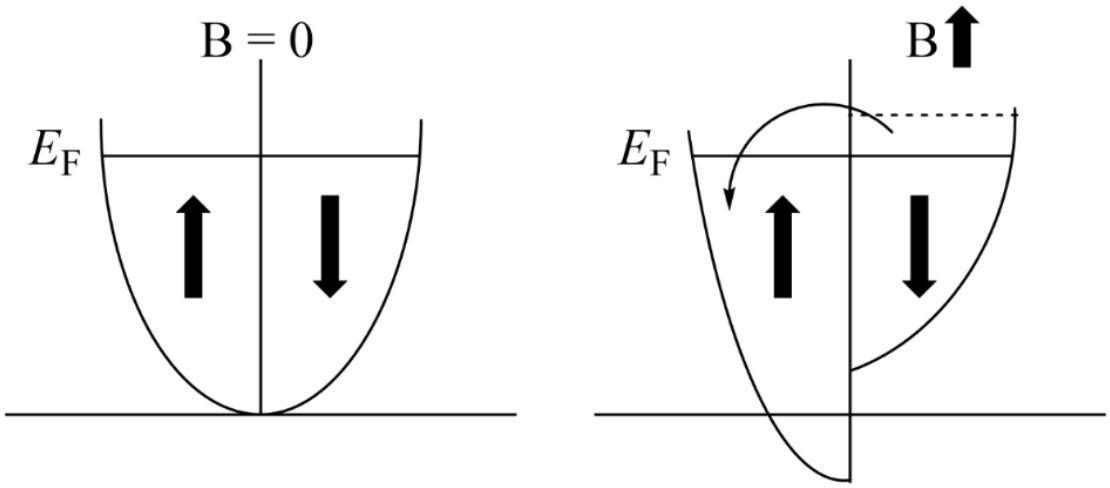


Figure 1.9 The change in the density of states (DoS) of a free electron when a magnetic field is applied.

1.4.2 Ferromagnetism

Similar to paramagnets, ferromagnets contain metal centres with unpaired electrons. This can occur in itinerant spin-polarised systems like Fe and Ni where one spin state is energetically preferred at the Fermi level or localised moment systems such as Au_4Mn[58] which couples along the *c* axis and has a $T_C \approx 387$ K or Rb_2CrCl_4 which has a $T_C \approx 63$ K with spins which order ferromagnetically within the *ab*-plane.[59]

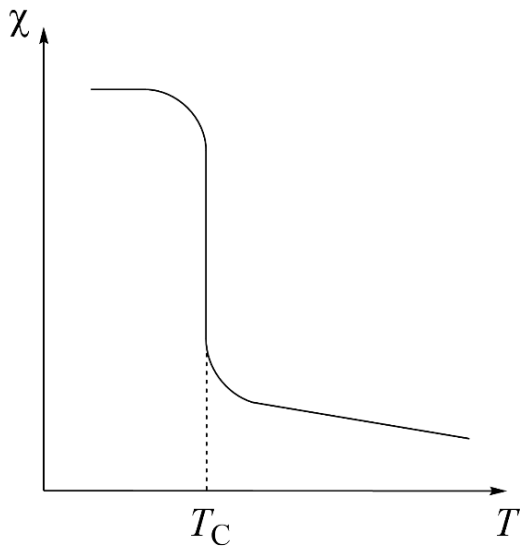


Figure 1.10 The change in magnetic susceptibility with temperature for a ferromagnetic material showing the long-range ordering Curie temperature, T_C.

Above this temperature, ferromagnets show similar behaviour to that of a paramagnet and obey the Curie-Weiss law. When an external magnetic field is applied, the magnetic domains align parallel to the field and produce a net magnetisation. Because the spins are locked in clusters of domains, the thermal randomisation of spins is opposed with the coupling within the domains keeping them aligned and hence in ferromagnets there is mutual co-alignment throughout the material, meaning it is much easier to reach saturation. This also means that below T_C, the increase in χ is much greater for a ferromagnet than for a paramagnet. This "paramagnetic to ferromagnetic" transition can be seen in Figure 1.10.

Ferromagnets can be classified as "soft" or "hard." Soft magnetic materials are those where movement of the domain wall is easy and hence it is relatively straightforward to magnetise and demagnetise soft magnets. On the other hand, in hard magnetic materials, it is difficult to magnetise and demagnetise the material. Movement of the domain wall can be extremely difficult and hence these types of material are used for permanent magnets. Hard magnets can retain their magnetism even once the external applied field has been removed.

The susceptibilities of ferromagnets tend to be relatively large and in the order of $1 – 100 \times 10^{-2}$ emu mol^{-1}.

1.4.3 Antiferromagnetism

The most common form of coupling between unpaired electrons is antiferromagnetically, whereby neighbouring spins align anti-parallel leading to a net magnetisation of 0. Again, there is competing interactions between the coupling of the spins and thermal randomisation. Long-range ordering of the spins is observed below the Néel temperature, T_N. Well above

this temperature, antiferromagnets show similar behaviour to that of a paramagnet and obey the Curie-Weiss law.

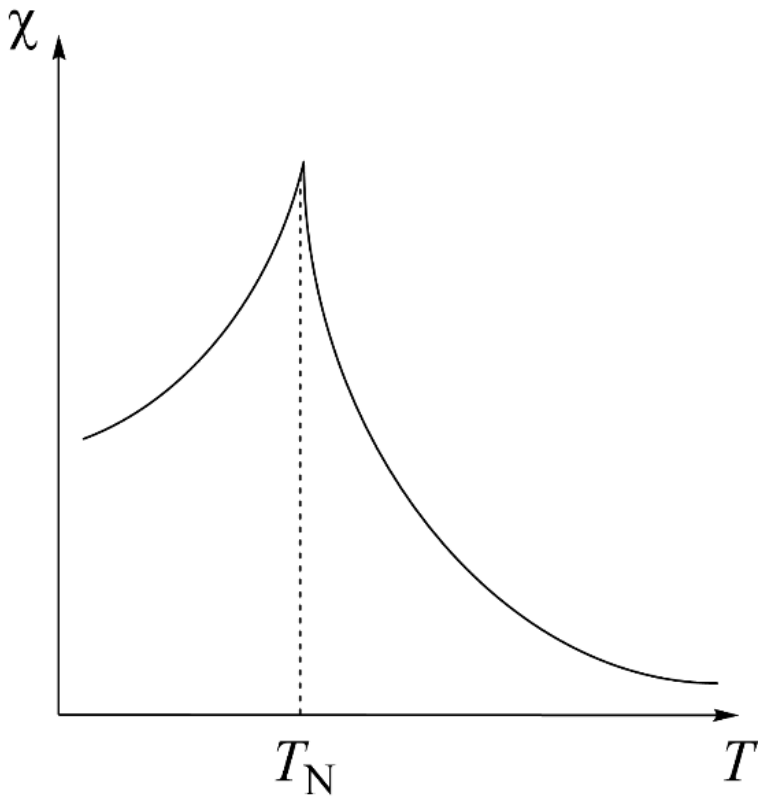


Figure 1.11 The change in magnetic susceptibility with temperature for an antiferromagnetic material showing the long-range ordering Néel temperature, T_N.

The susceptibility of an antiferromagnet decreases below T_N as shown in Figure 1.11. As the energy available for the thermal randomisation of spins decreases, the antiferromagnetic coupling between neighbouring metal centres dominates. This means the spins are less able to align with the field and a reduction in the susceptibility is observed. A clue to the dimensionality within an antiferromagnetic system can be garnered from the profile of the cusp in the susceptibility. A sharp transition usually indicates long-range 3D ordering whereas a broader cusp usually is indicative of shorter-range order with lower dimensionality. The susceptibilities of antiferromagnets tend to be small and in the order of $1 – 100 \times 10^{-4}$ emu mol^{-1}.

1.4.4 Diamagnetism

Diamagnetism is observed in all atoms or ions that contains closed shells of electrons. The application of an external field induces orbital rotation of the electrons around the nucleus. The resulting small currents produce a field that opposes the external one as is set out by Lenz's law. In the complex solids discussed in this thesis, because they contain first row transition metals with outer shell unpaired electrons, the diamagnetic contribution (which is small in magnitude and is of the order -1 to -100×10^{-6} emu mol^{-1}) can typically be dismissed as insignificant, especially if strongly paramagnetic ions are present.

1.4.5 Metamagnetism

Metamagnetic materials are observed to have a magnetic phase transition from antiferromagnetic to ferromagnetic by the application of a magnetic field. One such compound is $MnAu_2$. It has a spiral spin structure on Mn and undergoes a spiral to ferromagnetic phase transition in an applied field of 10 kOe at 300 K.[60] This kind of magnetism is also observed in compounds similar to those described within this thesis. In the homologous series $Sr_2MnO_2Cu_{2m-\delta}S_{m+1}$ where m = 2 and 3, $\delta \approx 0.5$, the Mn moments within the basal plane couple ferromagnetically whereas there is antiferromagnetic coupling between the MnO_2 sheets leading to A-type antiferromagnetism. Metamagnetism is observed in these two compounds, and it is found for $Sr_2MnO_2Cu_{3.5}S_3$ and $Sr_2MnO_2Cu_{5.5}S_4$ that below 25 K, an application of a 1.3 and 0.06 T field respectively leads to the compounds being driven into the fully ordered ferromagnetic state – i.e., the weak inter-layer antiferromagnetism is overcome by the applied field.[25]

1.4.6 Spin-glass materials

By definition, a glass is characterised as having an extended 3D network lacking symmetry and long-range periodicity. This concept can be applied to materials described as spin-glasses whereby the atoms of a glass represent the spins within one of these systems. Spin-glasses arise when there are strong interactions between spins but competition within the magnetic framework arising from disorder in the arrangement of spins results in magnetic frustration. Such an example of magnetic frustration is shown in Figure 1.12 in which the 3 moments cannot all interact in a mutually antiferromagnetic fashion.

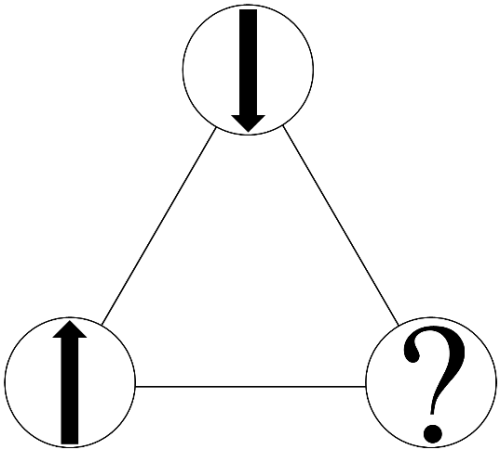


Figure 1.12 Schematic diagram showing spin frustration within a triangular lattice.

The susceptibility of a true spin glass should be static until its ordering temperature, T_G, however a true spin glass is not observed often in reality and long-range order may still persist within the sample, but any disorder present can enhance the glassiness and reduce the maximum susceptibility obtainable. Deviations in the ZFC / FC curves tend to be more pronounced in spin glasses due to the "locked-in" state of local domains differing in the presence or absence of a magnetic field and there is also a history dependence and so a hysteresis loop is normally displaced and does not close up when one is below the freezing temperature.

1.5 Models of magnetic exchange

The interactions between magnetic centres can proceed through various different mechanisms.

There are long-range through-space interactions which show r^{-3} dependence, however, these are generally too weak in magnitude to account for observable magnetic order and are usually suppressed even at very low temperatures by thermal energy.

In magnetic solids, through bond interactions are much more important. One such interaction being direct exchange which comes from overlapping orbitals. This is however very short range (showing r^{-12} dependence) and so is limited only to nearest-neighbour ions. Direct exchange looks similar to metal-metal bonding but in this exchange mechanism, the electrons remain localised on their respective metal centres. In the more complex solids discussed in this thesis, direct exchange is not very prevalent as the metal centres are too far apart to have direct orbital overlap and as such, an indirect pathway is needed to couple these centres through "bridging" orbitals which tend to be oxygen 2*p* orbitals. This is known as superexchange.

1.5.1 Superexchange

The delocalisation of electron density within a system can result in a lowering of energy which is favourable. Non-magnetic anions can bridge the gap between two magnetic metal centres which prevent them interacting via direct exchange. The super-exchange interaction, especially when self-coupling is involved (i.e., the same metal centre on either side of the anion) tends to be antiferromagnetic when orbitals align at 180 ° which is most common in

the compounds within this thesis and perovskites in general. The corresponding 90 ° coupling tends to be ferromagnetic. Superexchange can occur though σ-type or π-type interactions although σ-type superexchange is more dominant and results in a stronger coupling. An example of σ-type superexchange can be seen in Figure 1.13.

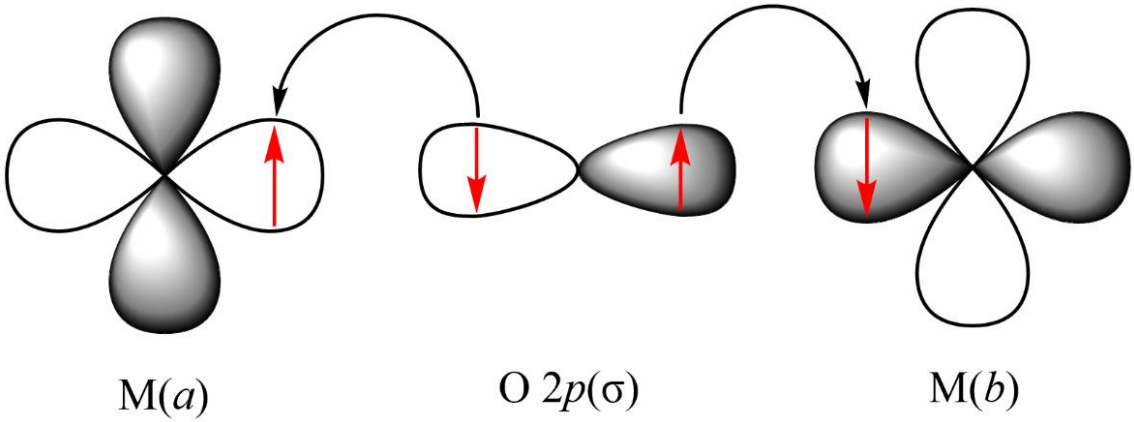


Figure 1.13 Antiferromagnetic coupling between 2 metal centres mediated by 180 ° superexchange through a bridging O 2*p* orbital.

It can be visualised using the cartoon in Figure 1.13 which shows 2 metal centres with a singly occupied e_g orbital and an O 2*p*(σ) orbital. Pauli's exclusion principle states that no two fermions (e.g., electrons) within the same atom can have the same 4 principal quantum numbers and so if the electron in M(*a*) is "spin-up" then it must interact with the "spin-down" electron of the O 2*p*(σ) orbital. To maintain spin neutrality, the other spin within the O 2*p*(σ) must be "spin-up" and interact with a "spin-down" electron in M(*b*).

Table 1.1 Néel temperatures for some first-row transition metal oxides.

Transition metal oxide	T_N / K
MnO	122
FeO	198
CoO	291
NiO	525

The strength of the interaction depends on the degree of geometric and energy overlap between the orbitals, this becomes more apparent when the Néel temperatures of the first-row transition metal oxides is observed which can be seen in Table 1.1. Going across the transition metal series, increasing nuclear charge leads to a lowering of the energy of the 3*d* orbitals leading to better energy overlap with the lower-laying O 2*p* orbitals, resulting in stronger superexchange and hence stronger magnetic interactions which require more thermal energy to overcome i.e., a higher Néel temperature.

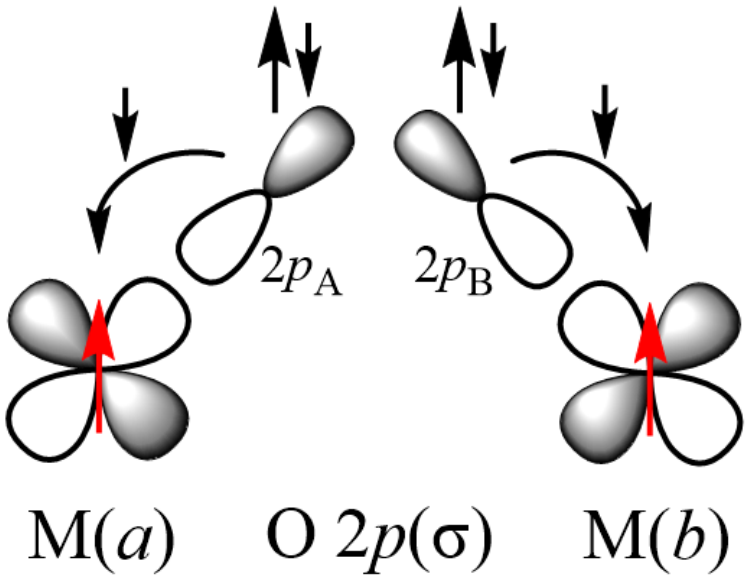


Figure 1.14 Ferromagnetic coupling through 90° superexchange.

Despite usually being antiferromagnetic, 180° superexchange can also be ferromagnetic. If the e_g of M(*a*) is partially filled and the e_g of M(*b*) is empty, then the electron density between M(*a*) and O 2*p*(σ) will interact as before but now electron density from O 2*p*(σ) is being donated into an empty M(*b*) e_g orbital. Hund's rule states that electrons in partially filled orbitals on the same ion will have parallel spins and therefore the resulting spins on the metal centres will be aligned parallel resulting in ferromagnetic coupling. The nature of this superexchange coupling can be generally described by the Goodenough-Kanamori rules.[61–63]

Ferromagnetic interactions can also be achieved 90 ° superexchange where spin correlation within the oxygen ligand favours parallel alignment of the transferred electron density. This scheme is shown above in Figure 1.14.

1.5.2 Double exchange

Double exchange interactions are important in compounds which display mixed-valence within the system and lead to ferromagnetism. The classic example of double exchange is in the rare earth manganites $Ln_{1-x}A_xMnO_3$ where *Ln* is a trivalent rare earth metal and *A* is a divalent alkaline earth metal. For double exchange to occur, there must be a large enough concentration of both cations so that it is possible to have continuous chains of alternating valence. In $Ln_{1-x}A_xMnO_3$, high spin Mn^{3+} has a singly occupied e_g electron and Mn^{4+} has an empty e_g set. There can therefore be a transfer of an electron from Mn^{3+} to Mn^{4+}.[64] Again, Hund's rule states that electrons in partially filled orbitals on the same ion will have parallel spins and therefore this double exchange can only happen when the t_{2g} and e_g electrons of both Mn^{3+} and Mn^{4+} are aligned parallel as shown in Figure 1.15. This delocalisation of electrons results in metallic behaviour.

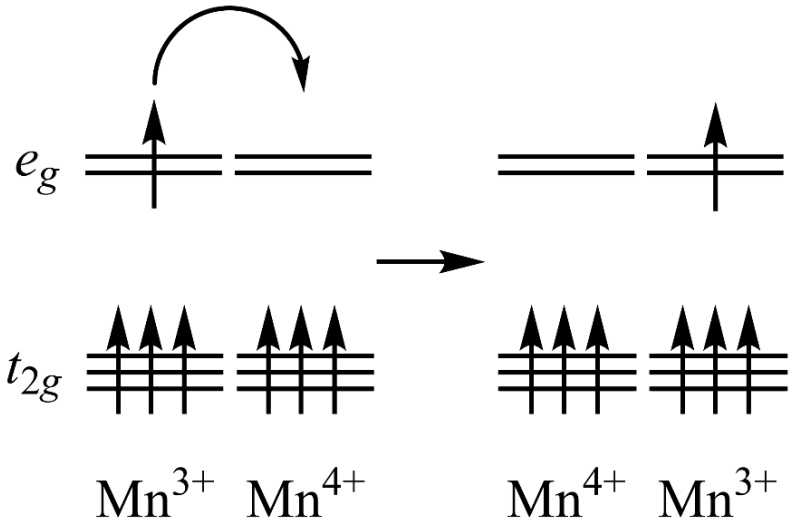


Figure 1.15 Ferromagnetic coupling through double exchange.

1.6 Topochemical alterations

A topochemical reaction is whereby the host structure remains largely unchanged. These reactions are usually done at lower temperatures than typical solid-state reactions and are useful for fine-tuning the electronic properties of the solid. Lower temperatures ensure that the host does not have enough free energy to counter the change in stoichiometry by altering the structure.

Topochemical reactions are used extensively in chapter 4 whereby *n*-Butyllithium is used to induce cation exchange on a series of Co-containing layered oxide chalcogenides. There are many examples within the literature of such reactions. The intercalation of Li into TiS_2 to form Li_xTiS_2 is continuous for $0 \leq x \leq 1$ which is most readily seen in the expansion of the *c* lattice parameter along the stacking direction and this system was especially important as it was a prototypical Li-ion battery electrode material.

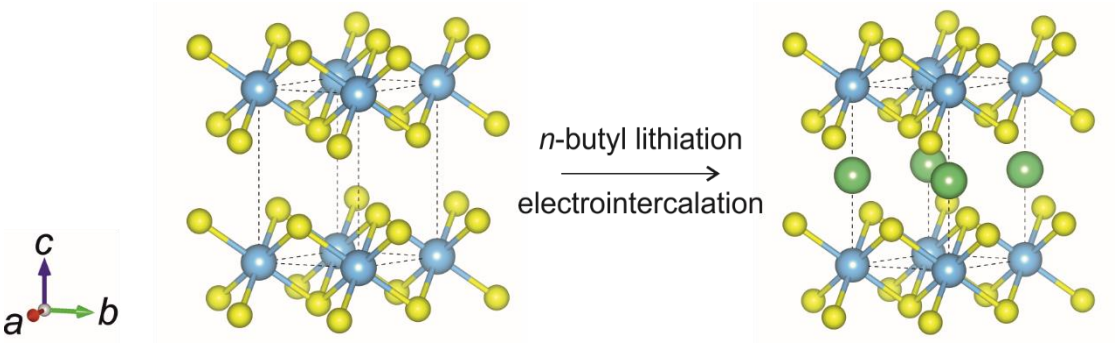


Figure 1.16 Intercalation of Li into TiS_2.[65]

Another example is the induction of superconducting behaviour in the Mott-Hubbard insulator La_2CuO_4. Large on-site electron-electron repulsions in Cu^{2+} *d*-bands result in this compound being an insulator. However, it can be heated in an oxygen rich environment to oxidise the Cu and result in a new phase – $La_2CuO_{4+\delta}$ which is observed to superconduct at a critical temperature, T_C, of 39 K.[66]

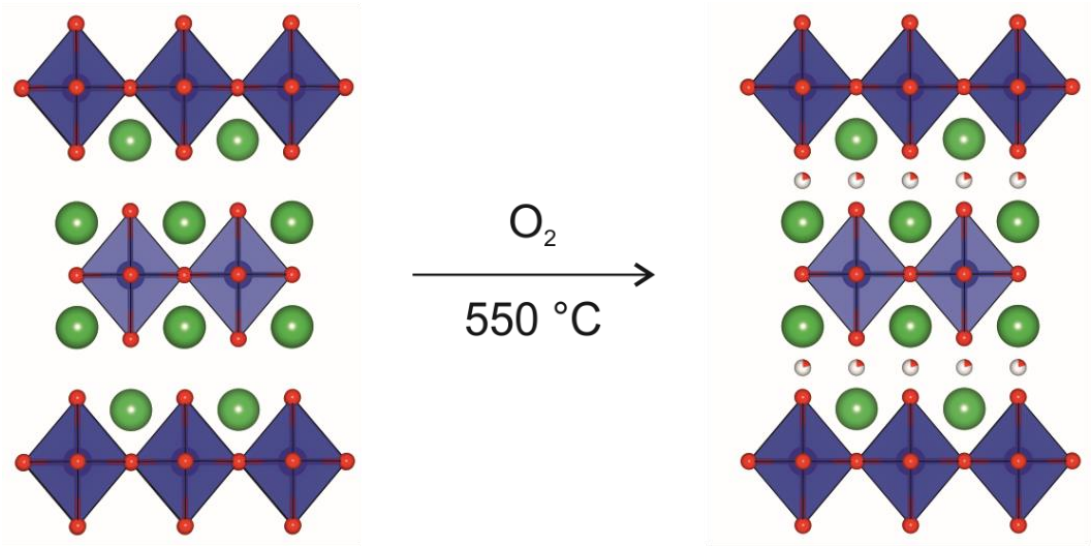


Figure 1.17 Topochemical oxidation of La_2CuO_4 to from $La_2CuO_{4+\delta}$.

Perhaps the most important topochemical reaction is that of the modern Li-ion battery which was developed by Goodenough et al., in 1980 using the layered oxide $LiCoO_2$[67] which was building on the aforementioned $LiTiS_2$ studied by Whittingham. This compound could be cycled between the parent phase and $Li_{0.5}CoO_2$ as shown in the reactions at the cathode (equation 1.10) and the anode (equation 1.11).

$$LiCoO_2 \leftrightarrow Li_{0.5}CoO_2 + 0.5\ Li^+ + 0.5\ e^- \quad (1.10)$$

$$C + 0.5\ Li^+ + 0.5\ e^- \leftrightarrow CLi_{0.5} \quad (1.11)$$

The reductive intercalation proceeds at a 4 V potential, and this was integrated by SONY using a carbon-based anode to produce a full battery system with a large power to mass ratio. The importance of this advancement in battery technology led to Goodenough, Whittingham and Yoshino to be awarded the Nobel prize for chemistry in 2019, emphasising how essential these types of chemical manipulations can be through real world applications.

1.7 Aims of this thesis

Mixed-anion solids display a rich array of properties associated with the identity of the transition metals. The highly elongated octahedral coordination environment in the oxide layers of the compounds described in this thesis, enforced by the crystal structure, offers a counterpoint to the more regular octahedral coordination generally found in pure oxide analogues such as perovskite and Ruddlesden−Popper oxide phases, and the possibility of non-stoichiometry on the coinage metal site in the chalcogenide layers leads to the possibility of composition and property-tuning using soft chemistry.

Chapter 3 describes the synthesis and properties of various Ni-containing mixed-anion solids, focussing on how both cationic and anion substitution can change the transport and magnetic properties within the solid. Mainly, traversing the solid solution between high-spin $Sr_2NiO_2Cu_2Se_2$ and low-spin $Sr_2NiO_2Cu_2S_2$ has allowed us to identify the point at which there is no longer any sign of magnetic Bragg scattering. A warren peak characteristic of short-range 2D-ordering was identified just before the loss of magnetic signal. The metastable oxide halide $Sr_2NiO_2Cl_2$ was also characterised using powder neutron diffraction (PND) and was found to have a similar magnetic structure to the closely related oxide chalcogenide analogues.

This work is been published in "High- versus Low-Spin Ni^{2+} in Elongated Octahedral Environments: $Sr_2NiO_2Cu_2Se_2$, $Sr_2NiO_2Cu_2S_2$, and $Sr_2NiO_2Cu_2(Se_{1-x}S_x)_2$. *Chem. Mater.* **2022**, *34* (21), 9503–9516. https://doi.org/10.1021/acs.chemmater.2c02002." and "Magnetic Ordering in the Layered Oxyhalide $Sr_2NiO_2Cl_2$. *Solid State Sci.* **2023**, *144*, 1293–2558. https://doi.org/10.1016/j.solidstatesciences.2023.107297."

Chapter 4 reports the soft chemical synthesis of $Sr_2CoO_2Cu_{2-x}Li_xCh_2$ (*Ch* = S, Se) and $Ae_2CoO_2Ag_{2-x}Li_xSe_2$ (*Ae* = Sr, Ba) using a novel, cycling approach. High resolution synchrotron powder X-ray diffraction (SPXRD) has been used to determine the result of cation exchange in the lattice parameters and magnetometry has been used to compared the compounds magnetic properties with the parent material. The key result is the use of PND to investigate the magnetic ordering in these novel materials and compare it with related analogues.

Chapter 5 investigates the solid solution $Ba_{3-x}Sr_xFe_2O_5Cu_2Ch_2$ (x = 1, 2; *Ch* = S, Se). Similar to the previously reported $Sr_{3-x}Ca_xFe_2O_5Cu_2Ch_2$ (x = 1, 2; *Ch* = S, Se)[14] there is a clear correlation between the alkaline earth cation sizes and their preference to occupy the appropriate larger 12-coordinate site or smaller 8-coordinate site. All the materials ordered antiferromagnetically similar to that reported by Sheath.[14] There is a clear correlation with the bond valence sums for the Fe^{3+} ions and total ordered saturated magnetic moment – showing the variation of ordered moment with degree of covalency.

This work is published in "Synthesis, Structure, Magnetism and Cation Ordering in $Ba_{3-x}Sr_xFe_2O_5Cu_2Ch_2$ (x = 0, 1, 2; *Ch* = S, Se) and $BaCa_2Fe_2O_5Cu_2S_2$. *J. Solid State Chem.* **2022**, *307*, 122841. https://doi.org/10.1016/J.JSSC.2021.122841."

The final chapter concludes the findings from this thesis and looks towards possible avenues of exploration for further projects.

Chapter 2

2 Experimental techniques

2.1 Synthetic methods

2.1.1 Solid-state synthesis

Due to the air-sensitivity of many of the starting materials used within this thesis, the preparation of samples was carried out within an inert-atmosphere glovebox (see section 2.1.2). Due to the nature of synthesis in the solid-state, the ceramic method was the method of choice for the initial synthesis of starting materials or precursors for soft-chemical manipulations.

This method involves weighing out stoichiometric amounts of high purity starting materials (usually powders) and grinding together in an agate mortar pestle for approximately 30 minutes or until the mixture was judged to be homogenous which was usually when the resulting mixture was smooth and homogeneous in colour. The reactants remained in the solid state throughout the duration of the reaction (even at the elevated temperatures required in ceramic synthesis) and so the rate limiting step of these reactions tended to be diffusion of particles at the inter-grain boundaries. For this reason, the mixture was loaded into a 13 mm pellet die and sealed under argon within two polyethylene bags before being pressed into a pellet, typically at 0.4 GPa, outside of the glovebox. This was to maximise the contacts between the grain boundaries to promote the reaction.

The pressed pellet was then loaded into an alumina crucible which prevented the basic group 2 oxides (i.e., SrO and BaO) from reacting with the acidic silica tube. These tubes were cut from a stock length to approximately 25 or 40 cm depending on whether liquid nitrogen immersion was required during the sealing process (see below). Silica is known to retain moisture relatively easily. Therefore, once the tubes were cut to the correct size and one end was flame-sealed, they were stored in a drying oven at 80 °C until needed for use. For reactants using especially moisture sensitive starting reactants such as SrS, the tube was heated under dynamic vacuum using a gas/oxygen blowtorch for a few minutes to drive off any residual moisture. A silica spacer of an approximate length of 1 cm was placed at the bottom of the tube to raise the alumina crucible above the level at which the tube is curved and hence has a smaller diameter. Otherwise, the thermal expansion of the alumina crucible under elevated temperatures could lead to the silica tube cracking and exposing the samples to air. Finally, a Young's Teflon valve was attached to the open end of the silica tube and closed to keep the atmosphere inert before being attached to the vacuum line. The silica tube was then evacuated to usually $\approx 10^{-2}$ mbar and sealed using a gas/oxygen blowtorch to result in a fully evacuated silica ampoule. The longer tubes mentioned above had their closed end submerged in liquid nitrogen as these samples contained sulfur and this prevented vaporisation of elemental sulfur during the sealing process which would have led to non-stoichiometry and hence impure products.

The dwelling temperatures used in this thesis ranged from 400-1200 °C. The lower end of this spectrum was to allow the volatile chalcogens such as sulfur to react without the vapour pressure within the evacuated ampoule getting sufficiently high to cause the tube to crack. The elevated temperatures are required to allow the low-mobility ions in the solid state to

cross the intergrain boundaries which result in the targeted thermodynamic product. Once the heating cycle was complete, the silica tube was lightly scored with a diamond-blade cutter which allowed the opening of the evacuated ampoule within the inert environment of the glovebox. The pellet was then reground, and reaction progress monitored using powder X-ray diffraction (PXRD). If the product was judged to not be of good enough quality, then the full procedure was repeated until it was pure according to PXRD.

2.1.2 Argon filled glovebox

A Glovebox Technology Ltd glovebox was used in the synthesis of all the compounds within this thesis and provided an inert atmosphere in which to work. This glovebox contains an oxygen sensor and normal working conditions were when the level of oxygen was below 1 ppm and on most occasions this reading was 0 ppm. The argon was circulated through a Dow Chemical copper catalyst to remove any oxygen, and molecular sieves were present in the catalyst column to remove any moisture present in the environment.

Over time, as would be expected, some oxygen and moisture can make their way into the glovebox and therefore it was necessary to regenerate the catalyst and molecular sieves every 1-2 months. The copper catalyst was regenerated via reduction using a H_2:N_2 (5 % H_2) flow and the molecular sieves were baked dry under vacuum. To limit the amount of moisture entering the glovebox along with the silica tubes, all apparatus ranging from Schlenk tubes to spatulas were pre-dried in ovens between 80-100 ℃.

Along with the sensors present within the glovebox, an alternative way to check the working environment was use a freshly cut piece of sodium metal. If this remained shiny for 30

minutes, then the conditions were deemed acceptable for the air-sensitive work performed in this thesis.

2.1.3 Preparation of starting material

2.1.3.1 *Ae*O (*Ae* = Ba, Sr, Ca)

*Ae*O (*Ae* = Ba, Sr, Ca) was prepared via the thermal decomposition of $AeCO_3$ under dynamic vacuum according to equation 2.1.

$$AeCO_3\ (s) \xrightarrow{\Delta} AeO\ (s) + CO_2\ (g) \qquad (2.1)$$

For SrO and CaO, approximately 7 g of $SrCO_3$ (Alfa 99.994 %) or $CaCO_3$ (Alfa 99.99 %) was first heated in a box furnace overnight in a crucible in air at 840 °C. The powder was then loaded into two 13 mm deep alumina boats as depicted in Figure 2.1 and placed in a 25 mm diameter silica tube which was sealed with two Swagelok end caps, one of which had an exit port which allowed connection the vacuum line. The attached set-up was placed in a split-tube furnace, with fans underneath the end caps which prevented the rubber O-rings from degrading. Care was taken once the system was evacuated to ensure that the seal was tight and there were no leaks.

The set-up was then heated at 840 °C at a ramp rate of 10 °C min^{-1} then allowed to dwell for 1 hour before heating to 1100 °C at 5 °C min^{-1} for a final dwell of 4 hours. The set-up was then allowed to cool down quickly by opening the split-tube furnace before being transferred to the glovebox under vacuum and the sample was then X-rayed to determine purity. A cold-trap was used during the reaction to condense the evolved CO_2 and prevent it from entering the vacuum pump (this also stopped potential backstreaming of oil into the vacuum line).

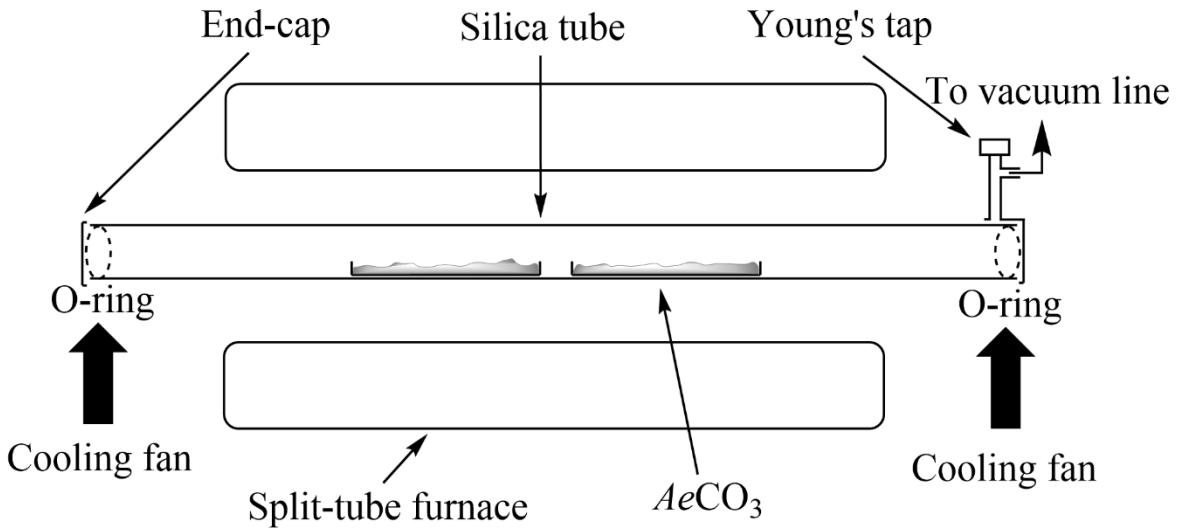


Figure 2.1 The set-up for synthesis of *Ae*O from *Ae*CO_3.

The synthesis of BaO from $BaCO_3$ was more complicated. BaO and $BaCO_3$ form a eutectic melt above 1030 ºC unless there is ≤ 5 % $BaCO_3$ according to the BaO / $BaCO_3$ phase diagram.[68] Hence repeat treatments at 950 ºC were used with intermittent grinding to drive off most of the CO_2 and once confirmed by X-ray diffraction that the amount of $BaCO_3$ was less than 5 %, a final heating at 1100 ºC was used.

2.1.3.2 *Ae*S (*Ae* = Ba, Sr)

*Ae*S were prepared via the reaction of $SrCO_3$ (Alfa 99.994 %) or $BaCO_3$ (Alfa 99.997 %) with CS_2 (Aldrich 99.5 %) under argon flow according to equation 2.2.

$$2\ AeCO_3\ (s) + CS_2(g) \xrightarrow{\Delta} 2\ AeS\ (s) + 3\ CO_2\ (g) \qquad (2.2)$$

Approximately 7 g of the carbonate was loaded into two 13 mm deep alumina boats and placed in a 25 mm diameter silica tube. A Swagelok end cap fitted with a Young's Teflon valve was attached to each side of the rube and a sealed fit was ensured by using Ultratorr O-ring seals. Cooling fans were placed underneath to ensure the O-rings did not degrade.

The set-up is shown in Figure 2.2. CS_2 is toxic and flammable and so great care was taken to ensure the set-up was air-tight. The reaction also took place in a fume hood.

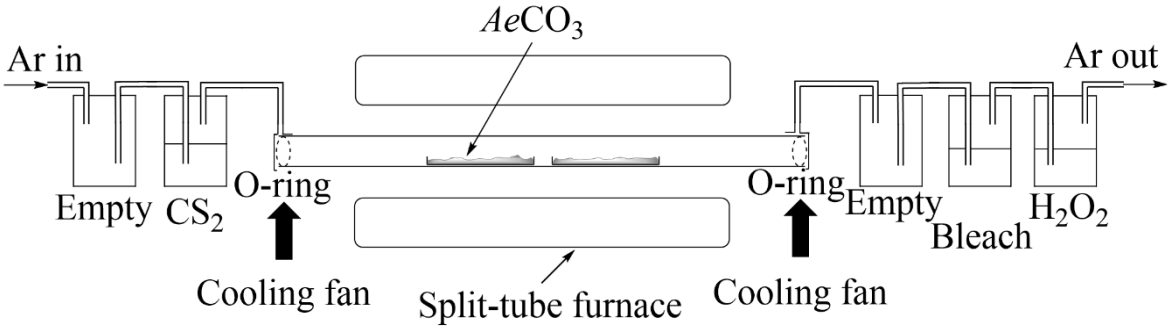


Figure 2.2 The set-up for synthesis of *Ae*S from *Ae*CO_3.

The argon was bubbled through the CS_2 at a rate of 2-4 bubbles per second which was deemed satisfactory for the reaction to proceed without the concentration of vaporised CS_2 being at a dangerous level. Any excess CS_2 that was unreacted was worked up first by a bleach bubbler and then finally any remaining was decomposed by an H_2O_2 bubbler.

Two heating cycles at 800 ºC with intermittent grinding were used with a ramp rate of 10 ºC min^{-1}. After the final heating cycle, the set-up was allowed to cool down to room temperature and the system was flushed with argon for 15 minutes before closing both Young's valves. The tube was then transferred to the vacuum line where it was evacuated and held at 700 ºC for 4 hours to remove any elemental sulfur which can form as a deposit on the powder due to the decomposition of CS_2. The resulting powders were moved to the glovebox to be stored under inert atmosphere due to the air sensitivity of both SrS and BaS. The powders were X-rayed to determine sample purity and it was often the case that small peaks that could be indexed as belonging to the parent carbonate were present in the diffractogram and so one further heating cycle was required.

2.1.3.3 Sublimation of Sr metal

The atmosphere in the glovebox is not perfect and so it is only natural that over time, especially for reactive metals like Sr, to oxidise within the glovebox. With that in mind, to make SrSe, (see 2.1.3.4), it was required that "clean" Strontium be used. Strontium metal was loaded into a steel bucket and placed inside a silica Schlenk as shown in Figure 2.3.

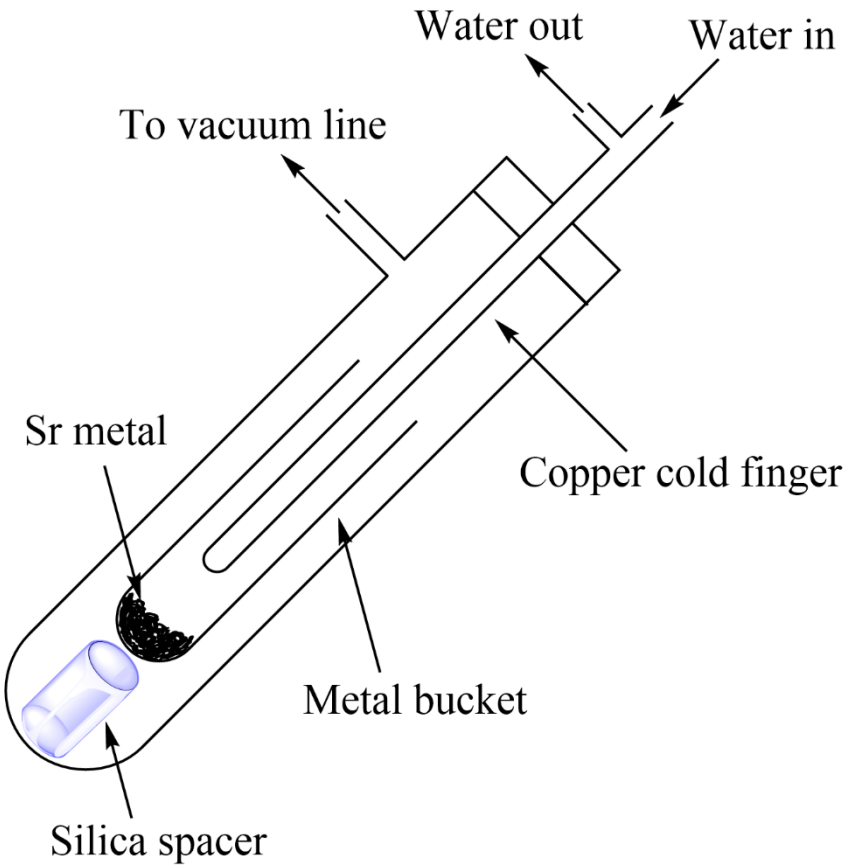


Figure 2.3 The set-up for the sublimation of Sr metal, the end with the metal is enclosed within a tube furnace for heating.

The Schlenk is then evacuated first with a standard vacuum and then using the ultra-high vacuum turbo pump. Water flows slowly through the cold finger, and this is where the clean Sr metal condenses. The setup was heated to 900 ℃ at 10 ℃ min^{-1} and was constantly checked to make sure the outlet water was not warming up and that the pressure remained at around 10^{-4} mbar and left for around 6 hours before the apparatus was cooled down and

transferred to the glovebox under vacuum for storage. The sublimed metal forms a boule on the end of the cold finger which was removed mechanically.

2.1.3.4 SrSe

SrSe was prepared using sublimed Sr (Alfa 99 %) and Se (Alfa 99.999%) by mixing the elements as shown in equation 2.3.

$$Sr + Se \rightarrow SrSe \qquad (2.3)$$

A mass of Sr close to 1g was weighed out, noted, and then cut as small as possible using pliers and a mass of Se calculated to result in a stoichiometric mixture was added. The two were mixed, but not ground to avoid mechanically initiating the highly exothermic reaction, loaded into an alumina crucible and sealed in an evacuated silica ampoule. It was then heated up to 400 ℃ at 0.5 ℃ min^{-1} and left to dwell for 12 hours and then ramped up to 700 ℃ at 0.5 ℃ min^{-1} for 6 hours with the resultant grey powder X-rayed to determine the purity and stored in the glovebox due to its air and moisture sensitivity.

2.1.3.5 Cu_2O

Cu_2O was prepared by thoroughly grinding and pelletising stoichiometric amounts of CuO (Aldrich 99.99 %) and elemental Cu (Alfa 99.999 %) at 1000 ºC for 16 hours in a silica tube. The pellet was not placed in an alumina crucible to avoid the formation of $CuAl_2O_4$. The resulting red powder was stored under inert atmosphere in the glovebox as it is not air stable.

2.1.4 Soft chemistry

Whereas the majority of parent compounds within this thesis were obtained using elevated temperature ceramic synthesis to obtain the thermodynamic product, the daughter compounds of these were only obtainable using lower temperature techniques. The use of lower temperatures allowed for kinetic products to be stabilised. These topochemical alterations led to intercalation, deintercalation or exchange of ions, usually in the chalcogenide layer, leaving the structure and composition of the perovskite metal oxide layer unaltered but changing the electron count. Soft chemical manipulations were performed on a Schlenk line. This consists of a dual manifold with 4 ports in the case of the Schlenk line used in this thesis. One manifold is connected to a vacuum line and the other to an inert gas source which was N_2 gas for the Schlenk line used for the duration of the work performed for this thesis. This set up allows for wet-chemistry to be performed on air-sensitive compounds and then to subsequently dry them for storage in the glovebox.

The first of these reactions is the deintercalation of coinage metal (i.e., copper or silver) using iodine with a reaction scheme shown in Figure 2.4. This has already been described for many compounds similar to the ones described in this thesis.

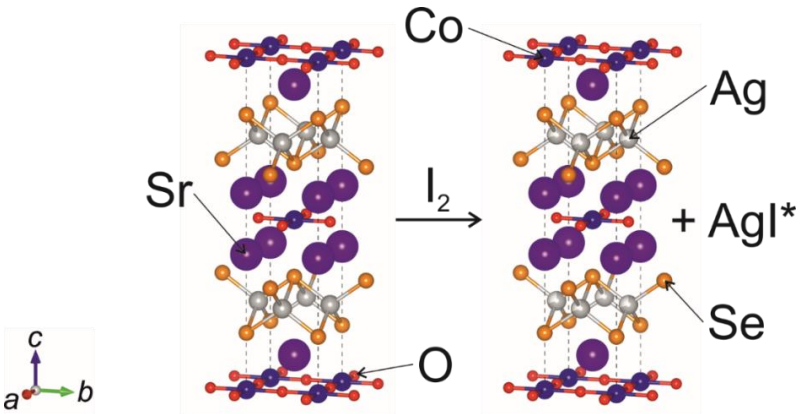


Figure 2.4 The deintercalation of Ag from $Sr_2CoO_2Ag_2Se_2$ using I_2. The * indicated AgI complexes such as $[AgI_2]^-$ which are soluble and can be washed away.

In this reaction, quantities of iodine (Alfa 99.99 %) determined by the targeted amount of deintercalation were dissolved in approximately 30 cm^3 MeCN, which itself was contained within a Schlenk tube containing molecular sieves to ensure the solvent was dry. This was then transferred to a Schlenk tube containing the reactant compound via a cannula by making use of inert-gas overpressure as well as an excess of NaI for Ag-containing compounds.

When dissolved in solution, NaI effectively provides a reservoir of I^- ions which encourage the formation of AgI complexes such as $[AgI_2]^-$.[69] These AgI complexes are much more soluble than AgI and thus can be washed away, removing them from the sample.

The set-up was then left to stir at room temperature for 2-3 days before being filtered and washed at least 3 times by further 30 cm^3 portions of MeCN. The resulting powder was then dried under dynamic vacuum for usually 1 hour and transferred to the glovebox before being X-rayed to determine the extent of reaction.

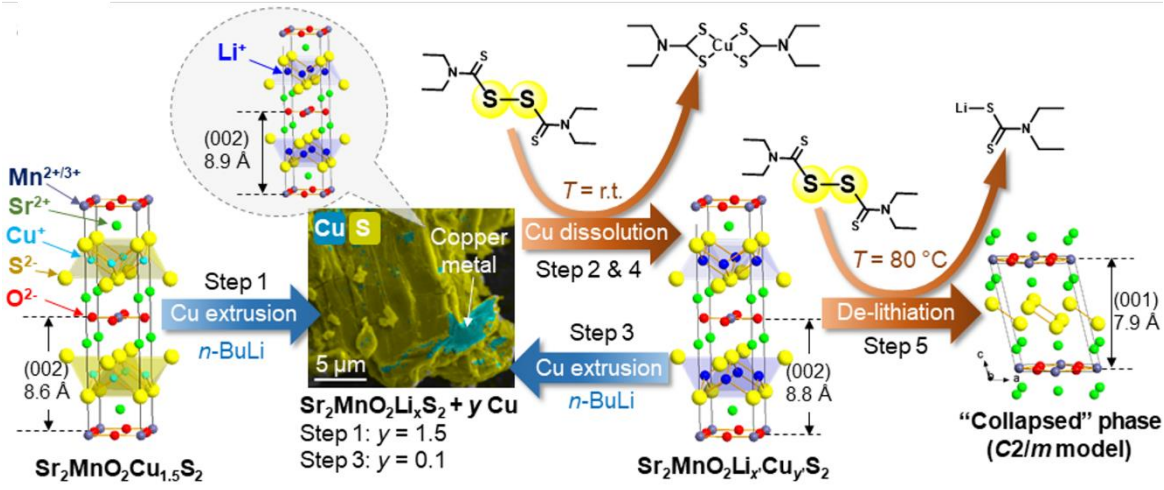


Figure 2.5 Reaction scheme for the synthesis of the "collapsed" phase of $Sr_2MnO_2S_2$.[70]

The second soft chemical reaction is seen in chapter 4. This cycling method to progress toward the so-called "collapsed" phase where no coinage metal was present in the chalcogenide layers was optimised by a previous post-doc in the group – Shunsuke Sasaki,[70]

with the reaction scheme he devised shown in Figure 2.5, building on previous efforts to lithiate the starting material $Sr_2MnO_2Cu_{1.5}S_2$.

Li / Cu exchange was done by stirring the parent compound under inert-atmosphere in a large excess of *n*-BuLi (1.6 M in hexanes) for 3 days at 50 ºC. *n*-BuLi was added to the reactant Schlenk flask using a cannula and inert-gas overpressure.

After 3 days the resultant powder was filtered and washed at least 3 times with hexane, which was contained within a Schlenk flask with molecular sieves to ensure its dryness. The powder was then dried under dynamic vacuum for 1 hour and returned to the glovebox where it was X-rayed to see the reaction progress. In the diffractograms, peaks could be seen which could be indexed as elemental copper. From this, the respective weight fractions from a Rietveld refinement could be used to determine an estimate of the reaction progress according to equation 2.4.

Then, following the reaction sheme in Figure 2.5, the lithiation in the case of Cu-containing compounds was followed by oxidative dissolution / chelation using disulfiram to remove the Cu with the cycling repeated until the most lithiated product was realised.

As seen in Chapter 4, the Co-containing oxide chalcogenides were much more resistant to this technique than their Mn analogues and so the reaction was stopped at the most lithiated phase as opposed to the "collapsed" phase which was achieved through the reaction of the lithiated phase with disulfiram at elevated temperatures as shown in Figure 2.5.

$$\frac{\text{Weight fraction (coinage metal)}}{\text{Weight fraction (main phase)}} = \frac{\text{Coinage metal per f. u.}}{\text{RMM (main phase)}} \qquad (2.4)$$

2.2 Characterisation techniques

2.2.1 Diffraction

Diffraction occurs when waves are scattered by objects in their path, giving rise to interference. All types of matter can interact with radiation. For example, amorphous materials can scatter radiation such as X-rays in all directions, with a broad distribution with respect to angle.

Diffractions key selling point however is with crystalline solids, whereby the solid consists of an atom or groups of atoms (a basis), located on a repeating array of points in space (a lattice). When radiation with a wavelength comparable to the interatomic distances is incident on the material, then the radiation is scattered in a highly structured way. With a periodic array of repeating unit cells in space, the interference of all the scattering objects across the whole sample results in constructive interference in a few special directions.

A successful diffraction experiment can tell us a lot about the crystal structure. Even with low intensity radiation such as in-house diffractometers, the lattice parameters and unit cell symmetry can be extracted with a high degree of precision which are directly related to the peak positions within the diffraction pattern. Furthermore, the constituent atoms and their relative positions within the unit cell can be determined using Rietveld refinement if there is a reasonably close starting model and are related to the relative peak intensities. Bond lengths, angles and, in the case of magnetic diffraction, magnetic moments can also be deduced from diffraction experiments.

In the following sections, two of the most important types of diffraction in solid-state chemistry are explored; X-ray and neutron diffraction.

2.2.1.1 X-ray diffraction

X-rays can interact with matter via two routes – scattering and absorption, and the interaction is almost entirely between the radiation and the electrons of the point scatterer. If the scattering process results in no net loss of energy, then it is said to be elastic, coherent scattering and these coherent X-rays are used in X-ray diffraction. Secondary scattering or incoherent scattering, commonly known as Compton scattering does not result in sharp peaks but instead contributes to the background profile.

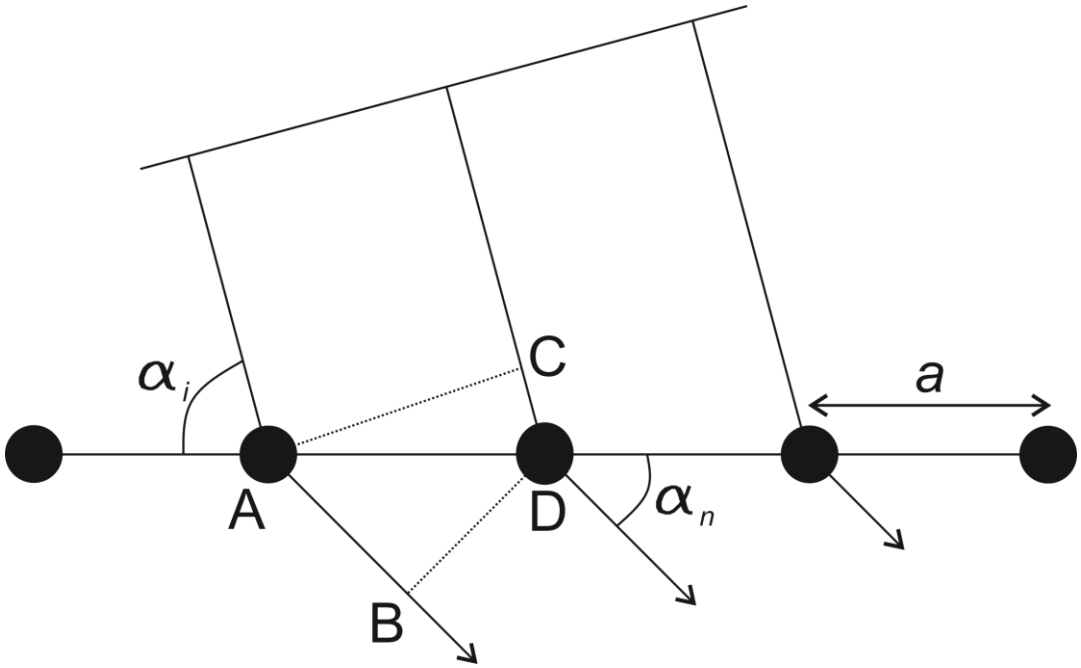


Figure 2.6 Laue scattering by a 1D lattice of monochromatic radiation.

In 1912, Max von Laue discovered the diffraction of X-rays by crystals[71] and explained 3-dimensional scattering as diffraction from a hypothetical 1-dimensional crystal to derive three Laue equations which represent each of the three crystallographic axes needed to present the crystal in 3 dimensions. This is schematically shown in Figure 2.6.

In the unspecified axis above, there is constructive interference between waves if the difference between their paths is a whole number of wavelengths as shown in equation 2.5.

$$(\mathrm{AB} - \mathrm{CD}) = a(\cos\alpha_n - \cos\alpha_i) = n_x\lambda \tag{2.5}$$

In equation 2.5, α_n and α_i are the angles between the axis and the diffracted and incident beams respectively and n_x is an integer. The other Laue equations can be similarly derived by considering diffraction in 2 perpendicular directions to obtain equations 2.6 and 2.7.

$$b(\cos\beta_n - \cos\beta_i) = n_y\lambda \tag{2.6}$$

$$c(\cos\gamma_n - \cos\gamma_i) = n_z\lambda \tag{2.7}$$

From this, if equations 2.6 and 2.7 are satisfied simultaneously then there will be constructive interference. The Laue equations represent a mathematically rigorous and accurate way to describe diffraction but are not commonly used in practice. Instead, Bragg's Law is used which is much simpler. In this alternative model of the process, diffraction occurs from the reflection of planes of atoms, known as Miller planes, within a crystal and these are denoted as {*hkl*}, where *h*, *k* and *l* denote coordinates within reciprocal space, and these planes intersect the cartesian coordinates at $\frac{a}{h}, \frac{b}{k}$ and $\frac{c}{l}$. Figure 2.7 can then be used to derive the relationship between the path difference and interplanar spacing – Bragg's Law as shown in equation 2.8.

$$n\lambda = 2d_{hkl}\sin\theta \tag{2.8}$$

In a powder diffraction experiment, monochromatic radiation is used to illuminate the sample with diffracted intensity measured as a function of 2θ which by Bragg's Law is directly related to the *d*-spacing which correlate to the atomic positions within the unit cell, however, this does throw up the problem of peaks with similar *d*-spacings overlapping due

to the width of the peaks which can hinder structure solution because the individual intensities are difficult to determine.

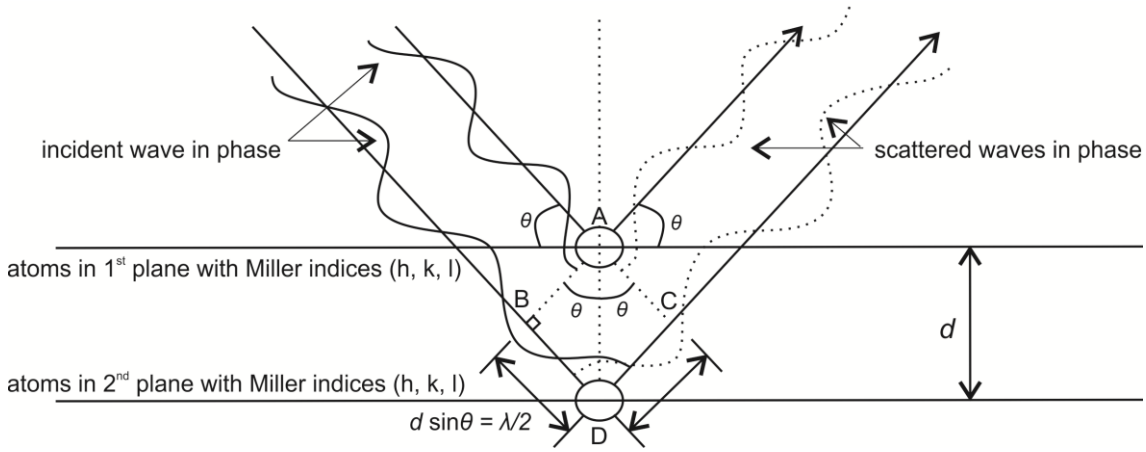


Figure 2.7 Schematic of the derivation of Bragg's law.

The intensities of the Bragg peaks, I_{hkl}, are directly related to the structure factor, F_{hkl} by the following equation:

$$I_{hkl} \propto |F_{hkl}|^2 \tag{2.9}$$

Where the structure factor F_{hkl} is due to waves scattered in the $2\theta_{hkl}$ direction by all atoms in the unit cell, and is given by:

$$F_{hkl} = \sum_{j=1}^{n} f_j \left(\cos 2\pi(hx_j + ky_j + lz_j)\, \mathrm{q} + i \sin 2\pi(hx_j + ky_j + lz_j)\right) q \tag{2.10}$$

In equation 2.10, n is the number of atoms, f_j is the atomic scattering factor which defines the contribution to the overall structure factor of the jth atom and x_j, y_j and z_j denote the coordinates of the jth atom. The scattering factor is proportional to the number of electrons in the atom and therefore, heavier atoms will dominate the intensity as shown in equation 2.11, where Z is the atomic number of the atom. The angular dependence of the diffraction intensities also means that the higher the scattering angle of the reflection then the more reduced it will be in intensity. This is because of the size of the separation of the electrons

within the scattering atom is comparable to the wavelength of the X-ray radiation i.e., the electron cloud is not a point scatterer. This means that two photons scattered by core electrons or outer electrons can have slightly different path lengths resulting in successively more destructive interference with increasing θ.

$$f_j(\theta)\ \alpha\ \frac{Z}{2}(1+\cos(2\theta) \tag{2.11}$$

The Debye-Waller term, q, is a representation of the thermal displacement when electron density is dispersed via atomic vibrations which results in a decrease in Bragg intensity with an increase in 2θ due to increased destructive interference with greater phase difference between the diffracted waves. For isotropic thermal displacement, q_{iso}, the formula is as shown in equation 2.12.

$$q_{iso} = e^{(\frac{-8\pi^2 U_{iso}\sin^2(\theta)}{\lambda^2})} \tag{2.12}$$

In an X-ray diffraction experiment, the crystallites which make up the bulk sample are orientated at random in every possible direction. Hence, once illuminated by radiation, there will be cones of intensity (known as Debye-Scherrer cones) detected on the flat detector as rings as opposed to spots as shown in Figure 2.8. This results in the typical intensity vs 2θ diffractograms used for structure refinement, where the intensities can be obtained by integrating the intensity of the whole ring or by taking a cut through the ring. The former gives higher intensities, whereas the latter method normally produces higher resolution.

Due to the fact that I_{hkl} is directly proportional to the magnitude of F_{hkl} squared, it means that only the magnitude of the structure factor, and not its phase can be directly extracted from a diffraction pattern, meaning that structure solution is a much more complex process than it would be otherwise. This is known as the phase problem. This problem can be made easier

through the use of higher resolution diffraction such as with synchrotron data or single crystals, where many independent intensities can be extracted so that techniques developed to help with structure solution such as the Patterson method[72], direct methods[73,74] and charge flipping[75] can be used to solve the structure ab initio.

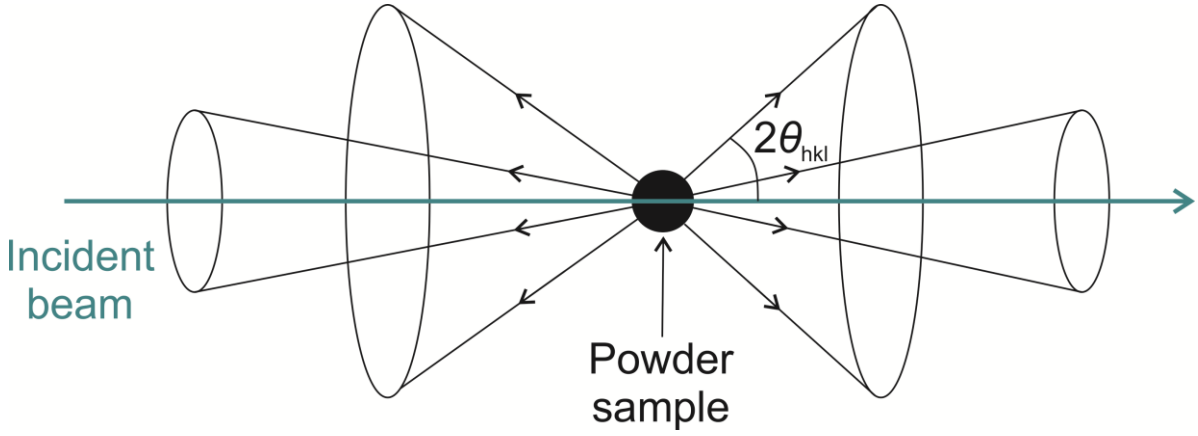


Figure 2.8 Debye-Scherrer cones produced by diffraction of a powder sample.

2.2.1.2 Neutron diffraction

Neutrons exhibit wave-particle duality which can be defined by the de Broglie equation in equation 2.13.

$$\lambda = \frac{h}{p} = \frac{h\,t}{m_{\mathrm{n}}\,L} \tag{2.13}$$

where h is Plancks constant, p is momentum, m_{n} is the mass of the neutron and v is velocity. Therefore, a neutron moving slowly enough will have a wavelength comparable to that of the interatomic distances in a crystal and interact with the crystal via diffraction.

There are two different types of neutron sources used worldwide for neutron diffraction: reactor sources and spallation sources.

A reactor source such as the ILL, Grenoble, France, generates neutrons from the radioactive decay of nuclear material. This reaction generates neutrons with wavelengths associated with the nuclear reaction. These neutrons are passed through a moderator to modify the range of energies and are then often monochromated and collimated before the beam is directed to the sample. For monochromatic neutrons, the obtained diffraction pattern shows intensities as a function of 2θ, as for the diffraction of monochromatic X-rays. A single wavelength neutron source, such as the D2B diffractometer at the ILL[76,77], has a $\Delta d/d$ that increases with increasing d spacing, (as well as a small increase at very low d-spacing), as it follows the Caglioti function.[78]

$$\sigma^2 = \frac{\mathrm{FWHM}}{8\ln 2} = U\tan^2(\theta) + V\tan(\theta) + W \qquad (2.14)$$

Where the parameters U, V and W are free parameters that describe the full width half maximum (FWHM) of the peak profile with their value depending heavily on what refinement software is used during data analysis.

For a "spallation" source such as the ISIS neutron and muon source, Harwell, UK, neutrons are produced when an ion source produces H^- ions that are accelerated in a linear accelerator (LINAC) to 37 % the speed of light. As they enter the synchrotron, a 0.3 μm thick aluminium oxide foil strips away the electrons to form a proton beam, which is then accelerated to 800 MeV, before colliding with a tungsten target to produce neutrons – a process known as spallation. The neutrons are then moderated to optimise their wavelength distribution for scattering experiments. 6 mm cylindrical vanadium cans were used to house the samples during experiments as the coherent scattering of V is so small that it makes a miniscule contribution to the Bragg scattering. 1-3 g of sample was then added to the V can and the setup sealed with an indium wire under the lid of the can. Indium is a soft metal and is very

malleable, it flattens as the lid is screwed on, providing a hermetic seal and it does not become brittle at cryogenic temperatures and therefore is suitable for low temperature use.

The path length as well as the multiple detectors (with multiple detectors used to reduce count time and increase the range of measured *d*-spacings), are fixed and so the time of flight is directly proportional to the *d*-spacing as shown in equation 2.15 which is equating Bragg's Law (equation 2.8) and the de Broglie relationship (equation 2.13) . This allows the *d*-spacings to be investigated by fixing the angle of the detector, θ, but varying the incident λ by using a white beam with neutrons of varying velocities, resolved according to their time-of-flight (ToF), *t*, which gives the additional advantage of not needed to monochromate the beam and thus using more of the available neutrons for the measurement.

$$\lambda = \frac{h}{p} = \frac{h\,t}{m_{\mathrm{n}}\,L} = 2d_{hkl}\sin\theta \tag{2.15}$$

The resolution function of a ToF diffractometer is shown in equation 2.16.

$$\frac{\Delta d}{d} = \left[\left(\frac{\Delta t}{t}\right)^2 + \left(\frac{\Delta L}{L}\right)^2 + (\Delta\theta\cot\theta)^2\right]^{\frac{1}{2}} \tag{2.16}$$

Long path lengths make the contribution to the first 2 terms small and $\Delta\theta\cot\theta$ tends to 0 as θ tends to 90 ° and therefore at high angles (larger 2θ) i.e., backscattering banks, there is higher resolution. For a fixed detector, this function is approximately constant, as such, the resolution of ToF diffractometers tends to be much higher than for single wavelength diffractometers at higher *d*-spacing, where magnetic scattering is most prominent. The resolutions of the ToF diffractometers used in this thesis can be seen in Tables 2.1 and 2.2.

2.2.1.3 Limits of X-ray diffraction compared to neutron diffraction

Since the wavelength of a neutron beam is several orders of magnitude greater than the size of the nucleus with which it interacts, radiation scattered from different parts of the nucleus does not have any significant difference in path length. Thus, the atomic scattering factor for neutrons displays no angular dependence and data can be collected up to angles as close to $2\theta = 180$ ° allowing for a much more detailed structural determination than is possible with X-rays such as HRPD at ISIS which is one of the highest resolution instruments worldwide with a backscattering bank situated at 176°.[79]

Furthermore, light atoms such as O and Li can be better located with neutrons as well as neighbouring elements being distinguishable to neutrons due to the outstanding contrast they provide due to the way neutrons interact with different nuclei. The change in scattering with atomic number is much less pronounced than is seen with X-rays i.e., the range of neutron scattering lengths is quite small,[80] and it is not systematic.

More importantly, for the purpose of this thesis, because neutrons possess spin ($S = ½$), they possess a magnetic dipole moment that can interact with unpaired electrons and consequently, are not only diffracted by the atomic nuclei. The intensity of magnetic Bragg peaks arising from the interference of the scattering from ordered arrays of magnetic moments is proportional to the magnitude of the ordered magnetic moment and because this scattering is from the electron cloud, it follows a similar 2θ dependence as seen with X-ray diffraction, but the intensity fall-off is much faster because the magnetic scattering is from the outer electrons.

Neutron sources are much less abundant worldwide and offer a much lower flux of radiation as compared with X-ray sources, meaning that larger samples (typically of the order of 2-3 g) and longer scan times are required to produce meaningful results, whereas X-ray diffraction can be performed on extremely small sample sizes with very fast collection times. The greater flux available using an X-ray source can also be sacrificed for resolution, as such, despite the many advantages that neutron diffraction has, X-ray diffraction remains the standard for structure solution with neutron diffraction commonly a complimentary technique or used to solve the magnetic structure of a material only once thorough X-ray analysis has been performed.

2.2.2 X-ray diffractometers

Laboratory X-ray production

To produce X-rays within the laboratory, a tungsten filament is heated to produce electrons which are accelerated through a voltage of 40 kV towards a Cu target which have sufficient energy to cause ionisation of an electron from the 1*s* shell of Cu which leads to spontaneous emission caused from an electron dropping down from the 2*p* shell (K_α 1.54 Å), or the 3*p* shell (K_β 1.39 Å).

Due to spin orbit coupling, there are 2 allowed excited states for the K_α radiation, $^2P_{3/2}$ and $^2P_{1/2}$ and a $K_{\alpha1}$: $K_{\alpha2}$ ratio of 2:1 is observed which results in shoulders on the diffraction peaks due to the miniscule difference in wavelength between the 2 transitions, $K_{\alpha1}$ (λ = 1.54051 Å) and $K_{\alpha2}$ (λ = 1.54433 Å). These shoulders are more prominent at higher angles.

Airtight sample holders with Mylar windows were used to run X-ray measurements of the samples in this thesis to prevent decomposition during the measurement. Finely ground sample was placed onto a lightly greased glass slide in the glovebox, any excess powder tapped off and the sample holders lid screwed on finger tight, ensuring a good seal with the O-ring. The samples were run from 2θ values of 7 ° - 70 °. The air-sensitive holders used did not permit spinning of the sample.

The resolution of the in-house diffractometers was sufficiently good to probe phase purity and lattice parameters; however, most high-quality samples were then sent to the higher energy I11 beamline at the Diamond Light Source (section 2.2.2.3) for further analysis.

Synchrotron X-ray production

Synchrotrons are a powerful source of X-rays which are produced by high energy electrons as they circulate around the synchrotron. The synchrotron used in this thesis was located at the Diamond Light Source in Oxfordshire, England.

At the Diamond Light Source, a high voltage cathode is heated under vacuum, giving the electrons in the material sufficient thermal energy to induce thermionic emission. Earthed anodes then accelerate these liberated electrons to 90 keV which is then boosted in a LINAC to an extreme relativistic energy of 100 MeV using radiofrequency (RF) cavities. From here, the electrons are injected into the booster synchrotron with 36 dipole bending magnets used to curve the electrons around the bends. As the energy of the electrons is ramped up, the magnetic field produced by the bending magnets is increased up to a maximum of 0.8 T before extraction to the storage ring once the energy is at 3 GeV.

The storage ring consists of 25 straight sections angled together to form a closed loop with the electron beam bent by use of 50 large electromagnets. Each magnet curves the electrons through an arc of 7.5 ° with an orbit of over 560 m. To minimise collisions with air particles the storage ring is maintained under vacuum with the electrons able to complete one full circuit in 2 millionths of a second. Radiation is produced when the magnets cause the electron beam to turn and lose energy, which produces a high flux, extremely collimated source of radiation. The electrons are then fed into the various beamlines with the make-up of the I11 beamline which was used in this thesis further looked at in section 2.2.2.3.

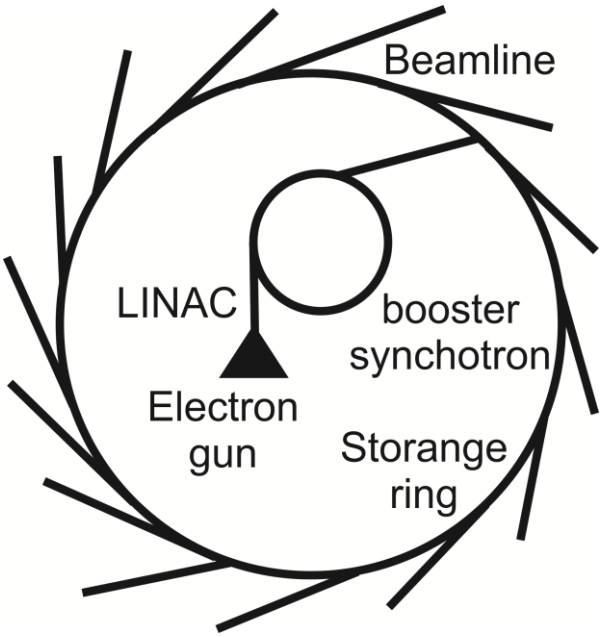


Figure 2.9 General schematic of a synchrotron.

2.2.2.1 Bruker d8 Advance ECO

The Bruker d8 Advance ECO is the highest intensity instrument in the Oxford Chemistry Inorganic Materials Characterisation Facility and operates in Bragg-Brentano geometry.[81,82] The sample position is fixed and mounted on a flat plate, and the X-ray source and LYNXEYE XE-T detector are rotated throughout the measurement. The detector has an

energy threshold which allows filtering of the K_β radiation. The resolution is lower on this instrument than those discussed below as there is no monochromator to remove $K_{\alpha 2}$ and so in the diffractograms, shoulders can be seen on the peaks, especially at higher angle, and there is greater peak overlap. Despite this, the increased intensity of the instrument allows for reasonably good patterns to be achieved in a relatively short time (≈ 25 mins), with a good signal-to-noise ratio to allow for phase identification and structural analysis. Due to the fact that the $K_{\alpha 2}$ wavelength is well known with a fixed intensity relative to $K_{\alpha 1}$, its presence can readily be accounted for in the Rietveld refinement of the collected data. Furthermore, the energy discriminating detector is useful in reducing the background from fluorescent X-rays caused by irradiation by Cu radiation in a case such as with Co.

2.2.2.2 PANalytical Empyrean

The PANalytical Empyrean diffractometer also operates in Bragg-Brentano geometry but has better resolution that the Bruker and so it was usually the diffractometer of choice when collecting in-house data. It has a low-background silicon strip detector and a Ge(111) single-bounce monochromator fitted which prevents $K_{\alpha 2}$ radiation reaching the sample which leads to better resolution, albeit at a reduced intensity. It has a fixed X-ray source and a moving detector and sample position.

2.2.2.3 The I11 beamline at Diamond Light Source

The I11 beamline[83] is a high resolution beamline which contains an in-vacuum undulator insertion device containing 900 permanent magnets of Sm_2Co_{17} which produce X-rays ranging in energies between 5 – 30 keV. The beam of radiation is collimated, and the edges trimmed using the primary slits before passing through a double-crystal-monochromator

containing Si(111) crystals (which are cooled by a closed-circuit liquid N_2 cooling system to maintain the crystals at a constant temperature) to increase beam stability. Harmonic rejection mirrors can remove any anomalous, high-energy photos before proceeding to the diffractometer. The set-up for the I11 beamline is shown in Figure 2.10.

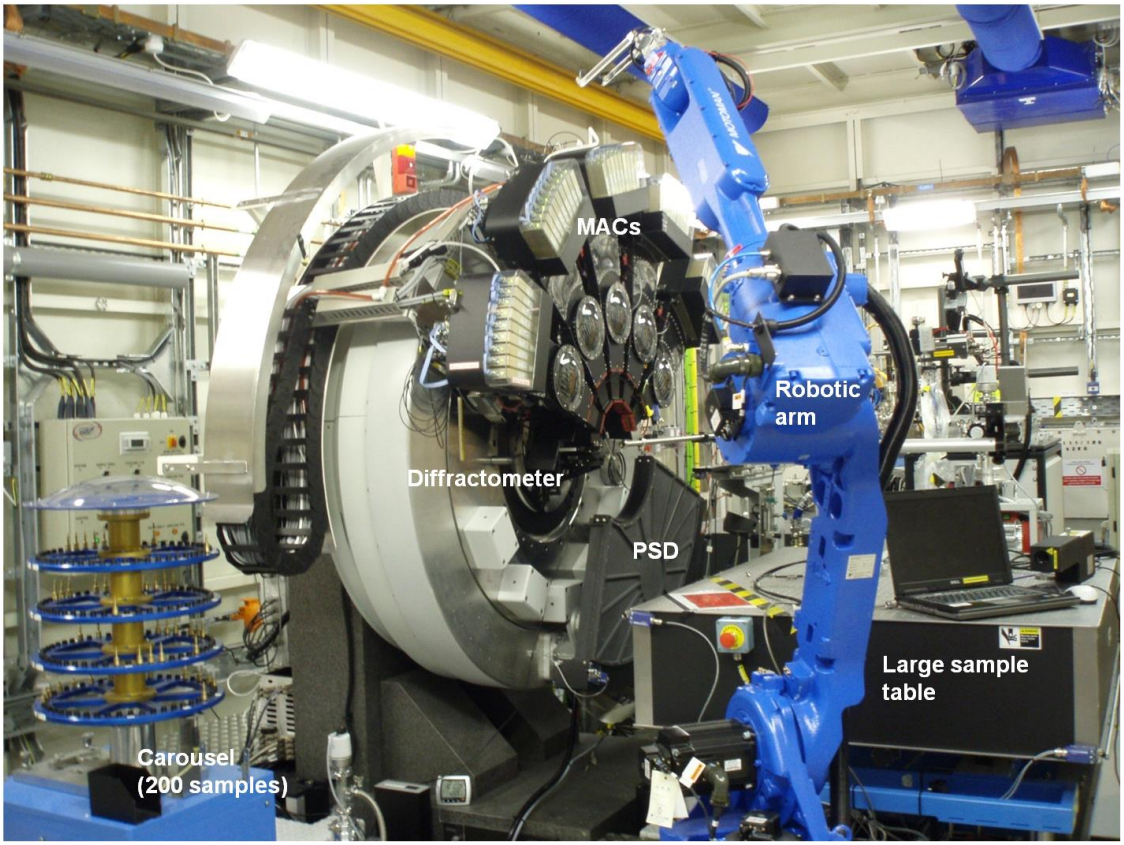


Figure 2.10 The I11 beamline at the Diamond Light Source.

The wavelength of the radiation used in this thesis was ≈ 0.826 Å with the precise wavelength determined on the day of the experiment via refinement of a silicon-standard calibration measurement.

The I11 beamline is equipped with a multi-analyser crystal (MAC) detector along with a position sensitive detector (PSD). The MAC detector was used for scans requiring the highest resolution. 5 MAC stages are placed above the beam with 45 perfect Si(111) analyser crystals incorporated within the stages, these scans typically last up to 30 minutes. A PSD

detector was also used to perform quick scans along with variable temperature scans. The detector is a Mythen-2 Si μ-strip comprised of 18 linear p-n junction strip detection modules mounted on the outer δ-circle of the diffractometer, with the ability to measure a full diffraction pattern in a few seconds. The resolution of the PSD is $\Delta d/d \approx 10^{-3} - 10^{-4}$ whereas the MAC detector has a resolution $\Delta d/d \approx 10^{-4}$.

Variable temperature scans allowed for changes in the lattice parameters and descent in symmetry to be investigated as a function of temperature. A cryostream or hot-air blower was used to cool or heat the sample at a constant rate of 6 $Kmin^{-1}$, however the fast scan times meant the uncertainty in the temperature for any given measurement was ≈ 1 K.

Once samples were known to be of sufficient quality as determined from laboratory data, they were prepared for analysis using synchrotron radiation on I11. The samples were mixed in a 1:1 ratio with ground glass or amorphous boron to minimise absorption effects and preferred orientation and loaded into 0.5 mm borosilicate capillaries inside the glovebox. Grease was used to seal the sample under argon before the capillaries were flame-sealed using wax. The sealed capillaries were then glued into a brass ferrule and screwed into a magnetic base which was subsequently loaded onto a carousel which was then automated with the samples loaded by a programmable robot which allowed for less dead time between measurements (because to change sample manually one has to open the hutch and then go through the hutch safety protocols which is extremely time consuming).

2.2.3 Neutron diffractometers

2.2.3.1 The WISH diffractometer at ISIS

WISH uses ^{3}He detectors, covering scattering angles from 10 ° - 170 ° and contains 10 banks located on two semi-cylindrical annuli.[84] The detectors at corresponding angles on each side of the instrument are summed to improve the quality of the data by improving the signal-to-noise ratio. E.g. Banks 1 & 10, 2 & 9, 3 & 8, 4 & 7 and 5 & 6 are equivalent (see Table 2.1). It is designed primarily for the characterisation of magnetic ordering and is optimised for high-resolution at medium-to-high *d*-spacings. The instrument is supplied with a high flux of neutrons which allow high resolution data with a good signal-to-noise ratio to be collected rapidly.

Table 2.1 The single frame resolution (running at 10 Hz), of each bank of the WISH diffractometer.

	$\Delta d/d$ / %	*d*-range / Å
Backscattering bank 5 & 6	0.3	0.55 – 5.0
Bank 4 & 7	0.4	0.7 – 5.8
90 bank 3 & 8	0.55	0.8 – 6.8
Bank 2 & 9	0.8	0.9 – 12.9
Low angle bank 1 & 10	1.6	1.6 – 48.0

2.2.3.2 The PEARL diffractometer at ISIS

PEARL is a high-flux, medium resolution diffractometer dedicated to high pressure measurements.[85] There are fourteen detector modules in total, each consisting of 78 ZnS scintillator elements of 3 mm width viewed in 2θ.

Nine detector modules constitute the 'transverse' bank with nominal $2\theta = 90°$, giving a 20 ms frame *d*-spacing range of ≈ 0.5 - 4.1 Å, with resolution $\Delta d/d \approx 0.39$ %. The 'longitudinal' bank consists of three detector modules covering the back-scattering range ($100° < 2\theta < 160°$), and two detector modules covering the low-angles ($20° < 2\theta < 60°$). The sample was loaded into an encapsulated gasket machined from null-scattering TiZr alloy.[86] A methanol/ethanol mixture (4:1) was used as the pressure-transmitting medium to provide quasi hydrostatic conditions[87] and was added to the sample chamber along with a small piece of elemental lead to act as an internal pressure marker for which the equation of state (EoS) is well known.[88]

The gasket assembly was secured between a pair of single toroidal profile anvils[89] made from zirconia/alumina for measurements in the low-pressure region and sintered diamond for analysis at elevated pressures. This set-up was then placed in a V3 Paris-Edinburgh press[90] and a sealing load applied. Diffraction patterns were obtained at the $2\theta = 90°$ detector which allowed for *d*-spacings between 0.5 and 4.1 Å to be accessed. The data was subsequently corrected for anvil attenuation using the Mantid software.[91]

2.2.3.3 The GEM diffractometer at ISIS

The General Materials (GEM) diffractometer[92,93] is used for high intensity, high resolution neutron diffraction with a detector array with 7270 elements within 86 modules. The detectors within GEM cover a scattering angle of 1.1° to 169.3° with the $\Delta d/d$ % and *d*-spacing range shown in Table 2.2.

Table 2.2 The resolution of each bank of the GEM diffractometer.

	$\Delta d/d$ / %	d-range / Å
Bank 6	0.3	0.11 – 1.90
Bank 5	0.5	0.15 – 2.77
Bank 4	0.7	0.21 – 4.00
Bank 3	1.4	0.35 – 6.93
Bank 2	2.3	0.65 – 13.12
Bank 1	3.4	0.9 – 25.18

2.2.4 Structural refinement

Refinement of powder diffraction data is dependent on the method of least squares minimisation of the residual function S (equation 2.17).

$$S = \sum_{i=1}^{\mathrm{N}} w_i \left(y_{\mathrm{obs},i} - y_{\mathrm{calc},i}(\boldsymbol{p}) \right)^2 \tag{2.17}$$

In this equation, w_i is the statistical weighting factor, $\frac{1}{y_i}$, which ensures that all points contribute evenly to the objective function, S, $y_{obs,i}$ and $y_{calc,i}$ are the observed and calculated intensities, respectively, at point i in the powder pattern of N points.

In a Pawley refinement,[94] only the space group is specified, and the lattice parameters and peak profile parameters are refined. The intensities of the peaks are allowed to freely refine (so there is no information on the arrangement of atoms), this gives a good indication of the best fit possible for the subsequent structural refinement. In a Rietveld refinement, which was used most often in this thesis, many different structural parameters were refined, such as atomic positions, site occupancies, thermal displacement parameters etc. TOPAS

Academic v6[95] was the software used for these refinements and CIF files were accessed from the Inorganic Crystal Structure Database (ICSD).[96] Within TOPAS, different peak shapes, preferred orientation functions etc, could also be chosen. The quality of fit was assessed by referring to the weighted profile, or R_{wp} value (equation 2.19). Lower R_{wp} usually indicates a better fit, this value should tend towards the expected R value, R_{exp} (equation 2.21).

The most common agreement factor is the profile R-factor, which measures the difference between the observed and calculated diffraction data. It sums up all the differences relative to the sum of all the observed values but gives an overemphasis on stronger reflections.

$$R_p = \frac{\sum_{i=1}^{\mathrm{N}} \left| y_{obs,i} - y_{calc,i}(\boldsymbol{p}) \right|}{\sum_{i=1}^{\mathrm{N}} w_i y_{obs,i}} \tag{2.18}$$

The shortcomings in the profile R-factor can be overcome by introducing a weighting scheme, w_i, which allows the weighted profile R-factor to be related directly to the residual function, S, in equation 2.19.

$$R_{wp} = \sqrt{\frac{\sum_{i=1}^{\mathrm{N}} w_i \left(y_{obs,i} - y_{calc,i}(\boldsymbol{p}) \right)^2}{\sum_{i=1}^{\mathrm{N}} w_i y_{obs,i^2}}} \tag{2.19}$$

If the peak-to-background ratio is low, then the R-values can be dominated by well-fitted background points and hence not particularly changed by the actual structural model. As such, if this is the case then the background can be subtracted from the observed scan intensities in the denominator and for example equation 2.20 would become;

$$R'_{wp} = \sqrt{\frac{\sum_{i=1}^{\mathrm{N}} w_i \left(y_{obs,i} - y_{calc,i}(\boldsymbol{p}) \right)^2}{\sum_{i=1}^{\mathrm{N}} w_i (y_{obs,i} - Bkg_i)^2}} \tag{2.20}$$

Even when corrected, profile *R*-values of different refinements can only be compared for identical statistical conditions. This can be achieved through use of the expected *R*-factor, which is a measure of the statistically best possible fit for the refinement based on counting statistics where N is the number of data points and P is the number of parameters.

$$R_{exp} = \sqrt{\frac{\mathrm{N} - \mathrm{P}}{\sum_{i=1}^{N} w_i (y_{obs,i^2}}} \tag{2.21}$$

The quality of a Rietveld refinement can be determined by calculating the ratio between the weighted profile *R*-value, R_{wp}, and the expected *R*-value, R_{exp}, leading to the goodness of fit ratio (GOF), χ, where a value between 1 and 1.5 is deemed to be satisfactory.

$$\chi = \frac{R_{wp}}{R_{exp}} = \sqrt{\frac{\sum_{i=1}^{\mathrm{N}} w_i \left(y_{obs,i} - y_{calc,i}(\boldsymbol{p})\right)^2}{\mathrm{N} - \mathrm{P}}} \tag{2.22}$$

However, these values can sometimes be misleading and be lower than would be expected. For example, if the background becomes more intense relative to the Bragg peaks, then the *R* values can become low, even if the fit is relatively poor. With this knowledge, it is necessary to also check that the visual fit is satisfactory, which can be seen by observing the difference plot which shows the difference between the experimental and calculated data, as well as ensuring that the refined structural model makes chemical sense.

For single crystal data, the Bragg *R*-value, R_{Bragg} can be used which is based on integrated reflection intensities rather than step scan intensities.

$$R_{Bragg} = \frac{\sum_{k=1}^{\mathrm{K}} \left| I_{obs,k} - I_{calc,k} \right|}{\sum_{k=1}^{\mathrm{K}} I_{obs,k}} \tag{2.23}$$

Here, $I_{obs,k}$ and $I_{calc,k}$ are the "observed" and calculated intensities of the k^{th} reflection out of K reflections. For overlapping reflections, the "observed" intensity is distributed to individual *hkl*- reflections according to the ratio of *calculated* intensities and this circular argument means that Rietveld R_{Bragg} values are often lower than may be expected and therefore should be treated with caution.

2.2.5 Electron microscopy and diffraction

As well as neutrons and X-ray diffraction, electron diffraction is an extremely useful, complimentary tool in structure determination, especially for materials where it may not necessarily be trivial to grow single crystals.

Because electrons are charged particles, they interact with samples mainly via the coulombic interaction with nucleic protons. The scattering amplitude, similar to X-rays, increases with increasing Z ,which is the charge of the nucleus and is related to the electron scattering factor f_e as in equation 2.24 where f_x is related to the extent of the shielding around the nucleus by non-core shells.

$$f_e(\theta)\ \alpha\ Z - f_x \tag{2.24}$$

The two main advantages of electron diffraction over X-ray diffraction is that electrons have a larger scattering amplitude and are also easier to focus, which means that a very small amount of material, often only grains in the nanometre scale are required to produce a diffraction pattern and also because the correlation length of electron diffraction is much smaller than that of X-ray diffraction, localised correlations within the sample can appear much more distinct whereas in an X-ray diffraction pattern they may appear more diffuse.

There are two main types of electron microscopy, Transmission Electron Microscopy (TEM) and Scanning Electron Microscopy (SEM).[97] TEM measures the electrons from the electron beam that are transmitted through the sample. This technique is used more to obtain diffraction patterns and to produce highly magnified images down to near-atomic resolution (≈ 0.2 nm).[98] SEM measures the X-rays and electrons emitted when the electron beam interacts with the sample, creating a magnified image and allowing for imaging and also semi-quantitative analysis as the X-rays emitted are characteristic of the different elements within the sample as shown in Figure 2.11.

The JEOL JSM-5510LV scanning electron microscope (SEM) requires a high vacuum (10^{-5} – 10^{-11} Torr) because electrons can easily be dispersed or scattered by other molecules such as air molecules. The electron gun has a tungsten filament and operates between 0.5 and 30 kV. It has a resolution of 3.5 nm at 30 kV in high vacuum mode and 4.5 nm in low vacuum mode. It has a working pressure range of 1 to 270 Pa. The 2 main detectors are the back-scattered electrons (BSE) detector and the secondary electrons (SE) detector. The BSE detector has lower spatial resolution, however, because the BSE intensity is proportional to the mean atomic number of the atoms in the sample, it can be useful to provide information on variations in sample composition. SE imaging is more surface sensitive due to the short electron escape depth and has higher spatial resolution, providing topographical information.

The instrument also features an Oxford Instruments EDS detector. EDS is a qualitative and quantitative X-ray analytical technique focussing on chemical composition of various samples for elements with $Z > 3$. When the electron beam collides with core electrons, it leads to an ejection of the core electron, leaving a vacancy which an electron from a higher energy shell can drop down into to fill as shown in Figure 2.11. The generated EDS spectrum

is then characteristic of the elements contained within the sample and their ratio and from this, the composition of the probed sample could be extracted.

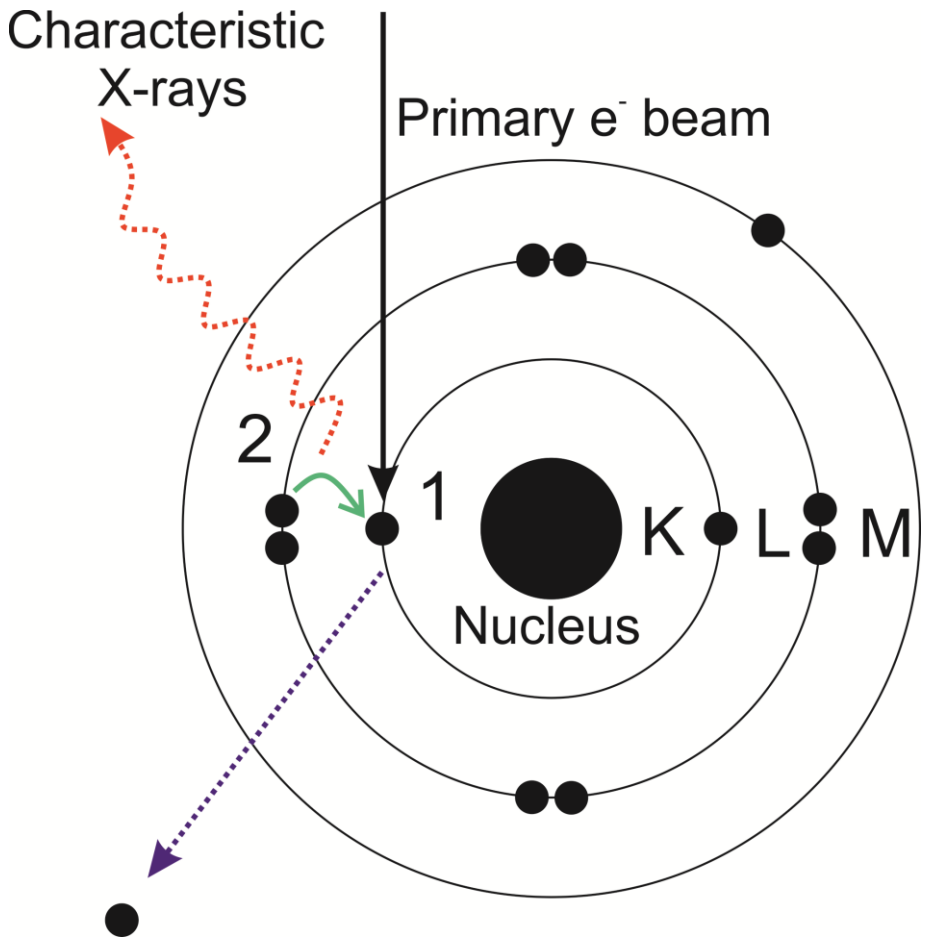


Figure 2.11 A schematic showing the basic principle of EDS.

2.2.6 X-ray absorption near-edge spectroscopy (XANES)

X-ray absorption is characterised by the sharp increases in absorption at specific X-ray photon energies.[99] The change in absorption corresponds to the energy required to eject a core electron into an excited state. The absorption edge is named depending on the origin from which the excited electron was ejected from (K-edge if the principal quantum number, *n*, =1, the L-edge if *n* = 2 and the M-edge if *n* = 3).

A typical X-ray absorption spectrum is shown in Figure 2.12. The extended X-ray absorption fine structure (EXAFS) is used to determine the radial distribution of atoms around an absorbing atom and elucidating the local structure. However, within this thesis, X-ray absorption near-edge spectroscopy (XANES) was used which is extremely useful in determining the coordination environment and more importantly for this work – the approximate oxidation state of the probed species which is influenced by the fact that a higher oxidation states have a more positive overall charge on the atom and hence requires more energy to excite an electron from the orbital.

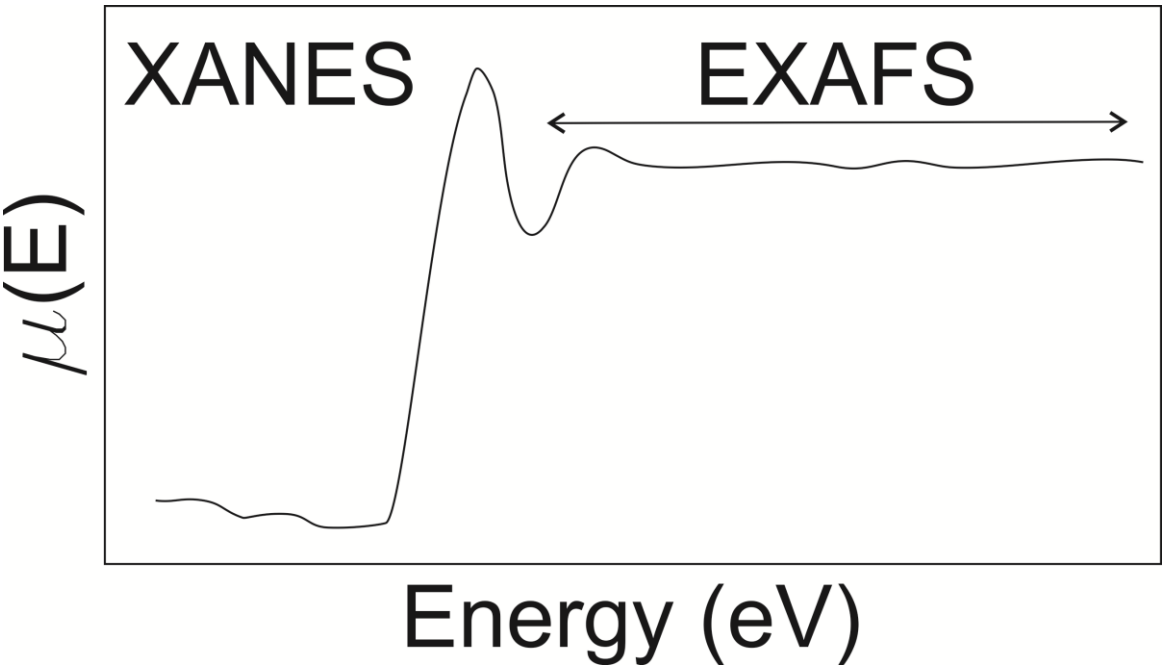


Figure 2.12 A typical XANES and EXAFS spectra.

2.2.6.1 The B18 beamline at the Diamond Light Source

The B18 beamline[100] is a general purpose instrument covering a wide range energy range from 2 – 35 keV. B18 has 3 main optical elements: a collimating mirror, a water-cooled double crystal monochromator and a focusing mirror. Si (111) crystals are the preferred monochromator because of the higher flux, but if high energies are required (22-35 keV)

then a pair of Si (311) crystals are used. They can also be used if an improved energy resolution is required. The measurements were a part of the block allocation group (BAG) SP14239.

Samples were ground with an inert matrix such as cellulose so as to be as homogeneous as possible before being pressed into a 13 mm pellet. Typically, the whole mass of the pellet was ≈ 100 mg and therefore the pellet was very thin and fragile so great care was needed when mounting it onto the sample holder. The pellet was secured with diamagnetic tape.

2.2.7 SQUID magnetometry

The magnetic susceptibility measurements in this thesis were measured using a Quantum design MPMS magnetometer. At its core is a Superconducting Quantum Interference Device (SQUID), consisting of a closed ring of superconductor divided by two thin layers of insulating material, forming two Josephson junctions.[101] When a current is applied, Cooper pairs of electrons are able to tunnel through the junction with no resistance i.e., a weak superconductor. There is however a critical current from which if this threshold is crossed, then the ring will then have a non-zero resistance with a quantifiable voltage established with a finite resistance.[102]

The samples were mounted in a cryostat chamber surrounded by an induction coil. It is magnetised by a He-cooled superconducting magnet and translated vertically to induce a current in the induction coil which is coupled directly to the SQUID which generates a voltage that is directly proportional to the magnetic moment of the sample.

The SQUID is extremely sensitive and can detect even very small magnetic moments with a detection limit down to 10^{-8} emu.

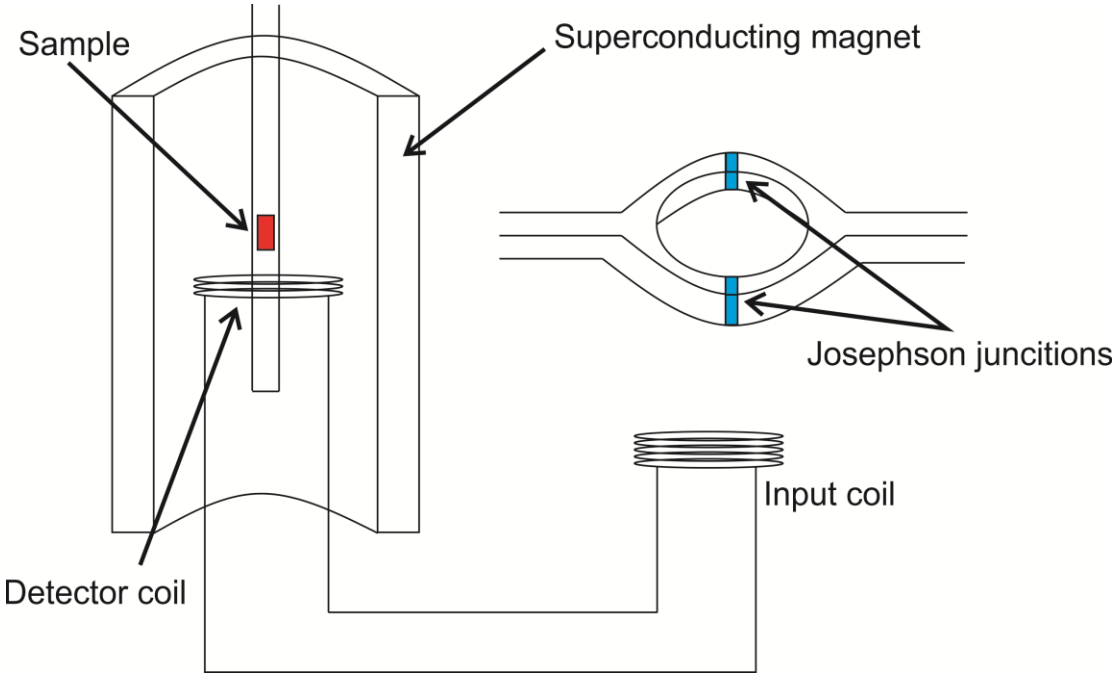


Figure 2.13 Schematic of the experimental set-up for SQUID magnetometry measurements.

2.2.7.1 DC susceptibility measurements

For measurements on the magnetometer, samples of mass usually in the range 30-40 mg were weighed out accurately in the glovebox. Outside of the glovebox, it was then placed inside a straw, with further gelatin capsules either side and a capsule with diamagnetic tape added to one end to secure the whole set-up. The magnetic moment of the sample, proportional to the magnetisation (*M*), was first measured against field (*H*) at room temperature to determine sample purity. If there was a linear relationship between the two, even at very low fields, then it was assumed that there were no ferro- or ferrimagnetic impurities in the samples and so a low field measurement of either 100 or 1000 Oe was conducted as a function of temperatures between 2 and 330 K. The samples were first cooled down with no field (zero-field cooled, ZFC) with data collected on warming before cooling down in an applied field (field-cooled, FC) and again collecting data on warming with the difference commonly being characteristic of the type of magnetism in the sample. If the

sample is a paramagnet or an antiferromagnet then it would be expected that there would be no difference in the ZFC and FC, but if there is a transition to something with a ferromagnetic component (which could include a canted antiferromagnet) or if it is a spin-glass then a difference would be observed. Further investigations into each sample's magnetic behaviour was done by measuring magnetisation isotherms where $-7 \leq H(\mathrm{T}) \leq +7$. The magnetisation was converted into molar susceptibility, χ_{mol} as shown by equation 2.25, where n is the number of moles of the compound.

$$\chi_{\mathrm{mol}} = \frac{M}{Hn} \tag{2.25}$$

However, it was quite common to find that there was not a linear relationship between M and H over the full range of fields and so a magnetisation against temperature program was run at 2 different fields well above the saturation point (typically 5 and 6 T, see Figure 2.14) and subtracted from one another to effectively "remove" the impurity to give a magnetic susceptibly intrinsic to that of the sample as shown in equation 2.26.

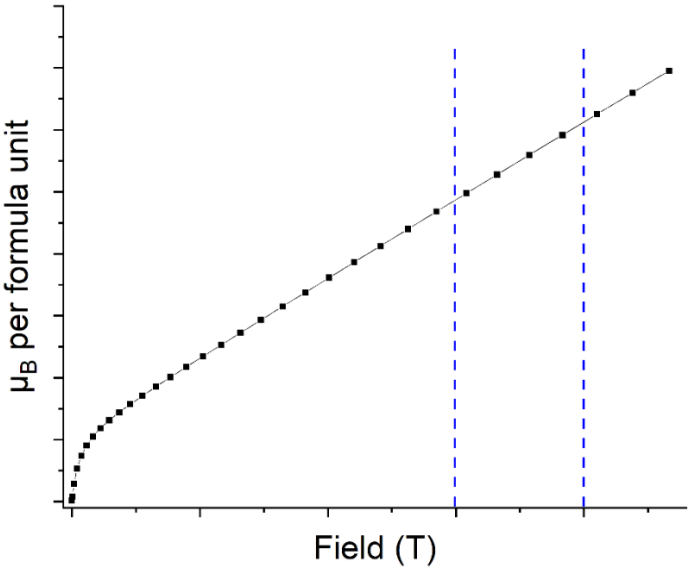


Figure 2.14 Non-linearity observed in samples with ferromagnetic impurity and the region between which *M vs T* measurements were performed to extract an intrinsic moment from where the impurity has fully saturated (blue lines).

$$\chi_{\text{mol}} = \frac{M(H_2) - M(H_1)}{(H_2 - H_1)n} = \frac{M(6\text{ T}) - M(5\text{ T})}{10000n} \quad (2.26)$$

2.2.8 Resistivity

Electrical resistivity was measured as a function of temperature (30 – 300 K) using a custom-built in-house setup. The equipment provided a constant predetermined current to the sample, whilst measuring the voltage every 20 seconds. A Gifford-McMahon closed-cycle refrigerator was used for cooling and a heater that was mounted on the set up was used to adjust the temperature.

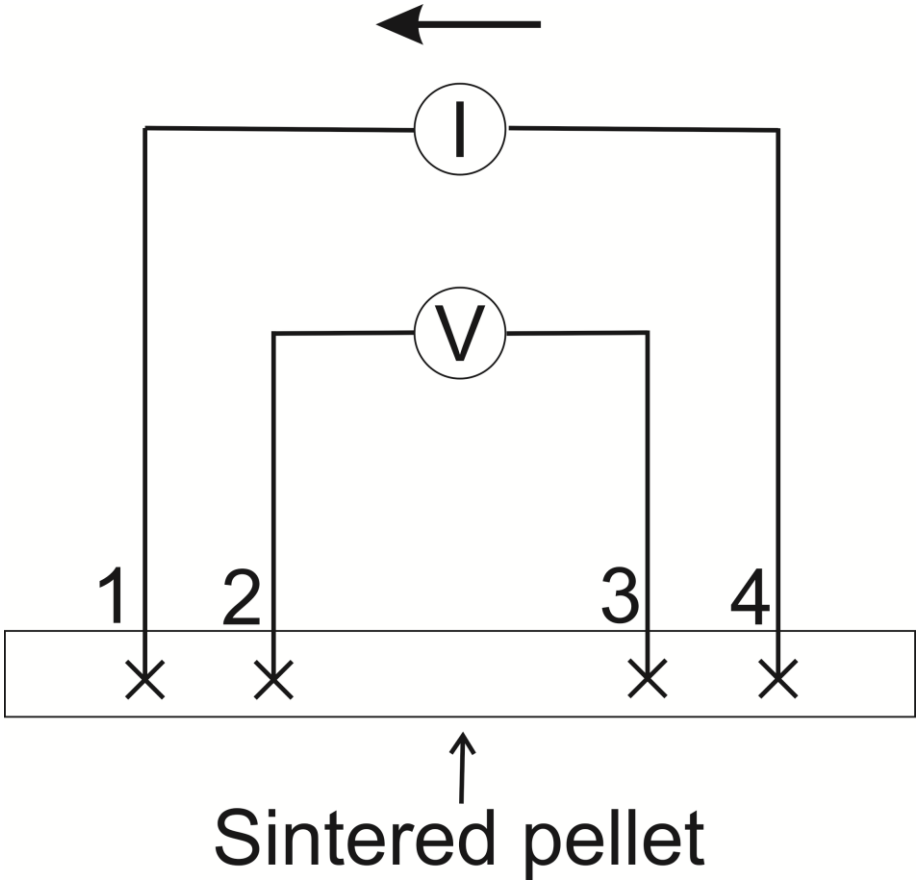


Figure 2.15 A graphic showing the experimental set-up for measuring the electrical resistivity of sintered pellets using the four-probe method.

Once a material was known to be phase-pure, a fresh pellet was prepared and a final heating at the synthesis temperature to sinter the pellet was done to improve the contacts between

the grain boundaries and give values which reflect the intrinsic properties of the bulk material as closely as possible. The pellets were then cut into a bar with copper wires used to connected the sample to the set-up which is shown in Figure 2.15.

For the four-probe set-up, a current is applied through contacts 1 and 4 of Figure 2.15 with the voltage measured across contacts 2 and 3. This method minimises the contact resistance and wire resistance and hence provides a more accurate measure of the resistivity, ρ, of the actual sample which is calculated using the equation 2.27 below.

$$\rho = \frac{RA}{l} = \frac{VA}{Il} \tag{2.27}$$

Here, R is the resistance which is measured as V / I, A is the cross-sectional area of the pellet and l is the length between contacts 2 and 3 from which the voltage is extracted from. This formula is valid only if there is a linear relationship between the voltage and current i.e., the material behaves in an ohmic manner which can be checked after mounting the sample and then choosing an appropriate current by measuring with different currents and choosing one whereby the measured resistance is not dependent on the current.

The samples were prepared under inert atmosphere up until the point at which the measurement was going to be done. The sample to be measured was then prepared in air with the remaining pellet after cutting the bar which was analysed using in-house PXRD to ensure the sintering process did not lead to any sample decomposition and that the bar was of high enough purity to yield a meaningful result. This set-up is only appropriate for compounds that are not air sensitive.

There are two general behaviours observed in resistivity measurements of a solid, both shown in Figure 2.16 which also shows the related density of states near the Fermi level, E_F, for both metallic and insulating behaviour.

In a metal, as the temperature is increased, so is its resistivity. This is because as the thermal energy within a system is increased, the atoms in the lattice vibrate more resulting in more collisions between the free electrons and other electrons and this reduction in the drift velocity is what leads to an increase in the resistivity.

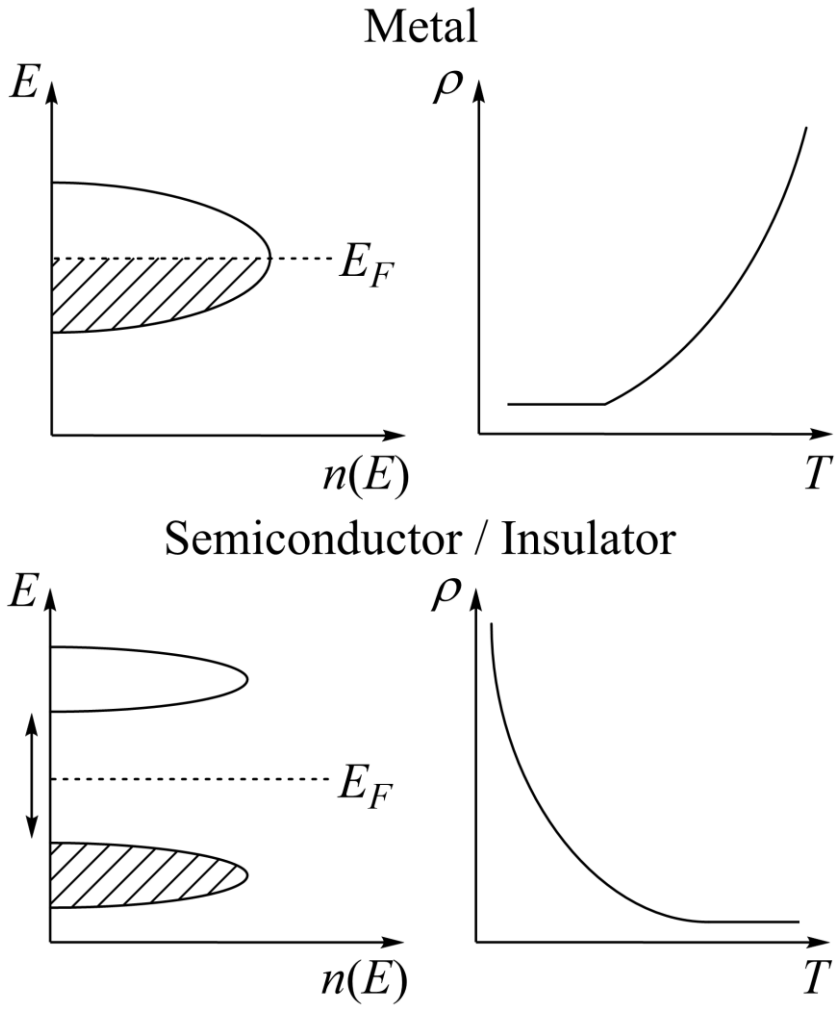


Figure 2.16 The density of states (DoS) of a metal and a semiconductor / insulator along with their resistivity as a function of temperature. Note. The difference in energies between the conduction and valence band in a semiconductor is approximately 1-2 eV whereas anything above this is generally described as an insulator.

In a semiconductor, the density of states is zero at E_F and hence there is an activation barrier to overcome the band gap to have an electron move from the valence band into the conduction band and results in the material having a larger concentration of charge carriers. The number of electrons in conduction band, *n*, is related to the temperature, *T*, by the following equation:

$$n \propto e^{\frac{-E_g}{2k_BT}} \tag{2.28}$$

Where E_g is the separation between the valence and the conduction bands and k_B is the Boltzmann constant.[103]

2.2.9 Raman spectroscopy

Raman spectroscopy is an extremely useful, non-destructive technique which is used to complement the other methodologies used in this thesis. The premise behind Raman spectroscopy lies behind the excitation of photons using monochromatic light.[104]

When light interacts with a material, the vast majority of is scattered with no net loss or gain of energy which is known as Rayleigh scattering. However, there are a small but distinguishable amount of these photons that are scattered with a net gain or loss of energy, which is known as Raman scattering, from which the energies of the vibrations are specific to the internal structure of the material under investigation. These scattering modes are shown in Figure 2.17.

In Raman scattering, if the photon relaxes into a higher-energy vibrational state then it is said to be Stokes scattering, with the emission of a lower energy photon whereas if the photon relaxes into a lower-energy vibrational state, it is said to be anti-Stokes scattering

which results in a higher energy photon being emitted. Quantum mechanically, both of these inelastic processes are equally likely but due to the fact that the majority of compounds are laying in the ground vibrational level, Stokes scattering is statistically more likely and hence used in Raman scattering measurements.

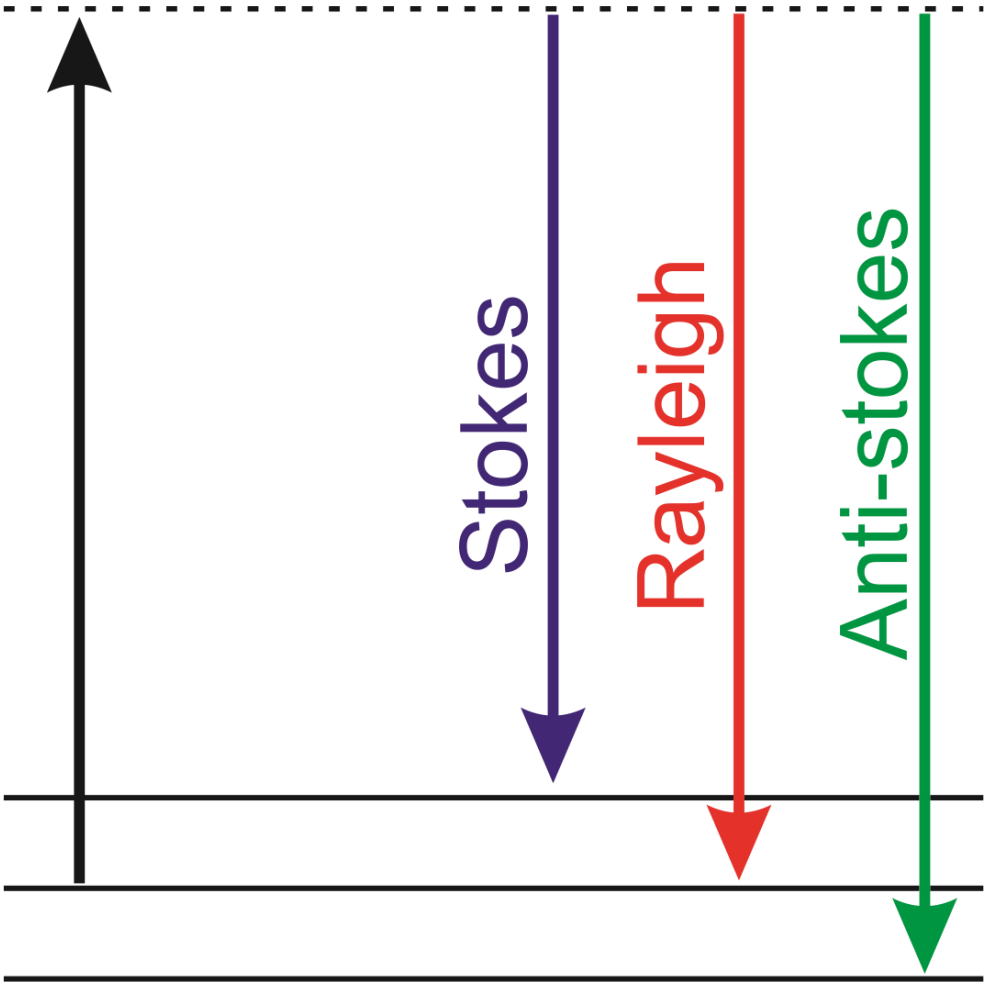


Figure 2.17 Vibrational transitions visible within materials showing the elastic (Rayleigh) and inelastic (Stokes and anti-stokes) scattering.

Raman measurements were carried out in-house on the ThermoScientific™ DXR3 SmartRaman spectrometer, equipped with 532 nm and 785 nm lasers. Laser power was fixed to 100 mW with obtainable spectrums from 100 cm^{-1} to 3500 cm^{-1}. The samples were loaded into 1.5 mm borosilicate capillaries to be loaded into the instrument which allowed air-sensitive samples to be measured.

2.2.10 Bond valence calculations

Bond valence calculations are used to estimate the oxidation states of atoms in a compound. The formula used to calculate these values is displayed in equation 2.29.

$$\sum_{All\ bonds} e^{\frac{R_0 - R}{b}} \tag{2.29}$$

R_0 is the bond valence parameter characteristic of the bond under investigation, R is the observed bond length and b is a constant, typically around 0.37 Å.[105] This method of determining the bond valence considers the local bonding sphere of anions directly bonded to the central cation to give an estimate of the valence of a cation within a certain geometry allowing for comparison with a wide range of known compounds.

Chapter 3

3 Structure-property relationships in Ni-containing mixed-anion solids

3.1 Introduction

The synthesis of $Sr_2NiO_2Cu_2S_2$ was first reported by Otzschi et al., in 1999,[15] albeit with relatively low purity due to the difficulty of avoiding the competing thermal decomposition by reduction of Ni^{2+} and Cu^{+} to the metals with the corresponding oxidation of S^{2-} to form SO_4^{2-} at elevated temperatures as according to equation 3.1:

$$Sr_2NiO_2Cu_2S_2 \xrightarrow{\Delta} \frac{1}{2}\,SrSO_4 + \frac{3}{2}\,SrS + Cu_2Ni \tag{3.1}$$

Following on from this work, Clarke et al., reported the use of a low-temperature synthetic approach to synthesise $Sr_2NiO_2Cu_2S_2$ using an alkali-metal halide flux which resulted in greatly enhanced sample purity and allowed for meaningful property measurements to be undertaken.[7]

Transitions observed in the magnetic susceptibility measurements and an increase in the elongation of the NiO_4S_2 octahedron on cooling appeared qualitatively consistent with a "high- to low-spin" transition for the Ni^{2+} ion on cooling, but the changes in the Ni–S / Ni–O ratio were approximately an order of magnitude smaller than what would be expected for such a change in the spin-state and this, coupled with the convoluted changes in the lattice parameters as a function of temperature indicated complex, unusual behaviour which was attributed to the electronic behaviour of the central Ni^{2+} cation.

More conclusively, the low-temperature PND data had no additional peaks to those attributed to the nuclear structure, consistent with a low-spin, diamagnetic Ni^{2+} ion coordinated in an elongated octahedral (i.e., almost square-planar) environment, in line with molecular compounds containing Ni^{2+} in a square-planar ligand field.

More recently, the selenide analogue, $Sr_2NiO_2Cu_2Se_2$, has been reported by Blandy.[40] It too shows unusual and complex behaviour. Magnetometry and variable temperature diffraction measurements seemed to suggest an electronic transition at ≈ 70 K, initially suspected to be a high-to-low-spin transition. However, it was observed in the low-temperature PND data collected at 5 K that there were additional Bragg peaks in the high *d*-spacing regime in addition to the nuclear peaks, suggesting that they were magnetic in origin and hence confirming that the Ni^{2+} cations in $Sr_2NiO_2Cu_2Se_2$ are localised and in the high-spin configuration.

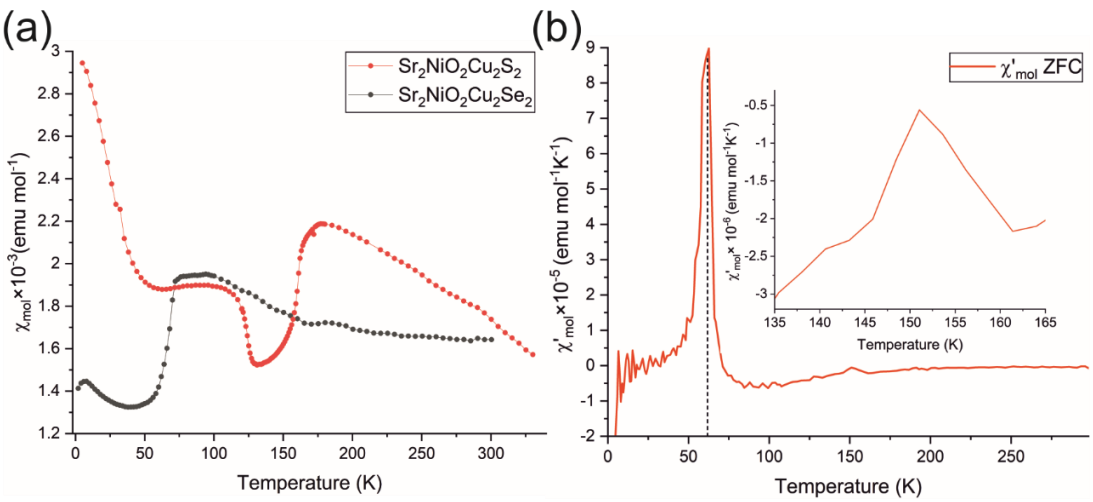


Figure 3.1(a) Magnetic susceptibility of $Sr_2NiO_2Cu_2Se_2$,[40] measured using a 4 – 3 T subtraction compared with the magnetic susceptibility of $Sr_2NiO_2Cu_2S_2$.[35] **(b)** First order derivative χ'_{mol} for $Sr_2NiO_2Cu_2Se_2$. Inset. χ'_{mol} for $Sr_2NiO_2Cu_2Se_2$ around the onset of magnetic ordering.

Rietveld refinement of the data determined that the magnetic moments order antiferromagnetically below ≈ 160 K on a $\sqrt{2}a \times \sqrt{2}a \times 2c$ expansion of the nuclear cell.

The refined, ordered Ni^{2+} moment had a magnitude of 1.31(2) μ_B at 5 K ($\mu_a = \mu_b = 0.46\ \mu_B$; $\mu_c = 1.14(2)\ \mu_B$), which is smaller than the 2 μ_B expected from spin only arguments for d^8 Ni^{2+} in a high-spin configuration but comparable to the calculated spin density of 1.60 μ_B per Ni^{2+} obtained for the antiferromagnetic state from DFT calculations,[38] and this reduction is likely due to the effects of covalency.

Recently, Matsumoto et al., reported that the isostructural analogues $Ae_2NiO_2Ag_2Se_2$ (*Ae* = Sr, Ba), with the larger coinage metal ion Ag^+ in the chalcogenide layer, were attainable using a high-pressure synthesis.[33] Their results showed, using a combination of experimental and computational methods that, in contrast with $Sr_2NiO_2Cu_2S_2$, but like in $Sr_2NiO_2Cu_2Se_2$, these compounds had Ni^{2+} ion in a high-spin configuration, which they ascribed to the reduced ligand field strength resulting from the longer Ni–O bonds enforced by the accommodation of the other larger ions and the weak contribution to the Ni bond valence from the apical selenide anions.

In the work in this chapter, the spin-state crossover from high-spin $Sr_2NiO_2Cu_2Se_2$ to low-spin $Sr_2NiO_2Cu_2S_2$ is explored as a function of composition by investigating the solid solution $Sr_2NiO_2Cu_2(Se_{1-x}S_x)_2$. Low temperature PND data (section 3.2.7) show that compositions up to and including $x = 0.344$ contain peaks that can be attributed to magnetic scattering, and analysis of the magnetic Bragg scattering as a function of increasing sulfide content reveal a smooth reorientation of the spin direction toward the *ab*-plane.

In a sample of nominal composition $Sr_2NiO_2Cu_2(Se_{0.656}S_{0.344})_2$, vestigial magnetic scattering is evident in the form of a highly asymmetric Warren peak, indicative of short-range ordering.

No evidence for magnetic ordering was observable for the more sulfide-rich systems with $x = 0.375$ and higher. Consistent with the behaviour of the magnetic ordering, there is a structural signature of the change from broadly high-spin to broadly low-spin behaviour as selenide is replaced by sulfide which is reflected in the changes of the NiO_4Ch_2 octahedra.

To complement this work on the oxide chalcogenides, the magnetic ordering of the previously synthesised oxide halide, $Sr_2NiO_2Cl_2$,[55] is also investigated. The sample which was characterised within this thesis was provided through collaboration with Yoshihiro Tsujimoto and Kazunari Yamaura whom are affiliated with the National Institute for Materials Science (NIMS) in Japan.

$Sr_2NiO_2Cl_2$ is isostructural with $Sr_2CuO_2Cl_2$[106] and $Sr_2CoO_2Cl_2$[107] (which are accessible in ambient pressure syntheses) and crystallises in the *I*4/*mmm* space group, similar to the layered oxide chalcogenides $Sr_2NiO_2Cu_2(Se_{1-x}S_x)$, and can be envisaged as infinite NiO_2 layers along with double rock salt Sr_2Cl_2 layers with the Ni-Cl bonds calculated to contribute between them just 16.8 % to the total bond valence sum which means the Ni^{2+} centres can be described as in highly elongated octahedra or pseudo-square-planar NiO_4 units with the difference between the oxide halide and oxide chalcogenides being the absence of coinage metal as shown below in Figure 3.2.

Tsujimoto et al., noted a cusp in the magnetic susceptibility suggestive of a magnetic ordering transition indicative that Ni^{2+} was in the high-spin, $S = 1$ state rather than low-spin and diamagnetic.[55] Furthermore, Zhou et al., performed a systematic theoretical study on $Sr_2NiO_2Cl_2$ and came to the conclusion that the unusual coordination environment plays a crucial role in the magnetic and electronic properties of $Sr_2NiO_2Cl_2$ and predicted G-type, antiferromagnetic ordering.[108]

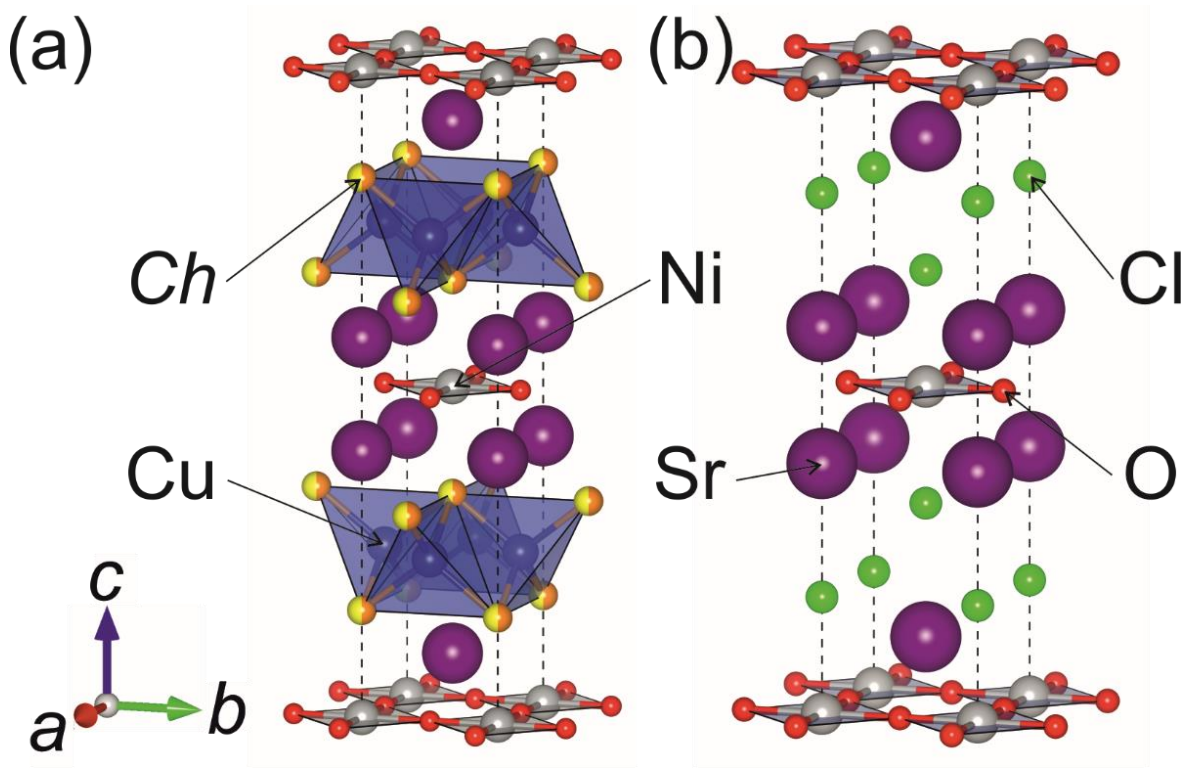


Figure 3.2(a) The structure of $Sr_2NiO_2Cu_2Ch_2$ (*Ch* = S, Se). **(b)** The structure of $Sr_2NiO_2Cl_2$.

The work carried out in this chapter has been recently published in *Chemistry of Materials*[38] and the *Journal of Solid-State Sciences*[109] with the author's direct contribution being the investigation of the solid solution $Sr_2NiO_2Cu_2(Se_{1-x}S_x)_2$, the application of pressure to $Sr_2NiO_2Cu_2Se_2$ and the characterisation of the layered oxide chloride $Sr_2NiO_2Cl_2$, which was prepared via collaboration.

3.2 Synthesis and characterisation of the solid solution $Sr_2NiO_2Cu_2(Se_{1-x}S_x)_2$

3.2.1 Synthesis of $Sr_2NiO_2Cu_2(Se_{1-x}S_x)_2$ $0 \leq x \leq 0.5$

Samples of $Sr_2NiO_2Cu_2(Se_{1-x}S_x)_2$ for $0 \leq x \leq 0.5$ were synthesised from a mixture of SrO (obtained via thermal decomposition under dynamic vacuum of $SrCO_3$ (Alfa 99.994 %), at initially 840 °C with a final treatment at 1100 °C as outlined in section 2.1.3.1), Ni (Alfa 99.996 %), Cu (Alfa 99+ %), and an appropriate amount of S (Alfa 99.999 %) or Se (Alfa 99.999 %).

The powders were ground together, pelletised with an applied force 0.4 GPa, loaded into an alumina crucible and sealed in an evacuated silica ampoule (19 mm o.d.) with the sample-containing ends of the ampoules submerged in liquid N_2 during flame sealing to avoid the vaporisation of elemental S.

These samples were then preheated at 400 °C, ramping up at 10 °C min^{-1}, for 12 hours to avoid the vapour pressure inside the silica tube getting too high while the chalcogen reacted, before final heating at 950 °C for 16 hours, again ramping at 10 °C min^{-1}. The tube was subsequently quenched in an ice/water mixture.

Blandy demonstrated that attempts to synthesise $Sr_2NiO_2Cu_2Se_2$ at temperatures lower than 950 °C resulted in significant amounts of impurities and different lattice parameters for the main phase compared with those found in the purest products.[40] This was partially due to Ni / Cu disorder between the oxide and chalcogenide layers whereby Cu^{2+} in the oxide layer with a d^9 configuration resulted in a more elongated c / a ratio, reminiscent of a Jahn-Teller distortion and for this reason, the quenching step was necessary.

3.2.2 Synthesis of $Sr_2NiO_2Cu_2(Se_{1-x}S_x)_2$ $0.625 < x \leq 0.875$

For the more S-rich compounds ($0.625 \leq x \leq 0.875$), it was discovered in this work that using a high-temperature approach similar to that used for the Se-rich end, led to significant amounts of $Cu_{1-x}Ni_x$ alloy, SrS and $SrSO_4$ impurities (see Figure 3.3) and therefore, a synthetic route similar to that used for $Sr_2NiO_2Cu_2S_2$[7] was used, whereby a low-melting alkali-metal halide flux consisting of 0.56:0.44 CsI: NaI was employed which was calculated by Smura to be ideal for the synthetic temperature of 500 °C as the melting point remains below the synthesis temperature ± 3 % of the specified composition of the alkali-metal halide flux, allowing for some degree of inaccuracy within the experimental procedure.[35]

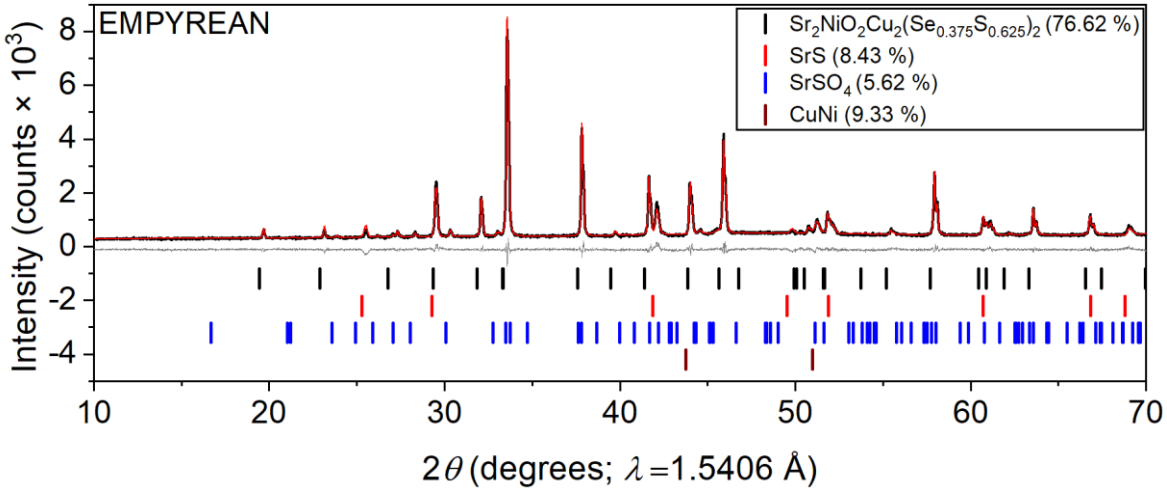


Figure 3.3 Rietveld refinement of an attempted synthesis of S-rich $Sr_2NiO_2Cu_2(Se_{1-x}S_x)_2$ (x = 0.625), using a high temperature approach.

This eutectic mixture with a melting point of 435 °C[110] was prepared using "ultra-dry" CsI (Alfa 99.998 %) and NaI (Alfa 99.9 %) which was predried at 300 °C for 12 hours in a muffle furnace prior to use. The iodide mixture was then ground together with the reaction mixture which consisted of SrS, SrSe, NiO (Aldrich 99.99 %) and Cu_2O in the molar ratio 2-x:x:1:1 under argon. SrS was made by heating $SrCO_3$ (Alfa, 99.99 %) at 800 °C in a flow of CS_2 (Aldrich, 99.5 %) gas, as described in section 2.1.3.2. SrSe was made by heating

sublimed Sr and Se up to 400 °C at 0.5 °C min^{-1} followed by a dwell of 12 hours and then ramping to 700 °C at 0.5 °C min^{-1} for 6 hours as detailed in section 2.1.3.4. Cu_2O was synthesised by heating CuO (Aldrich 99.99 %) and elemental Cu (Alfa 99.999 %) powders in a 1:1 molar ratio at 1000 °C for 16 hours, as detailed in section 2.1.3.5.

The sample / flux mixture was heated in an alumina crucible which was sealed within an evacuated silica ampoule at 500 °C for 15 hours. This was repeated until no further change was observed in the diffraction pattern, which was usually after three heating cycles. Using a low-temperature synthetic route encourages the formation of the S-rich solid solution phases without leading to the thermal decomposition of the target phase.

3.2.3 Room temperature powder X-ray diffraction

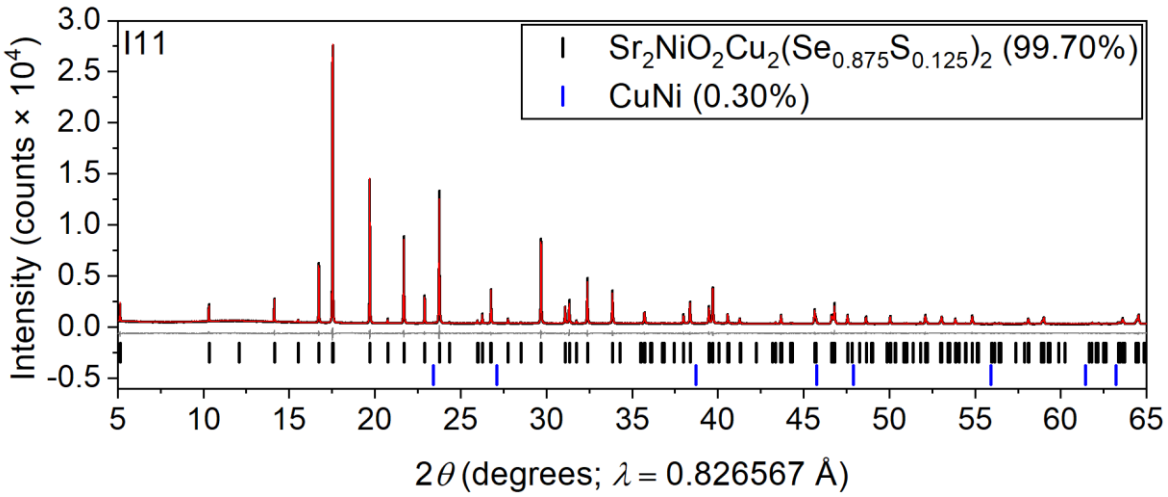


Figure 3.4 Rietveld refinement of $Sr_2NiO_2Cu_2(Se_{0.875}S_{0.125})_2$ from data collected on the I11 beamline at Diamond Light Source Ltd, shown are data: black; fit: red; difference: grey. R_{wp} = 7.510 %; χ^2 = 1.714.

The structure and composition of the samples within the solid solution were originally probed using the in-house diffractometers. Once the samples were known to be of high purity, they were prepared for high-resolution PXRD using the high resolution

diffractometer at the I11 beamline at Diamond Light Source Ltd[83] with the samples prepared as outlined in section 2.2.2.

Rietveld refinement of the resulting data confirmed that all members of the $Sr_2NiO_2Cu_2(Se_{1-x}S_x)_2$ solid solution crystallise in the tetragonal *I*4/*mmm* space group with the structural model used during Rietveld refinement outlined in Table 3.1 and a representative refinement shown in Figure 3.4.

The structures of the compounds are similar to those of both end members, as expected, with both S and Se refined to occupy the same crystallographic site which is not unreasonable due to their size compatibility and comparable valence orbital energies as outlined in section 1.3.1.

During the refinement, the lattice parameters of the metallic alloy refined to a value between that of elemental Cu (3.6150 Å) and Ni (3.5238 Å),[9] from which an approximate composition could be calculated on the assumption that there is a linear change in the lattice parameters as a function of composition which has been shown by Coles to be approximately true.[111]

Table 3.1 Structural Model for $Sr_2NiO_2Cu_2(Se_{1-x}S_x)_2$ ($0.125 \leq x \leq 0.5$).

Atom	Position	*x*	*y*	*z*
Sr	4*e*	0	0	*z*Sr
Ni	2*a*	0	0	0
Cu	4*c*	0	0.5	0.25
O	4*d*	0	0.5	0
Se	4*e*	0	0	*zCh*
S	4*e*	0	0	*zCh*
Space group = *I*4/*mmm*				

3.2.4 Room temperature powder neutron diffraction

Multiple samples of $Sr_2NiO_2Cu_2(Se_{1-x}S_x)_2$ with different values of x were probed using high-resolution PND measurements on the WISH diffractometer at ISIS.

The anti-site disorder between Ni and Cu could be easily resolved using neutrons due to their differing coherent neutron scattering lengths (10.3 and 7.718 fm respectively)[80] and with a refined occupancy of Cu of 0.01(3) in $Sr_2NiO_2Cu_2(Se_{0.875}S_{0.125})_2$ and a similar refined value in the other compositions probed, it can be assumed within error that the oxide layer is occupied solely by Ni^{2+} with Cu^{+} occupying the chalcogen layer which is in line with the end member $Sr_2NiO_2Cu_2Se_2$ and what would be expected based on HSAB theory with Ni being a "harder" cation than Cu.

PND was also used to confirm the exact composition which was assumed to be the targeted phase due to the lack of impurities as side phases. A representative Rietveld refinement of the series is shown in Figure 3.5.

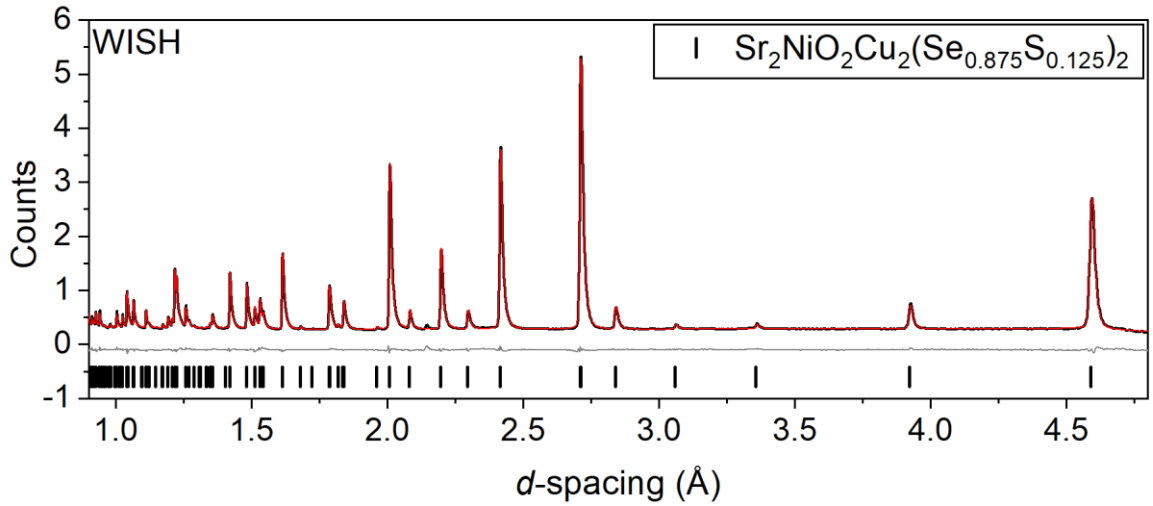


Figure 3.5 Rietveld refinement of $Sr_2NiO_2Cu_2(Se_{0.875}S_{0.125})_2$ from data collected on the WISH diffractometer at ISIS at room temperature, shown are data: black; fit: red; difference: grey. R_{wp} = 2.165 %; χ^2 = 0.012.

Table 3.2 shows refined structural parameters from the solid solution. As expected, the lattice parameters reduce as larger Se^{2-} is replaced by smaller S^{2-} with the selected bond lengths mirroring this trend.

The extracted refined parameters for $Sr_2NiO_2Cu_2(Se_{1-x}S_x)_2$ ($0.125 \leq x \leq 0.5$), are shown below in Table 3.2 with the thermal displacement parameters shown in Table 3.3. The lattice parameters and volume change in the expected way based on ionic radii arguments where larger Se^{2-} anions are being successively replaced within the structure by smaller S^{2-} anions.

Interestingly, there is not a large variation in the *Ch*–Cu–*Ch*, α and *Ch*–Cu–*Ch*, β angles which is likely due to the increase in both *a* and the Cu-Se bond distance which can be accommodated with the angle remaining constant.

Table 3.2 Comparison of structural parameters for $Sr_2NiO_2Cu_2(Se_{1-x}S_x)_2$ ($0.125 \leq x \leq 0.5$) at RT.

	$(Se_{0.875}S_{0.125})_2$	$(Se_{0.75}S_{0.25})_2$	$(Se_{0.625}S_{0.375})_2$	$(Se_{0.5}S_{0.5})_2$
a (Å)	4.01790(4)	4.00594(4)	3.99345(3)	3.982128
c (Å)	18.3754(3)	18.3516(3)	18.3021(2)	18.290647
c / *a*	4.57338(8)	4.58111(9)	4.58304(7)	4.59318
Volume (Å^3)	296.644(7)	294.498(8)	291.877(6)	290.041
M–O (Å)	2.00895(2)	2.00297(2)	1.99673(2)	1.99106
M–*Ch* (Å)	3.089(1)	3.082(1)	3.078(1)	3.07474
M–*Ch* /*M*–O	1.5374(5)	1.5387(6)	1.5424(6)	1.54427
Ch–Cu–*Ch* (Å)	2.5104(4)	2.5059(7)	2.4949(6)	2.4916(6)
Ch–Cu–*Ch*, α (°) [2]	106.31(3)	106.13(4)	106.32(4)	106.09(6)
Ch–Cu–*Ch*, β (°) [4]	111.08(2)	111.17(2)	111.07(2)	111.19(3)
z(Sr)	0.41183(8)	0.41153(8)	0.41109(9)	0.41058(8)
z(*Ch*)	0.16713(8)	0.16782(5)	0.16827(6)	0.16841(6)

However, as can be seen clearly in Figure 3.6, a closer look at the local coordination environment shows a different picture, whereby even though there is only a slight downturn in the Ni-O bond length (as would be expected with a "high-to-low-spin-like" transition), the increase in the Ni-*Ch* distance is much more pronounced and its increase dominates the Ni-*Ch* / Ni-O ratio, becoming larger even though the average chalcogen size is decreasing, further reinforcing the idea that the elongation of the NiO_4Ch_2 octahedra is configuration-driven.

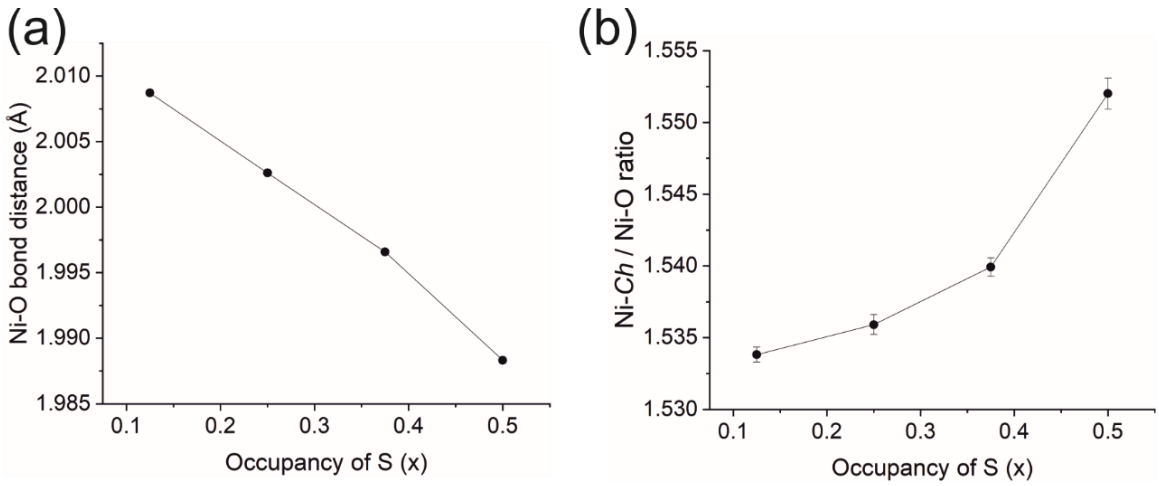


Figure 3.6(a) The Ni-O bond lengths and **(b)** Ni-*Ch* / Ni-O ratio for the more Se-rich members of the solid solution $Sr_2NiO_2Cu_2(Se_{1-x}S_x)_2$. The data including the more S-rich compounds can be seen in Figure 3.13.

Table 3.3 Refined U_{iso} parameters for $Sr_2NiO_2Cu_2(Se_{1-x}S_x)_2$ ($0.125 \leq x \leq 0.5$) from PND at RT

	$Sr_2NiO_2Cu_2(Se_{0.875}S_{0.125})_2$	$Sr_2NiO_2Cu_2(Se_{0.75}S_{0.25})_2$	$Sr_2NiO_2Cu_2(Se_{0.625}S_{0.375})_2$	$Sr_2NiO_2Cu_2(Se_{0.5}S_{0.5})_2$
U_{iso}(Sr1) (Å^2)	0.0129(4)	0.0093(4)	0.0101(4)	0.0084(3)
U_{iso}(Ni1) (Å^2)	0.0172(5)	0.0129(4)	0.0126(5)	0.0233(5)
U_{iso}(Cu1) (Å^2)	0.0234(5)	0.0193(5)	0.0182(6)	0.0202(4)
U_{iso}(O1) (Å^2)	0.0134(5)	0.0115(5)	0.0107(5)	0.0192(6)
U_{iso}(*Ch*1) (Å^2)	0.0167(5)	0.0139(6)	0.0128(6)	0.0206(8)

3.2.5 Variable temperature SPXRD

Various compositions of the selenide-rich members of the $Sr_2NiO_2Cu_2(Se_{1-x}S_x)_2$ solid, where the system seems to be approaching the spin-state crossover based on the elongation of the octahedron were also measured as a function of temperature using SPXRD from 100 – 300 K using the cryostream on the I11 beamline at the Diamond Light Source.[83]

Individual Rietveld refinements were observed visually, looking for any evidence of peak-splitting or extra superstructure peaks which would suggest a lowering of symmetry or a cell expansion on cooling as well as performing a sequential Rietveld refinement of the data which allowed for rapidly extracting the refined parameters with the result shown below in Figure 3.7 which displays the changes in the *c* / *a* ratio.

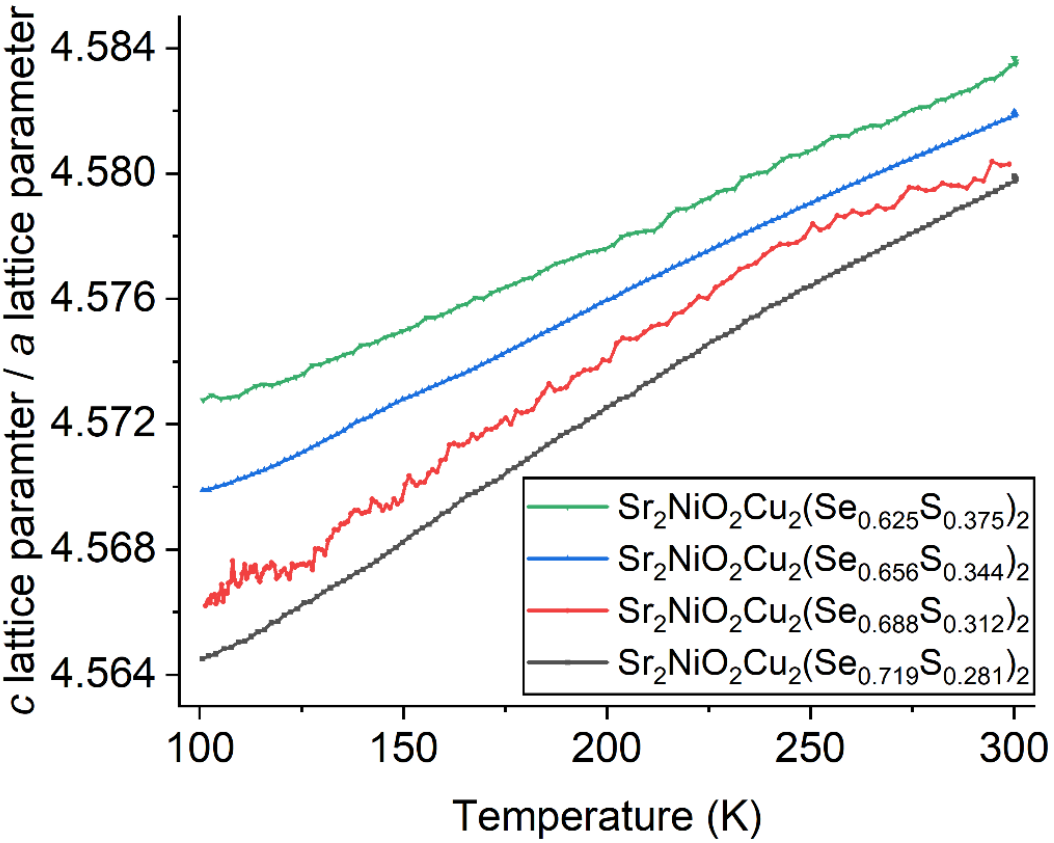


Figure 3.7 Changes in the *c* / *a* ratio as a function of temperature for $Sr_2NiO_2Cu_2(Se_{1-x}S_x)_2$ $0.281 \leq x \leq 0.375$. Data collected on the I11 beamline at the Diamond Light Source Ltd.[83]

There were no observable changes in the lattice parameters that were not accountable by that of thermal expansion as shown by Figure 3.7, although the data for $Sr_2NiO_2Cu_2(Se_{0.688}S_{0.312})$ is clearly a lot nosier than the other samples and has a different profile. Attempts to rectify this have been unsuccessful despite the Rietveld refinement showing good statistical and visual agreement and so this is seemingly an instrumental issue and so instead the neutron data was focused on which also provided a much wider spectrum of compositions for comparison.

3.2.6 Magnetometry

The *M vs H* isotherm for many of these samples was non-linear at low fields suggesting some ferromagnetic impurity, most likely the aforementioned $Cu_{1-x}Ni_x$ alloy, was present. This was < 1 % by mass from the refinement, but because of the magnitude of ferromagnetism as opposed to antiferromagnetism, even small quantities can dominate the magnetic susceptibility of the samples.

This impurity had saturated at higher fields where the *M vs H* isotherm was linear and so the magnetic susceptibility of various samples up to the loss of long-range magnetic ordering were measured using a 6 T – 5 T subtraction, allowing for direct comparison with the results shown in Figure 3.8.

The samples in the solid solution, i.e., $x \neq 0$ in Figure 3.8, do not seem to have the same pronounced kink in the susceptibility as $Sr_2NiO_2Cu_2Se_2$ (but visible to an extent in $Sr_2NiO_2Cu_2(Se_{0.875}S_{0.125})_2$ and even less-so in $Sr_2NiO_2Cu_2(Se_{0.75}S_{0.25})_2$).

The more S-rich compounds measured on the SQUID (x = 0.375 and 0.5), have a distinct feature at low temperatures which is of unknown origin. The S-rich compounds are missing

the kink that was identified as coinciding with T_N in the more Se-rich analogues which would suggest they have the low-spin Ni^{2+} configuration which is investigated in section 3.2.7.

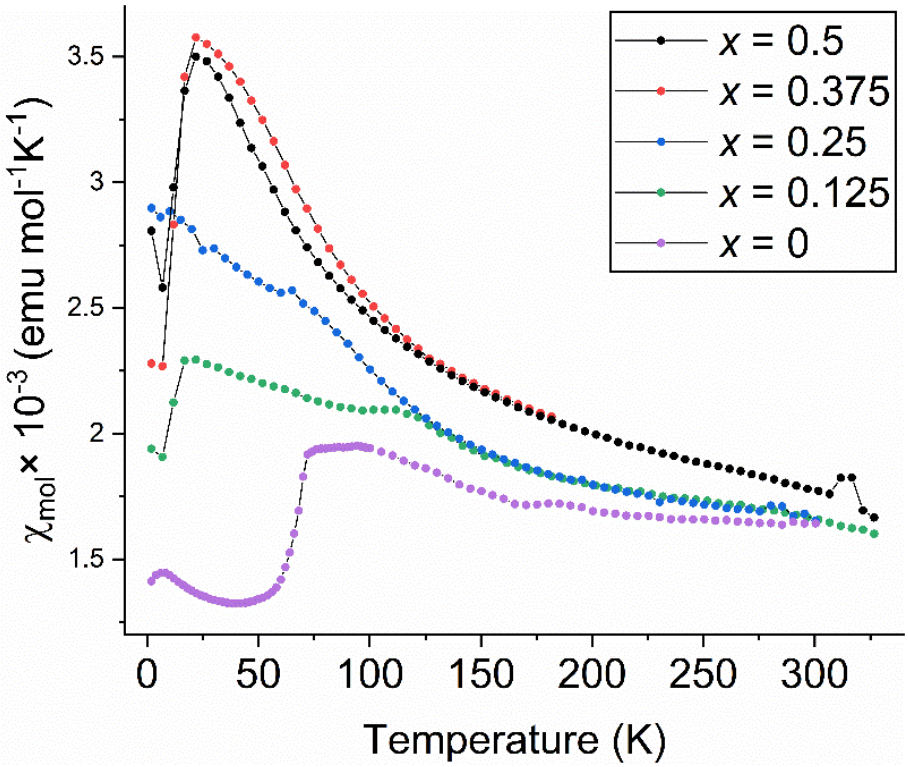


Figure 3.8 SQUID data for the $Sr_2NiO_2Cu_2(Se_{1-x}S_x)_2$ series of compounds for $0 \leq x \leq 0.5$ measured using a 6 T – 5 T subtraction (as described in section 2.2.7.1).

3.2.7 Traversing the spin-state crossover in $Sr_2NiO_2Cu_2(Se_{1-x}S_x)_2$ using PND

Due to the fact that there are magnetic Bragg peaks observed for $Sr_2NiO_2Cu_2Se_2$,[40] whereas there were none observed for $Sr_2NiO_2Cu_2S_2$ at low temperatures,[35] together with the very different Ni−*Ch* / Ni−O ratios in the two compounds, suggested that in the solid solution $Sr_2NiO_2Cu_2(Se_{1-x}S_x)_2$, a high- to low-spin transition would be evident as a function of composition with increasing *x* by monitoring the structural parameters and/or the magnetic behaviour.

To probe this, one-gram batches of four initial samples, $Sr_2NiO_2Cu_2(Se_{0.875}S_{0.125})_2$, $Sr_2NiO_2Cu_2(Se_{0.75}S_{0.25})_2$, $Sr_2NiO_2Cu_2(Se_{0.625}S_{0.375})_2$, and $Sr_2NiO_2Cu_2(Se_{0.5}S_{0.5})_2$, were

measured on the ToF WISH diffractometer at ISIS. A representative plot is shown in Figure 3.9, where the asterisks denote intensity accounted for by magnetic reflections.

Ni^{2+} has a spin-only magnetic moment of 2 μ_B and therefore the magnitude of the magnetic scattering would be anticipated to be relatively small. As such, WISH is the ideal instrument with its high signal-to-noise ratio in the region of the magnetic scattering meaning that small magnetic ordered moments of the order of 0.3 μ_B or less are distinguishable from the background[23] for all of the compounds explored within this chapter including the oxide halide $Sr_2NiO_2Cl_2$ explored in section 3.3.

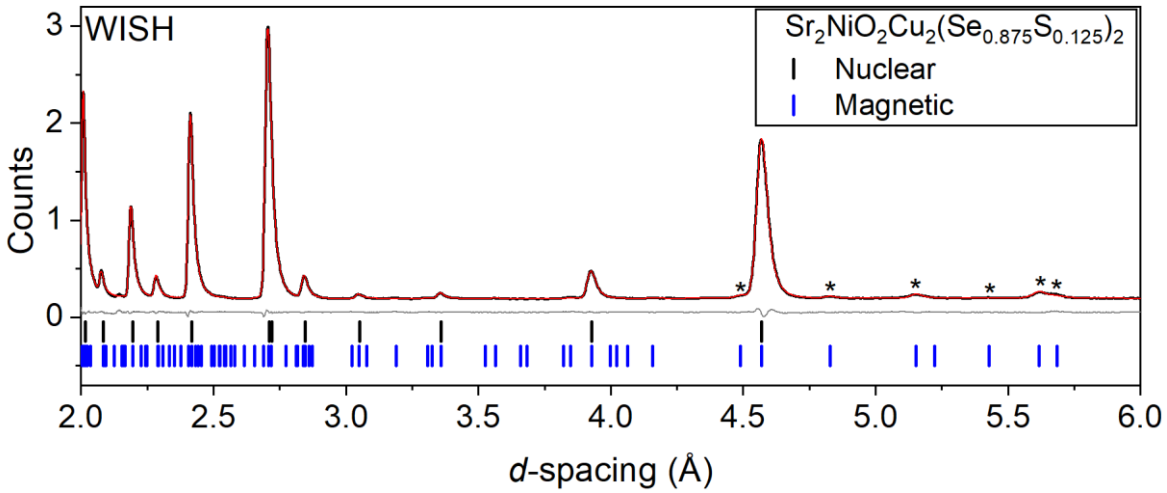


Figure 3.9 Rietveld refinement at 1.5 K of $Sr_2NiO_2Cu_2(Se_{0.875}S_{0.125})_2$ against bank 3/8 of the WISH diffractometer at ISIS. shown are data: black; fit: red; difference: grey. R_{wp} = 4.544 %; χ^2 = 0.020.

On analysis of the data, it was clear that for the x = 0.375 sample and the more S-rich compositions, that there was no magnetic Bragg scattering, but there was however a significant evolution of the magnetic peaks in the range $0 \leq x \leq 0.25$ before their disappearance by x = 0.375, which was suggestive of a change in the magnetic structure as x was increased i.e., the samples became more S-rich.

Therefore, to pinpoint the changes and the transition to the state with no observable magnetic long-range order with greater accuracy, samples with higher compositional resolution were probed. Three further samples, $Sr_2NiO_2Cu_2(Se_{0.719}S_{0.281})_2$, $Sr_2NiO_2Cu_2(Se_{0.688}S_{0.312})_2$ and $Sr_2NiO_2Cu_2(Se_{0.656}S_{0.344})_2$ were measured on WISH, with measurements made from 1.5 K up to the Néel temperature. The normalised raw data for all seven samples measured at 1.5 K are shown below in Figure 3.10.

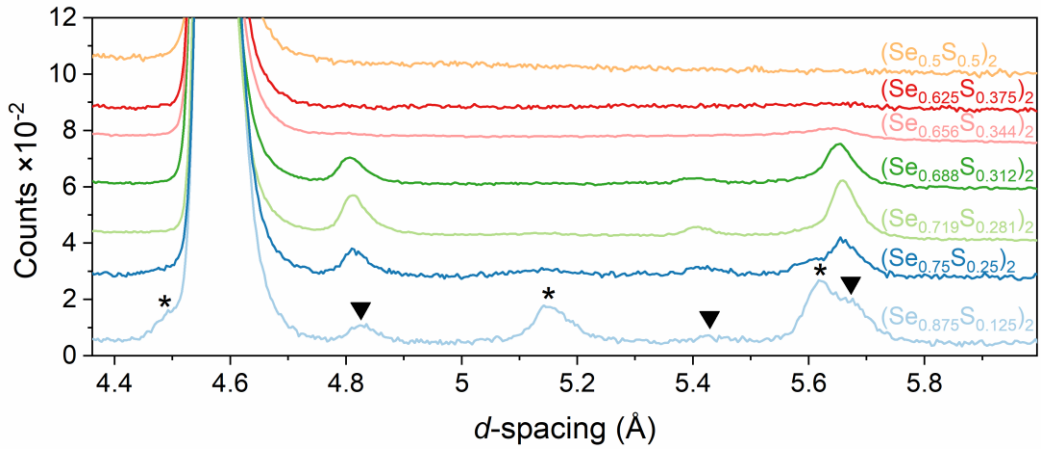


Figure 3.10 Normalised raw data for $Sr_2NiO_2Cu_2(Se_{1-x}S_x)_2$ ($0.125 \leq x \leq 0.5$) from bank 3/8 of the WISH diffractometer at ISIS.

On inspection of the magnetic Bragg peaks, it was apparent that they could be grouped into two different sets, similar to those in the end member $Sr_2NiO_2Cu_2Se_2$ (i.e., $x = 0$). The peaks marked with an asterisk in Figure 3.10 decrease in intensity with increasing S content, whereas the peaks marked with an inverted triangle initially increased in intensity and then subsequently decreased.

The magnetic model for $Sr_2NiO_2Cu_2Se_2$ was used as the starting point for the refinements (see Figure 3.12, $x = 0$, which is magnetic space group $P_C4_12_12$ (92.117) in the Belov, Neronova and Smirnova (BNS) scheme.[38]) of the solid solution due to the similarity of the observable magnetic peaks in the diffractograms; this model has Ni^{2+} moments that are

modelled on a $\sqrt{2}a \times \sqrt{2}a \times 2c$ expansion of the nuclear cell and activating the mX3+ mode (to give intensity to peaks marked with inverted triangles in Figure 3.10) and mP4 mode (asterisks in Figure 3.10) with the associated tick marks shown in Figure 3.11, accounted for all the peaks in the diffractogram as shown below by the alignment of the magnetic Bragg peaks and the tick marks which belong to each magnetic mode.

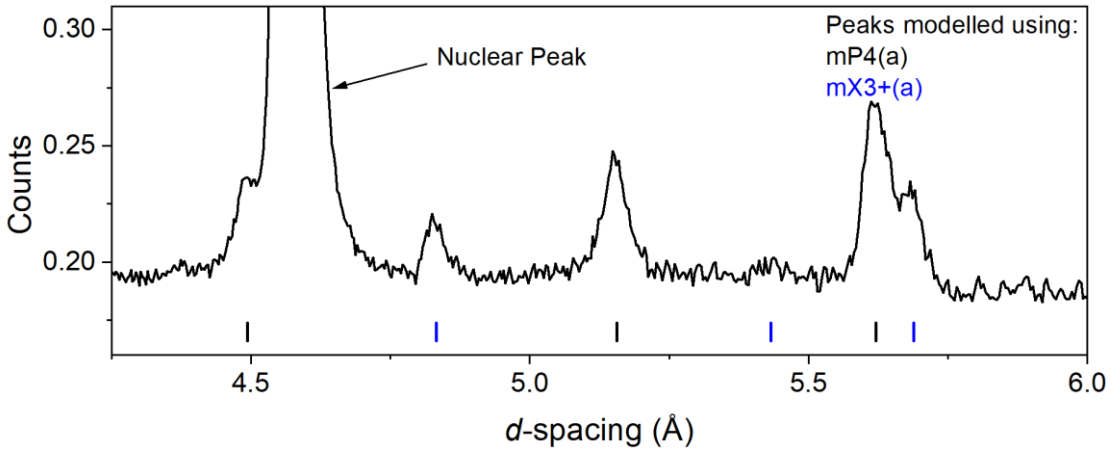


Figure 3.11 Annotated powder neutron diffraction pattern of $Sr_2NiO_2Cu_2Se(_{0.875}S_{0.125})_2$, measured using WISH at 1.5 K. The magnetic peaks are indexed using the expanded magnetic cell and the colour coding indicates which peaks are modelled by the mP4(a) mode (k-vector: (½, ½, ½)) and the $mX3^+$(a) mode (k-vector: ((½, ½, 0)).

From Figure 3.10, it can then be inferred from the changes in intensity that upon increasing x in $Sr_2NiO_2Cu_2(Se_{1-x}S_x)_2$, i.e., making the samples more S-rich, the Ni^{2+} moments undergo a spin reorientation toward the basal plane as the magnitude of the mP4 mode decreases which can be seen visually in Figure 3.12 below and this is quantified by the extracted parameters from Rietveld refinement of each phase which can be seen in Figure 3.13.

There is no evidence for a spin-reorientation for any composition as a function of temperature. The magnetic moment is proportional to the square root of the intensity, and as can be seen from Figure 3.13, there is no great discernible reduction in the total integrated

intensity before the magnetic peaks disappear, and so the refined values of the magnitude of the ordered moment in Figure 3.13 are relatively constant.

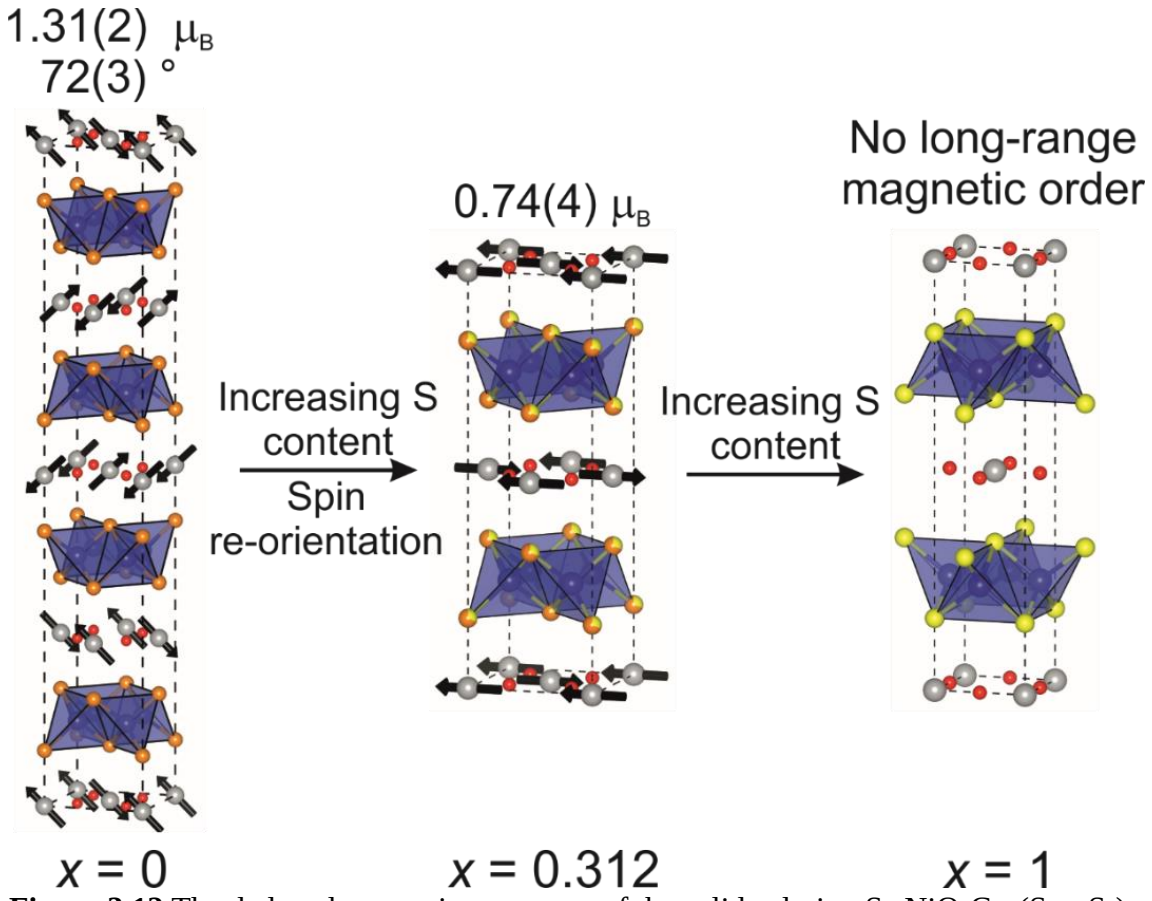


Figure 3.12 The deduced magnetic structures of the solid solution $Sr_2NiO_2Cu_2(Se_{1-x}S_x)_2$.

There were no magnetic Bragg peaks observed for $Sr_2NiO_2Cu_2(Se_{0.656}S_{0.344})_2$; however, in this sample there was additional intensity around the same *d*-spacing as the magnetic peaks of the more Se-rich phases in the form of a highly asymmetric peak which disappeared on warming as can be seen in Figure 3.14.

The Warren function shown below was used to model the additional peak in Figure 3.14 with a fit of the data to the Warren function shown in Figure 3.15 and extracted parameters in Table 3.4.

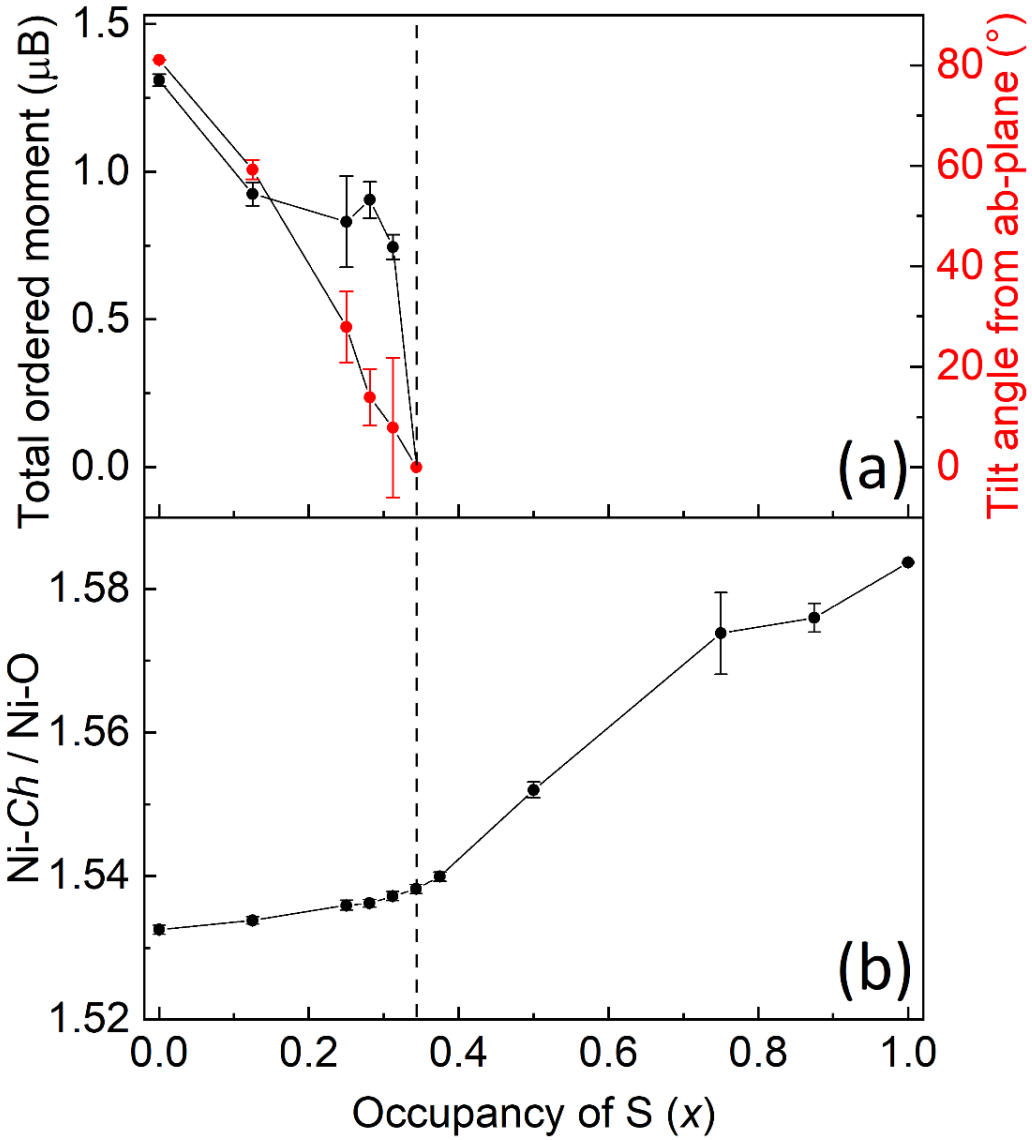


Figure 3.13(a) The change in the magnitude of the total ordered moment and the tilt angle from the *ab*-plane along with **(b)** The Ni-*Ch* / Ni-O ratio as a function of Se occupancy in $Sr_2NiO_2Cu_2(Se_{1-x}S_x)_2$. The dashed line is a guide to the eye whereby the moment of $Sr_2NiO_2Cu_2(Se_{0.656}S_{0.344})$ has been fixed to 0 due to the presence of only short-range magnetic order (see Figure 3.15) and this coincides with an upturn in the axial elongation of the Ni^{2+} environment.

$$S(\boldsymbol{Q}) = \frac{1}{2\pi\sigma_{\perp}^{2}} \exp\left[-\frac{1}{2}\left(\frac{|\boldsymbol{Q}-\tau|_{\perp}}{\sigma_{\perp}}\right)^{2}\right] \frac{X_i}{\pi} \frac{1}{1+(X_i|\boldsymbol{Q}-\tau|_{\parallel})^{2}} \qquad (3.2)$$

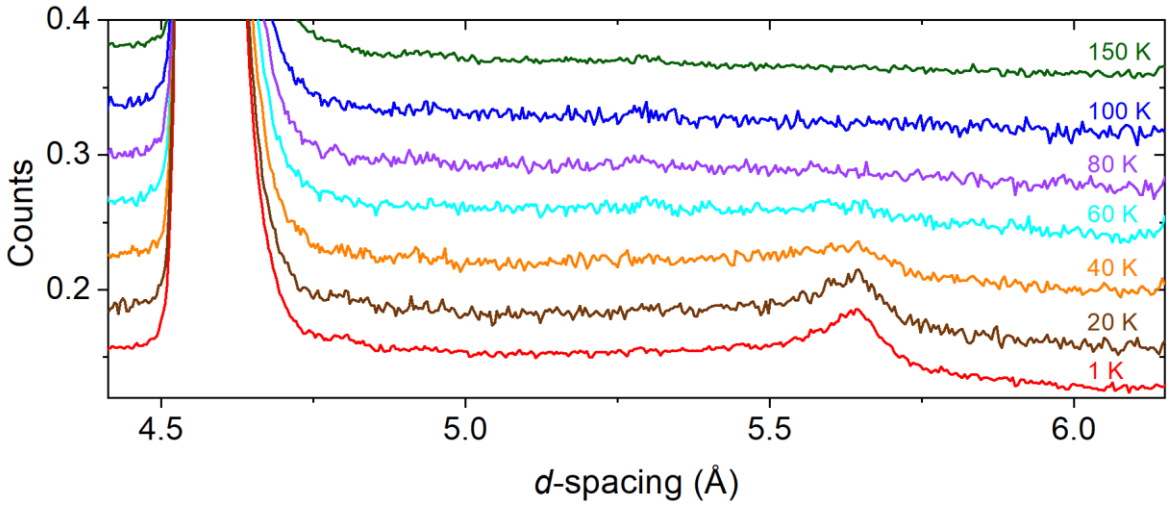


Figure 3.14 The appearance of a highly asymmetric peak on cooling in $Sr_2NiO_2Cu_2(Se_{0.656}S_{0.344})_2$ which can be modelled using a Warren function.

The Gaussian and Lorentzian parts describe the long-range, in-plane correlation and the short-range correlation along lattice parameter *c* respectively. $\sigma_\perp$ represents the in-plane peak width, X_i is the correlation length and τ is the position of the centre of the peak. The integrated intensity of this feature at 1.5 K was much weaker than that in the more Se-rich phases. It was indexed as the 100 reflection on a $\sqrt{2}a \times \sqrt{2}a \times c$ expansion of the nuclear cell. This peak profile has been seen in related compounds such as $Sr_2MnO_2Cu_{1.8}Te_2$[26] as well as $Sr_2MnO_2Mn_2As_2$.[112]

This is consistent with antiferromagnetic nearest-neighbour ordering of high-spin Ni^{2+} ions with an estimated correlation length of 100(5) Å. It is thus inferred that there is an increasing number of low-spin, diamagnetic Ni^{2+} ions present in the compound as the sulfide content increases, and so antiferromagnetic long-range order is disrupted by the Ni^{2+} spin-state disorder, hence the Warren-type peak and the reduced intensity of the magnetic scattering.

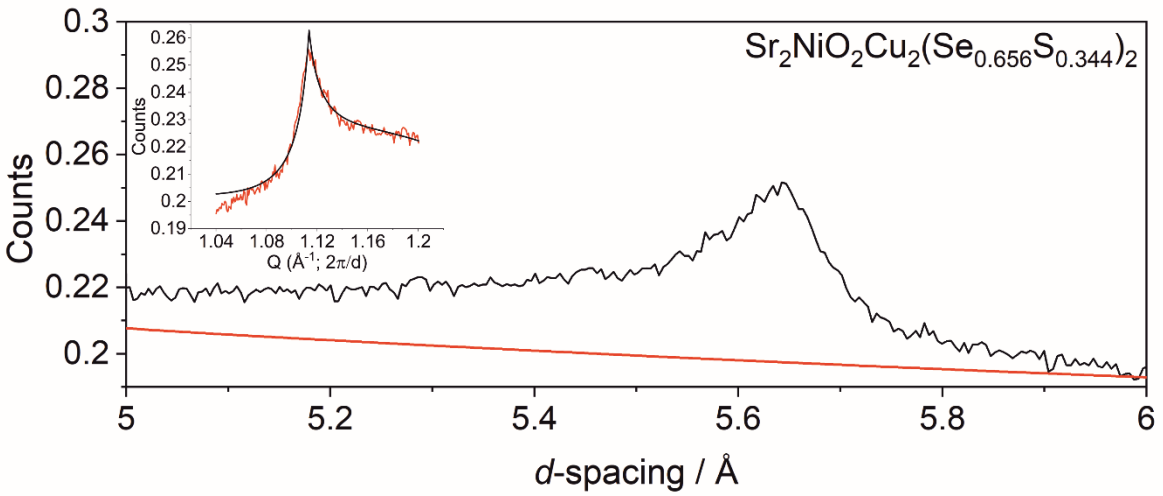


Figure 3.15 Zoomed in region of the Rietveld refinement of $Sr_2NiO_2Cu_2(Se_{0.656}S_{0.344})_2$ from bank 2/9 of the WISH diffractometer at ISIS showing additional intensity not accounted for by the nuclear model (red). The inset shows this additional peak fitted to a Warren-like peak function.

Table 3.4 The extracted Warren peak[113–115] parameters as according to equation 3.2.

Model	Warren-like
σ	0.066(3)
τ_1	1.214(8)
τ_2	1.1136(2)
X_i	97(5)
Reduced χ^2	7.5416×10^{-6}
R-Square (COD)	0.96841
Adj. R-Square	0.96774

For more S-rich compounds, there is no additional intensity observed compared with the nuclear model, and so it can be concluded that close to $Sr_2NiO_2Cu_2(Se_{0.656}S_{0.344})_2$, there is a change in the bulk magnetic behaviour of the compounds consistent with the Ni^{2+} ions becoming low-spin, and this is consistent with the sharp increase in the Ni−*Ch* / Ni−O ratio as *x* increases (Figure 3.13) even as the amount of the smaller chalcogenide increases. It

would be expected that the Ni-*Ch* bond would decrease as the average anion size decreased as the lattice parameters decrease, but from Figure 3.13 it can be seen that the opposite occurs.

However for the low-spin-state to be favoured, as shown below in Figure 3.16, the difference in energy between dx^2-y^2 and dz^2 must be sufficient so that the low-spin-state is more favourable. Within the solid solution $Sr_2NiO_2Cu_2(Se_{1-x}S_x)_2$, the average chalcogen size decreases as *x* increases and this in turns shortens the Ni-O bond length (which is equal to half of the *a* lattice parameter), this, coupled with the simultaneous increase in the Ni-*Ch* bond length across the series is the driving force behind the changes in the *d*-orbital energies, and thus the change in spin configuration.

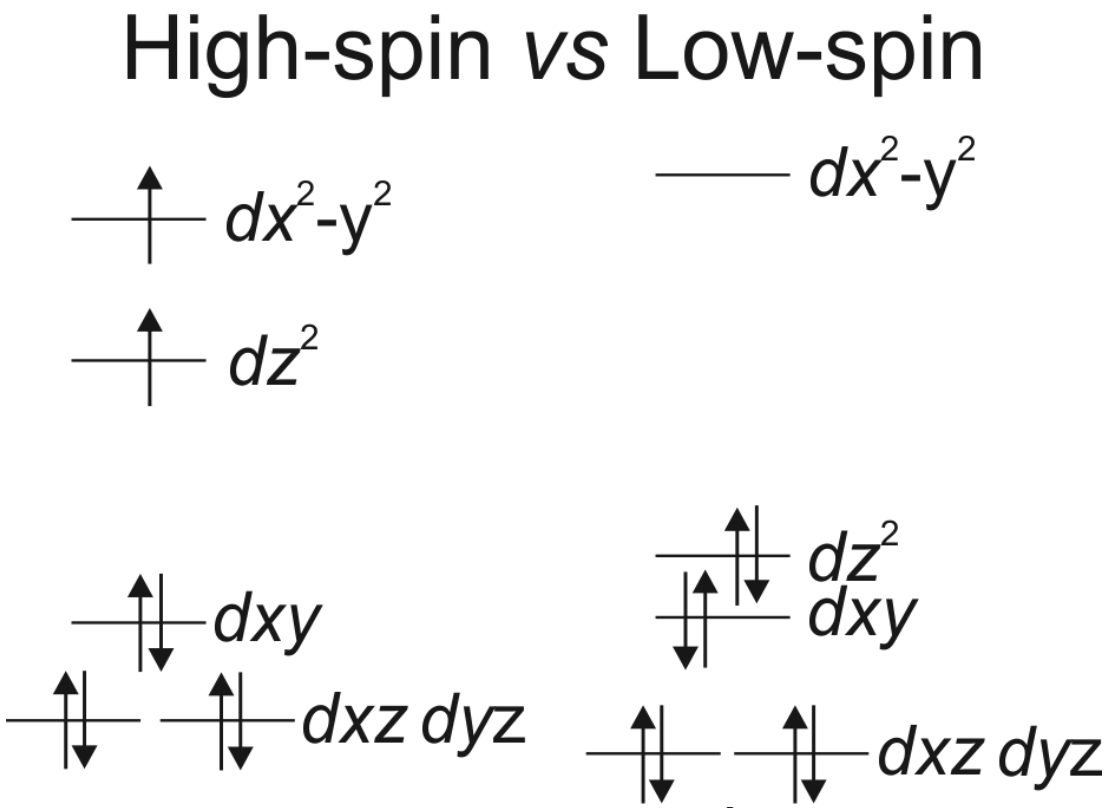


Figure 3.16 The *d*-orbital occupancies for high-spin Ni^{2+} in an elongated octahedral environment compared to low-spin at the square-planar limit.

3.2.8 Variable temperature PND.

During the investigation into the magnetic ordering of these materials using the WISH diffractometer at ISIS,[84] it was also possible to take measurements at regular intervals giving variable temperature data down to 1.5 K and allowing comparison for PND data collected for $Sr_2NiO_2Cu_2Se_2$ on OSIRIS[116] and $Sr_2NiO_2Cu_2S_2$ on POLARIS.[117]

The obvious outlier in the data is the oxide sulfide, which displays complex behaviour which is yet to be fully resolved.[7] Even though the normalised changes in the *c* / *a* ratio are small across the series as seen in Figure 3.17, there is a visible trend for the more Se-rich materials whereby the *c* / *a* ratio decreases at an increased rate when there is more Se in the sample which would be consistent with the Ni^{2+} ion becoming "more high-spin-like" due to the less elongated octahedron.

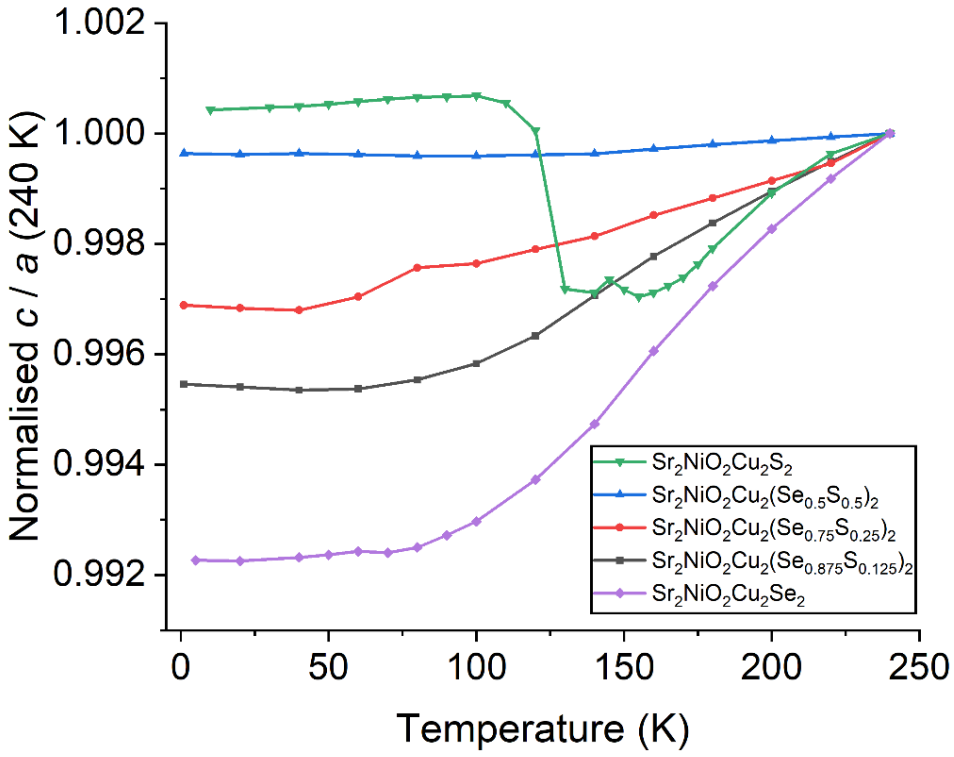


Figure 3.17 Changes in the *c* / *a* ratio as a function of temperature for $Sr_2NiO_2Cu_2(Se_{1-x}S_x)_2$ $0 \leq x \leq 1$. Data from WISH at ISIS for the solid solution, POLARIS for $Sr_2NiO_2Cu_2S_2$ and OSIRIS for $Sr_2NiO_2Cu_2Se_2$.

The normalised Ni-O bond length (Figure 3.18) which is equal to half the *a* lattice parameter also shows a clear trend with the oxide sulfide again being anomalous.

$Sr_2NiO_2Cu_2Se_2$, $Sr_2NiO_2Cu_2(Se_{0.875}S_{0.125})_2$ and $Sr_2NiO_2Cu_2(Se_{0.75}S_{0.25})_2$ show a diminishing upturn in the Ni-O bond length, coinciding roughly with the onset of magnetic ordering and so both of these plots suggest that magnetostriction is the origin of this behaviour. This behaviour was also seen in the variable temperature SPXRD data of $Sr_2NiO_2Cl_2$ (discussed in section 3.3.3), where discontinuities in the Ni-O bond length are observed around the onset of long-range magnetic order.

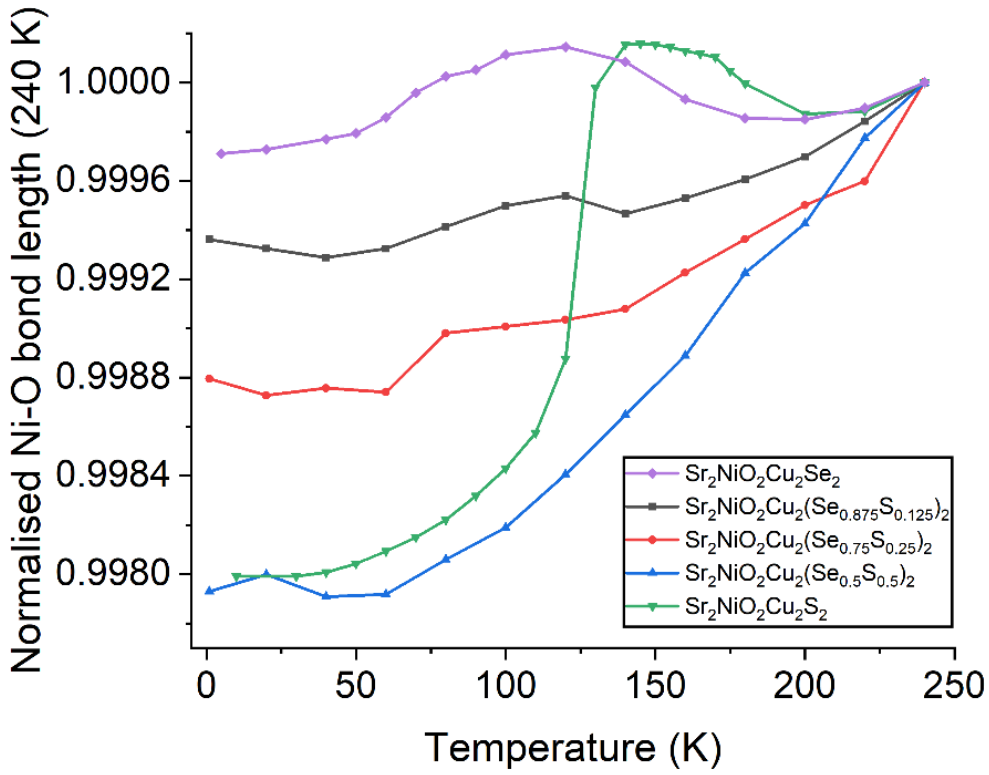


Figure 3.18 Changes in the Ni-O bond length as a function of temperature for $Sr_2NiO_2Cu_2(Se_{1-x}S_x)_2$ $0 \leq x \leq 1$. Data from WISH at ISIS for the solid solution, POLARIS for $Sr_2NiO_2Cu_2S_2$ and OSIRIS for $Sr_2NiO_2Cu_2Se_2$.

3.2.9 Computational results for $Sr_2MO_2Cu_2Ch_2$ (*M* = Co, Ni, Cu, Zn ; *Ch* = S, Se)

Experimentally, the elongation ratio of the MO_4Ch_2 (*M* = Co, Ni, Cu, Zn; *Ch* = S , Se) octahedra for $Sr_2MO_2Cu_2Ch_2$ tends to be similar in magnitude for a given metal ion as shown below in Figure 3.19, reflecting the fairly similar sizes of S^{2-} and Se^{2-}. The obvious outliers being $Sr_2NiO_2Cu_2S_2$ and $Sr_2NiO_2Cu_2Se_2$ which have a much larger difference in the Ni-*Ch* / Ni-O ratio. Also included in Figure 3.19 is the array of compounds from the solid solution $Sr_2NiO_2Cu_2(Se_{1-x}S_x)_2$ investigated in this chapter which shows a sharp increase in the M-*Ch* / M-O ratio as a function of *x* as shown in Figure 3.13(b).

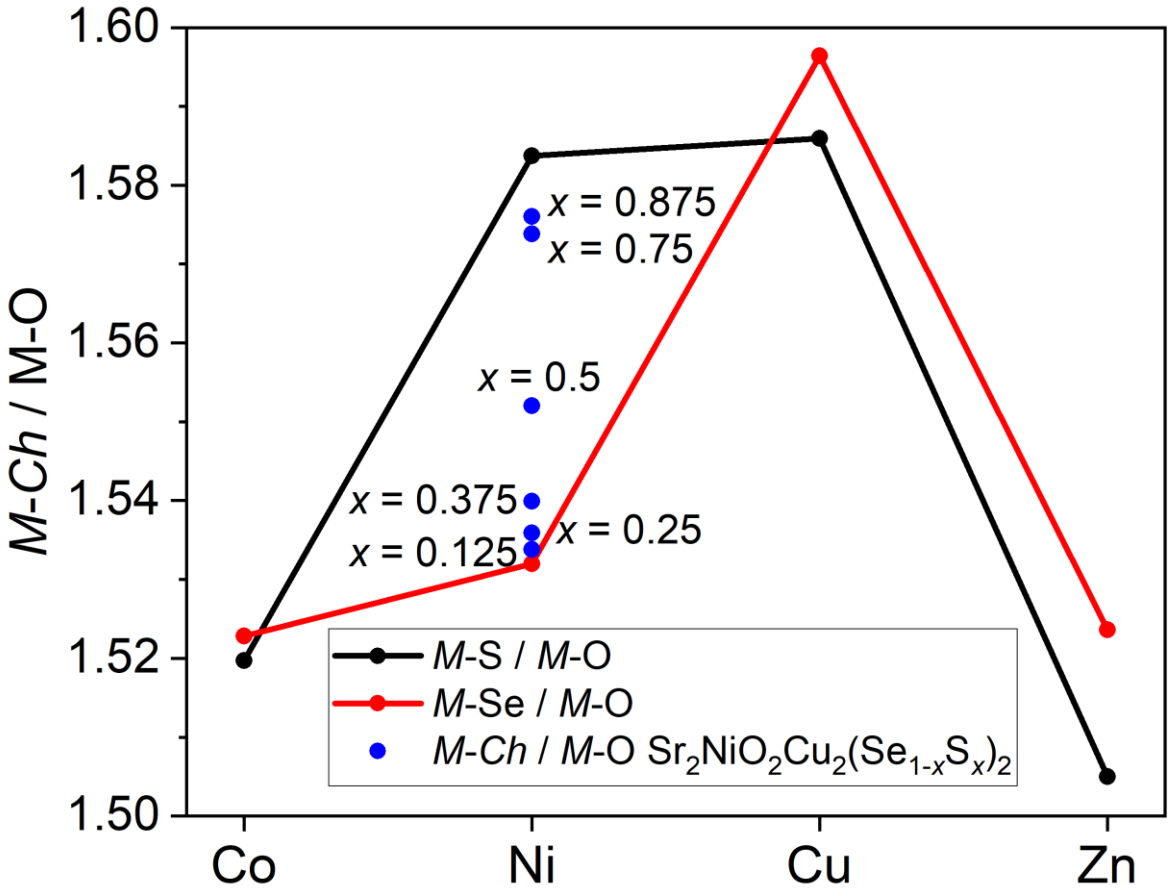


Figure 3.19 Experimental values of the M-*Ch* / M-O ratios for $Sr_2MO_2Cu_2Ch_2$ (*M* = Co, Ni, Cu, Zn; *Ch* = S (black), Se (red)) compounds at ambient temperature. The blue dots are values for the solid solution $Sr_2NiO_2Cu_2(Se_{1-x}S_x)_2$.

In order to investigate this, calculations on $Sr_2NiO_2Cu_2Se_2$, $Sr_2NiO_2Cu_2S_2$ and related compounds were carried out by Shuai Liu and Ziyu Lu who are a part of John McGrady's research group within Oxford Chemistry.

DFT calculations on the series $Sr_2MO_2Cu_2Ch_2$ (*M* = Co, Ni, Cu, Zn; *Ch* = S, Se) were carried out using the VASP software package,[118,119] version 6.2.1, with the PBE functional[120] and a plane-wave cut-off of 850 eV. A more thorough description of the computational procedure can be seen in Appendix A.1.

The key results are shown below in Figure 3.20 which describes the *M*-*Ch* / *M*-O ratio for $Sr_2MO_2Cu_2Ch_2$ (*M* = Co, Ni, Cu, Zn; *Ch* = S (black), Se (red)) compounds with a high, low, or, for the case of the Ni-containing oxide chalcogenides, a hybrid spin-state consisting of a mixture of high- and low-spin sites (see Appendix A.1 for the computational procedure).

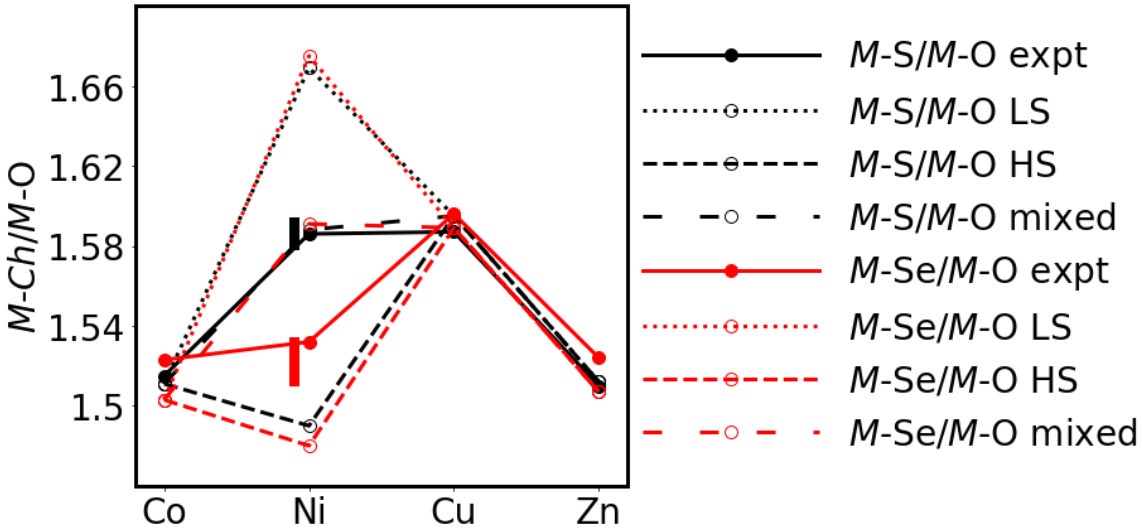


Figure 3.20 Calculated (open symbols/dashed lines) and experimental values (closed symbols/solid lines) of the *M*-*Ch* / M-O ratios for $Sr_2MO_2Cu_2Ch_2$ (*M* = Co, Ni, Cu, Zn; Ch = S (black), Se (red)) compounds. The experimental points are the ambient temperature values. The vertical bars indicate the range of values found experimentally for the *M*-*Ch* / *M*-O ratios for $Sr_2NiO_2Cu_2S_2$[35] and $Sr_2NiO_2Cu_2Se_2$[40] between base and ambient temperatures which can be seen in Appendix B.

The calculations revealed that when the transition metal was Co, Cu or Zn, the agreement between experiment and computation was extremely good, but from Figure 3.20 above, it was clear that the Ni-containing compounds were anomalous as neither full high- or low-spin calculations could correctly capture the experimental shape of the NiO_4Ch_2 octahedra.

Table 3.5 below shows an overview of both the experimental results along with the corresponding calculated results for Ni^2 in a high, low or in the case of $Sr_2NiO_2Cu_2S_2$ – "mixed" spin-state, using a value of U_{Ni} = 2 eV.

For a given value of *U*, the low spin-state is stabilised in the sulfide compared to the selenide, but it must also be noted that increasing the value of *U* can force the Ni^{2+} in the oxide sulfide into the high-spin regime and so the computational data must be interpreted with caution and with reference to the experiments.

Table 3.5 Comparison of experimental and calculated lattice parameters and selected bond lengths of $Sr_2NiO_2Cu_2S_2$ and $Sr_2NiO_2Cu_2Se_2$.

	$Sr_2NiO_2Cu_2S_2$				$Sr_2NiO_2Cu_2Se_2$		
	exp	DFT			exp	DFT	
		HS	LS	Mixed		HS	LS
a / Å[a]	5.544	5.615	5.417	5.508	5.694	5.710	5.504
c / Å	18.12	17.271	18.454	17.910	18.406	17.844	19.249
Ni-O / Å	1.96	1.985	1.915	1.903 1.992	2.013	2.019	1.946
Ni-E / Å	3.11	2.967	3.195	3.140 3.044	3.084	2.989	3.270
Ni-E/Ni-O	1.586	1.494	1.668	1.588	1.532	1.481	1.681
μ(Ni)	0.0	1.60	0.0	1.60 0.0	1.31(2)	1.60	0.0
Energy / eV		+0.27	0.0	+ 0.03		0.0	+ 0.26

[a]Note that a $\sqrt{2}a \times \sqrt{2}a \times c$ expansion of the structural cell is used for the computation.

For the selenide, the high-spin-state lies 0.26 eV per unit cell lower in energy than the low spin-state and it also offers a better match with regards to the structural parameters. For the sulfide, the low spin-state is computed to be the more stable spin-state, laying 0.27 eV per unit cell below the high spin-state. The "mixed" entry is a model whereby high- and low-spin Ni^{2+} ions are both arranged within each layer in a checkerboard arrangement (more details on the procedure in Appendix A.1). This model had remarkable agreement with the experimental data for the sulfide, contrary to the case where it was assumed to be fully low-spin. However further work would be required to investigate the local spin structure in these materials, this is explored later in the discussion in section 3.4.

A broader discussion incorporating the other first-row transition metals and the sensitivity of the spin-state to a given value of *U* can be seen in Appendix A.2.

3.2.10 Structural response of $Sr_2NiO_2Cu_2Se_2$ to pressure

PND measurements on the PEARL neutron diffractometer at the ISIS facility[85] were used to probe changes in the crystal structure of $Sr_2NiO_2Cu_2Se_2$ as a function of applied pressure. In particular, to investigate whether applying pressure and thus increasing the ligand field strength could drive $Sr_2NiO_2Cu_2Se_2$ into the low-spin regime found in the sulfide analogue.

Low-temperature measurements down to 100 K on PEARL were accessed by immersing the Paris−Edinburgh cell in a liquid nitrogen bath, but it was clear in performing these low-temperature measurements that the magnetic Bragg scattering in $Sr_2NiO_2Cu_2Se_2$ at this temperature was not sufficiently intense, because of the relatively small long-range-ordered moment, to be observable above the background noise which was fairly large due to the small sample size and the sample environment needed for the high pressures.

Hence, monitoring changes in the magnetic scattering under the application of pressure was not possible, so the experiment relied on solely looking at structural changes performed over 3 portions of beam time and including 4 runs.

During the 1st experiment, run A focused on the low-pressure region and was performed at ambient temperature using zirconia-toughened alumina (ZTA) anvils. The load was increased in steps of 5 tonnes to reach an applied pressure of 2.2 GPa before being increased in smaller increments of 2 tonnes (which translated to pressure increases of approximately 0.1−0.2 GPa each) during which a kink was seen in the c / a ratio (Figure 3.21(a)) and the Ni-Se bond length at 3.2 Gpa.

During the second experiment, a subsequent run B, also with ZTA anvils was used to again look at the low-pressure region to determine if the anomaly during run A was a real effect or not. In addition, in run C, sintered diamond (SD) anvils were used to apply a force of 50, 60, and 70 tonnes to study the higher-pressure region, which resulted in a maximum applied pressure of 7.3(1) GPa.

There was also found to be a kink in the Ni−Se bond distance at an applied pressure 4 GPa for run B using the ZTA anvils (Figure 3.21(b)), which was indicative of a possible structural anomaly, however as can also be seen in Figure 3.21(b) run C, using the SD anvils showed a relatively smooth decrease in the Ni-Se bond length and hence the anomalies found in runs A and B were determined to be experimental artefacts which may have arisen due to small changes in the sample position even though during the experiment precautions were taken to account for this.

During the final session of beam time, run D again used the SD anvils to focus on the high-pressure region, however, despite applying a larger load of 80 tonnes in run D as opposed to 70 tonnes in run C, the refined pressure was highest during run C.

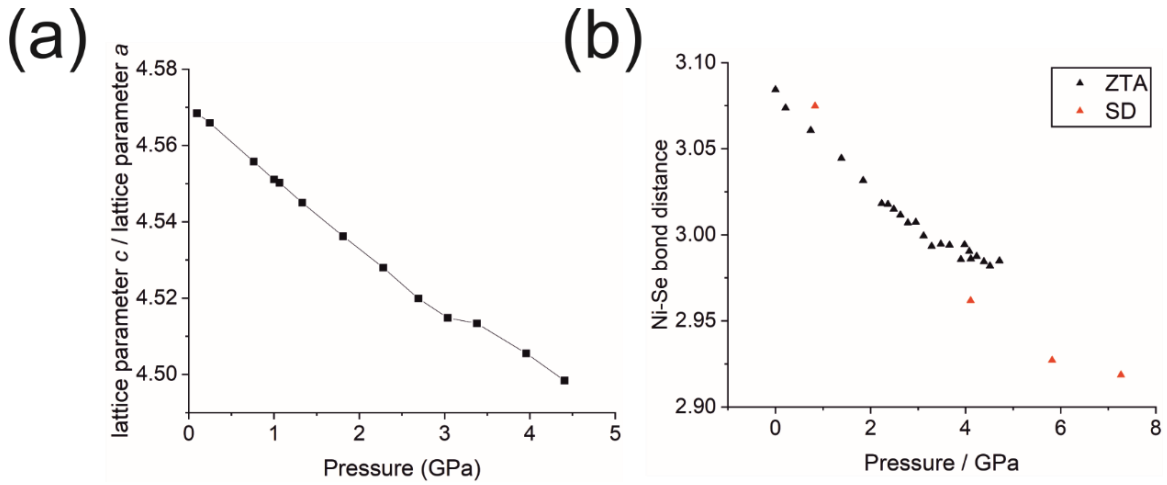


Figure 3.21(a) An observed kink in the *c* / *a* ratio of $Sr_2NiO_2Cu_2Se_2$ at 3.2 GPa during run A which lead to further investigation during run B. The error bars are within the points of the plot. **(b)** An observed kink in the Ni-Se bond length $Sr_2NiO_2Cu_2Se_2$ at 4GPa during run B (black), that was not evident in the subsequent run C (red).

Discounting the anomalous *c* / *a* ratio and the Ni-Se bond length from the runs A and B which used the ZTA anvils, over the full range of pressures explored, there was no obvious anomaly in the behaviour of the lattice parameters or the structural parameters which is corroborated by runs C and D, suggesting that up to pressures of 7.3(1) GPa, there is no change in the Ni^{2+} spin-state and that the observed anomalies in the data during both runs A and B were experimental artifacts.

A transition from the high-spin to low-spin regime would be accompanied by a shortening of the Ni−O distance (i.e., the *a* lattice parameter) and an increase in the Ni−Se / Ni−O ratio, as seen in the experimental and computational comparison between $Sr_2NiO_2Cu_2S_2$ and $Sr_2NiO_2Cu_2Se_2$, because of an electron being transferred from the more antibonding $dx^2 - y^2$

orbital into the lower energy dz^2 orbital, with a reminder of the *d*-orbital occupancy for high- and low-spin d^8 Ni^{2+} shown in Figure 3.16.

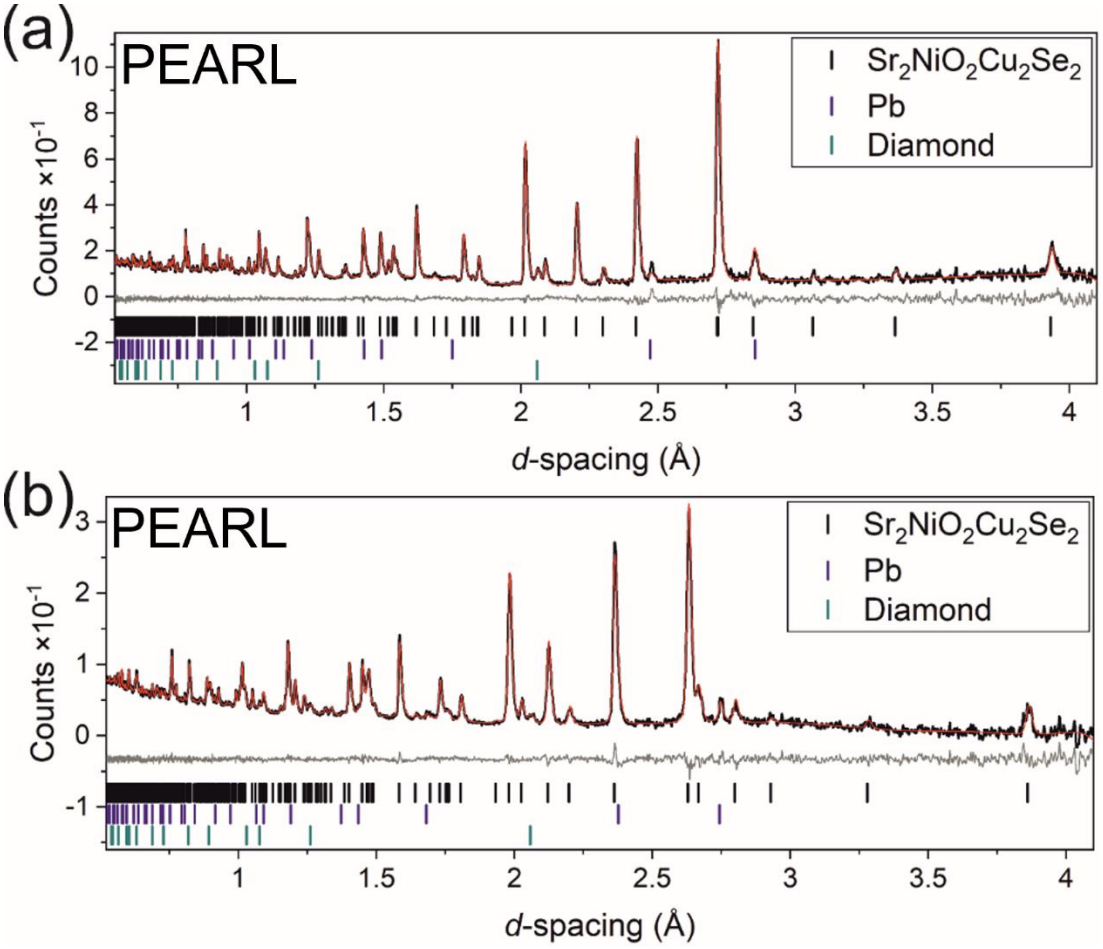


Figure 3.22(a) PND of $Sr_2NiO_2Cu_2Se_2$ (quenched from 950 °C), at ambient pressure R_{wp} = 4.771 %; χ^2 = 0.751 **(b)** 7.2 GPa (obtained with an applied load of 90 tonnes in the Paris-Edinburgh cell) R_{wp} = 4.793 %; χ^2 = 0.744, measured on the PEARL diffractometer at ISIS. It shows the experimental data in black, the fit from the model in red and the difference between the two in grey. Pb is used as an internal barometer. These measurements were collected during run D.

Anomalies in the changes in the bond lengths (i.e., behaviour under pressure that would suggest some electronic change) are not observed. Evidently, the increase in the ligand field strength under a pressure of 7.3(1) GPa is not sufficient to drive the selenide system into the low-spin regime, although it cannot be ruled out that such a transition might occur at higher pressures.

Table 3.6 Refined parameters during run D for $Sr_2NiO_2Cu_2Se_2$ and Pb from the refinements in Figure 3.22 using SD anvils.

Applied pressure / GPa	0	7.2(1)
a lattice parameter (Å)	4.02456(5)	3.9577(6)
c lattice parameter (Å)	18.3844(5)	17.5782(5)
Ni-O bond length (Å)	2.01228(3)	1.97888(3)
c / *a*	4.5681(1)	4.4415(2)
Pb volume $(Å)^3$	120.76(7)	107.30(5)

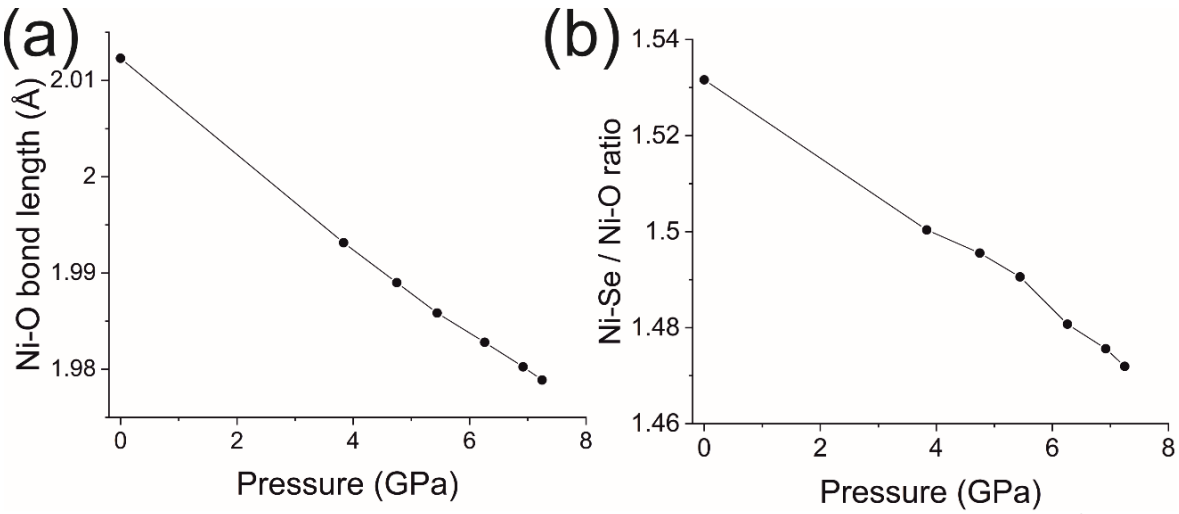


Figure 3.23(a) Plots of the Ni-O bond distance (= *a* / 2) along with **(b)** the Ni^{2+} environment as a function of pressure focusing on the high-pressure region using the SD anvils from run D. The error bars for the Ni-O bond lengths are within the data points due to the precision with which the lattice parameters can be refined.

Table 3.6 displays some refined parameters from the data measured on loading and at 7.2(1) GPa from run D with the complete data set for the whole pressure sweep displayed in Figure 3.23 and Table 3.7.

Table 3.7 Refined parameters for $Sr_2NiO_2Cu_2Se_2$ from PEARL from run D.

	40 tonnes	50 tonnes	60 tonnes	70 tonnes	80 tonnes
p (GPa)	3.84(5)	4.75(6)	5.39(8)	6.3(1)	6.9(1)
a (Å)	3.98632(4)	3.97798(5)	3.97191(5)	3.96578(5)	3.96051(7)
c (Å)	17.9193(4)	17.8217(4)	17.7511(4)	17.6731(4)	17.6104(6)
Ni-O (Å)	1.99316(2)	1.98899(2)	1.98595(3)	1.98289(3)	1.98025(4)
c / *a*	4.4952(1)	4.4801(1)	4.4692(1)	4.4564(1)	4.4465(2)
Pb *v* ($Å^3$)	112.67(4)	111.07(4)	110.03(4)	108.71(5)	107.76(6)

The smooth variation of the volume, *V*, as a function of pressure, *P*, across the series of measurements indicated that the dependence could be fitted to a third-order Birch−Murnaghan equation of state[121] (equation 3.3, Figure 3.24). Using the EosFit7-GUI software,[122] the following parameters were obtained from the data, focusing on the low-pressure region from which there are more data points available: V_0 = 298.66(15) $Å^3$, the bulk modulus $K_0 = -V_0(\partial P/\partial V)$ = 63.1(18) GPa, and its first pressure derivative $K_{0'}$ = 10.5(8) (Figure 3.24).

$$P = \frac{3K_0}{2}\left[\left(\frac{V_0}{V}\right)^{\frac{7}{3}} - \left(\frac{V_0}{V}\right)^{\frac{5}{3}}\right]\left\{1 - \frac{3}{4}(4 - K_0')\left[\left(\frac{V_0}{V}\right)^{\frac{2}{3}} - 1\right]\right\} \quad (3.3)$$

Similar treatment of the cell parameters *a* and *c* can also be analysed by treating them as a volume component (Figure 3.25), that is, a^3 and c^3, which resulted in two directional compressibilities. The *a*-axis yields a bulk modulus of $K_0(a)$ of 119(3) GPa and a $K_{0'}(a)$ of 1.7(13), whereas the *c*- axis has a bulk modulus $K_0(c)$ of 42.8(6) GPa with a $K_{0'}(c)$ = 3.2(3).

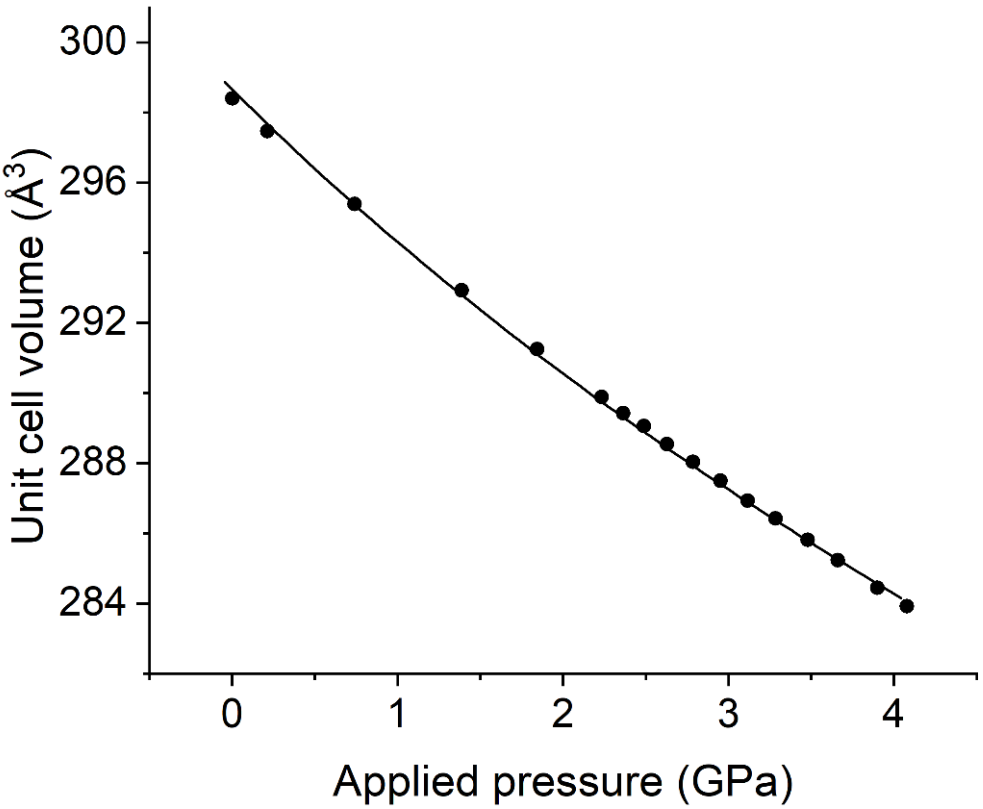


Figure 3.24 Variation with pressure of the cell volume of $Sr_2NiO_2Cu_2Se_2$ collected during run B and stopping before the anomalous data is encountered. Error bars reside within the data points. The solid line is the fit to the data using a third-order Birch-Murnaghan EoS (Equation 3.3).

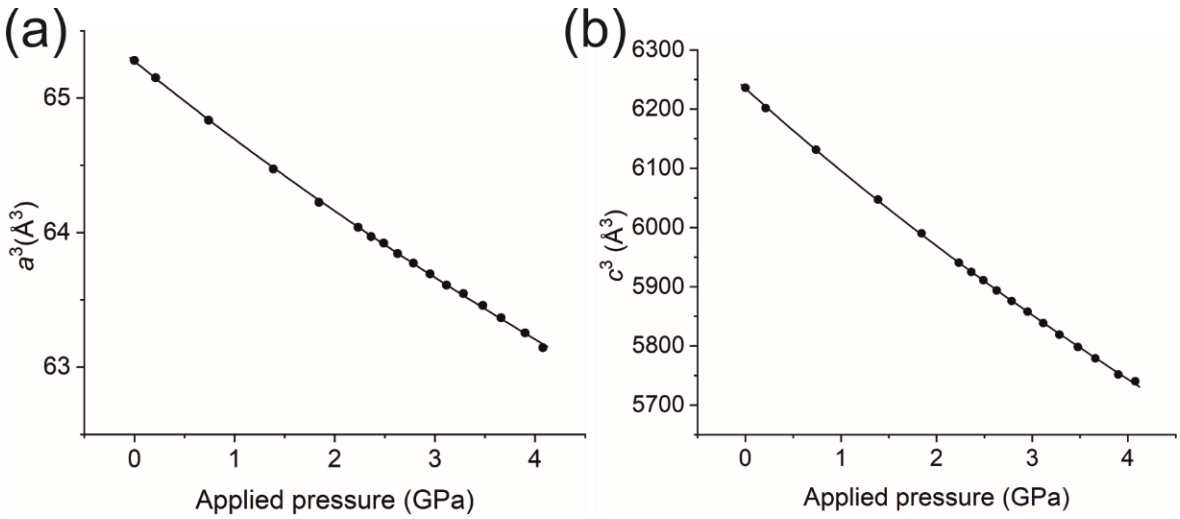


Figure 3.25 Variation with pressure of the *a* and *c* lattice parameter of $Sr_2NiO_2Cu_2Se_2$ collected during run B and stopping before the anomalous data is encountered. Error bars reside within the data points. The solid line is the fit to the data using a third-order Birch-Murnaghan EoS (Equation 3.3).

The *ab*-plane being less compressible than the *c*-axis is a common feature of layered structures, whereby there tends to be higher atom density as well as bonds laying parallel to the *ab*- plane such as the Ni−O bonds in the compounds described in this study, which greatly restrict the compression along this direction. These differing compressibilities led to a reduction in the *c / a* ratio of 2.77% as the pressure was increased to 7.3(1) GPa.

3.2.11 SEM / EDX

The synthetic pathway used during the synthesis of the solid solution $Sr_2NiO_2Cu_2(Se_{1-x}S_x)$ led to crystallites that varied in their visible crystallinity. To the naked eye, Se-rich compounds ($0 \leq x \leq 0.5$) which were synthesised under high-temperature conditions sparkled under lights whereas the more S-rich compounds ($0.5 < x \leq 1$) appeared as dull powders, however, there was no evidence of crystal growth for either of the end member samples.

Furthermore, EDX was used to confirm the compositions of 3 samples, $Sr_2NiO_2Cu_2Se_2$, $Sr_2NiO_2Cu_2SeS$ as well as $Sr_2NiO_2Cu_2S_2$ with the latter being of particular interest due to the use of a wash to remove the flux.

Despite the obvious visual differences in the crystallites, surprisingly, the morphology of both are quite similar as shown in Figure 3.26 with the aggregates being on average smaller for $Sr_2NiO_2Cu_2S_2$. The crystallites were again similar in $Sr_2NiO_2Cu_2SeS$, however, there were a few much more crystalline particles as shown in Figure 3.27 with a much more regular shape, suggesting that future efforts at the growth of larger crystals should be attempted. EDX mapping was important for this composition to observe the chalcogen distribution throughout the sample to see if there were any Se- or S-dense regions which

Chapter 3. Structure-property relationships in Ni-containing mixed-anion solids could have led to local structure variations. The results of this are shown in Figure 3.28 which shows that there is an even distribution of the two chalcogens throughout the sampled area at the resolution of this technique.

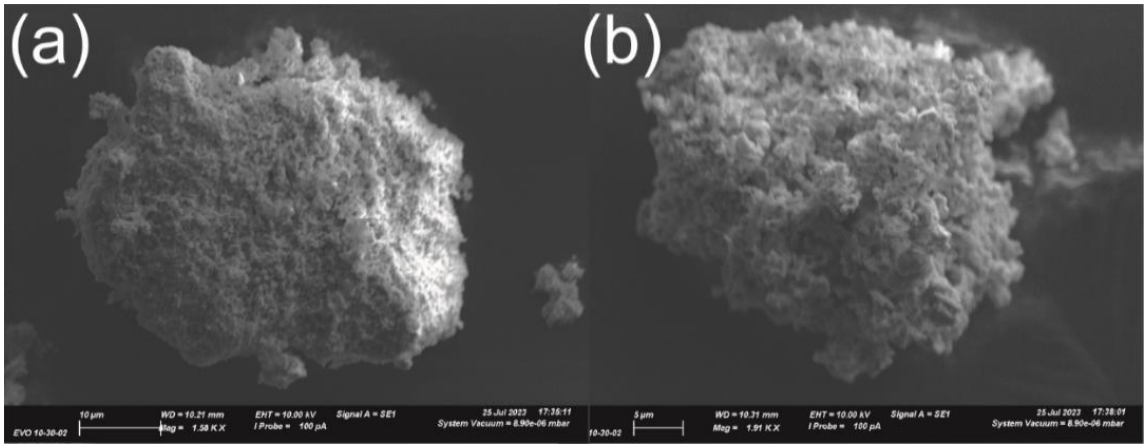


Figure 3.26 SEM imaging of **(a)** $Sr_2NiO_2Cu_2Se_2$ and **(b)** $Sr_2NiO_2Cu_2S_2$. Note the slightly different scales use (see scale bars).

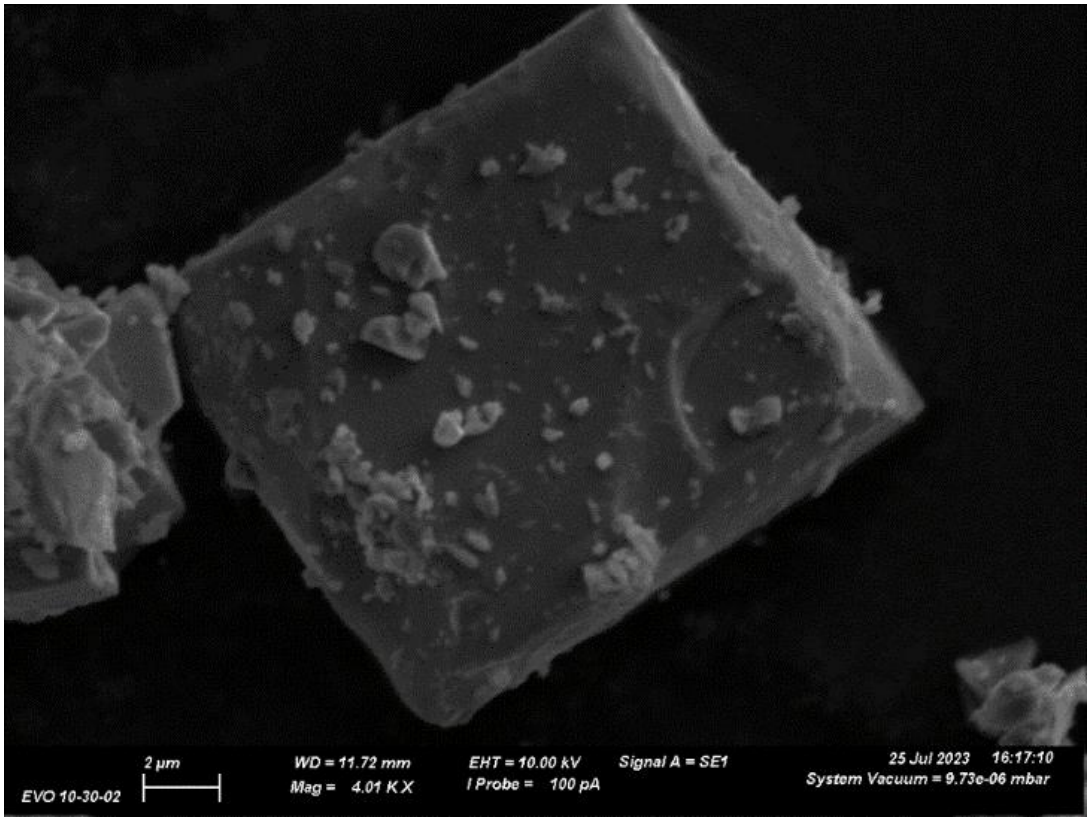


Figure 3.27 SEM imaging of $Sr_2NiO_2Cu_2SeS$.

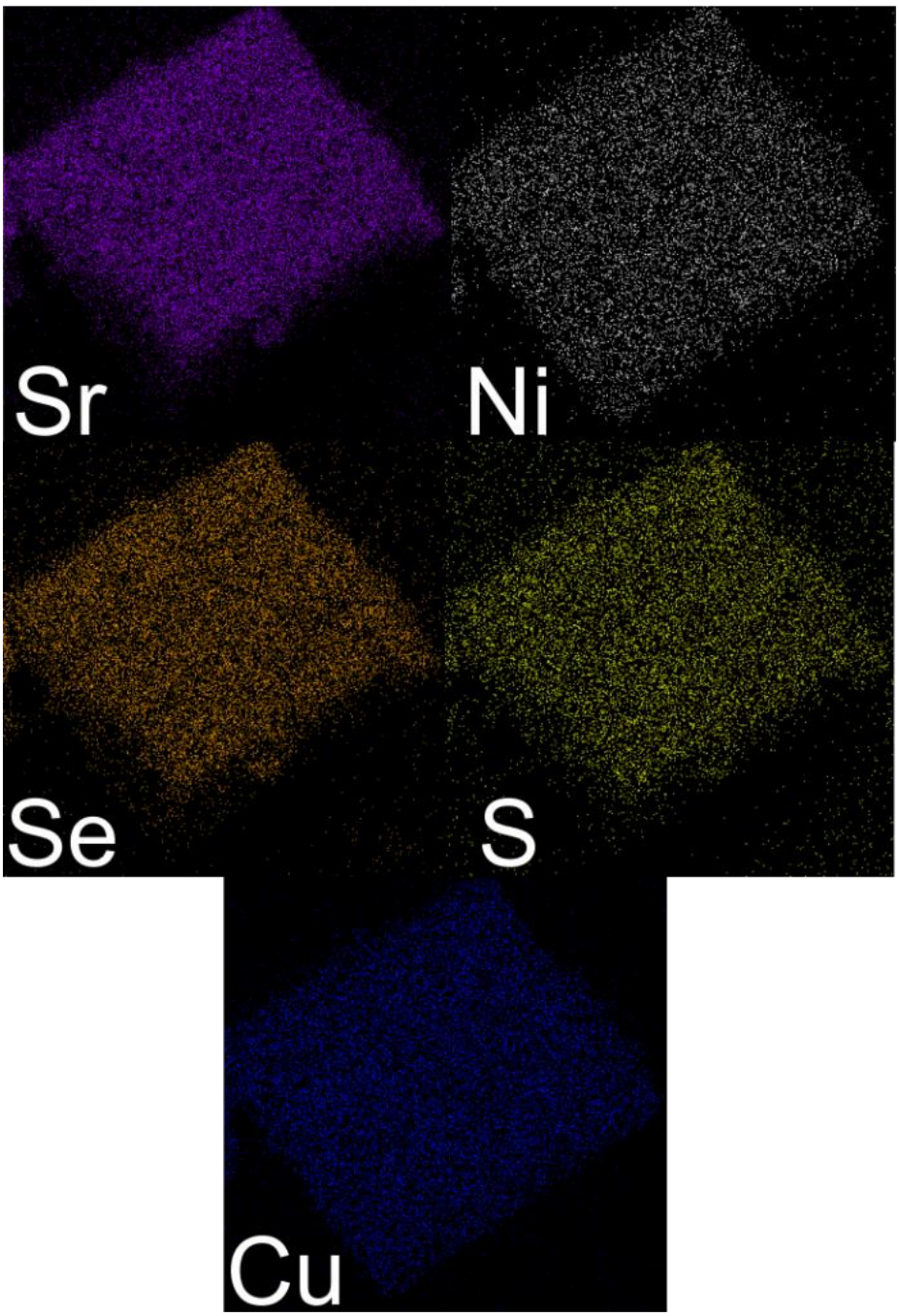


Figure 3.28 EDX mapping of $Sr_2NiO_2Cu_2SeS$.

Different points were also chosen within each site to gain an average composition of each of the 3 samples. The results are shown in Figures 3.29 – 3.31 with the derived atomic percentage (at %) shown in Tables 3.8 – 3.10.

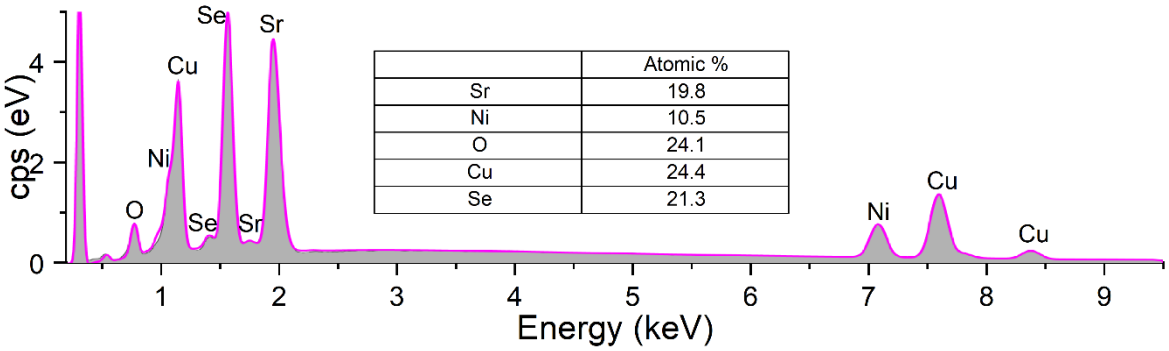


Figure 3.29 EDX elemental analysis results for $Sr_2NiO_2Cu_2Se_2$. Due to its low atomic mass, O content is an estimate.

Table 3.8 Average EDX elemental analysis results for $Sr_2NiO_2Cu_2Se_2$. Due to its low atomic mass, O content is an estimate.

Sr (at %)	Ni (at %)	O (at %)	Cu (at %)	Se (at %)
2.1(1)	1.0(1)	2.4(1)	2.2(1)	2.1(1)

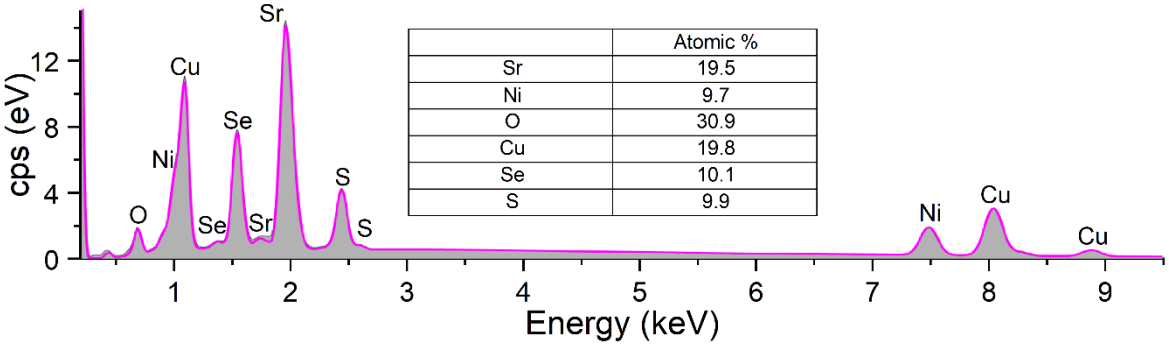


Figure 3.30 EDX elemental analysis results for one point in $Sr_2NiO_2Cu_2SeS$.

Table 3.9 Average EDX elemental analysis results for $Sr_2NiO_2Cu_2SeS$. Due to its low atomic mass, O content is an estimate.

Sr (at %)	Ni (at %)	O (at %)	Cu (at %)	Se (at %)	S (at %)
2.1(1)	1.0(1)	2.2(1)	2.0(1)	1.1(1)	1.1(1)

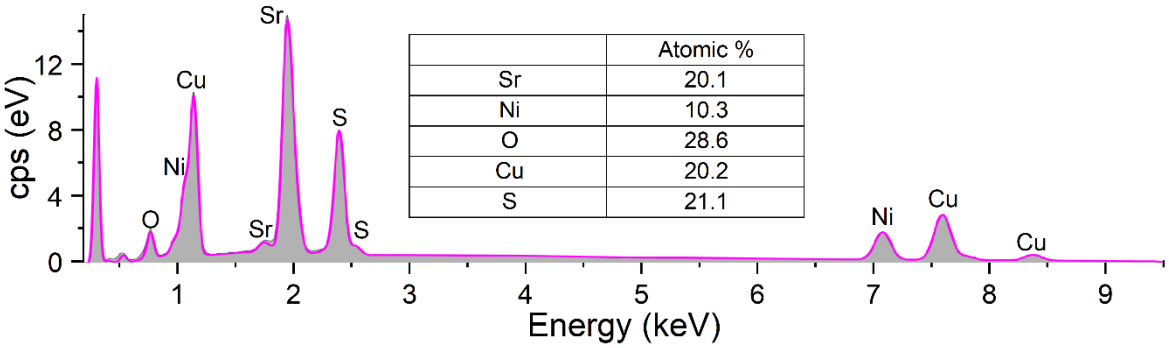


Figure 3.31 EDX elemental analysis results for one point in $Sr_2NiO_2Cu_2S_2$.

Table 3.10 Average EDX elemental analysis results for $Sr_2NiO_2Cu_2S_2$. Due to its low atomic mass, O content is an estimate.

Sr (at %)	Ni (at %)	O (at %)	Cu (at %)	S (at %)
1.8(1)	1.0(1)	2.1(1)	2.0(1)	1.9(1)

The average compositions hence derived from the average atomic percentage of all 3 samples is $Sr_{2.1(1)}Ni_{1.0(1)}O_{2.4(1)}Cu_{2.2(1)}Se_{2.1(1)}$, $Sr_{2.1(1)}Ni_{1.0(1)}O_{2.2(1)}Cu_{2.0(1)}Se_{1.1(1)}S_{1.1(1)}$ and $Sr_{1.8(1)}Ni_{1.0(1)}O_{2.1(1)}Cu_{2.0(1)}S_{1.9(1)}$ and therefore the samples are stoichiometric within the experimental uncertainty – even the oxide sulfide which was washed after being prepared in the alkali halide metal flux.

3.2.12 Resistivity

The electrical resistivity of 2 pellets either side of the spin-state crossover were measured between 30 K and 300 K using the standard 4 probe method as outlined in section 2.2.8. The samples were annealed at 950 °C and kept within an evacuated ampoule until the measurement was ready to be taken.

The presence of the $Cu_{1-x}Ni_x$ alloy within the sample means that the data have to be treated with caution as it is a metallic impurity and may improve the contacts and enhance the conductivity.

The general trend of an increase in the resistivity on cooling as shown in Figure 3.32 is consistent with semiconducting behaviour but the absolute value of the resistivity is quite low – i.e., not a bad conductor which is similar to what was observed in $Sr_2NiO_2Cu_2Se_2$ which had a similar magnitude in resistivity but metallic behaviour as a function of temperature.[38]

The measured resistivity of $Sr_2NiO_2Cu_2(Se_{0.5}S_{0.5})_2$ (low-spin Ni^{2+} as shown by PND in section 3.2.7) was also measured but the data was extremely noisy and nothing useful could be extracted.

The best way to measure the transport properties of these materials would be on orientated single crystals.

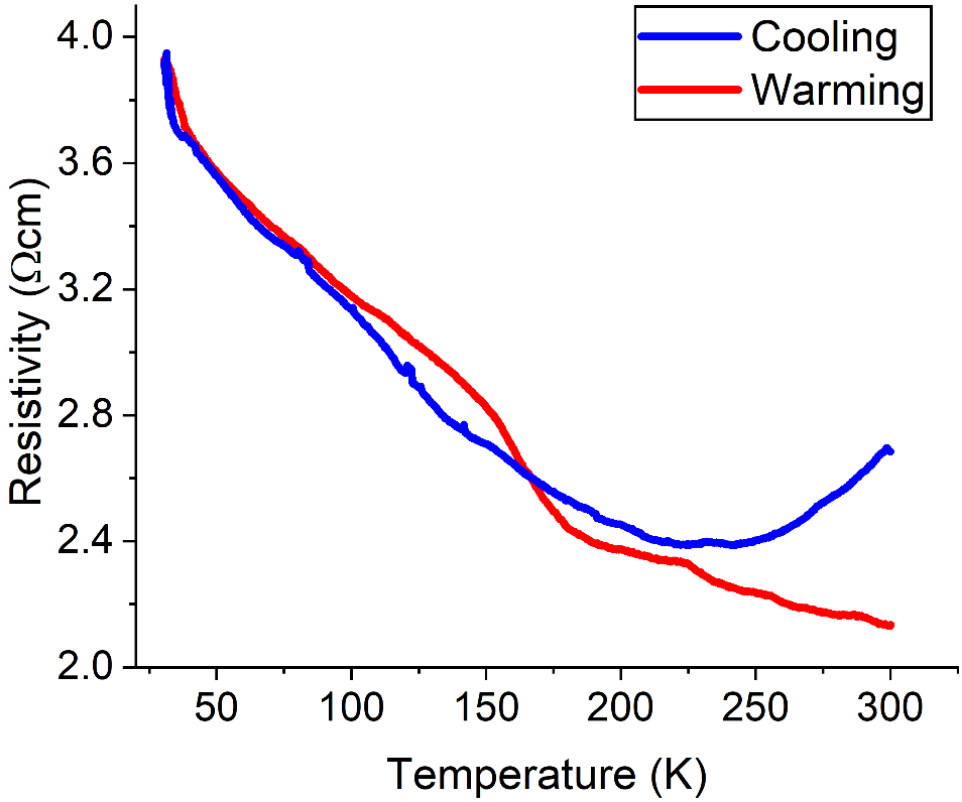


Figure 3.32 Bulk resistivity of $Sr_2NiO_2Cu_2(Se_{0.875}S_{0.125})_2$, measured in a constant current of 0.01 mA as a function of temperature ($30 \leq T(K) \leq 300$).

3.3 Synthesis and characterisation of $Sr_2NiO_2Cl_2$

3.3.1 Synthesis of $Sr_2NiO_2Cl_2$

The sample of $Sr_2NiO_2Cl_2$ used for the analysis in this thesis was synthesised in a refinement of the method reported by Tsujimoto et al., in their communication reporting the discovery of this phase.[55] It was found that using NiO as a nickel source yielded a much purer product than when elemental nickel powder was used as shown in Figure 3.33.

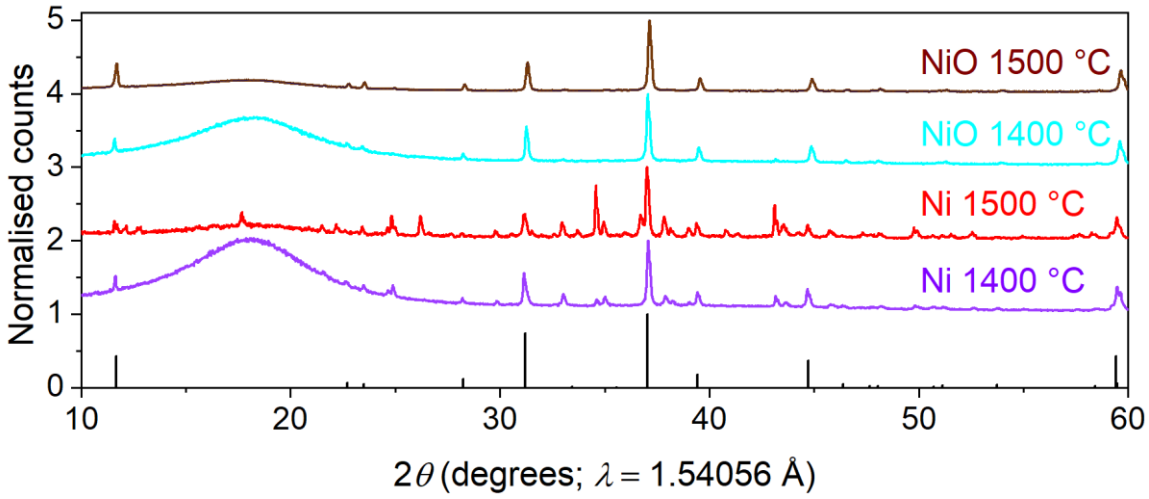


Figure 3.33 PXRD data of $Sr_2NiO_2Cl_2$ after different synthetic approaches along with the simulated pattern.

Equimolar amounts of in-house synthesised SrO (from the thermal decomposition of $SrCO_3$ (Rare Metallic Co., Ltd, 99.9 %)) at 1300 °C in a flowing O_2 atmosphere, NiO (Kojundo Chemical Laboratory Co., Ltd, 99.9 %) and $SrCl_2$ (Rare Metallic Co., Ltd, 99.9 %), both of which were stored in an Ar-filled glovebox immediately after receiving them were thoroughly mixed together with 2 × 0.4 g (0.8 g per reaction) pellets enclosed within a Pt capsule.

This capsule was then loaded into a belt-type, high-pressure apparatus with an applied pressure of 3 GPa and heated at 1400 or 1500 °C for a dwell time of 1 hour.

The sample was then subsequently quenched rapidly to room temperature with a slow release of pressure, yielding a dark green solid.

The 1.6 g sample that was used for PND was a mixture of the batches prepared at 1400 and 1500 °C (2 × 0.8 g batches).

This synthetic procedure was carried out at Research Centre for Materials Nanoarchitechtonics (MANA), National Institute for Materials Science (NIMS), Japan, by Yoshihiro Tsujimoto and Kazunari Yamaura.

3.3.2 Room temperature PXRD and PND

The reaction progression was monitored at the Research Centre for Materials Nanoarchitechtonics, Japan, using a Rigaku MiniFlex-600 diffractometer with a mixture of both $CuK_{\alpha 1}$ and $CuK_{\alpha 2}$ radiation.

Due to the air and moisture sensitivity of $Sr_2NiO_2Cl_2$, the portions extracted for the X-ray measurements were covered in paraffin oil prior to measurement to avoid degradation of the sample, and then discarded.

Synchrotron powder X-ray diffraction for detailed structural analysis using higher resolution, higher intensity and higher-*Q* powder data was performed by the author using the I11 beamline at the Diamond Light Source,[83] UK with radiation of wavelength λ = 0.824385(10) Å (calibrated before the session using a silicon standard).

Samples were prepared as outlined in section 2.2.2.3. A comparison between the samples prepared using Ni as the Ni source (previously reported by Tsujimoto et al.,[55]) and NiO (this work[109]) can been seen in Appendix C.1.

PND was used by the author to probe changes in the crystal structure as a function of temperature and to characterise the long-range magnetic ordering proposed by the computation of Zhou et al.,[108] as well as previous magnetometry performed by Tsujimoto et al.[55]

The sample of $Sr_2NiO_2Cl_2$ prepared at NIMS from NiO was loaded into a 6 mm vanadium can and sealed with indium wire and measured on the ToF WISH diffractometer at the ISIS facility, UK.[84]

Rietveld refinements of SPXRD / PND data of this sample provided through collaboration and collected at ambient temperature are shown below in Figure 3.34.

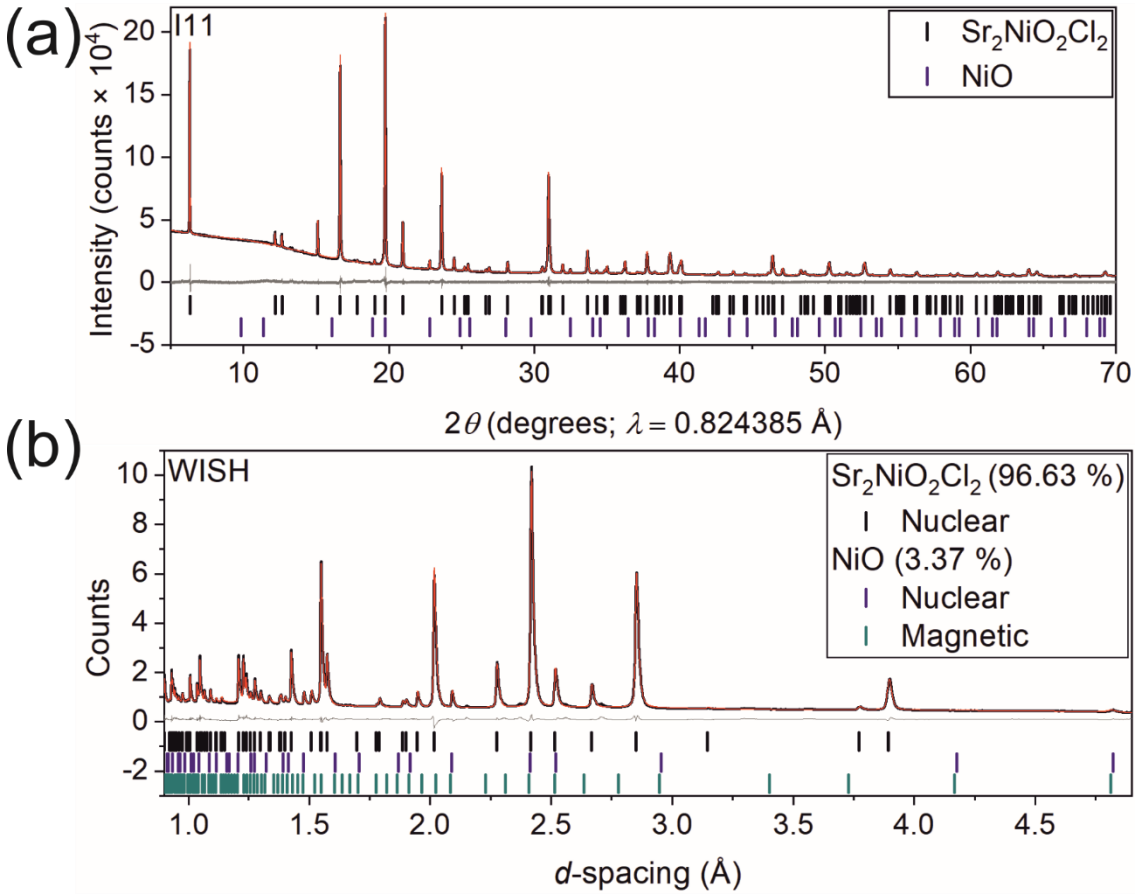


Figure 3.34(a) Room temperature Rietveld refinement of $Sr_2NiO_2Cl_2$ against SPXRD. R_{wp} = 2.283 %; $\chi 2$ = 2.500 and **(b)** Rietveld refinement of $Sr_2NiO_2Cl_2$ against bank 5/6 of the WISH diffractometer at ISIS. R_{wp} = 1.989 %; $\chi 2$ = 0.023.

Rietveld refinement confirmed that $Sr_2NiO_2Cl_2$ crystallises in the tetragonal *I*4/*mmm* space group with similar lattice parameters to those previously reported.[55] The extracted structural parameters obtained from SPXRD and PND are displayed in Table 3.11 below.

Table 3.11 Structural Rietveld refinement against powder X-ray and powder neutron diffraction data for $Sr_2NiO_2Cl_2$

Radiation	SPXRD	PND
Diffractometer	I11	WISH
a (Å)	4.02967(1)	4.03417(2)
c (Å)	15.09577(9)	15.1058(1)
v (Å^3)	245.129(2)	245.841(3)
z(Sr)[a]	0.39248(3)	0.39255(8)
z(Cl)[a]	0.17887(7)	0.17907(6)
U_{11}(Sr) (Å^2)	0.0042(5)	0.0159(4)
U_{33}(Sr) (Å^2)	0.0130(4)	0.0155(8)
U_{11}(Ni) (Å^2)	0.0031(4)	0.0109(4)
U_{33}(Ni) (Å^2)	0.0146(6)	0.0203(7)
U_{11}(O) (Å^2)	0.003(2)	0.0126(5)
U_{22}(O) (Å^2)	0.000(1)	0.0117(6)
U_{33}(O) (Å^2)	0.025(2)	0.0215(6)
U_{11}(Cl) (Å^2)	0.0116(4)	0.0177(3)
U_{33}(Cl) (Å^2)	0.0123(8)	0.0212(7)

[a] Sr, 4*e*(0,0,*z*); Ni, 2*a*(0,0,0); O, 4*c*(0, ½,0); Cl, 4*e*(0,0,*z*)

$Sr_2NiO_2Cl_2$ is isostructural with other oxide halides prepared at ambient or high pressures (see Table 3.12), and is an ordered variant of the *n* = 1 Ruddlesden-Popper series of compounds with the K_2NiF_4 structure.

The refined structural parameters are compared in Table 3.12 with comparison to closely related oxide halide analogues as well as the oxide chalcogenides investigated in section 3.2.

A comparison of the structure of $Sr_2NiO_2Cl_2$ and the oxide chalcogenides described in section 3.2[38] is shown in Figure 3.2. Formally, the oxide chalcogenides $Sr_2NiO_2Cu_2Ch_2$ are related to the oxide halides by the replacement of the halide by chalcogenide and balancing of the charge by incorporation of Cu^+ coinage metal ion in the chalcogenide layers.

The separation of the adjacent NiO_2 layers which are related by the body centring translations is smaller in the oxide chloride because of the lack of an ion between adjacent layers of chloride ions. The lack of this ion competing for the halide results in a shorter Ni-Cl distance in $Sr_2NiO_2Cl_2$ than the Ni-Se distance in $Sr_2NiO_2Cu_2Se_2$, while the two have very similar Ni-O distances. This suggests a less anisotropic ligand field in $Sr_2NiO_2Cl_2$ than in $Sr_2NiO_2Cu_2Se_2$, and so the high-spin Ni^{2+} found in $Sr_2NiO_2Cu_2Se_2$ was also expected for $Sr_2NiO_2Cl_2$ as proposed in the computational study by Zhou et al.[108]

This is in contrast to $Ba_2PdO_2Cl_2$ which displays diamagnetic behaviour in the ZFC / FC temperature dependence indicating the low-spin configuration.[55] This reinforced the hypothesis that the spin-state is intrinsically linked to the d^8 metal coordination environment as shown in Table 3.12, which shows that $Ba_2PdO_2Cl_2$ has a much more elongated octahedral environment as opposed to $Sr_2NiO_2Cl_2$ (refer to Figure 3.16) where presumably an increase in ΔE between dx^2-y^2 and dz^2 due to greater covalency and a decrease in pairing repulsions with the larger orbitals enabling a low-spin configuration for the second row metal.

However, despite the clear difference between the coordination environments and spin-states between the Ni and Pd cases, it is unclear to what extent this is due to the properties of the transition metal cation and what is due to the incorporation of larger Ba^{2+} cations into the crystal structure forcing the highly square-planar environment by increasing the Pd-Cl distance on steric grounds (note that $Sr_2PdO_2Cl_2$ is not known).

Table 3.12 Comparison of structural parameters for $Sr_2MO_2Cl_2$ (*M* = Mn, Co, Ni, Cu, Zn), $Ba_2PdO_2Cl_2$ as well as the closely relate oxide chalcogenide analogues, $Sr_2NiO_2Cu_2S_2$ and $Sr_2NiO_2Cu_2Se_2$.

Compound	$Sr_2MnO_2Cl_2$	$Sr_2CoO_2Cl_2$	$Sr_2NiO_2Cl_2$	$Sr_2CuO_2Cl_2$
Reference	Ref.[55]	Ref.[107]	This work	Ref.[106]
Radiation	PXRD	PND	PND	PND
a (Å)	4.09669(2)	4.06022(3)	4.03417(2)	3.97160(4)
c (Å)	14.9944(2)	15.11710(2)	15.1058(1)	15.61260(3)
c / *a*	3.66013(4)	3.72322(3)	3.74447(3)	3.93106(2)
Volume (Å^3)	251.648(2)	249.211(2)	245.840(3)	246.267(3)
M–O (Å) [4][a]	2.04835(1)	2.03011(1)	2.01708(1)	1.9858(1)
M–Cl (Å) [2][a]	2.750(5)	2.7342(7)	2.7076(9)	2.859(1)
M–Cl / *M*–O	1.3425(2)	1.3468(2)	1.3423(5)	1.4397(3)

Compound	$Sr_2ZnO_2Cl_2$	$Ba_2PdO_2Cl_2$	$Sr_2NiO_2Cu_2S_2$	$Sr_2NiO_2Cu_2Se_2$
Reference	Ref	Ref	Ref.[7]	Ref.[38]
Radiation	PND	SPXRD	PND	PXRD/PND
a (Å)	4.06877(9)	4.12886(1)	3.92159(2)	4.026470(8)
c (Å)	15.19680(3)	16.80766(4)	18.11558(15)	18.40612(4)
c / *a*	3.73500(2)	4.07077(2)	4.61945(4)	4.57128(1)
Volume (Å^3)	251.581(3)	286.528(2)	278.597(5)	298.408(1)
M–O (Å) [4][a]	2.03439(1)	2.06443(1)	1.96080(1)	2.013235(4)
M–Cl (Å) [2][a]	2.762(1)	3.1625(19)	3.1054(8)	3.0843(3)
M–Cl / *M*–O	1.358(2)	1.532(3)	1.5837(4)	1.5320(1)

3.3.3 Variable temperature powder X-ray diffraction

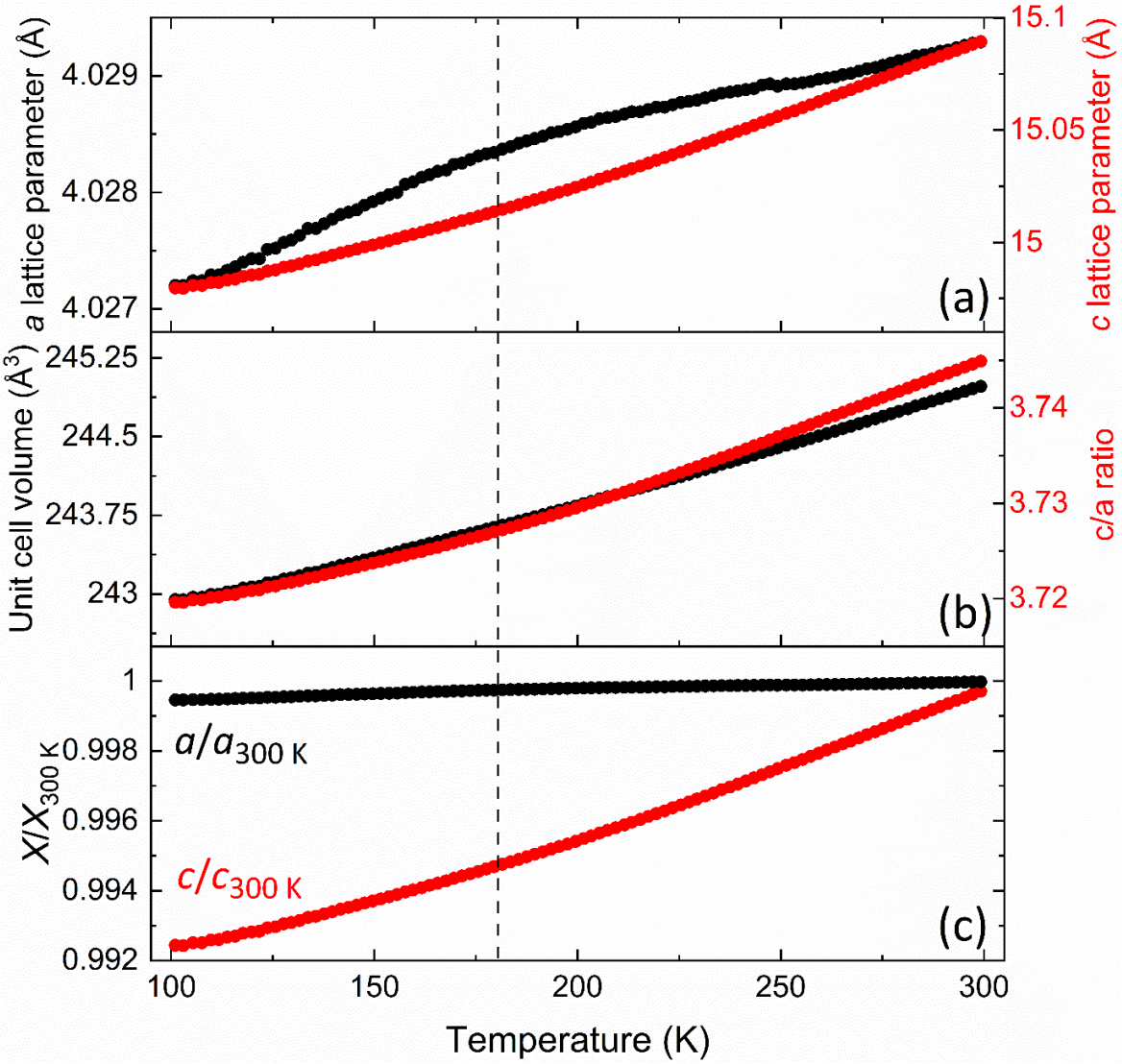


Figure 3.35(a) Refined lattice parameters of *a* and *c* for $Sr_2NiO_2Cl_2$ from I11 data, **(b)** unit cell volume and *c* / *a* ratio, **(c)** *a* and *c* values normalised to their values at 300 K. Error bars are within the plotted points, the dashed line is a guide to the eye around T_N.

Variable temperature PXRD did not suggest any lowering of symmetry or discontinuities of the lattice parameters but did show a small downturn in the change of the *a* lattice parameter on cooling and hence the Ni-O distance (= *a* / 2) coinciding with the magnetic ordering temperature, which is most likely magnetostrictive in origin (see Figures 3.36 and 3.37). The behaviour of the normalised lattice parameters is typical of that of layered materials whereby

they are much less compressible within the basal plane within which the rigid NiO_2 sub-lattice is orientated.

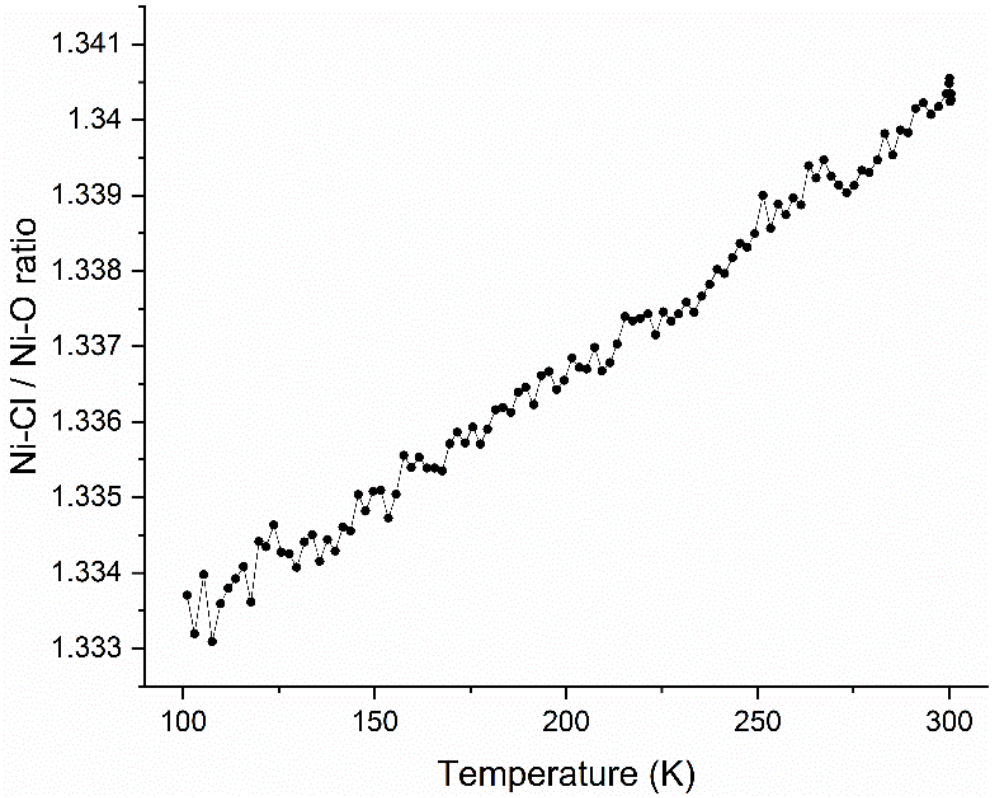


Figure 3.36 The Ni-Cl / Ni-O bond ratio as a function of temperature of $Sr_2NiO_2Cl_2$.

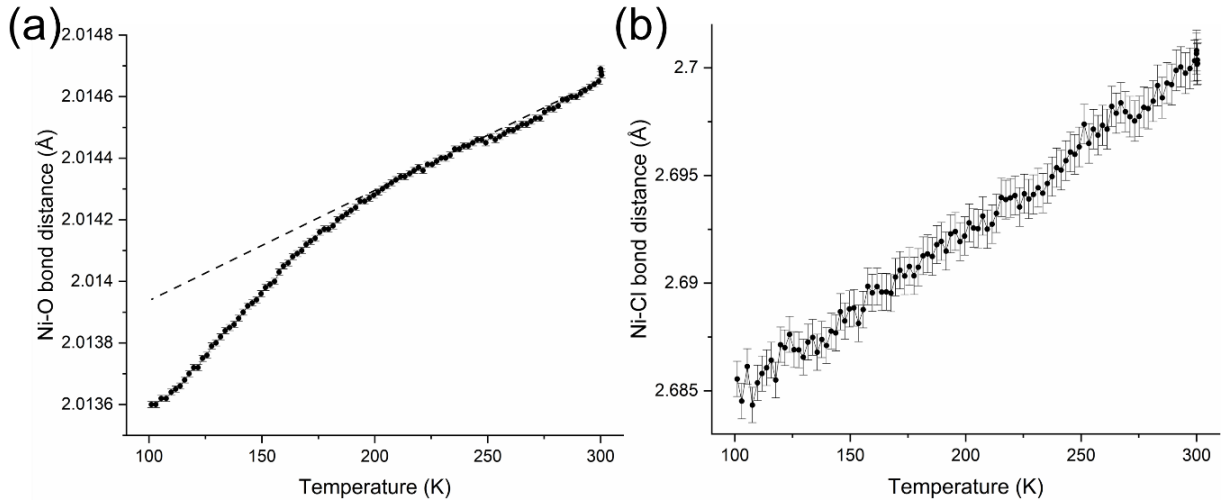


Figure 3.37(a) The Ni-O and **(b)** Ni-Cl bond lengths of $Sr_2NiO_2Cl_2$ as a function of temperature.

3.3.4 Magnetometry

Magnetometry measurements were qualitatively consistent with those previously reported[55] which can be seen in Appendix C.2. $Sr_2NiO_2Cl_2$ exhibits a broad maximum similar to those commonly found in low-dimensional antiferromagnetic systems around 150-180 K which was tentatively identified as the Néel temperature (inset of Figure 3.38(a)).

The 5 K magnetisation isotherm shows displacement away from the origin, suggesting that there is a glassy component to the magnetism of the sample (Figure 3.38(b)), and it is possible that this, together with the divergence of the ZFC and FC curves, is due to a miniscule amount of impurity which might also lead to the large upturn in the susceptibility at low temperature.

The difference in in the susceptibility at room temperature compared to the previous report[55] is likely down to the change in the Ni-source in the synthesis yielding a much purer product (see Figure 3.33).

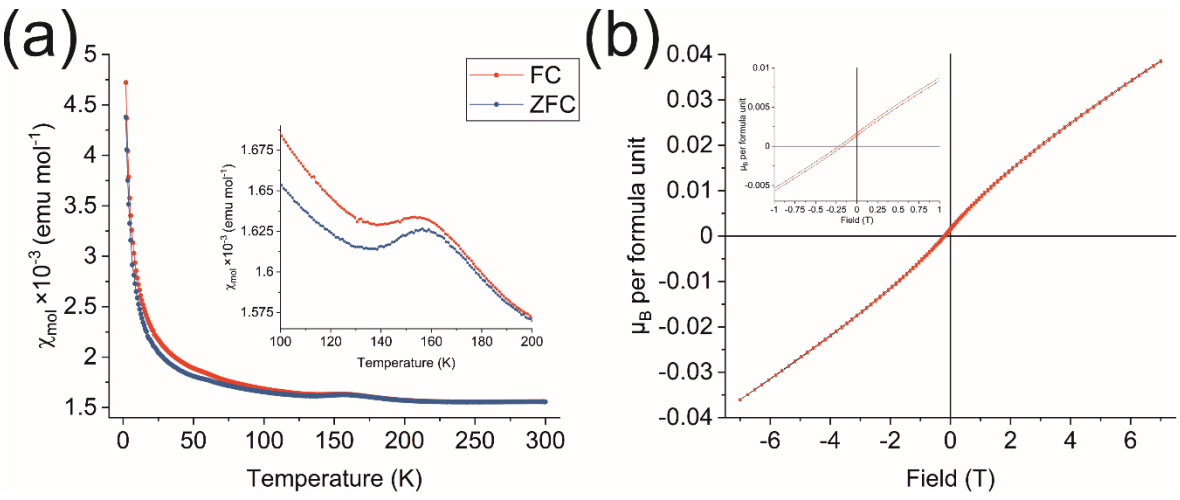


Figure 3.38(a) ZFC / FC magnetic susceptibility of $Sr_2NiO_2Cl_2$ measured at 100 Oe. **(b)** *M vs H* isotherm of $Sr_2NiO_2Cl_2$ measured at 5 K after cooling in a 7 T field.

3.3.5 Variable temperature PND to probe magnetic ordering

The magnetic susceptibly data for this compound suggested that the onset of long-range magnetic ordering was at approximately 160 K. To probe this further, low temperature PND was used. Rietveld refinement against the data at 1.5 K is shown in Figure 3.39 with all data on cooling shown in Figure 3.40.

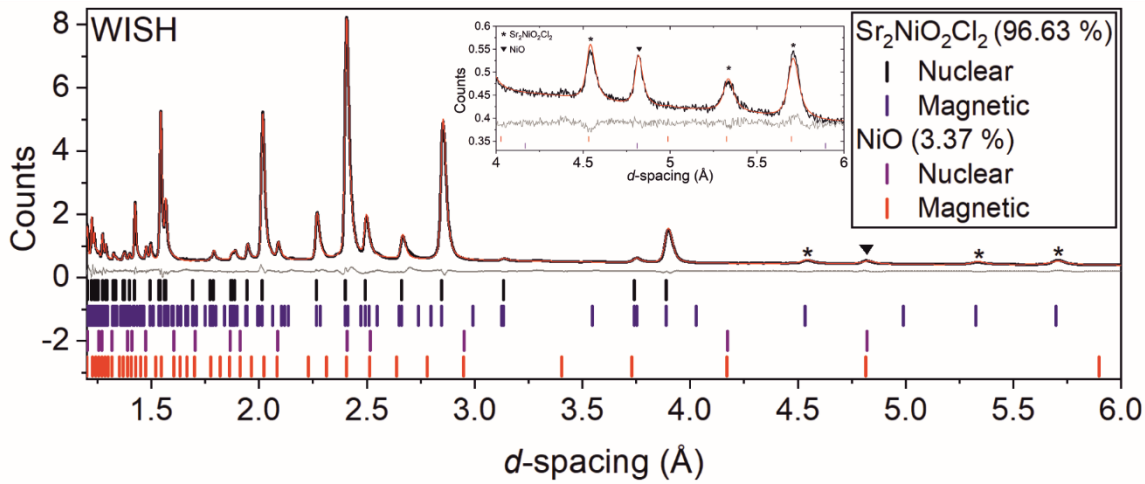


Figure 3.39 Rietveld refinement at 1.5 K of $Sr_2NiO_2Cl_2$ against bank 2/9 of the WISH diffractometer at ISIS. R_{wp} = 3.019 %; $\chi 2$ = 0.031.

The data had peaks at relatively large *d*-spacing which were not accounted for by the nuclear model and grew in intensity on cooling as shown in Figure 3.41 and which are annotated in Figure 3.39 with asterisks suggesting that they were magnetic in origin; also present is the characteristic dominant (111) magnetic reflection from the small amount of NiO impurity denoted by a triangle in Figure 3.39[123] with the remaining, less intense magnetic reflections (relative to the (111)) lost within the background due to the small amount of NiO present along with the relatively weak scattering from the Ni^{2+} moments.

The magnetic Bragg peaks were indexed on a propagation vector, k = (½ ½ 0), expansion of the nuclear cell and subsequent symmetry mode analysis was conducted using the ISODISTORT software.[124] The structure was analysed assuming the symmetry space group

*P*1, so that all possible modes could be considered. In conjunction with TOPAS V6,[95] it was determined that a singular magnetic symmetry mode did not yield a satisfactory fit to the data and so a combination of modes was investigated.

It was found that a combination of the mX2+ and mX3+ modes gave a visually and statistically satisfactory fit during Rietveld refinement (fit shown in inset of Figure 3.39).

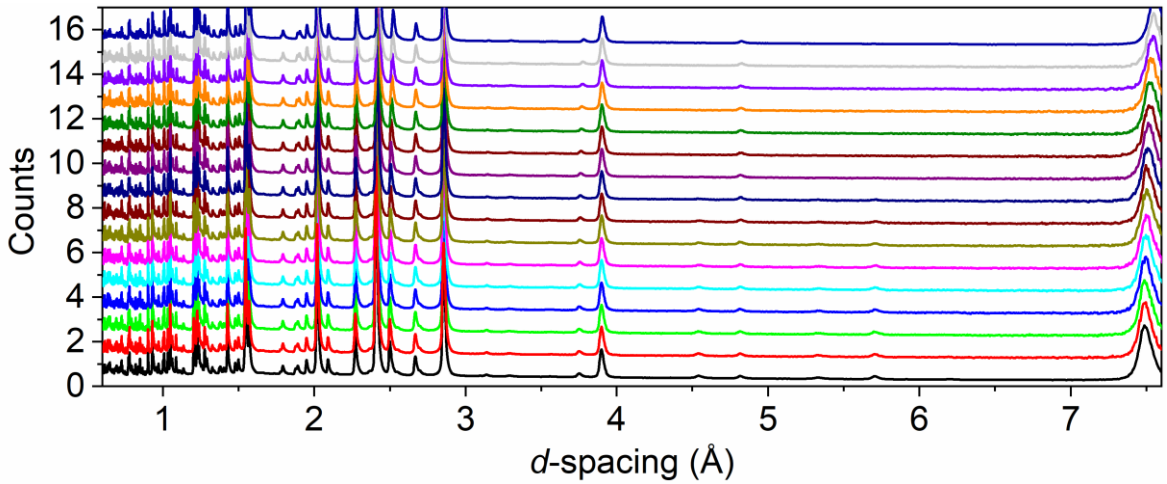


Figure 3.40 Waterfall plot of the collated data between 300 K (top) and 1.5 K (bottom). No structural distortions were evident which would manifest itself as peak splitting with the movement of individual peaks being due to thermal contraction.

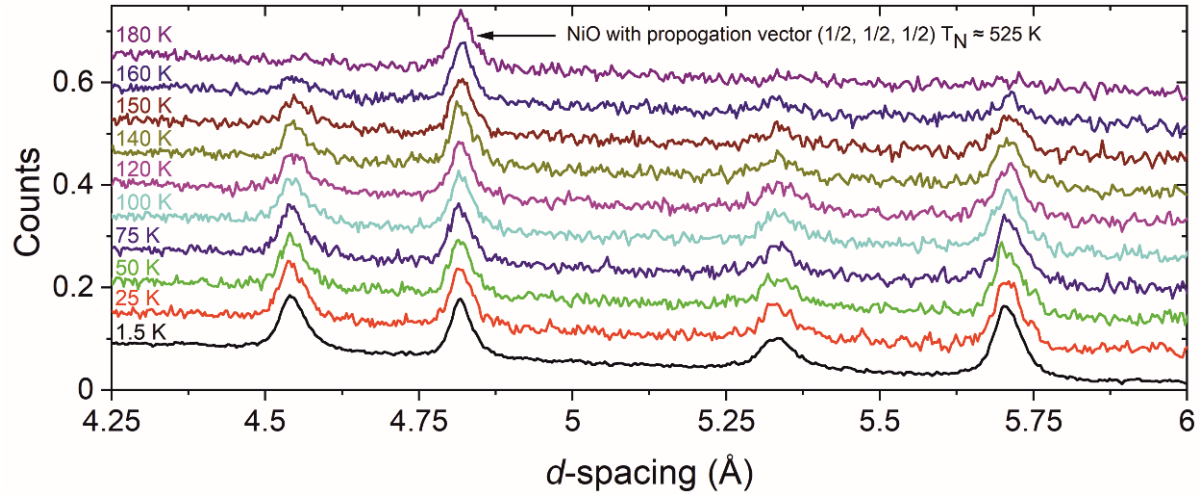


Figure 3.41 Raw PND data for $Sr_2NiO_2Cl_2$ from the 2/9 bank of the WISH diffractometer.

Once the magnetic symmetry modes were identified, ISODISTORT allowed for the determination of the magnetic space group symmetry. It was found that the P_cbca magnetic space group (61.439 in the Belov, Neronova and Smirnova (BNS) scheme) or $C_pm'ca'$ magnetic space group (64.16.543 in the Opechowski and Guccione (OG) scheme)[125] was the highest-symmetry magnetic space group that could account for the observed magnetic intensity from the PND data. This is in contrast to the selenide, $Sr_2NiO_2Cu_2Se_2$, which has the magnetic space group $P_C4_12_12$ (92.117 in the BNS scheme).[38]

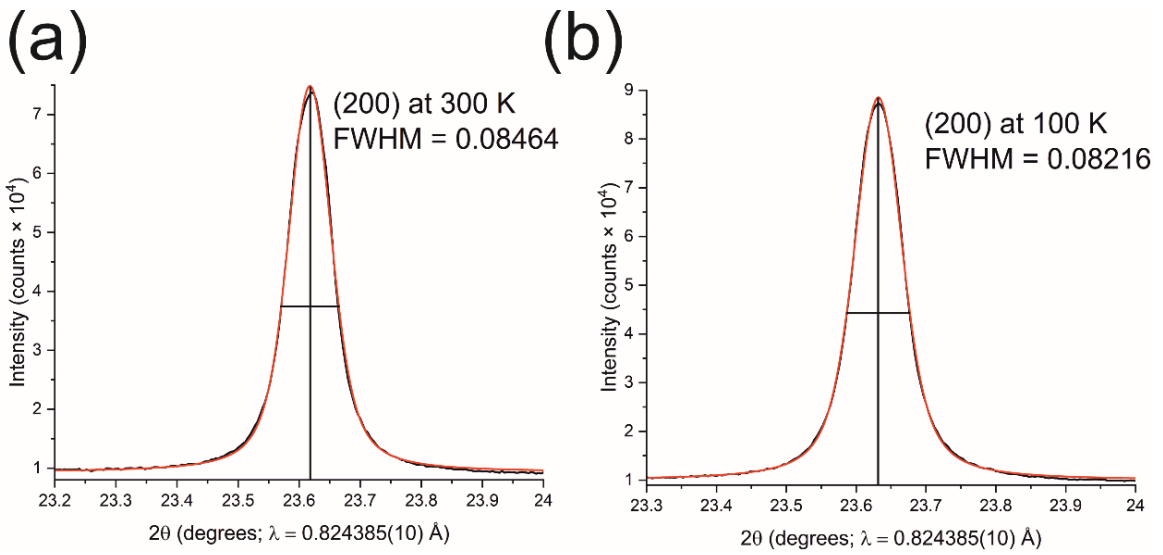


Figure 3.42 The 200 Bragg peak at **(a)** 300 K and **(b)** 100 K fitted to a Voigt function from which the FWHM can be extracted. There is no suggestion of peak broadening below the magnetic ordering transition.

The magnetic structure shows a lowering in symmetry from the nuclear cell but no structural distortion is evident within the resolution of the powder data as shown in Figure 3.42. Despite the difference in the magnetic space groups between the oxide chloride and the oxide selenide, the result is qualitatively similar as far as each layer is concerned with magnetic moments aligned in a similar orientation as shown in Figure 3.43, with the difference in the magnetic structures being the doubling along the *c* axis in the oxide selenide.

This results in Ni^{2+} moments arranged antiferromagnetically as shown in Figure 3.43. The refined Ni^{2+} moment has a magnitude of 1.57(7) μ_B at 1.5 K (μ_a = μ_b 1.00(7) μ_B; μ_c = 1.22(6) μ_B. As well as being similar to the selenide-rich members of the series $Sr_2NiO_2Cu_2(Se_{1-x}S_x)_2$[38] described in section 3.2, it also quantitively agrees with the results from the computational study conducted by Zhou et al.[108]

The reduction from the spin-only magnetic moment of 2 μ_B can be attributed to a degree of covalency in the bonding which is common for transition metal oxides and it is consistent with the calculated spin density of 1.6 μ_B.[108]

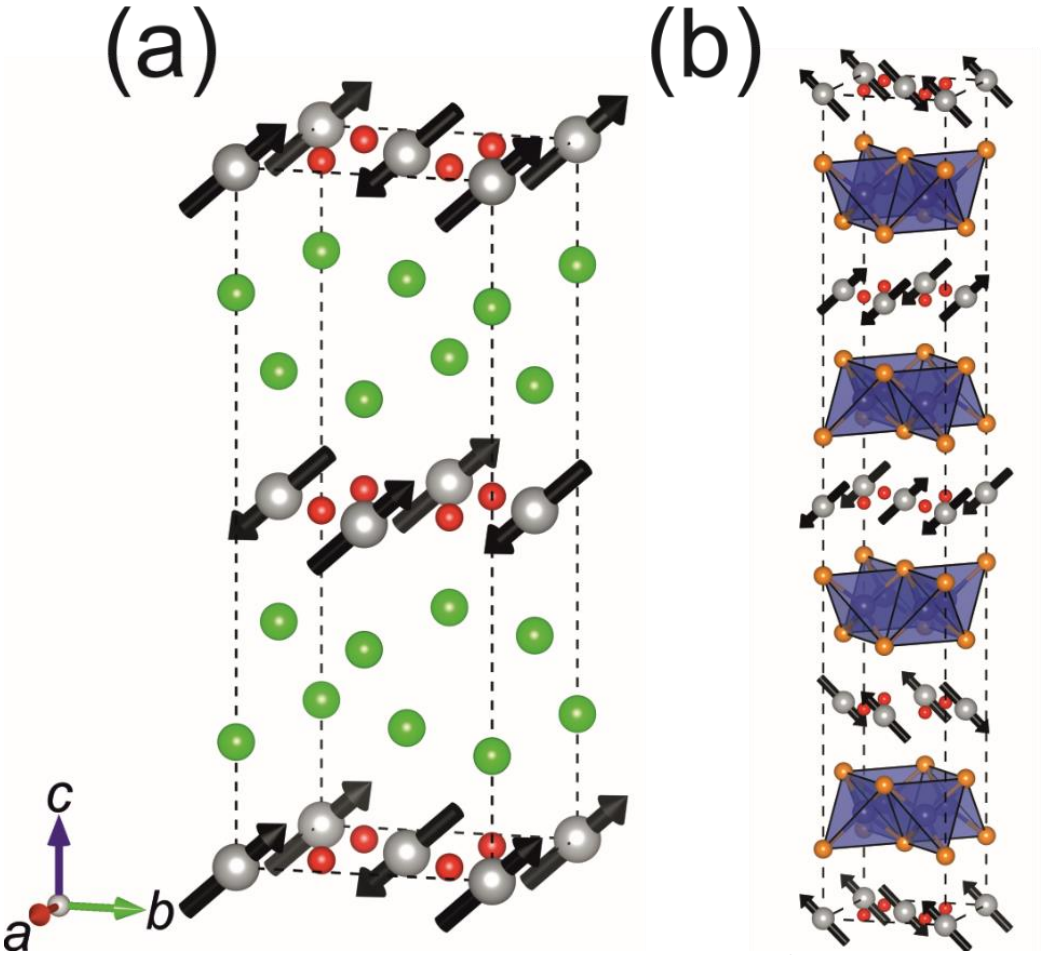


Figure 3.43(a) The magnetic structure of $Sr_2NiO_2Cl_2$ with Ni^{2+} moments arranged antiferromagnetically and tilted between the *ab*-plane and the *c*-axis **(b)** The magnetic structure of the Se-rich members of the $Sr_2NiO_2Cu_2(Se_{1-x}S_x)_2$. Note the doubling of the *c* axis for the oxide chalcogenide.

Figure 3.44 shows the evolution of the Ni^{2+} moment on heating from the saturated value of 1.57(7) μ_B. From this, it is inferred that the Néel temperature (T_N) of this material can be extrapolated to ≈ 180 K, where the long range ordered moment develops. The drop in susceptibility below 150 K coincides approximately with the saturation of the long-range-ordered moment. But like in many of these layered materials, the onset of long-range magnetic order is not very clear using magnetometry.

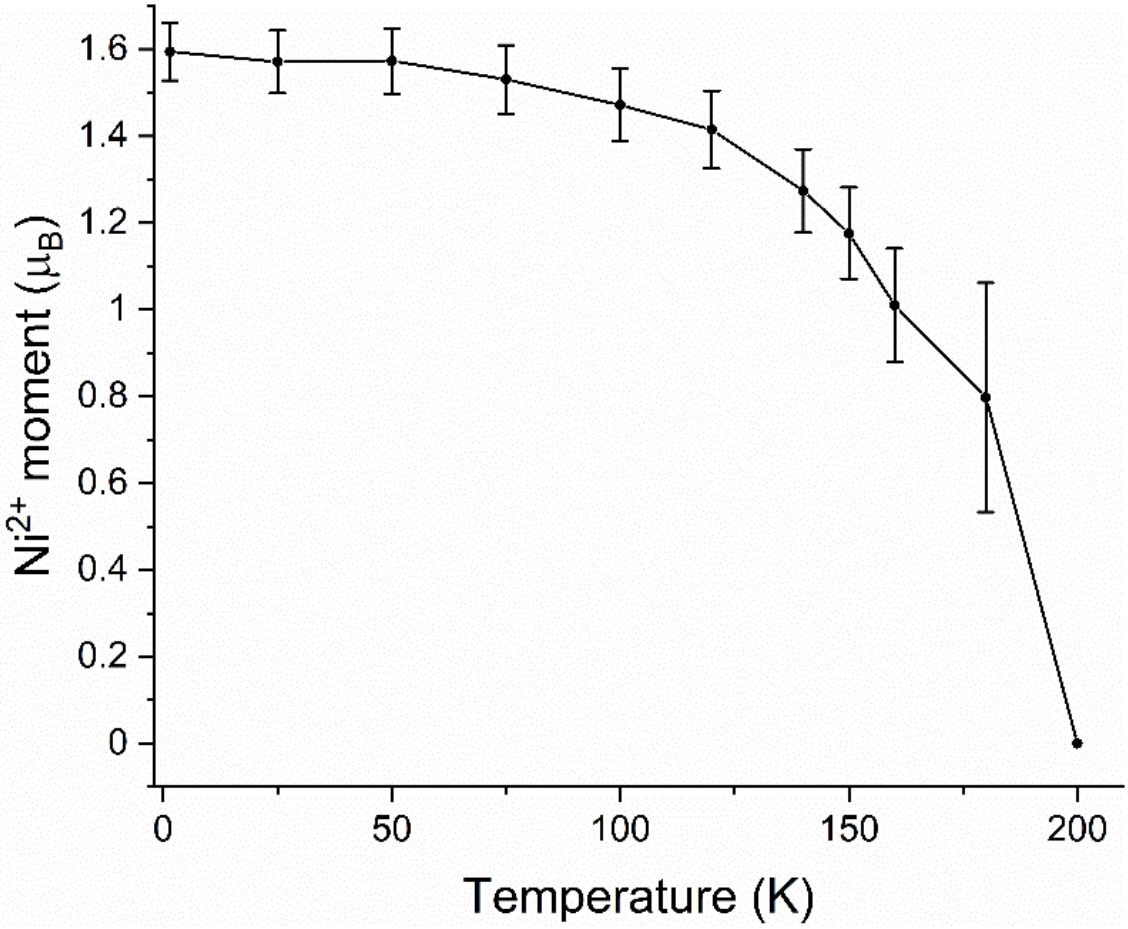


Figure 3.44 Thermal evolution of the ordered Ni^{2+} moment in $Sr_2NiO_2Cl_2$.

3.4 Discussion

The change in behaviour between the $Sr_2NiO_2Cu_2Se_2$ and $Sr_2NiO_2Cu_2S_2$ end members was observed directly as a function of composition in the solid solution $Sr_2NiO_2Cu_2(Se_{1-x}S_x)_2$.

PND data revealed that compositions up to and including x = 0.344 showed magnetic scattering, and analysis of the magnetic Bragg scattering as a function of increasing sulfide content showed a smooth reorientation of the spin direction towards the *ab*-plane.

For more S-rich systems with x = 0.375 and higher, no evidence for long-range magnetic ordering was found. Consistent with the behaviour of the magnetic ordering, there is a structural signature of the change from broadly high-spin to broadly low-spin behaviour as selenide is replaced by sulfide (Figure 3.13). The Ni-*Ch* / Ni-O ratio (with the mixture of sulfide and selenide ions located on a single average site) shows a very gentle upturn on increasing S-content up until x = 0.375 (the first composition which does not have magnetic Bragg scattering) and then increases more sharply as the S-content increases further. This is consistent with the Ni ions remaining high-spin in the Se-rich compositions and accordingly, in the Se-rich phases that show long-range magnetic order there is only a small decrease in the long range ordered moment carried by the Ni^{2+} ions.

For the more S-rich compositions, the Ni-*Ch* / Ni-O ratio increases sharply even though the mean chalcogenide ion radius is decreasing, thus the Ni environment is clearly becoming more axially elongated, consistent with the formation of low-spin Ni^{2+} ions.

This spin-state disorder arising inherently from the chemical disorder associated with making a solid solution would be expected to disrupt the long-range magnetic ordering found

in the selenide-rich phases leading to a loss of magnetic Bragg peaks as the sulfide content increases, as is observed.

The sample $Sr_2NiO_2Cu_2(Se_{0.656}S_{0.344})_2$, showing the Warren peak is the most S-rich composition measured that has antiferromagnetic ordering with a significant correlation length. The sulfide end member $Sr_2NiO_2Cu_2S_2$ has only one type of Ni environment, and while the attractive conclusion is that the lack of magnetic long-range order[11] in this case is because this compound contains only diamagnetic Ni^{2+} ions, the computational results and the fact that there are low-temperature structural and magnetic anomalies mean that it cannot be ruled out that $Sr_2NiO_2Cu_2S_2$ has Ni in a spin-state that is intermediate between the high and low spin-states.

Diffraction is a technique that probes structures over many unit cells i.e., not a local probe, and as such, only the average structure is observed. Local variation in the coordination environment may lead to different spin-states in the solid solution. For example, NiO_4S_2 octahedra may have a low-spin Ni^{2+} cation whereas NiO_4Se_2 octahedra have a high-spin Ni^{2+} cation. A local structural probe such as X-ray or neutron Pair Distribution Functions (PDF) analysis or Ni-edge EXAFS would be required to confirm if there are different environments within the solid solution $Sr_2NiO_2Cu_2(Se_{1-x}S_x)_2$. Analysis of a mixed state for NiO_4SeS where the Ni-*Ch* bond length varies in C_{4v} symmetry did not offer better statistics in the Rietveld refinement.

According to the detailed DFT calculations carried out on the oxide chalcogenides to support this experimental work, which were performed using different values for *U* (which quantifies on-site electron-electron repulsions) it was found that the high-spin-state ($(dz^2)^1$ $(dx^2\text{-}y^2)^1$) was favoured for $U = 2$ eV and for higher values for $Sr_2NiO_2Cu_2Se_2$.

In contrast, for the sulfide $Sr_2NiO_2Cu_2S_2$, a comparable set of calculations showed that the low spin-state ($(dz^2)^2$) was marginally favoured for U = 2 eV and in fact for any given value of U, the sulfide was stabilised relative to the selenide.

The computational model used for $Sr_2MO_2Cu_2Ch_2$ (M = Co, Ni, Cu, Zn) replicates the structural data extremely well for the Co, Cu and Zn analogues (both sulfide and selenide) and so captures the important structural features for this class of compound.

However, the calculated Ni^{2+} environments suggest that the NiO_4Se_2 octahedron in the selenide is experimentally slightly more elongated than it should be if it was fully high-spin and the optimised calculated structure for the sulfide in the low-spin-state has an even more elongated NiO_4S_2 environment than is found experimentally.

The calculations are thus fairly consistent with the inference about the spin-states from the structural data and the occurrence, or not, of magnetic ordering, but suggest that in both compounds the situation is finely balanced and that the simple high-spin *vs* low-spin binary choice for the spin-state in these compounds where the Ni^{2+} ions are not fully isolated is most likely a simplification.

In other recent work, a ground state consistent with S = 1 (i.e., high-spin) was suggested for both $Ba_2NiO_2Ag_2Se_2$ and $Sr_2NiO_2Ag_2Se_2$ but, while the former showed magnetic long-range order, no magnetic Bragg peaks were observed, even at 6 K in $Sr_2NiO_2Ag_2Se_2$ even though it obeys they Curie-Weiss law, with C = 1.09(6) emu K mol^{-1} and θ = –158(11) K, and so it was hypothesised to be in a spin-glass state.[33]

It should be noted that $Sr_2NiO_2Ag_2Se_2$ was not synthesised phase pure and had unidentified impurities in the Rietveld refinement and so it is not implausible that this sample is non-

stoichiometric and there are site vacancies leading to disorder. Ni^{2+} is unlikely to be oxidised and so for $Sr_2NiO_2Ag_2Se_2$, XANES at the Se K-edge may be useful to determine if there are any vacancies from which a shift to higher energies would be seen as Se^{2-} becomes slightly oxidised.

In view of the differences between the experimental and computational environments for Ni, particularly in $Sr_2NiO_2Cu_2S_2$, further computation was performed and a model involving a 50/50 split of high- and low-spin Ni^{2+} cations in a checkerboard arrangement led to calculated results that almost replicate the experimental structural data for $Sr_2NiO_2Cu_2S_2$ along with underestimations in the experimental lattice parameters much more in line with those found for the Co, Cu and Zn analogues (see Appendix A.1 for more details).

While this result could be somewhat fortuitous, it could suggest that $Sr_2NiO_2Cu_2S_2$ contains a mixture of high-spin and low-spin Ni^{2+} cations and Ni^{2+} spin disorder results in a loss of magnetic Bragg peaks. Alternatively, the localised electron picture may not be appropriate. Further local probe experiments such as muon-spin rotation spectroscopy or ^{61}Ni Mössbauer spectroscopy would be needed to investigate this further with the growth of large single crystals desirable for probing directional physical properties.

However, it is clear there is some degree of localisation in $Sr_2NiO_2Cu_2Se_2$ as proven by the observation of long-range magnetic ordering within the square-planar NiO_2 sheets. The Ni^{2+} moments in $Sr_2NiO_2Cu_2Se_2$, which are in a highly elongated NiO_4Se_2 octahedron order antiferromagnetically below 160 K. The behaviour of this compound is similar to that of the isostructural $Ba_2NiO_2Ag_2Se_2$.[33] These observations confirm that the Ni^{2+} ion is in a high spin-state.

In contrast $Sr_2NiO_2Cu_2S_2$[7] does not exhibit any magnetic Bragg peaks and therefore there is no evidence for long-range magnetic ordering. $Sr_2NiO_2Cu_2S_2$ has a more elongated NiO_4S_2 octahedron than $Sr_2NiO_2Cu_2Se_2$ with Ni-O bonds that are 2.6 % shorter than those in the NiO_4Se_2 octahedron of $Sr_2NiO_2Cu_2Se_2$, making dx^2-y^2 more antibonding, and the Ni-S distance in $Sr_2NiO_2Cu_2S_2$ is slightly longer than the corresponding Ni-Se distance in $Sr_2NiO_2Cu_2Se_2$, making dz^2 less antibonding as shown below in Figure 3.45, and so in the sulfide the octahedron is much more highly elongated, consistent with a low-spin configuration for Ni^{2+} (i.e., diamagnetic ions with dx^2-y^2 unoccupied). The obvious conclusion which ties all these parameters together would be that the Ni^{2+} ions in $Sr_2NiO_2Cu_2S_2$ are low-spin. However, as discussed in section 3.2.8, computation has shown that it may not be as simple as a binary choice of high- and low-spin and that a hybrid state with both high- and low-spins could be more appropriate for these Ni-containing oxide chalcogenides.

Indeed, both $Sr_2NiO_2Cu_2Se_2$ and $Sr_2NiO_2Cu_2S_2$ display further subtleties in the details of their crystal structures and in the temperature dependence of their crystal structures and some of their properties. In $Sr_2NiO_2Cu_2Se_2$ the computation reproduced very well the experimental Ni-O and Ni-Se bond lengths, and the magnitude of the calculated spin density localised on Ni in the antiferromagnetic state.

However, examination of the changes in the Ni coordination environment as a function of temperature show that above the region of the magnetic ordering transition, the NiO_4Se_2 octahedron is slightly more elongated than one would expect by analogy with isostructural compounds, and it becomes less elongated on cooling and this is reflected in the behaviour of the lattice parameters.

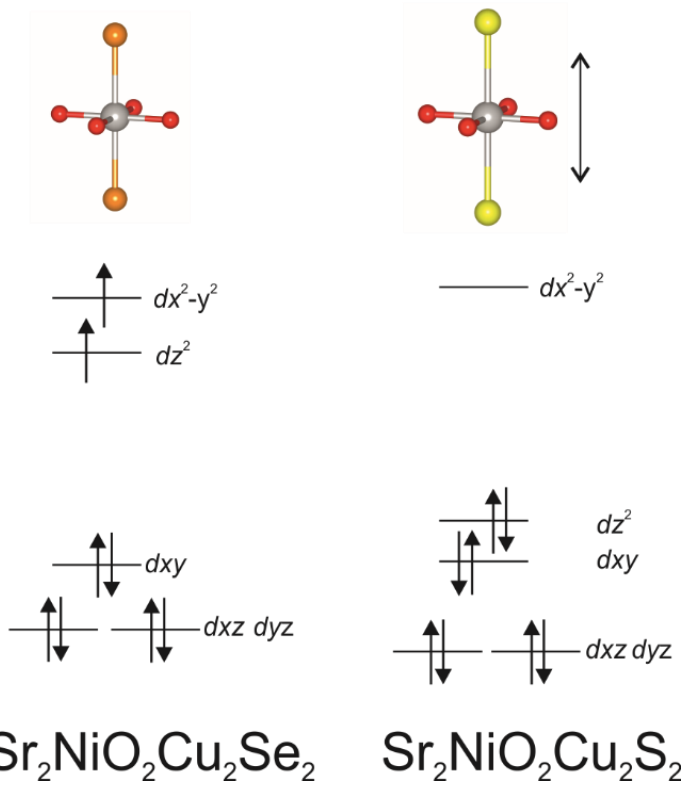


Figure 3.45 Ligand field diagrams for $Sr_2NiO_2Cu_2Ch_2$ (*Ch* = S, Se).

Furthermore, $Sr_2NiO_2Cu_2Se_2$ shows a high temperature resistivity that is characteristic of metallic behaviour and this also shows an anomaly around the magnetic ordering transition in which the resistivity increases slightly on cooling, before decreasing again on further cooling.[38] An attractive interpretation of this is that the metallic behaviour arises from hole states in the top of the selenide-based band, formed by some transfer of electrons into the energetically nearby $3dz^2$ band of Ni (i.e., selenide slightly reduces the Ni cations) are shown to be at similar energies above E_F.[38] This would result in a more elongated NiO_4Se_2 octahedron than expected (more electrons in Ni/Se antibonding states), and it is well known that compounds with similar CuSe layers can readily accommodate holes in anti-bonding states at the top of the Cu-3*d*/Se-4*p*-based band leading to metallic behaviour.[42,126] The upturn in the resistivity and the decrease in axial elongation of the Ni octahedron on cooling

would then correspond to partial electron transfer from Ni $3dz^2$ to Se or they may also be associated with the onset of long range antiferromagnetic order.

To further understand the strange behaviour in these Ni-containing oxide chalcogenides, large single crystals would be required to more accurately determine the sample's transport properties.

An adapted synthetic approach has enabled $Sr_2NiO_2Cl_2$ to be synthesised under high pressure on the bulk scale and with higher purity than previously reported.[55] Detailed analysis of the crystal structure and comparison with the closely related oxide chalcogenides $Sr_2NiO_2Cu_2Se_2$ and $Sr_2NiO_2Cu_2S_2$ show that when there is competition with Ni for the apical non-oxide anion such as in the oxide chalcogenides, the NiO_4X_2 octahedron is more elongated and the apical anion makes a smaller contribution to the Ni bond valence sum: chloride anions contribute a total of 16.8 % to the total Ni BVS in $Sr_2NiO_2Cl_2$ while $Sr_2NiO_2Cu_2Se_2$ and $Sr_2NiO_2Cu_2S_2$ have a coordination closer to square-planar with contributions of 9.33 and 6.05 % respectively from selenide and sulfide anions.

$Sr_2NiO_2Cl_2$ is thus firmly in the high-spin Ni^{2+} regime while high-spin $Sr_2NiO_2Cu_2Se_2$ and low-spin $Sr_2NiO_2Cu_2S_2$ straddle the high-spin / low-spin crossover. [9,38]

Long-range magnetic ordering in $Sr_2NiO_2Cl_2$ can be indexed on a $\sqrt{2}a \times \sqrt{2}a \times c$ expansion of the nuclear cell, with moment orientations and a magnitude which are similar to that found for the high-spin Ni^{2+} oxide chalcogenides. The spectrum of spin-states for related materials containing Ni^{2+} ions in highly elongated environments is shown in Figure 3.46 with the crossover as a function of Ni-O bond length depicted.

3.5 Conclusion

In this chapter, the synthesis of the solid solution $Sr_2NiO_2Cu_2(Se_{1-x}S_x)_2$ has been reported. The more Se-rich compounds for $x \leq 0.5$ required a high temperature synthesis to achieve complete cation segregation between Ni and Cu, whereas the S-rich compounds for $x > 0.5$ required a low-temperature synthesis to avoid target phase decomposition.

PND measurements were able to pinpoint the spin-state crossover as a function of composition from high-spin $Sr_2NiO_2Cu_2Se_2$ to low-spin $Sr_2NiO_2Cu_2S_2$, going from fully 3-dimensional ordering through a lower 2-dimensional ordered state in $Sr_2NiO_2Cu_2(Se_{0.656}S_{0.344})_2$ before loss of any sign of long-range magnetic order for more S-rich compositions.

$Sr_2NiO_2Cu_2Se_2$ was also subjected to high-pressure to determine if the ligand field could be increased sufficiently to drive it into the low-spin regime. However, the measurements performed in this thesis concluded that this was not possible up to 7.3(1) GPa.

Finally, the previously synthesised oxide chloride $Sr_2NiO_2Cl_2$ was also investigated using PND to determine its magnetic structure. Magnetic peaks could be indexed on a $\sqrt{2}a \times \sqrt{2}a \times c$ expansion of the nuclear cell with localised Ni^{2+} moments with a magnitude of 1.57(7) μ_B at 1.5 K, which is consistent with calculation and with the closely related oxide chalcogenide analogue, $Sr_2NiO_2Cu_2Se_2$.

In conclusion, the number of compounds with Ni^{2+} in this highly-elongated environment has been expanded upon and it has been shown that the spin-state is consistent across the series

as shown in Figure 3.46, whereby a limiting Ni-O bond length of just over 2 Å seems to be the critical length at which the spin-state switches between bulk high- and low-spin.

The comparisons of the solid solution $Sr_2NiO_2Cu_2(Se_{1-x}S_x)$ with the selenide end-member $Sr_2NiO_2Cu_2Se_2$ and sulfide end-member $Sr_2NiO_2Cu_2S_2$, as well as with related compounds underpinned by detailed computational investigations show that the structural and physical properties of these layered nickel oxide chalcogenides are complex and there is competition between spin-states which can be tuned by chemical substitutions to tune the ligand field.

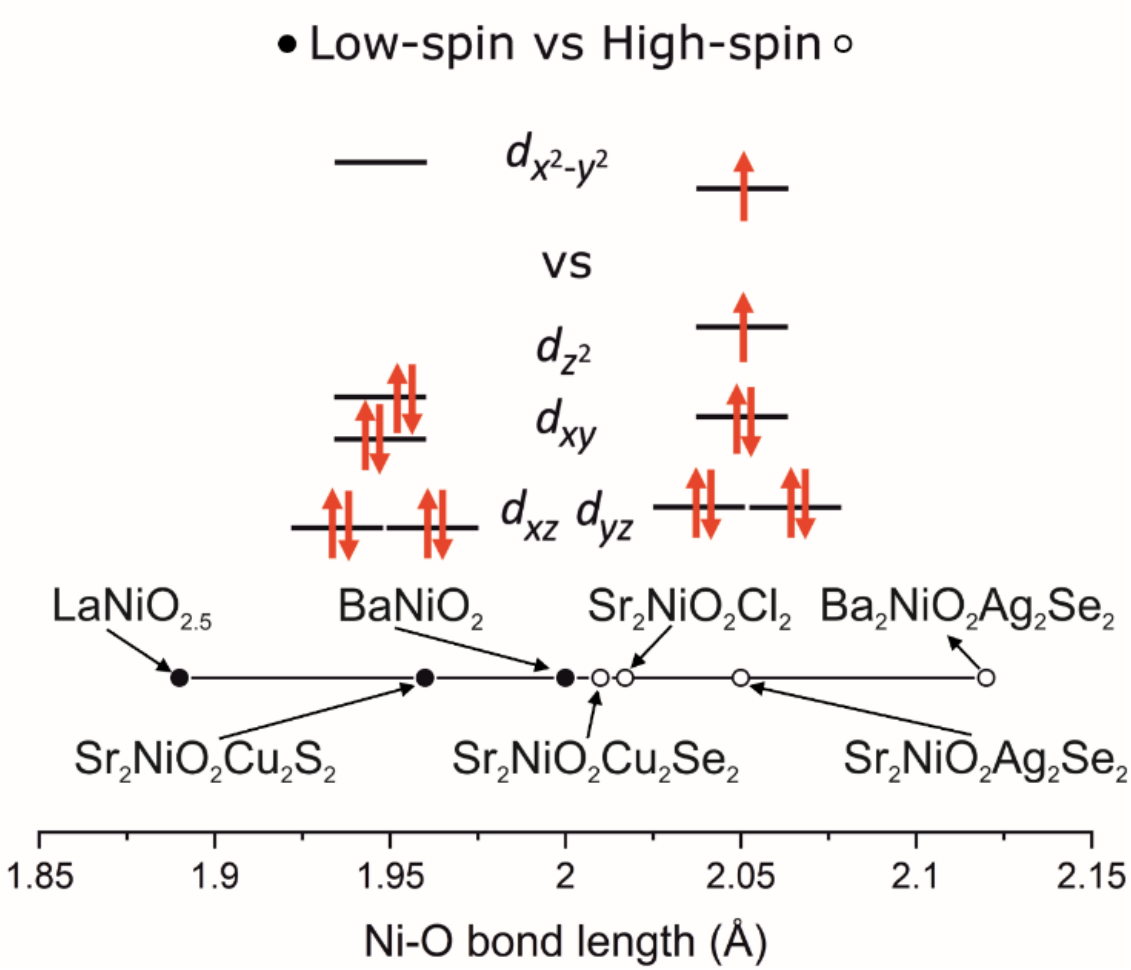


Figure 3.46 Ni-O bond length comparison and the spin-state for various Ni^{2+} containing solids.[7,33,38,127,128]

These measurements on polycrystalline samples underline the complex behaviour in these systems as functions of temperature and composition, resulting from the fact that not only is there a choice of accessible Ni spin-states, but that the chalcogenide states are in close energetic proximity to the Ni^{2+} frontier states. The contrasting thermal evolution of the structural, magnetic and transport properties of the sulfide and selenide end members, together with the evolution of structure and magnetism across the solid solution and the computational results that suggest that the simple binary notion of high-spin and low-spin-states carried by Ni^{2+} ions in these phases is likely a simplification of the true state, show that further investigations on single crystal samples are merited to enable the subtleties of these compounds to be fully accounted for.

Chapter 4

4 Soft chemistry of Co-containing oxide chalcogenides

4.1 Introduction

The Co analogues of the $m = 1$, $n = 1$, $Ae_2MO_2X_2Ch_2$ (section 1.3.1.2 and Figure 1.5) structure type are a rare example of Co^{2+} in a pseudo square-planar environment and are the most compositionally abundant of the first row transition metals that adopt this configuration, having originally been discovered by Zhu and Hor[16] in 1997 for the oxide sulfides $Sr_2CoO_2Cu_2S_2$ and $Ba_2CoO_2Cu_2S_2$.

This series of oxide chalcogenides has since been expanded to include a vast array of known compositions with *Ae* = Ba, Sr, *X* = Cu, Ag and *Ch* = S, Se and Te.[20,21,26,34]

The majority of these Co-containing oxide chalcogenides as-made at high temperatures order antiferromagnetically as is predicted by the Goodenough-Kanamori rules[61,62] and normally found for 180° interactions between similar ions.

Smura built upon the work of Zhu and Hor by investigating the solid solution $Ba_{2-x}Sr_xCoO_2Cu_2S_2$ and discovered that the size of the long-range ordered magnetic moment carried by the Co^{2+} ion increases in magnitude as the CoO_4S_2 polyhedron becomes increasingly tetragonally elongated with decreasing *x*, i.e., more Ba-rich.[21]

This relationship was strengthened by Herkelrath with investigation of the 2 novel compounds, $Ae_2CoO_2Ag_2Se_2$ (*Ae* = Ba, Sr).[20] In both cases, it was noted that the magnetic

moment of Co^{2+} was larger than what would have been predicted using the spin-only formula and so it was proposed that there was a significant orbital contribution to the moment, quantitively similar to that of CoO which has an ordered moment with a magnitude of ≈ 4 μ_B with an orbital contribution arising from the unevenly occupied, degenerate, t_{2g} state in the octahedral environment for high spin d^7 Co^{2+}.

The soft chemistry of these compounds has also been extensively studied – especially the Cu containing analogues – with Smura showing that $Sr_2CoO_2Cu_2S_2$ was reactive with respect to *n*-BuLi,[35] whereas Harris demonstrated that the mobile Cu ions could be deintercalated using I_2 to produce the novel phase $Sr_2CoO_2Cu_{1.78}S_2$[129] where no vacancy ordering was observed (unlike the oxidative deintercalation of $Sr_2MnO_2Cu_{1.5}S_2$ where a modulated superstructure of copper-vacancies is observed)[19] because the vacancy concentration was not high enough – reinforcing the difficulty of oxidation of Co^{2+} as opposed to Mn^{2+}.

The deintercalation chemistry of $Sr_2CoO_2Cu_2S_2$, $Sr_2CoO_2Cu_2Se_2$ and $Sr_2CoO_2Ag_2Se_2$ were also investigated by Blandy.[40] Most notably, $Sr_2CoO_2Ag_2Se_2$ was found to undergo an antiferromagnetic to ferromagnetic ordering transition on the partial deintercalation of Ag.

In the most-deintercalated composition $Sr_2CoO_2Ag_{1.5(2)}Se_2$, there were many complex interactions which change dramatically as a function of temperature. The magnetisation isotherms identified four regions of interest; paramagnetic, potentially metamagnetic, soft ferromagnetic and ferromagnetic with a large spin-glass component as shown below in Figure 4.1, although a true picture of the magnetism within this deintercalated phase was never confirmed, with the current hypothesis being that it is an itinerant ferromagnet.[40]

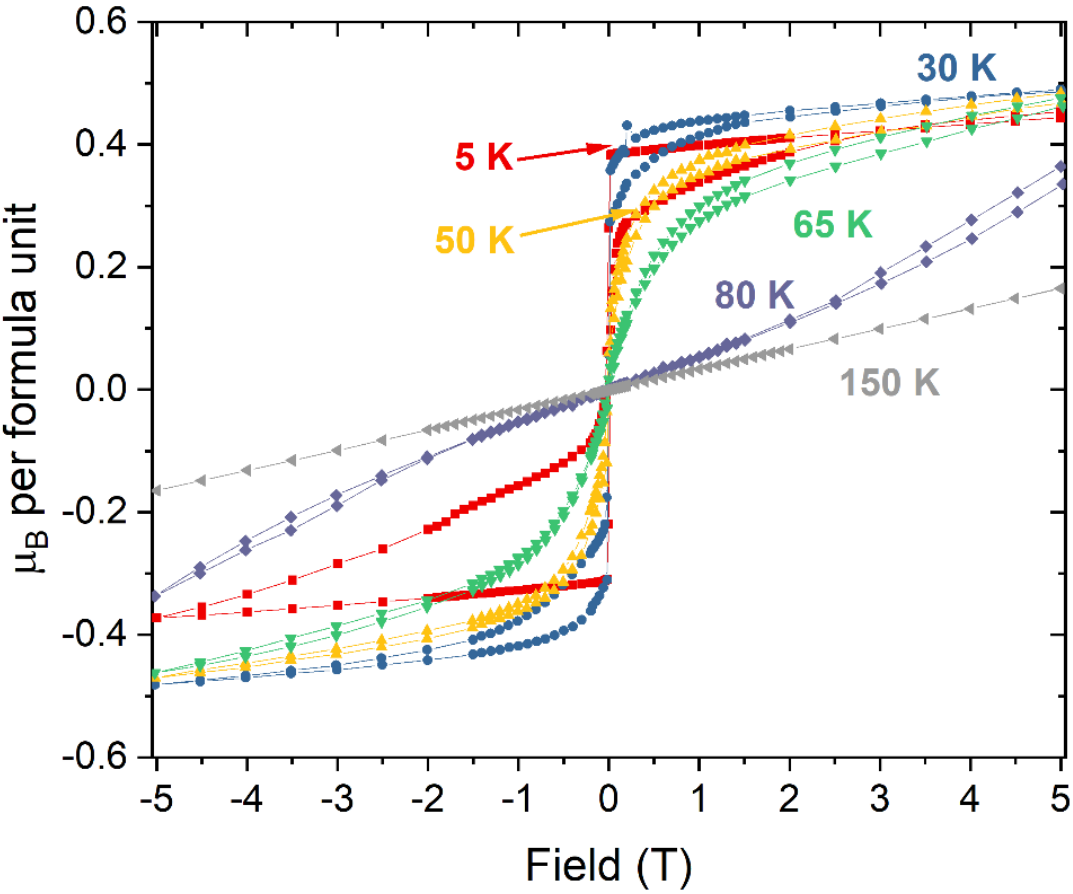


Figure 4.1 *M* vs *H* isotherms, measured at various temperatures for $Sr_2NiO_2Ag_{1.5(2)}Se_2$. Before each measurement, the sample was cooled from 300 K in a 5 T field.[40]

$Sr_2CoO_2Cu_2Te_2$ is not reactive with I_2[40] and was found to be also unreactive towards *n*-BuLi in this work (see Appendix D), presumably kinetically slow due to the much larger Te^{2-} ions.

4.2 Li / Cu exchange in $Sr_2CoO_2Cu_2Ch_2$ (*Ch* = S, Se)

4.2.1 Synthesis and cycling

Samples of $Sr_2CoO_2Cu_2Ch_2$ (*Ch* = S, Se) "parent" materials for subsequent soft chemistry were synthesised from a mixture of SrO (obtained via thermal decomposition under dynamic vacuum of $SrCO_3$ (Alfa 99.994 %), at initially 840 °C with a final treatment at 1100 °C with the full procedure outlined in section 2.1.3.1), Co (Alfa 99.998 %), Cu (Alfa 99 + %), and either S (Alfa 99.999 %) or Se (Alfa 99.999 %).

The mixture for the sulfide was preheated at 400 °C, ramping up at 10 °C min^{-1}, for 12 hours to avoid the vapor pressure inside the silica tube getting too high while the chalcogen reacted, before a final heating at 800 °C for 48 hours, again ramping at 10 °C min^{-1}.

The selenide reaction was preheated at 640 °C, ramping up at 10 °C min^{-1}, for 12 hours before a final heating at 800 °C for 48 hours. The general experimental procedure for solid-state synthesis is outlined in section 2.1.1.

The procedure for obtaining the soft-chemical products is outlined in section 2.1.4 and involves initially the reaction of parent material under an inert atmosphere with *n*-BuLi (1.6 M in hexanes) for 3 days at 50 ºC (equation 4.1) in a Schlenk flask before filtering and stirring in a solution of 2 equivalents of disulfiram which chelates the extruded Cu and a small quantity of anhydrous DMF under inert atmosphere on the Schlenk line.

$$Sr_2CoO_2Cu_2S_2 + n - BuLi \xrightarrow{\Delta} Sr_2CoO_2Cu_{2-x}Li_x + Cu \qquad (4.1)$$

During attempts to extract coinage metal from the manganese analogue, $Sr_2MnO_2Cu_2S_2$, Sasaki discovered that the use of a small amount of solvent with the disulfiram oxidant

initially led to better copper dissolution before adding the full portion of solvent of approximately 40 cm^3 and stirring overnight at room temperature.[70]

The powder was then filtered and washed with anhydrous THF until the filtrate was colourless, this tended to require multiple cycles and was often left sitting overnight in THF.

After the final filtration and drying for 1 hour under dynamic vacuum, the powder was transferred to the glovebox and X-rayed to determine the quantity of copper that had been removed.

The whole procedure was repeated until on reaction with *n*-BuLi, no more Bragg peaks that could be assigned to elemental copper were observed, indicating that no more extrusion of coinage metal by lithiation was achievable. The full procedure is outlined in section 2.1.4.

There was a large loss of product due to the extensive washing on using disulfiram and so for the Cu-containing neutron samples, following the final lithiation, from which it was known from previous experiments that further treatment with *n*-BuLi after disulfiram treatment would not induce any more cation exchange, the extruded copper was not removed and hence there is some residual elemental copper remaining in the samples.

This cycling technique allowed more Cu to be removed / exchanged than was previously achieved by I_2 alone as the use of disulfiram appears to prefer Cu oxidation as opposed to Li extraction which is at odds with the use of I_2, which preferentially removes Li, allowing for the reinsertion of some Cu on repeated treatments.

4.2.2 PXRD / PND

The changes in the amount of extruded Cu was observed through Rietveld refinement as by assuming full occupation of the tetrahedral site, the scattering should be able to give an accurate measure of the Cu content.

This was confirmed independently by looking at the ratio of the coinage metal to the main phase (assuming all phases are crystalline) which is outputted in TOPAS Academic V6[95] and calculated as outlined in section 2.1.4 and more specifically equation 2.4. Because the difference in the ionic radii between Li^+ and Cu^+ is not very large, changes in the lattice parameters are small, so they are not a very good proxy for the composition.

Table 4.1 Structural Model for $Sr_2CoO_2Cu_{2-x}Li_xCh_2$ (*Ch* = S, Se).

Atom	Position	*x*	*y*	*z*
Sr	4*e*	0.5	0.5	*z*Sr
Co	2*a*	0	0	0
O	4*d*	0.5	0	0
Cu	4*c*	0.5	0	0.25
Li	4*c*	0.5	0	0.25
Ch	4*e*	0	0	*z*Ch
Space group = *I*4/*mmm*				

$Sr_2CoO_2Cu_{2-x}Li_xS_2$

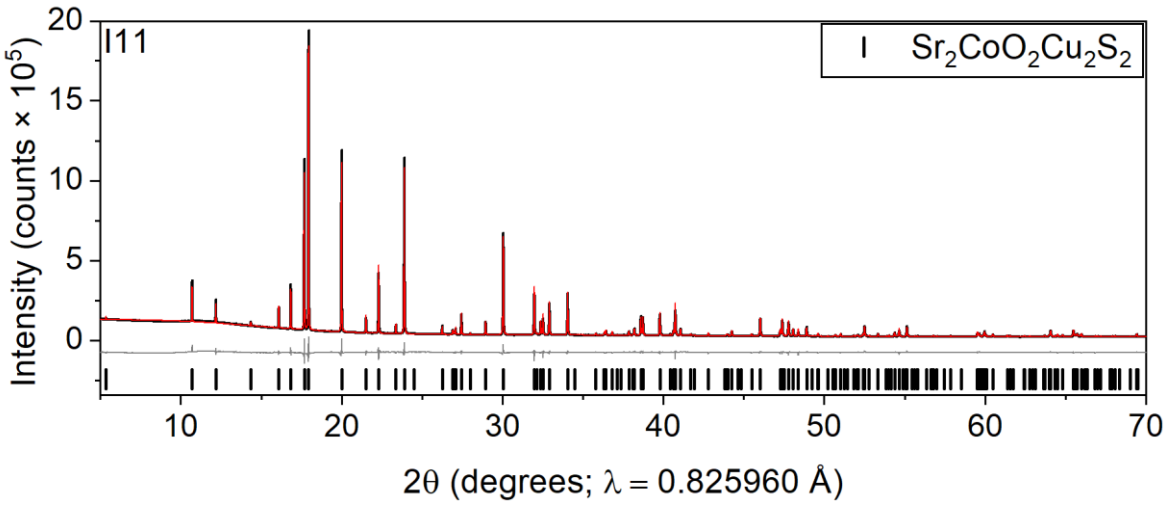


Figure 4.2 Rietveld refinement of $Sr_2CoO_2Cu_2S_2$ from data collected on the I11 beamline at Diamond Light Source Ltd. R_{wp} = 3.761 %; χ^2 = 8.290.

Due to the Cu containing $Sr_2CoO_2Cu_2Ch_2$ (*Ch* = S, Se) compounds being more resistant to the cycling technique than their Mn oxide chalcogenides counterparts, the collapsed phase[70] with all metal ions removed from the chalcogenide layers could not be realised and hence for both, for the most lithiated phase, a modified *I*4/*mmm* model as used for the parent material reflecting Li / Cu exchange was used with the model shown in Table 4.1. This gave a good visual and statistical fit to all of the data.

The parent material used to perform soft chemical manipulations targeting the lithiated sulfide was prepared as previously demonstrated in the literature[40] with Rietveld refinement of $Sr_2CoO_2Cu_2S_2$ shown in Figure 4.2.

On the first cycle with *n*-BuLi, it was clear from Rietveld refinement that Li / Cu exchange had occurred, owing to the appearance of Bragg peaks that could be assigned to elemental Cu. On inspection of the diffraction peaks as shown in Figure 4.3(a), along with the main peak, some of the less intense peaks were seemingly split and there was not good agreement

between the data and a single, lithiated phase which in this case refined to a Cu occupancy of 0.71(1) i.e., of nominal composition $Sr_2CoO_2Cu_{1.42(2)}Li_{0.58(2)}S_2$.

However, refining this partially lithiated phase along with a phase that matched the parent material, with the same lattice parameters as refined from SPXRD data (see Table 4.2 and 4.3) and a Cu occupancy of 0.98 in the sulfide layer which was not allowed to refine, gave a good fit to the data with the result shown in Figure 4.3(b).

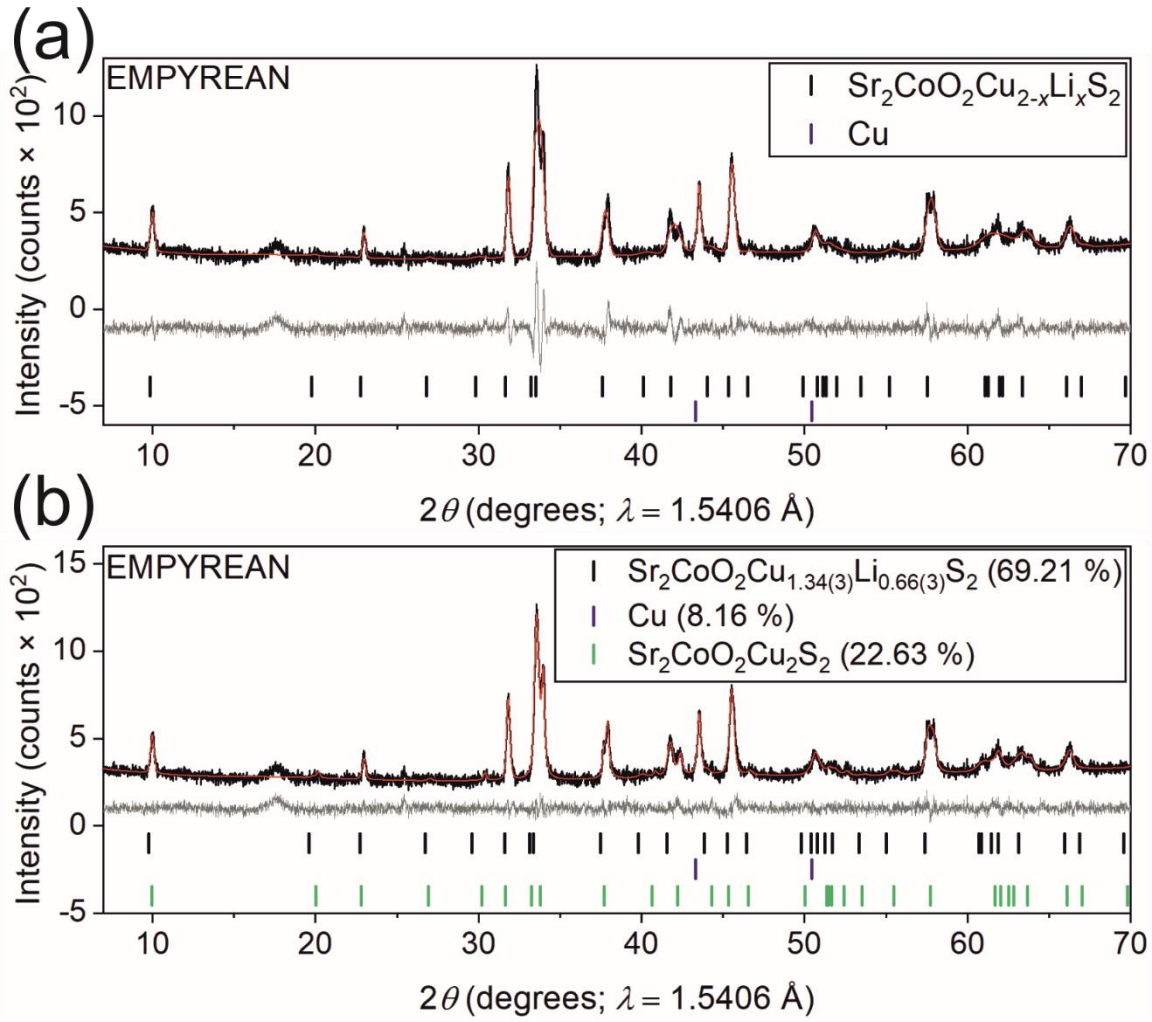


Figure 4.3(a) Rietveld refinement of $Sr_2CoO_2Cu_{1.42(2)}Li_{0.58(2)}S_2$ from data collected on the ICL PANalytical Empyrean with only one phase. R_{wp} = 7.799 %; χ^2 = 1.414. **(b)** Rietveld refinement of $Sr_2CoO_2Cu_{1.34(3)}Li_{0.66(3)}S_2$ from data collected on the ICL PANalytical Empyrean including refinement of the parent. R_{wp} = 6.462 %; χ^2 = 1.171. Note that the hump at ≈ 18 ° is an instrumental artefact.

Mass analysis of the weight %, which is outputted during Rietveld refinement of the crystalline products, allowed for the stoichiometry of each element to approximately be determined with the calculated result (normalised to Cu) being Sr:Co:O:Cu:S = 1.91:0.96:1.91:2:1.91 and thus the mass balance is maintained from this result.

Once the elemental Cu had been oxidised and chelated with disulfiram and removed from the sample, a further lithiation followed by more oxidation/chelation and washing away of the extruded Cu was performed resulting in a single phase of the lithiated sulfide as shown below in Figure 4.4.

Due to the loss of material during transfer between various containers during the soft-chemistry performed, it was decided that one further lithiation would be performed without the follow-up with disulfiram as previous experiments had shown another treatment with *n*-BuLi did not induce any more cation exchange. This maximised the Li / Cu exchange whilst minimising the amount of material lost allowing for greater availability of sample for neutron diffraction which requires greater amounts than X-ray diffraction for better counting statistics.

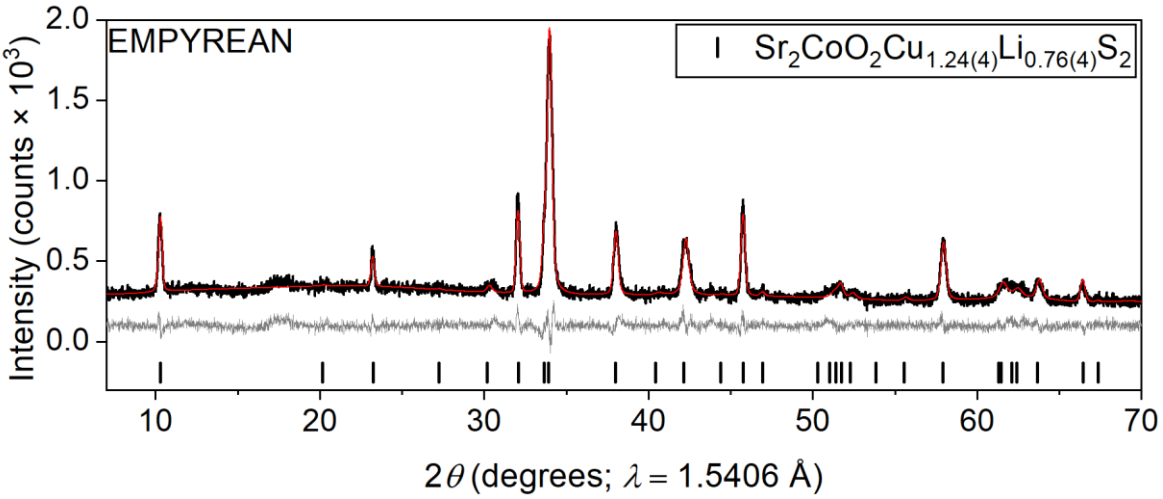


Figure 4.4 Rietveld refinement of $Sr_2CoO_2Cu_{1.24(4)}Li_{0.76(4)}S_2$ from data collected on ICL PANalytical Empyrean. R_{wp} = 6.325 %; χ^2 = 1.154.

As pointed out earlier, Li^+ and Cu^+ are similar in size and this is emphasised in Table 4.2 and Table 4.3 which shows the parent $Sr_2CoO_2Cu_2S_2$ compared to the most lithiated compound produced during *n*-BuLi / disulfiram cycling and how similar their refined parameters are.

Table 4.2 Comparison of lattice parameters for $Sr_2CoO_2Cu_{2-x}Li_xS_2$.

Sample	$Sr_2CoO_2Cu_2S_2$	$Sr_2CoO_2Cu_{1.24(4)}Li_{0.76(4)}S_2$	$Sr_2CoO_2Cu_{1.214(8)}Li_{0.786(8)}S_2$
Radiation	X-ray	X-ray	Neutron
Diffractometer	I11	Empyrean	GEM
a (Å)	3.98141(3)	3.9967(3)	3.9909(7)
c (Å)	17.6662(1)	17.807(2)	17.804(4)
Volume (Å^3)	280.039(5)	284.45(6)	283.570(4)

Although the X-ray scattering of Li is weak and Li cannot be accurately located with this technique, the assumption that the lithiated phases have fully occupied sites in the chalcogenide layer enables this technique to be used to determine the composition. Neutrons, which scatter more strongly from Li, give an independent measure of the Li:Cu ratio on these sites.

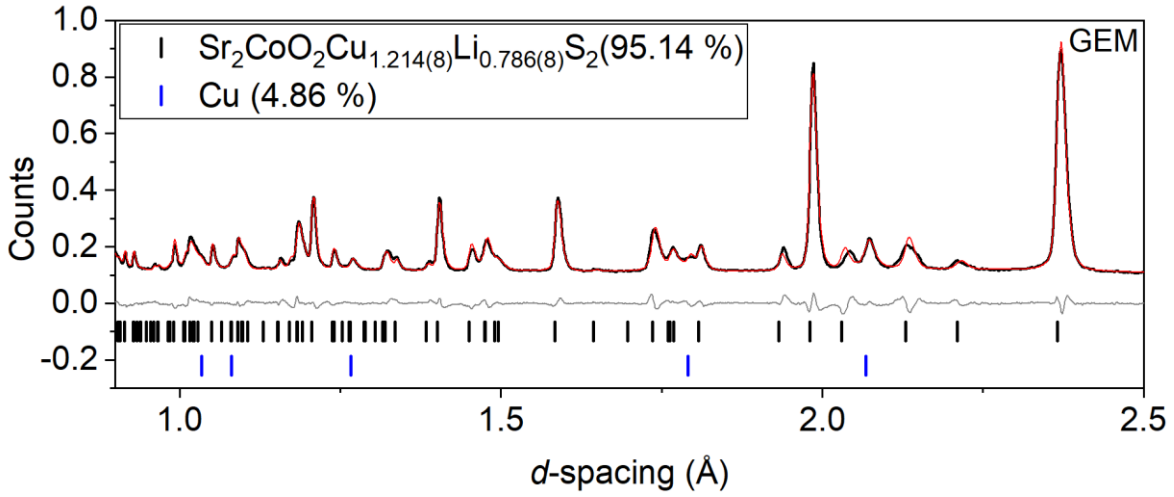


Figure 4.5 Rietveld refinement of $Sr_2CoO_2Cu_{1.214(8)}Li_{0.786(8)}S_2$ from data collected on bank 5 of the GEM diffractometer at the ISIS neutron and muon source at room temperature. R_{wp} = 4.202 %; χ^2 = 0.007.

For all the compounds investigated within this chapter there was excellent agreement between the two complementary techniques. In addition, neutrons enabled the magnetic structures to be determined. Rietveld refinement of $Sr_2CoO_2Cu_{1.214(8)}Li_{0.786(8)}S_2$ from bank 5 of the GEM diffractometer shown in Figure 4.5.

Table 4.3 Comparison of refined parameters for $Sr_2CoO_2Cu_{2-x}Li_xS_2$.

Sample	$Sr_2CoO_2Cu_2S_2$	$Sr_2CoO_2Cu_{1.24(4)}Li_{0.76(4)}S_2$	$Sr_2CoO_2Cu_{1.214(8)}Li_{0.786(8)}S_2$
Radiation	X-ray	X-ray	Neutron
Diffractometer	I11	Empyrean	GEM
z(Sr)	0.09263(2)	0.0917(2)	0.09145(7)
z(S)	0.17095(5)	0.1718(6)	0.1715(2)
Cu occupancy	0.980(2)	0.62(2)	0.607(4)
Li occupancy	N/A	0.38(2)	0.393(4)
Sr U_{11} (Å^2)	0.0061(2)	0.010(3)	0.0041(2)
Sr U_{33} (Å^2)	0.0061(2)	0.010(3)	0.0061(5)
Co U_{11} (Å^2)	0.0078(2)	0.013(1)	0.0005(3)
Co U_{33} (Å^2)	0.0078(2)	0.013(1)	0.0001(5)
O U_{11} (Å^2)	0.0079(6)	0.018(2)	0.0076(3)
O U_{22} (Å^2)	0.00794(6)	0.018(2)	0.0051(4)
O U_{33} (Å^2)	0.0079(6)	0.018(2)	0.0186(6)
Cu U_{11} (Å^2)	0.0176(2)	0.024(4)	0.0010(2)
Cu U_{33} (Å^2)	0.0176(2)	0.024(4)	0.0321(7)
Li U_{11} (Å^2)	N/A	0.034(3)	0.053(2)
Li U_{33} (Å^2)	N/A	0.034(3)	0.02(1)
S U_{11} (Å^2)	0.0064(2)	0.013(2)	0.015(2)
S U_{33} (Å^2)	0.0064(2)	0.013(2)	0.129(4)
R_{wp} (%)	3.761	6.325	4.198
χ^2	8.290	1.154	0.007

Note that X-ray data was treated isotropically where $U_{11} = U_{22} = U_{33}$.

$Sr_2CoO_2Cu_{2-x}Li_xSe_2$

For the selenide, again, the parent was synthesised as previously reported resulting in a phase pure product as shown in Figure 4.6.[40]

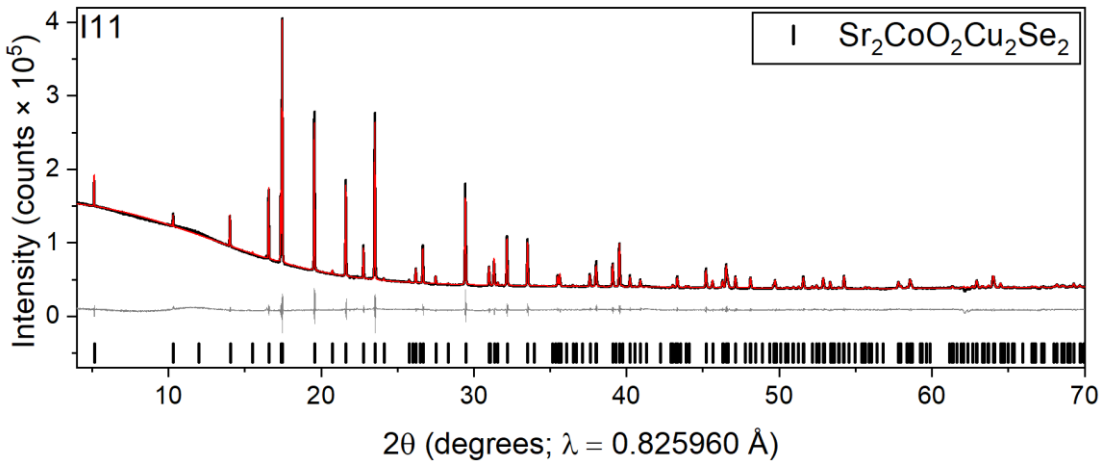


Figure 4.6 Rietveld refinement of $Sr_2CoO_2Cu_2Se_2$ from data collected on the I11 beamline at Diamond Light Source Ltd. R_{wp} = 1.761 %; χ^2 = 4.209.

Similar to what was observed with the sulfide, initial reaction with *n*-BuLi resulted in the diffractogram as shown in Figure 4.7, which again indicated a bi-phasic mixture with one phase fixed to the parent, $Sr_2CoO_2Cu_2Se_2$ and the other indicating Li / Cu exchange had taken place as would be expected with the appearance of Cu Bragg peaks. Mass analysis of the phase fractions resulted in a Sr:Co:O:Cu:Se = 2.10:1.05:2.10:2:2.10.

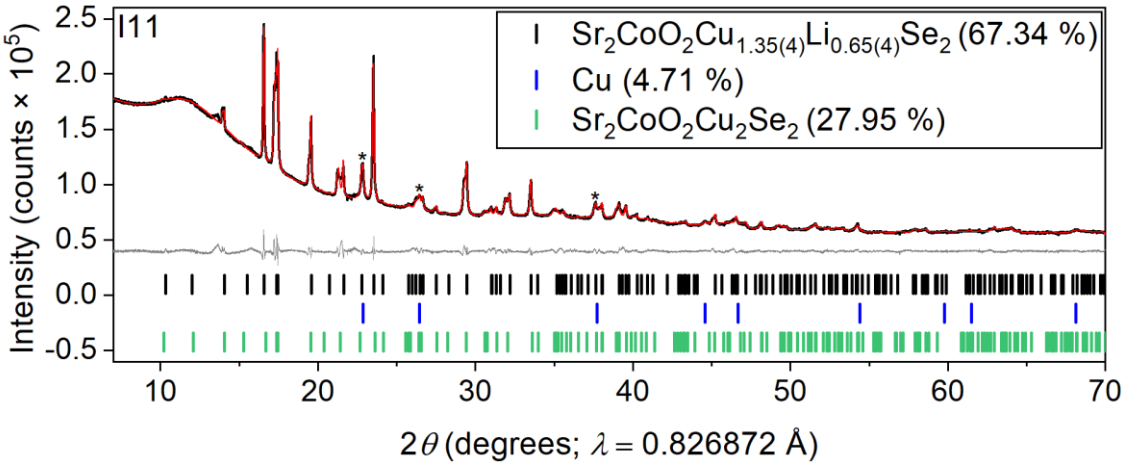


Figure 4.7 Rietveld refinement of $Sr_2CoO_2Cu_{1.35(4)}Li_{0.65(4)}Se_2$ from data collected on the I11 beamline at Diamond Light Source Ltd. R_{wp} = 1.207 %; χ^2 = 3.673.

Further cycling as outlined in the experimental section allowed for a pure sample of the lithiated phase which was then prepared for synchrotron X-ray diffraction as outlined in section 2.2.2.3 with the resulting Rietveld refinement shown in Figure 4.8.

Again, X-ray diffraction can only tell how much scattering there is on the tetrahedral site. Despite Li not scattering X-rays strongly, assuming this site is fully occupied by Cu and Li following the lithiation, the value of *x* can be derived from Rietveld refinement allowing the composition to be determined unambiguously.

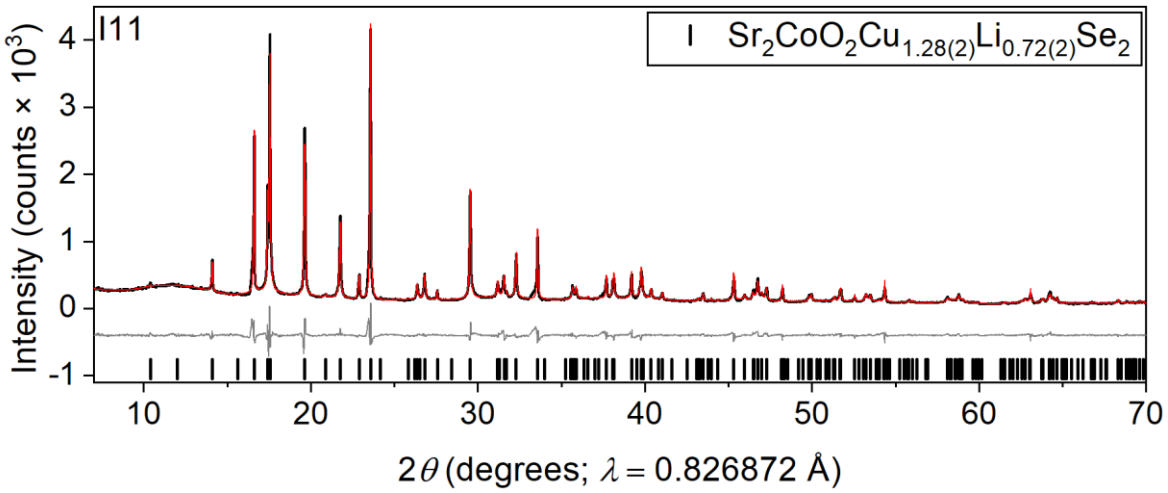


Figure 4.8 Rietveld refinement of $Sr_2CoO_2Cu_{1.28(2)}Li_{0.72(2)}Se_2$ from data collected on the I11 beamline at Diamond Light Source Ltd. R_{wp} = 8.672 %; χ^2 = 1.722.

Similar to the sulfide, previous experiments had shown how many cycles were required to reach the limit of Cu / Li exchange and could be reliably reproduced. In this knowledge, due to the loss of material using the disulfiram route, one less reaction with disulfiram could be planned for, maximising the material available for PND.

Rietveld refinement of the lithiated sample against bank 5 of the GEM diffractometer at ISIS is shown in Figure 4.9.

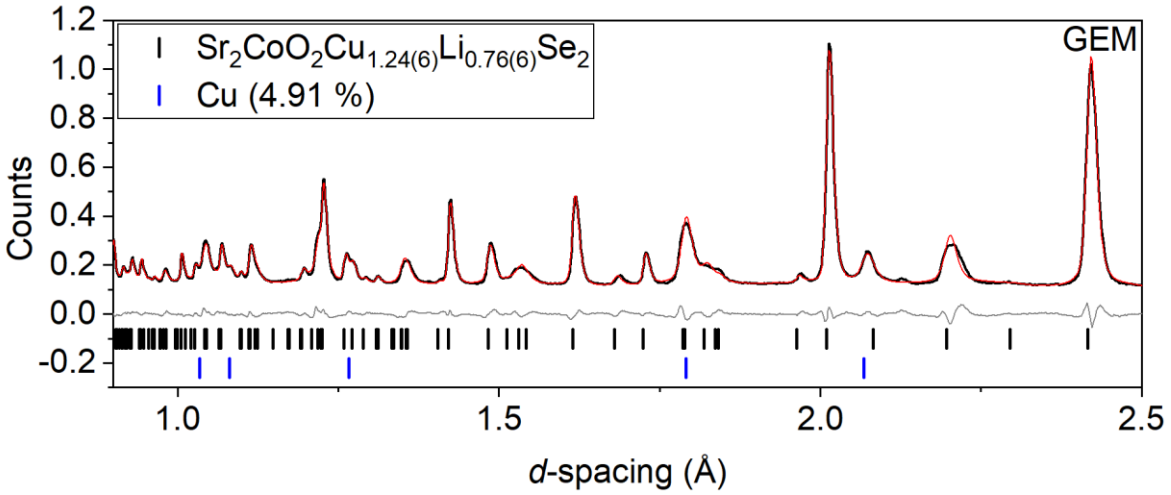


Figure 4.9 Rietveld refinement of $Sr_2CoO_2Cu_{1.24(6)}Li_{0.76(6)}Se_2$ from data collected on bank 5 of the GEM diffractometer at the ISIS neutron and muon source at room temperature. R_{wp} = 3.421 %; χ^2 = 0.007.

Table 4.4 Comparison of lattice parameters for $Sr_2CoO_2Cu_{2-x}Li_xSe_2$.

Sample	$Sr_2CoO_2Cu_2Se_2$	$Sr_2CoO_2Cu_{1.28(2)}Li_{0.72(2)}Se_2$	$Sr_2CoO_2Cu_{1.24(6)}Li_{0.76(6)}Se_2$
Radiation	X-ray	X-ray	Neutron
Diffractometer	I11	I11	GEM
a (Å)	4.05005(8)	4.0441(2)	4.0423(3)
c (Å)	18.3506(4)	18.2177(9)	18.297(2)
Volume (Å^3)	301.00(1)	297.94(3)	298.97(5)

It can be seen from Tables 4.4 and 4.5, similar to the sulfide analogue, that due to the small size difference of Cu^+ and Li^+ that the structural model is actually quite similar for both the parent and lithiated phase. X-ray and neutron powder diffraction both give excellent agreement regarding the composition.

Table 4.5 Comparison of refined parameters for $Sr_2CoO_2Cu_{2-x}Li_xSe_2$.

Sample	$Sr_2CoO_2Cu_2Se_2$	$Sr_2CoO_2Cu_{1.28(2)}Li_{0.72(2)}Se_2$	$Sr_2CoO_2Cu_{1.24(6)}Li_{0.76(6)}Se_2$
Radiation	X-ray	X-ray	Neutron
Diffractometer	I11	I11	GEM
z(Sr)	0.08843(4)	0.0899(2)	0.08750(6)
z(Se)	0.16761(4)	0.1684(2)	0.16814(7)
Cu occupancy	0.9966(3)	0.64(2)	0.62(3)
Li occupancy	N/A	0.36(2)	0.38(3)
Sr U_{11} (Å^2)	0.0024(3)	0.010(3)	0.0031(2)
Sr U_{33} (Å^2)	0.0024(3)	0.010(3)	0.0097(3)
Co U_{11} (Å^2)	0.0013(4)	0.004(3)	0.005(1)
Co U_{33} (Å^2)	0.0013(4)	0.004(3)	0.005(2)
O U_{11} (Å^2)	0.005(1)	0.005(6)	0.011(1)
O U_{22} (Å^2)	0.005(1)	0.005(6)	0.043(2)
O U_{33} (Å^2)	0.005(1)	0.005(6)	0.022(2)
Cu U_{11} (Å^2)	0.0150(4)	0.006(6)	0.034(2)
Cu U_{33} (Å^2)	0.0150(4)	0.00(6)	0.022(3)
Li U_{11} (Å^2)	N/A	0.019(4)	0.0231(5)
Li U_{33} (Å^2)	N/A	0.019(4)	0.0322(3)
Se U_{11} (Å^2)	0.0028(3)	0.008(3)	0.000(3)
Se U_{33} (Å^2)	0.0028(3)	0.008(3)	0.006(2)
R_{wp} (%)	1.761	8.678	4.501
χ^2	4.208	1.724	0.009

Note that X-ray data was treated isotropically where $U_{11} = U_{22} = U_{33}$.

4.2.3 Variable temperature SPXRD

Variable temperature SPXRD data was collected on the I11 beamline[83] at The Diamond Light Source for $Sr_2CoO_2Cu_{2-x}Li_xSe_2$. The other 3 samples in this chapter were all prepared

for data collection also, but unfortunately were not collected / unusable which was most likely due to air exposure due to a failed capillary or possibly beam damage of the sample.

Despite this, these samples are likely sufficiently similar that this data can be representative of the lithiated series. As seen below in Figure 4.10, within error there are no obvious anomalies in the dependences and as such the trends seen can be explained by thermal expansion of the sample.

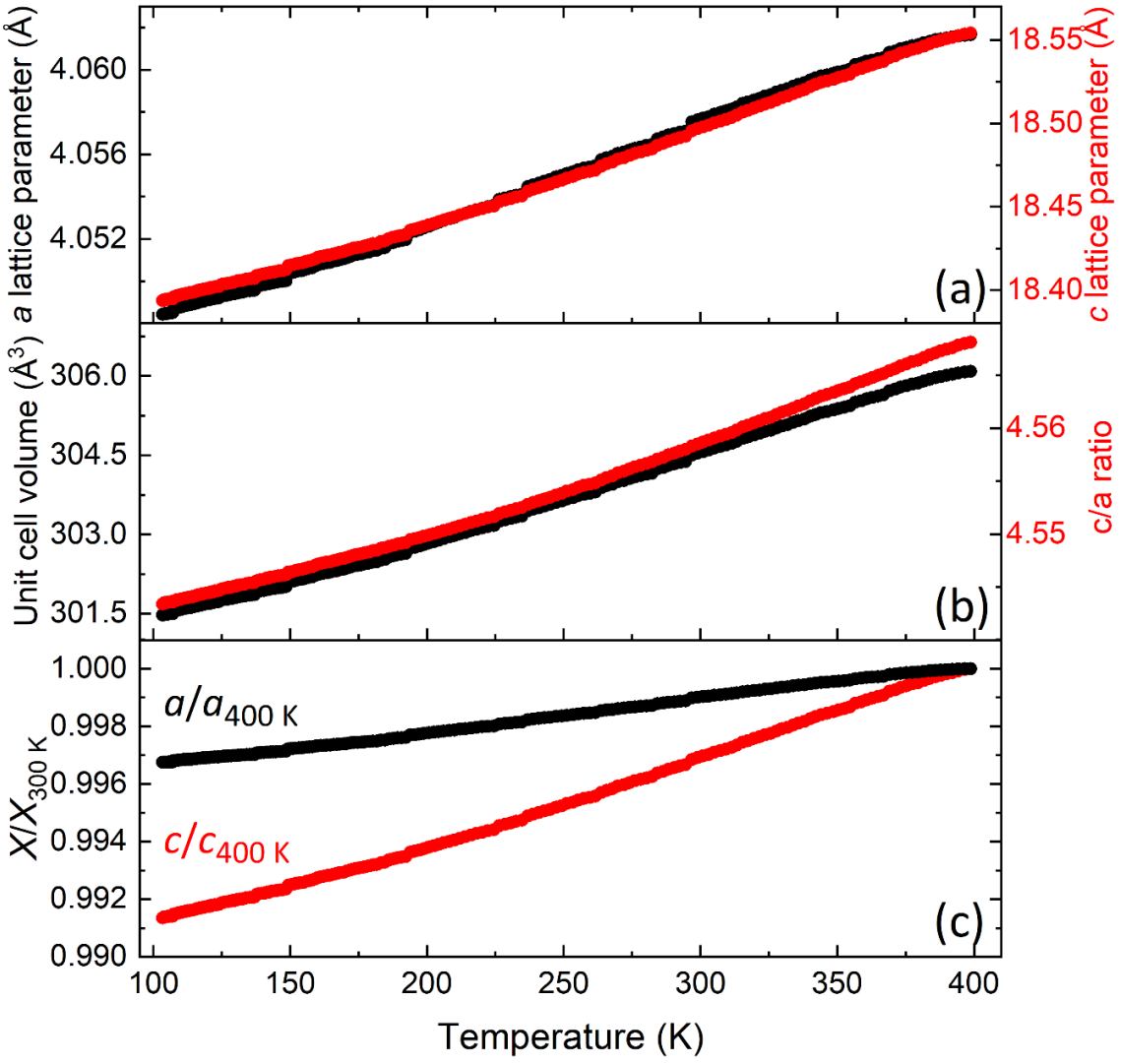


Figure 4.10 Refined structural parameters for $Sr_2CoO_2Cu_{2-x}Li_xSe_2$ from I11 data.

4.2.4 Magnetometry

Magnetometry measurements were performed on these samples to see if there were any changes to the magnetic susceptibility after the reductive treatment during the synthesis.

Due to the nature of the synthetic strategy for these phases, it was not uncommon for trace amounts of ferromagnetic impurities such as Co to arise which was visible in low field of *M vs H* plots and so it was necessary to perform a 6 / 5 T subtraction as outlined in section 2.2.7.1 for all of the measurements to compliment the ZFC / FC measurements at 100 Oe. These additional plots can be seen in Appendix E.1.

At high fields, this curve was linear and hence the moment of the magnetic impurity was saturated which allowed for *M vs T* to be measured twice at fields higher than the saturation field of the impurity and then the resulting magnetisation at the higher field subtracted from the analogous result at the lower field. This gives the intrinsic moment of the paramagnetic or antiferromagnetic phases present in the sample by effectively eliminating the contribution of the magnetic impurity that were clearly obvious in *M vs H* plots at low field. These plots can be seen in Appendix E.2.

No useful information was able to be extracted from attempted Curie-Weiss analysis because these materials magnetically order close enough to room temperature that the inverse relationship in the paramagnetic regime seen for those samples that obey the Curie-Weiss law does not apply. This could be overcome by changing the magnetometer set-up to the oven function but was deemed unnecessary due to the availability of neutron diffraction data and the fact that the lithiated samples are not synthesised at elevated temperatures and hence may decompose.

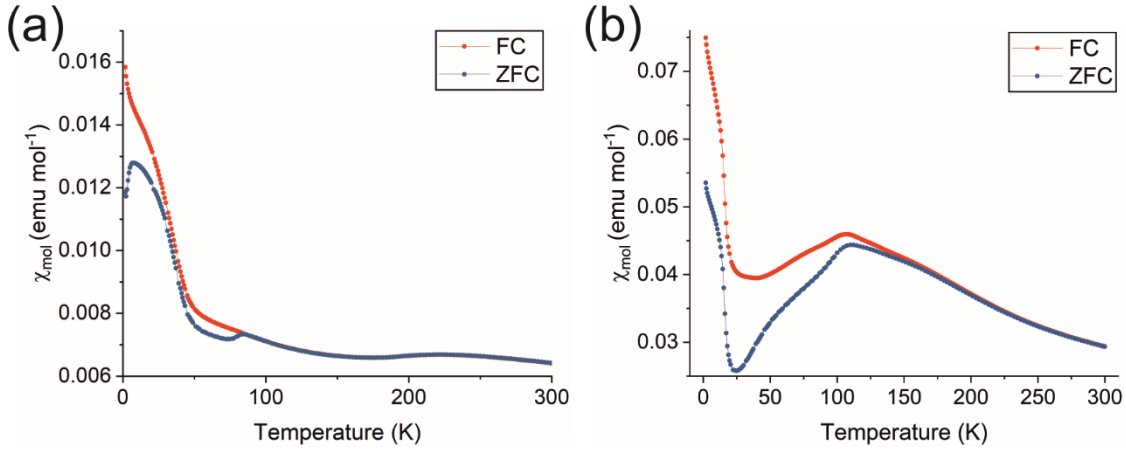


Figure 4.11 ZFC and FC magnetic susceptibility curves of **(a)** $Sr_2CoO_2Cu_2S_2$ and **(b)** $Sr_2CoO_2Cu_{2-x}Li_xS_2$ measured in a field of 100 Oe.

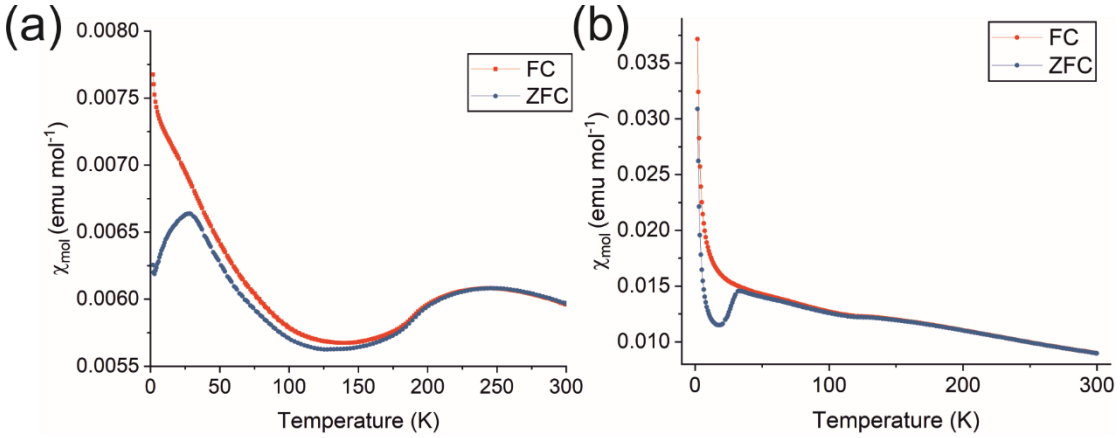


Figure 4.12 ZFC and FC magnetic susceptibility curves of **(a)** $Sr_2CoO_2Cu_2Se_2$ and **(b)** $Sr_2CoO_2Cu_{2-x}Li_xSe_2$ measured in a field of 100 Oe.

It is difficult to draw conclusions from the magnetometry data from both Figures 4.11 and 4.12. Both "parent" compounds have broad cusps near room temperature indicating reduced dimensionality and antiferromagnetic ordering which has since been confirmed by neutron diffraction data (discussed later in section 4.2.5).

The two lithiated "daughter" compounds have their corresponding transitions at a lower temperature than the parent materials and also have a χ_{mol} which is almost an order of magnitude larger, with the magnitude likely due to the ferromagnetic impurity which is yet

to saturate at the measurement field of 100 Oe, the corresponding high-field subtractions can be seen in Appendix E.1.

A common characteristic for both is the divergence between the ZFC and FC plots indicating a glassy component to the magnetism which as discussed in section 4.4, has repercussions for the size of the long-range ordered moment in these lithiated materials.

Figure 4.13 shows the magnetisation isotherms measured at 5 K which are displaced from the origin and do not close up at high fields which confirms that that there is a glassy component to the magnetism, but it is difficult to ascertain how much contribution there is from the sample and how much is from an impurity phase.

Despite this ambiguity, as shown in the next section, it cannot be true that these materials are pure glasses due to the presence of long-range magnetic order.

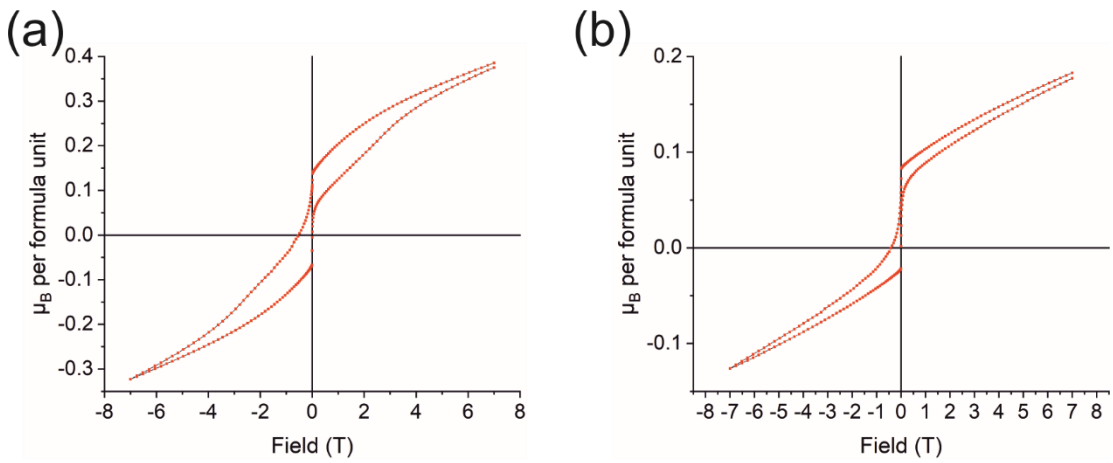


Figure 4.13 *M* vs *H* isotherms of **(a)** $Sr_2CoO_2Cu_{2-x}Li_xS_2$ and **(b)** $Sr_2CoO_2Cu_{2-x}Li_xSe_2$ measured at 5 K in the range $-5 \leq H\,(\mathrm{T}) \leq +5$.

4.2.5 Low temperature PND to probe magnetic ordering

Approximately 2 g of both $Sr_2CoO_2Cu_{1.214(8)}Li_{0.786(8)}S_2$ and $Sr_2CoO_2Cu_{1.24(6)}Li_{0.76(6)}Se_2$ were measured using PND on the GEM diffractometer at the ISIS facility at 5 K to deduce the magnetic structure of these lithiated phases and compare them to related structural analogues.

As suggested by the magnetometry measurements in section 4.2.4, it was predicted that these phases would magnetically order and it was seen that there were additional peaks to those from the nuclear structure at low temperature and in the high *d*-spacing region, suggesting that they were magnetic in origin and most likely due to antiferromagnetic ordering due to the profile of the susceptibility and its magnitude.

These peaks could be indexed on a $\sqrt{2}a \times \sqrt{2}a \times c$ expansion of the unit cell, suggesting that the primary interaction between the spins was nearest-neighbour antiferromagnetic coupling within the CoO_2 planes.

The resulting Rietveld refinements of both $Sr_2CoO_2Cu_{1.214(8)}Li_{0.786(8)}S_2$ and $Sr_2CoO_2Cu_{1.24(6)}Li_{0.76(6)}Se_2$ are shown below in Figure 4.14.

To obtain the fits to the magnetic peaks in Figure 4.14, the data was initially analysed in *P*1 symmetry using ISODISTORT.[124] Using *P*1 allows for all possible modes to be considered before searching for a higher symmetry space group.

Consistent with their "parent" compounds, the magnetic intensity could be accounted for using a combination of the mX3+ and mX4+ modes which as shown below visually in Figure 4.15, represents antiferromagnetic coupling within the *ab*-plane with the refined long-range

ordered magnetic moments on the Co^{2+} ions shown in Table 4.6 of 3.41(4) μ_B and 3.21(7) μ_B for $Sr_2CoO_2Cu_{1.214(8)}Li_{0.786(8)}S_2$ and $Sr_2CoO_2Cu_{1.24(6)}Li_{0.76(6)}Se_2$ respectively. Consistent with previously reported, closely related analogues with elongated CoO_4X_2 octahedra, this is larger than the predicted spin-only value for Co^{2+} of 3 μ_B with the possibilities behind this discussed further in section 4.4.

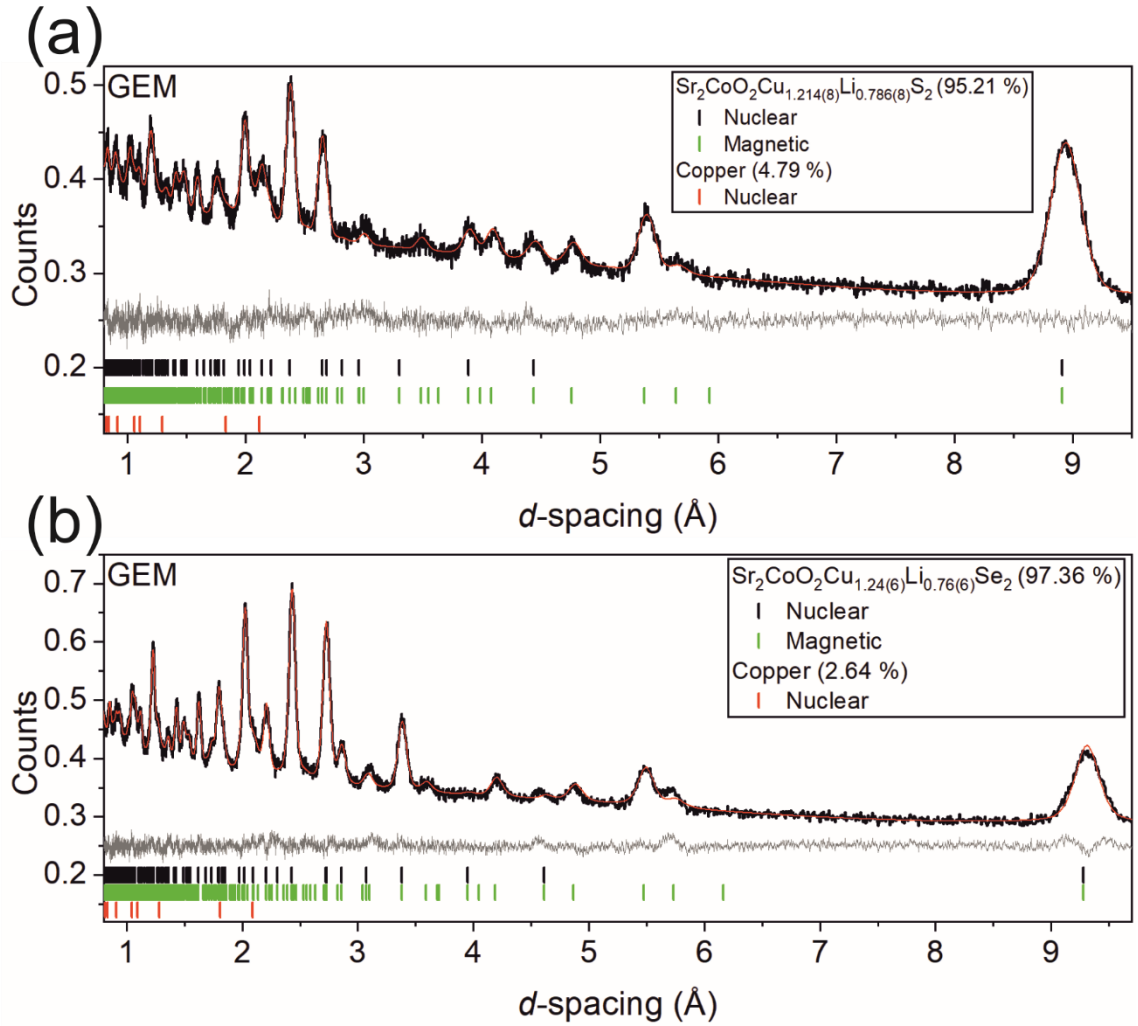


Figure 4.14(a) Rietveld refinement of $Sr_2CoO_2Cu_{1.214(8)}Li_{0.786(8)}S_2$. R_{wp} = 2.071 %; χ^2 = 0.008 and **(b)** Rietveld refinement of $Sr_2CoO_2Cu_{1.24(6)}Li_{0.76(6)}Se_2$. R_{wp} = 1.908 %; χ^2 = 0.007 collected at 5 K on the GEM diffractometer at the ISIS pulsed neutron and muon source.

Searching over specific *k*-points in ISODISTORT relating to the mX3+ and mX4+ mode yielded the tetragonal magnetic space group P_C4_2/n (86.73) in the Belov, Neronova and

Smirnova (BNS) scheme or the *P*$_P$*4*$_2$*/m'* magnetic space group (84.7.719) in the Opechowski and Guccione (OG) scheme[125] as the highest-symmetry magnetic space group that could account for the observed magnetic intensity from the PND data.

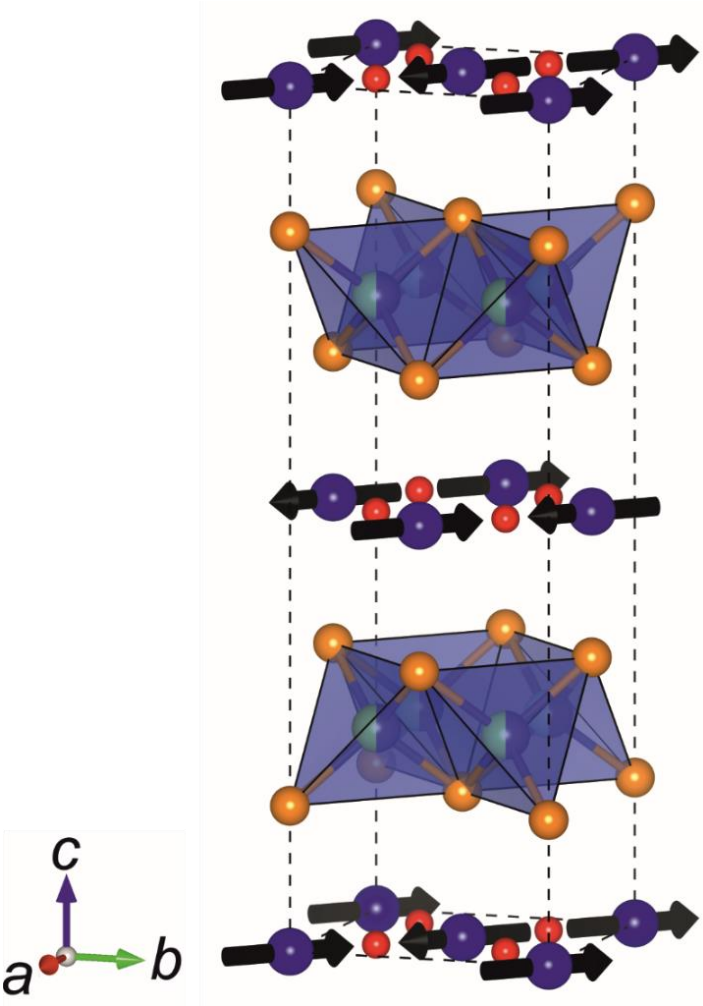


Figure 4.15 The magnetic structure of $Sr_2CoO_2Cu_{2-x}Li_xCh_2$ (*Ch* = S, Se).

Table 4.6 Refined parameters for the magnetic ordering of $Sr_2CoO_2Cu_{2-x}Li_xCh_2$ (*Ch* = S, Se) measured at 5 K using PND on the GEM diffractometer at ISIS.

	$Sr_2CoO_2Cu_{1.214(8)}Li_{0.786(8)}S_2$	$Sr_2CoO_2Cu_{1.24(6)}Li_{0.76(6)}Se_2$
μ_a (μ_B)	1.03(3)	0.74(5)
μ_b (μ_B)	3.25(5)	3.12(6)
$\lvert\mu\rvert$ (μ_B)	3.41(4)	3.21(7)

4.2.6 XANES

The changes in the cobalt oxidation states were measured using synchrotron XANES on the B18 beamline at the Diamond Light Source.[100] The plan was to compare the parent materials with their "daughter" compounds synthesised under reducing conditions (this work) and oxidising conditions (synthesised by Blandy).[40]

The spectra for $Sr_2CoO_2Cu_{2-x}Li_xCh_2$ (*Ch* = S, Se) are shown below in Figure 4.16. Unfortunately, the datasets for $Sr_2CoO_2Cu_{1.214(8)}Li_{0.786(8)}S_2$ and $Sr_2CoO_2Cu_{1.89(4)}Se_2$ were blank and not measured during the experiment so cannot be included here.

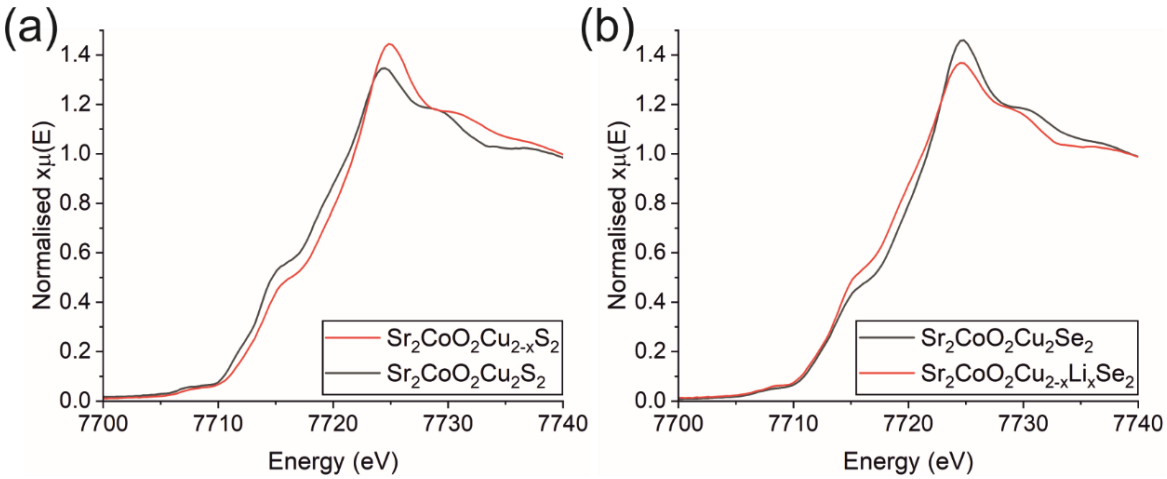


Figure 4.16 Co K-edge XANES spectra for $Sr_2CoO_2Cu_{2-x}Li_xCh_2$ (*Ch* = S, Se).

As outlined in section 2.2.6, XANES is incredibly useful for probing oxidation state changes between samples and here it would be expected that oxidation of Co^{2+} would lead to a shift of the absorption edge to higher energy whereas reduction would lead to a shift to lower energy and for these compounds, the first part of the edge was assumed to be an indicator of the Co^{2+} oxidation state.

For $Sr_2CoO_2Cu_{2-x}S_2$, it is clear from Figure 4.16(a) that reaction of $Sr_2CoO_2Cu_2S_2$ with iodine (i.e., oxidising conditions) leads to a clear shift to higher energy and so the average oxidation state of Co is greater than 2.

The reaction of $Sr_2CoO_2Cu_2Se_2$ with *n*-BuLi leads to Cu / Li exchange which keeps the tetrahedral site fully occupied and therefore the Co oxidation state should remain at +2 and as can be seen in Figure 4.16(b), the feature at the beginning of the edge remains the same for both the parent sample and the lithiated phase consistent with the Co oxidation state remaining constant.

4.3 Li / Ag exchange in $Ae_2CoO_2Ag_2Se_2$ (*Ae* = Sr, Ba)

4.3.1 Synthesis and cycling

Parent samples of $Ae_2CoO_2Ag_2Se_2$ (*Ae* = Sr, Ba) were synthesised from either SrO (obtained via thermal decomposition under dynamic vacuum of $SrCO_3$ (Alfa 99.994 %), at initially 840 °C with a final treatment at 1100 °C) or BaO which was synthesised from the thermal decomposition of $BaCO_3$ (Alfa 99.997 %), under vacuum with repeat treatments at 950 °C and a final heating at 1100 °C with the full procedures for both outlined in section 2.1.3.1, Co (Alfa 99.998 %), Ag (Alfa 99.99 %), and Se (Alfa 99.999 %).

Both were preheated at 640 °C, ramping up the temperature at 10 °C min^{-1}, for 12 hours before a final heating at 840 °C for 48 hours. The general experimental procedure for solid-state synthesis is outlined in section 2.1.1.

The procedure for obtaining the soft-chemical products is outlined in section 2.1.4 and for the Ag-containing $Ae_2CoO_2Ag_2Se_2$ (*Ae* = Sr, Ba) compounds, involves the repeated treatment of the parent material under an inert atmosphere with *n*-BuLi (1.6 M in hexanes) for 3 days at 50 ºC.

No alternative to disulfiram could be found in order to chelate Ag and remove it from the mixture. As such, the end of the reaction was judged to be when in the normalised diffractograms, there was no change in the magnitude of the elemental Ag peaks which tended to be after 2 or 3 cycles.

4.3.2 PXRD / PND

Due to the much larger disparity in size between Ag^+ and Li^+, for these compounds it was much clearer to see how much Ag had been extruded visually by looking at the lattice parameters which contracted causing an obvious shift to higher angle of the Bragg reflections. As well as the extracted value from Rietveld refinement for the Ag occupancy of the tetrahedral sites, it was again useful to calculate the mass of Ag extruded as outlined in equation 2.4 of section 2.1.4 as an independent measure of the amount of extruded Ag (assuming all phases are crystalline).

The model used for Rietveld refinement of these phases was similar to that of the Cu analogues and is shown below in Table 4.7.

Table 4.7. Structural Model for $Ae_2CoO_2Ag_{2-x}Li_xSe_2$.

Atom	Position	*x*	*y*	*z*
Ae	4*e*	0.5	0.5	*z*Ae
Co	2*a*	0	0	0
O	4*d*	0.5	0	0
Ag	4*c*	0.5	0	0.25
Li	4*c*	0.5	0	0.25
Se	4*e*	0	0	*z*Se
Space group = *I*4/*mmm*				

The reaction was mostly complete after one cycle but it was found that subsequent treatment was able to extrude a little more Ag. Presumably, this is similar to when the reaction is done with I_2 where some coinage metal can go back into the structure as Li is preferentially removed from the structure.

$Sr_2CoO_2Ag_{2-x}Li_xSe_2$

First of all, looking at the Sr analogue, the parent material used to perform soft chemical manipulations on was prepared as previously demonstrated in the literature[20] with Rietveld refinement of $Sr_2CoO_2Ag_2Se_2$ shown in Figure 4.17.

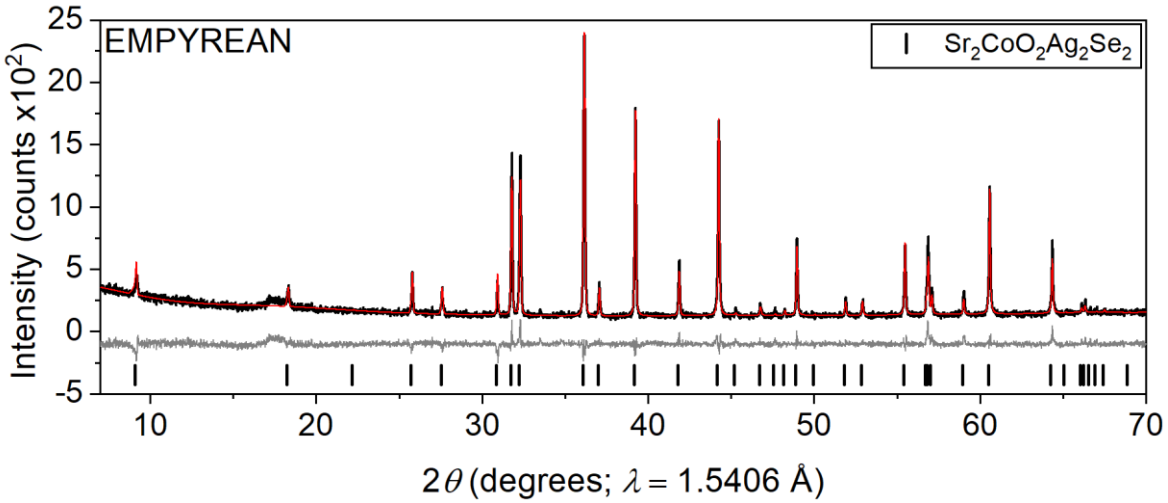


Figure 4.17 Rietveld refinement of $Sr_2CoO_2Ag_2Se_2$ from data collected on the on the ICL PANalytical Empyrean. R_{wp} = 7.510 %; χ^2 = 1.714.

On the first cycle with *n*-BuLi, the X-ray diffractogram already had clearly shifted to higher angles suggesting a much smaller unit cell. This was accompanied by the appearance of a much broader peak shape and the appearance of Bragg peaks from elemental Ag. Further treatment with *n*-BuLi was able to induce only a small amount of further Ag / Li exchange and any more treatment after the 2nd cycle ended up with very little change in the lattice parameters of the main phase as well as the intensity of the Ag peaks.

Unlike the Cu analogues where disulfiram could be used to remove Cu, the Ag-containing compounds were only treated repeatedly with *n*-BuLi and therefore there was much less product loss on washing and more treatments could be performed with a minimum of 3 performed for each of the Ag-containing samples for neutron measurements.

Once the repeated treatments were complete and there were no discernible changes in the lattice parameters of the main phase, the sample was prepared for higher resolution SPXRD data on the I11 beamline at the Diamond Light Source as outlined in section 2.2.2.3, with Rietveld refinement of $Sr_2CoO_2Ag_{0.34(2)}Li_{1.66(2)}Se_2$ using the MAC detector shown below in Figure 4.18.

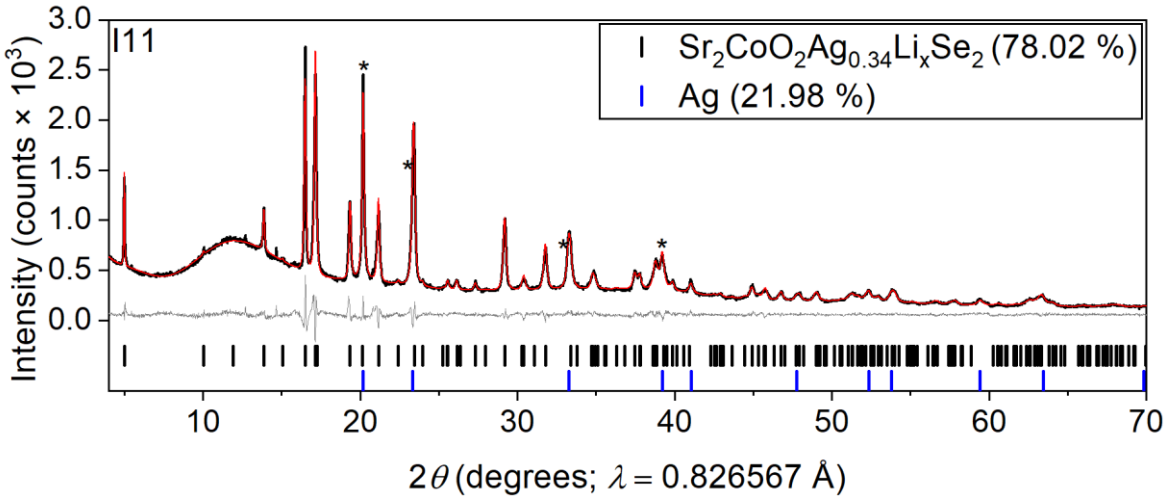


Figure 4.18 Rietveld refinement of $Sr_2CoO_2Ag_{0.34(2)}Li_{1.66(2)}Se_2$ from data collected on the I11 beamline at Diamond Light Source Ltd, the * indicate reflections from elemental Ag. R_{wp} = 7.510 %; χ^2 = 1.714.

The refined Ag occupancy of 0.34(2) on the tetrahedral site in the selenide layers was also backed up by the weight fractions when calculating the extruded Ag using equation 2.4 which gives a Ag occupancy of 0.33(1) per formula unit.

Due to Li^+ and Ag^+ having such a difference in their ionic size (0.59 Å for Li^+ as opposed to 1.0 Å for Ag^+),[9] the amount of lithiation can be readily seen by the lattice parameters as shown in Table 4.8, which shows the parent $Sr_2CoO_2Ag_2Se_2$ compared to the most lithiated compound produced using multiple reactions with *n*-BuLi as calculated using SPXRD and PND for 2 samples produced from the same parent with exactly the same experimental treatment.

Table 4.8 Comparison of lattice parameters for $Sr_2CoO_2Ag_{2-x}Li_xSe_2$.

Sample	$Sr_2CoO_2Ag_2Se_2$	$Sr_2CoO_2Ag_{0.34(2)}Li_{1.66(2)}Se_2$	$Sr_2CoO_2Ag_{0.38(2)}Li_{1.62(2)}Se_2$
Radiation	X-ray	X-ray	Neutron
Diffractometer	I11	I11	GEM
a (Å)	4.10621(2)	4.0608(2)	4.0629(1)
c (Å)	19.4332(1)	18.862(2)	18.865(2)
Volume (Å^3)	327.662(4)	311.04(5)	311.412(2)

Again, along with determining the magnetic structure, PND was used in a complimentary way to confirm the site occupancy and extent of Ag / Li exchange with Figure 4.19 below showing the Rietveld refinement of $Sr_2CoO_2Ag_{0.38(2)}Li_{1.62(2)}Se_2$ using neutron diffraction on the GEM diffractometer.

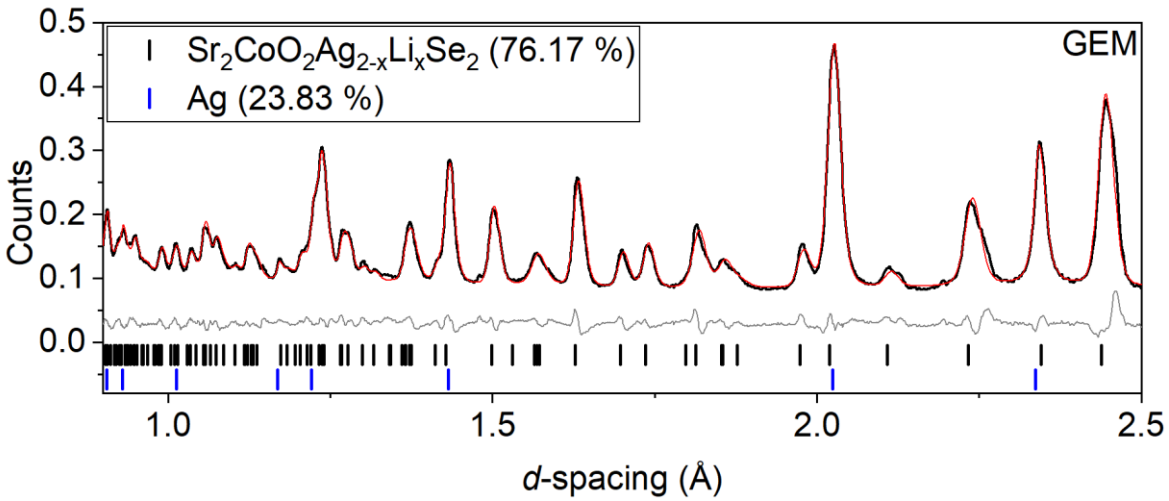


Figure 4.19 Rietveld refinement of $Sr_2CoO_2Ag_{0.38(2)}Li_{1.62(2)}Se_2$ from bank 5 of the GEM diffractometer at ISIS neutron and muon source at room temperature. R_{wp} = 3.561 %; χ^2 = 0.005.

The refined value for the Ag occupancy of 0.38(2) is in good agreement with both the X-ray and also from calculation using equation 2.4 in section 2.1.4 which gives a value of 0.37(1) Ag per formula unit.

Table 4.9 Comparison of refined parameters for $Sr_2CoO_2Ag_{2-x}Li_xSe_2$.

Sample	$Sr_2CoO_2Ag_2Se_2$	$Sr_2CoO_2Ag_{0.34(2)}Li_{1.66(2)}Se_2$	$Sr_2CoO_2Ag_{0.38(2)}Li_{1.62(2)}Se_2$
Radiation	X-ray	X-ray	Neutron
Diffractometer	I11	I11	GEM
z(Sr)	0.08287(4)	0.0867(2)	0.0858(3)
z(Se)	0.15512(4)	0.1656(2)	0.1673(2)
Ag occupancy	0.974(2)	0.17(1)	0.188(1)
Li occupancy	N/A	0.83(1)	0.812(1)
Sr U_{11} (Å^2)	0.0010(2)	0.002(2)	0.0053(9)
Sr U_{33} (Å^2)	0.0010(2)	0.002(2)	0.0034(7)
Co U_{11} (Å^2)	0.0024(2)	0.018(1)	0.000(3)
Co U_{33} (Å^2)	0.0024(2)	0.018(1)	0.007(4)
O U_{11} (Å^2)	0.0076(9)	0.015(5)	0.004(1)
O U_{22} (Å^2)	0.0076(9)	0.015(5)	0.002(1)
O U_{33} (Å^2)	0.0076(9)	0.015(5)	0.019(3)
Ag U_{11} (Å^2)	0.0120(5)	0.021(2)	0.014(2)
Ag U_{33} (Å^2)	0.0120(5)	0.021(2)	0.008(2)
Li U_{11} (Å^2)	N/A	0.029(4)	0.000(5)
Li U_{33} (Å^2)	N/A	0.029(4)	0.025(5)
Se U_{11} (Å^2)	0.0005(2)	0.013(3)	0.0085(8)
Se U_{33} (Å^2)	0.0005(2)	0.013(3)	0.003(2)
R_{wp} (%)	2.875	7.510	3.561
χ^2	5.987	1.714	0.005

Note that X-ray data was treated isotropically where $U_{11} = U_{22} = U_{33}$.

$Ba_2CoO_2Ag_{2-x}Li_xSe_2$

For the Ba analogue, again, the parent was synthesised as previously reported[20], resulting in a phase pure product as shown in Figure 4.20.

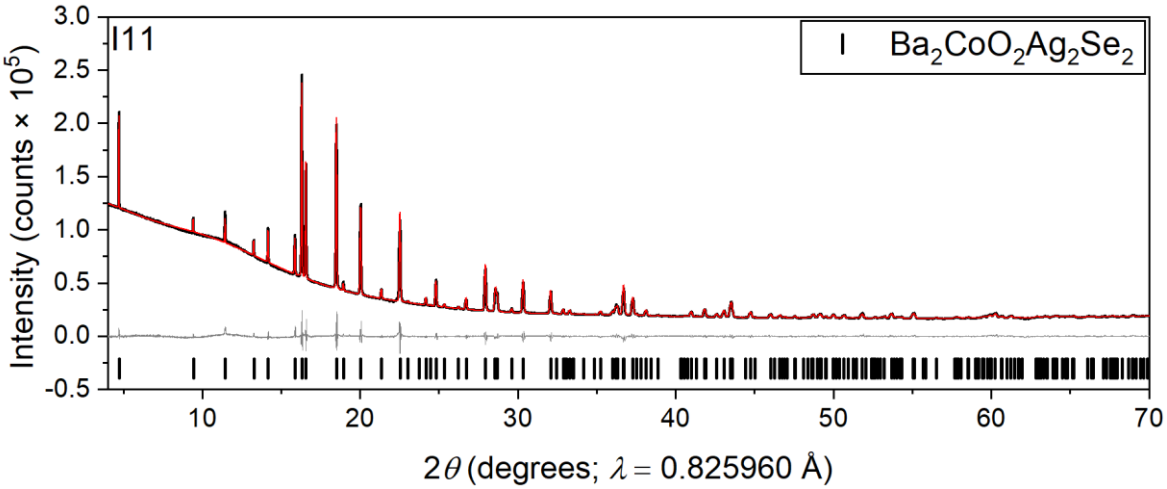


Figure 4.20 Rietveld refinement of $Ba_2CoO_2Ag_2Se_2$ from data collected on the I11 beamline at Diamond Light Source Ltd. R_{wp} = 1.982 %; χ^2 = 3.713.

Similar to what was observed with the Sr analogue, initial reaction with *n*-BuLi resulted in a shift of the diffractogram to higher angle indicating a reduction in the size of the unit cell which would be expected on the exchange of much larger Ag^+ ions within the structure with Li^+ cations.

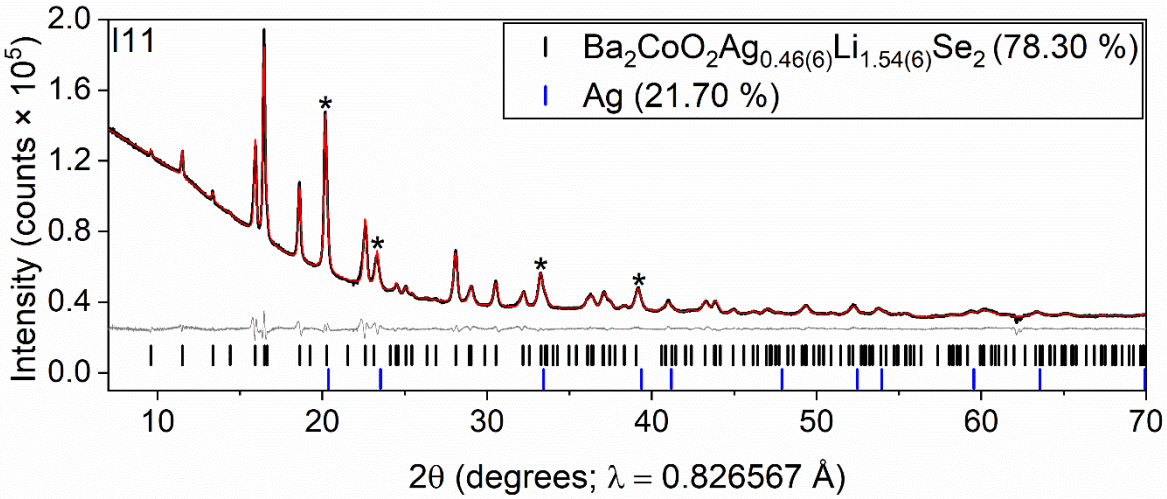


Figure 4.21 Rietveld refinement of $Ba_2CoO_2Ag_{0.46(6)}Li_{1.54(6)}Se_2$ from data collected on the I11 beamline at Diamond Light Source Ltd. R_{wp} = 1.549 %; χ^2 = 3.586.

Further treatment with *n*-BuLi gave diminishing returns, with only a small amount of Ag being able to be extruded after the first reaction. Once the reaction was known to have gone to completion, high resolution SPXRD was collected on the I11 beamline at the Diamond

Light Source with the resulting Rietveld refinement shown above in Figure 4.21. The refined Ag occupancy of 0.46(6) on the tetrahedral site in the selenide layers was also backed up by the weight fractions when calculating the extruded Ag using equation 2.4 which gives a Ag occupancy of 0.40(1) per formula unit, agreeing well with the refined value.

It is clear that more coinage metal can be extruded in the lithiated phases investigated within this thesis when the coinage metal is Ag due to its increased ionic mobility. However, it is also curious that whereas a similar level or coinage extrusion occurs for the Cu analogues, slightly more Ag can be removed from $Sr_2CoO_2Ag_2Se_2$ than in $Ba_2CoO_2Ag_2Se_2$.

A different sample with one extra cycle with *n*-BuLi was also measured using PND on the GEM diffractometer at ISIS with refinement against bank 5 at room temperature shown below in Figure 4.22.

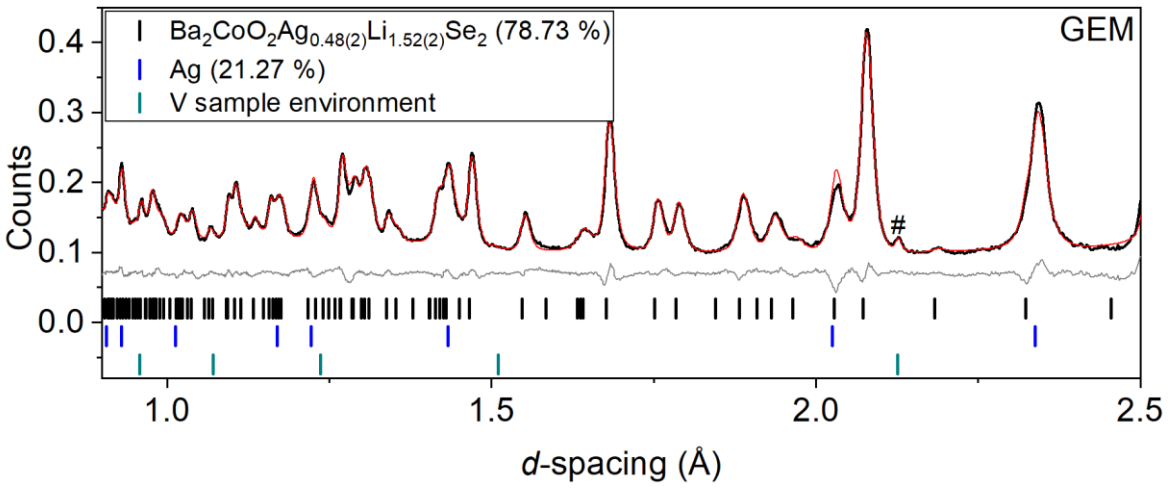


Figure 4.22 Rietveld refinement of $Ba_2CoO_2Ag_{0.48(2)}Li_{1.52(2)}Se_2$ from bank 5 of the GEM diffractometer at ISIS neutron and muon source at room temperature. R_{wp} = 3.213 %; χ^2 = 0.005. The # represents scattering from the V sample holder.

In contrast to the Cu analogues and similarly to $Sr_2CoO_2Ag_{2-x}Li_xSe_2$, as seen below in Table 4.10, the extent of lithiation is readily seen in these samples due to the size difference in Li^+ and Ag^+ with further refined results shown in Table 4.11.

Table 4.10 Comparison of lattice parameters for $Ba_2CoO_2Ag_{2-x}Li_xSe_2$.

Sample	$Ba_2CoO_2Ag_2Se_2$	$Ba_2CoO_2Ag_{0.46(6)}Li_{1.54(6)}Se_2$	$Ba_2CoO_2Ag_{0.48(2)}Li_{1.52(2)}Se_2$
Radiation	X-ray	X-ray	Neutron
Diffractometer	I11	I11	GEM
a (Å)	4.22721(8)	4.18352(9)	4.1881(7)
c (Å)	20.0693(4)	19.8587(6)	19.8373(5)
Volume (Å^3)	358.62(2)	347.56(2)	347.95(4)

Table 4.11 Comparison of refined parameters for $Ba_2CoO_2Ag_{2-x}Li_xS_2$.

Sample	$Ba_2CoO_2Ag_2Se_2$	$Ba_2CoO_2Ag_{0.46(6)}Li_{1.54(6)}Se_2$	$Ba_2CoO_2Ag_{0.48(2)}Li_{1.52(2)}Se_2$
Radiation	X-ray	X-ray	Neutron
Diffractometer	I11	I11	GEM
z(Ba)	0.08774(4)	0.09135(6)	0.09117(9)
z(Se)	0.16251(6)	0.17106(8)	0.17294(6)
Ag occupancy	1.000(1)	0.23(3)	0.24(1)
Li occupancy	N/A	0.77(3)	0.76(1)
Ba U_{11} (Å^2)	0.0071(3)	0.008(2)	0.002(3)
Ba U_{33} (Å^2)	0.0071(3)	0.008(2)	0.005(2)
Co U_{11} (Å^2)	0.0043(5)	0.001(2)	0.003(1)
Co U_{33} (Å^2)	0.0043(5)	0.001(2)	0.000(3)
O U_{11} (Å^2)	0.011(3)	0.012(5)	0.0176(2)
O U_{22} (Å^2)	0.011(3)	0.012(5)	0.0102(3)
O U_{33} (Å^2)	0.011(3)	0.012(5)	0.0312(2)
Ag U_{11} (Å^2)	0.0203(5)	0.021(3)	0.016(5)
Ag U_{33} (Å^2)	0.0203(5)	0.021(3)	0.029(6)
Li U_{11} (Å^2)	N/A	0.014(3)	0.016(5)
Li U_{33} (Å^2)	N/A	0.014(3)	0.032(5)
Se U_{11} (Å^2)	0.009(2)	0.013(1)	0.0003(4)
Se U_{33} (Å^2)	0.009(2)	0.013(1)	0.0086(8)
R_{wp} (%)	1.982	1.549	3.746
χ^2	3.713	3.586	0.007

Note that X-ray data was treated isotropically where $U_{11} = U_{22} = U_{33}$.

4.3.3 Magnetometry

Magnetometry measurements were performed on these samples to see if there were any changes to the magnetic susceptibility after the reductive treatment during the synthesis.

Similarly to the Cu analogues, it was not uncommon for trace amounts of ferromagnetic impurities such as Co to arise which was visible in low field of *M vs H* plots and so it was necessary to perform a 6 / 5 T subtraction as outlined in section 2.2.6.1 for some of the measurements.

These samples do not obey the Curie-Weiss law as they presumably magnetically order close to room temperature in line with similar compounds (variable temperature PND would be required to determine the T_N for these lithiated phases). Therefore, it was not possible to extract meaningful Curie-Weiss parameters and it was again deemed not necessary to obtain these due to the availability of neutron diffraction data.

Figures 4.23 and 4.24 below show the magnetic susceptibility for both $Sr_2CoO_2Ag_2Se_2$ and $Ba_2CoO_2Ag_2Se_2$ and their lithiated "daughter" compounds respectively measured in a field of 100 Oe.

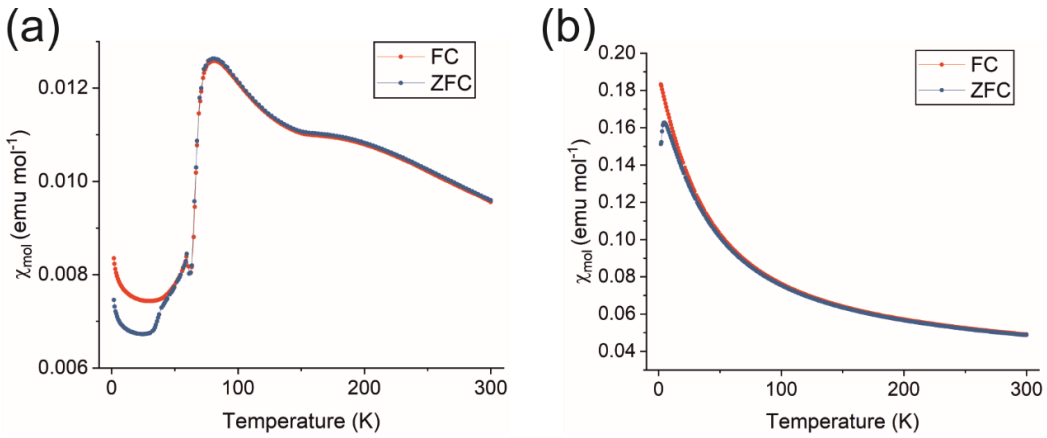


Figure 4.23 ZFC and FC magnetic susceptibility curves of **(a)** $Sr_2CoO_2Ag_2Se_2$ and **(b)** $Sr_2CoO_2Ag_{2-x}Li_xSe_2$ measured in a field of 100 Oe.

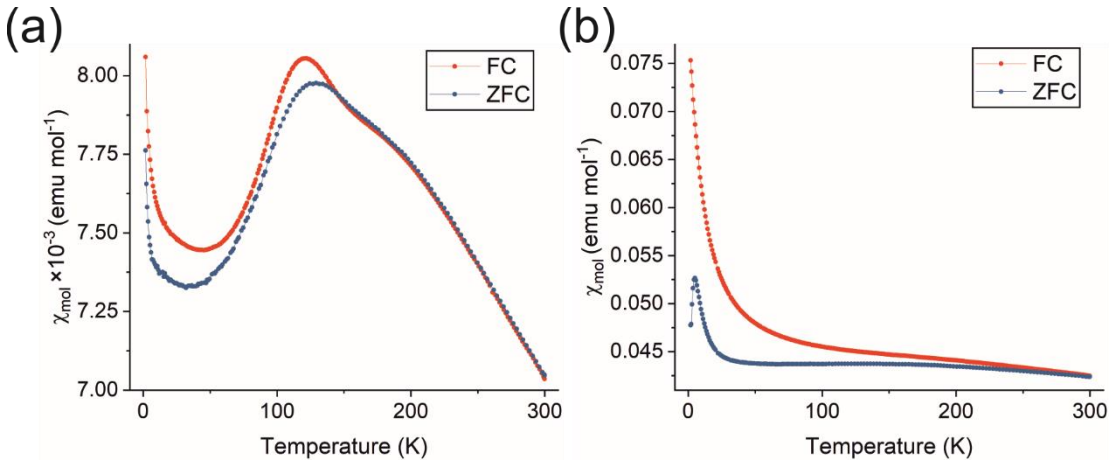


Figure 4.24 ZFC and FC magnetic susceptibility curves of **(a)** $Ba_2CoO_2Ag_2Se_2$ and **(b)** $Ba_2CoO_2Ag_{2-x}Li_xSe_2$ measured in a field of 100 Oe.

Both parent materials have a clear anti-ferromagnetic ordering transition in their magnetic susceptibility albeit they are broad features from which an exact value of T_N cannot be extracted accurately but their "daughter" compounds do not show any obvious transitions.

The *M vs H* plot for $Ba_2CoO_2Ag_{2-x}Li_xSe_2$ is shown below in Figure 4.25(a), there is a large initial gradient at low field before levelling off at high field which implies there is a ferromagnetic impurity within the sample perhaps which was beyond the limit of detectability by X-rays. This will increase the magnitude of the magnetic susceptibility measured in a low field (Fig 4.24), and partially account for the divergence of ZFC and FC curves.

The corresponding plot for $Sr_2CoO_2Ag_{2-x}Li_xSe_2$ can be seen in the appendix E.2. The magnetisation for this sample does not saturate within the measured fields and so a ferro-subtraction is not possible.

A high-field subtraction was performed for $Ba_2CoO_2Ag_{2-x}Li_xSe$ as according to section 2.2.6.1 to give an intrinsic moment by effectively eliminating the contribution from the impurity and give a FC susceptibility which should be more a true representation of the

magnetic susceptibility of the sample. This gave the resulting plot below for $Ba_2CoO_2Ag_{2-x}Li_xSe_2$. It has a broad hump, probably indicating antiferromagnetic ordering just below room temperature.

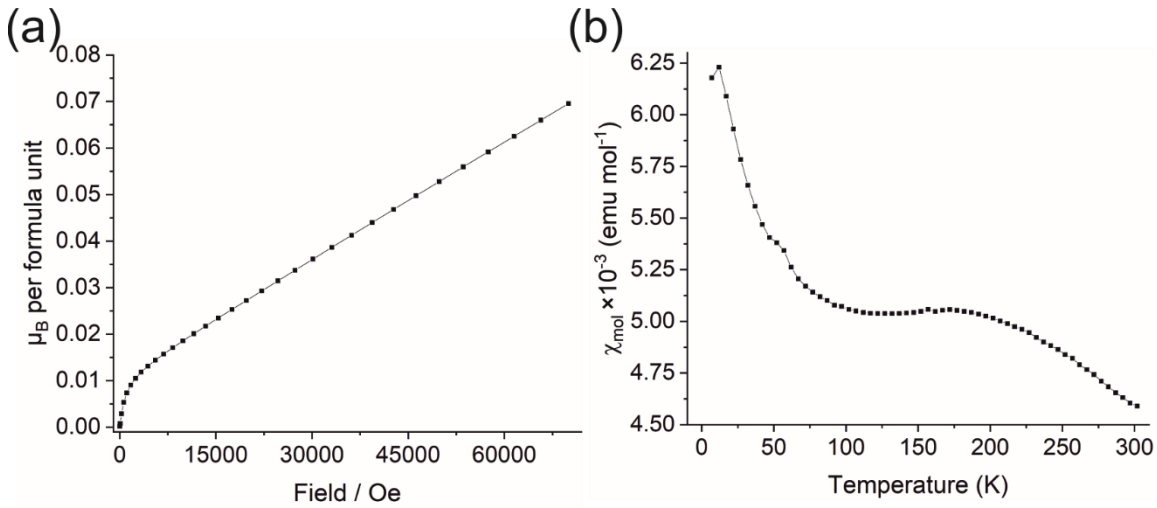


Figure 4.25(a) *M* v *H* plot for $Ba_2CoO_2Ag_{2-x}Li_xSe_2$. **(b)** Field-cooled magnetic susceptibility of $Ba_2CoO_2Ag_{2-x}Li_xSe_2$, measured using a 6 – 5 T subtraction (as described in section 2.2.7.1).

4.3.4 Low temperature PND to probe magnetic ordering

Approximately 2.5 g of both $Sr_2CoO_2Ag_{2-x}Li_xSe_2$ and $Ba_2CoO_2Ag_{2-x}Li_xSe_2$ were measured using PND on the GEM diffractometer at the ISIS facility at 5 K to deduce the magnetic structure of these lithiated phases and compare them to related structural analogues.

Despite the ambiguous results from the magnetometry, it would be expected due to the close structural proximity of these phases to the parent / Cu analogues that $Sr_2CoO_2Ag_{0.38(2)}Li_{1.62(2)}Se_2$ and $Ba_2CoO_2Ag_{0.48(2)}Li_{1.52(2)}Se_2$ would perhaps have similar magnetic structures.

A similar treatment as that described in section 4.3.4 using ISODISTORT[124] to determine the magnetic structure yielded the same result as that of the Cu analogues and unsurprisingly

the same magnetic space group as the corresponding "parent" materials, $Sr_2CoO_2Ag_2Se_2$ and $Ba_2CoO_2Ag_2Se_2$.[20]

The resulting Rietveld refinements for $Sr_2CoO_2Ag_{0.38(2)}Li_{1.62(2)}Se_2$ and $Ba_2CoO_2Ag_{0.48(2)}Li_{1.52(2)}Se_2$ are shown below in Figure 4.26.

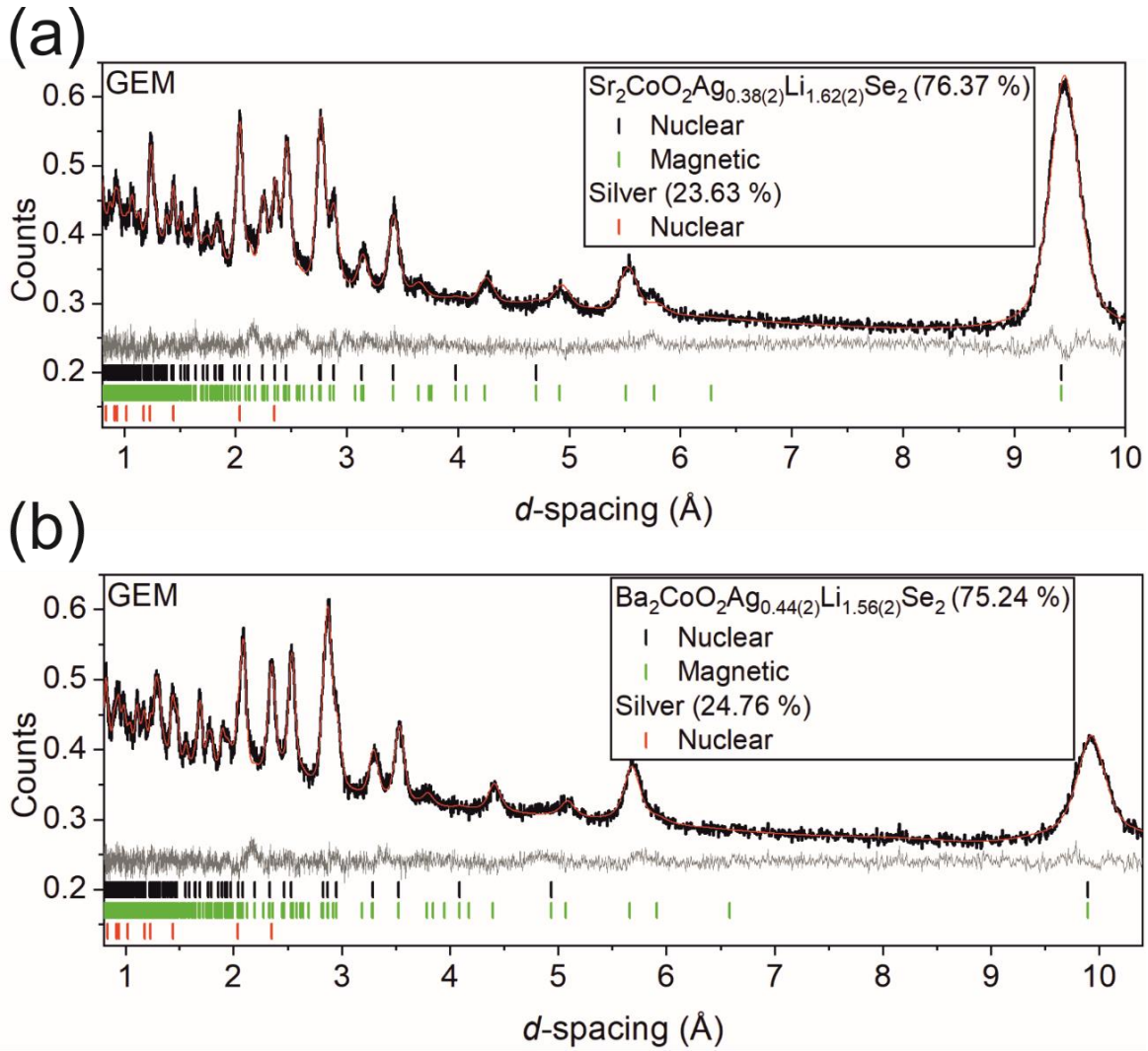


Figure 4.26(a) Rietveld refinement of $Sr_2CoO_2Ag_{0.38(2)}Li_{1.62(2)}Se_2$ R_{wp} = 2.463 %; χ^2 = 0.008 and **(b)** Rietveld refinement of $Ba_2CoO_2Ag_{0.48(2)}Li_{1.52(2)}Se_2$ R_{wp} = 2.218 %; χ^2 = 0.009 collected at 5 K on the GEM diffractometer at ISIS neutron and muon source.

This gave a similar magnetic structure to the Cu analogues and can be seen visually in Figure 4.15. The refined magnetic parameters are shown below in Table 4.12.

Table 4.12 Refined parameters for the magnetic ordering of $Ae_2CoO_2Ag_{2-x}Li_xSe_2$ (*Ae* = Sr, Ba) measured at 5 K using PND on the GEM diffractometer at ISIS.

	$Sr_2CoO_2Ag_{0.38(2)}Li_{1.62(2)}Se_2$	$Ba_2CoO_2Ag_{0.48(2)}Li_{1.52(2)}Se_2$
μ_a (μ_B)	0.99(8)	1.47(7)
μ_b (μ_B)	3.34(8)	3.22(6)
$\lvert\mu\rvert$ (μ_B)	3.48(8)	3.55(6)

4.3.5 XANES measurements

The Co oxidation state was measured using synchrotron XANES on the B18 beamline at the Diamond Light Source. The spectrum of $Sr_2CoO_2Ag_{2-x}Li_xSe_2$ is shown below in Figure 4.27.

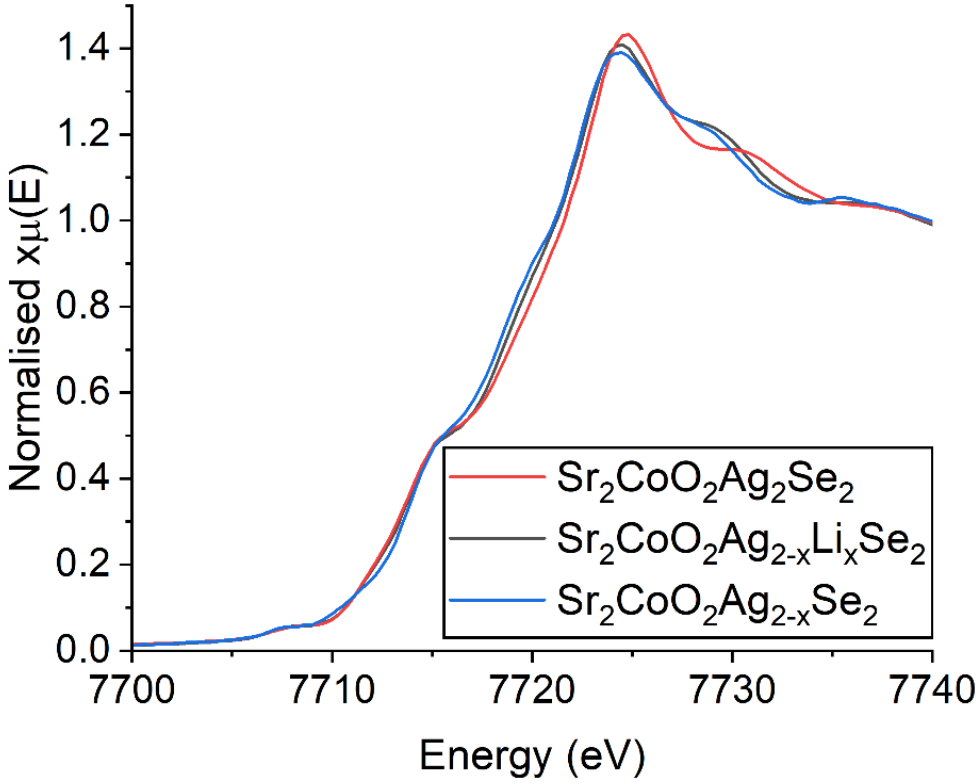


Figure 4.27 Co K-edge XANES spectra for $Sr_2CoO_2Ag_{2-x}Li_xSe_2$.

This was of particular interest because Blandy had previously seen that oxidative deintercalation treatment of $Sr_2CoO_2Ag_2Se_2$ with iodine indicated at least four regimes in most-deintercalated $Sr_2CoO_2Ag_{1.5(2)}Se_2$ as a function of temperature: paramagnetic, metamagnetic, soft ferromagnetic and ferromagnetic with a large spin-glass component which can be seen in Figure 4.1.[40]

Because $Sr_2CoO_2Ag_2Se_2$ is fully occupied with Ag and in $Sr_2CoO_2Ag_{2-x}Li_xSe_2$, the tetrahedral site is fully occupied, then it would be expected that the Co oxidation state would be the same. However oxidative deintercalation should result in a shift to higher energy showing the average oxidation state of Co has gone above +2. It can be difficult when the edge has steps as shown above in Figure 4.27 to determine the exact place for the edge, but assuming it is at ≈ 714 eV when the edge begins, it can be seen that $Sr_2CoO_2Ag_{2-x}Li_xSe_2$ and $Sr_2CoO_2Ag_2Se_2$ have similar values of xμ(E) whereas there is a clear small shift to the right for $Sr_2CoO_2Ag_{2-x}Se_2$ which is made under oxidising conditions.

More XANES experiments would be required at the Se-edge to ensure that it is not Se being oxidised in these materials.

4.4 Discussion / Conclusion

This chapter has reported the synthesis of 4 new Co-containing oxide chalcogenide phases obtained via a novel cycling synthetic route. All of these compounds retain their parent space group of *I*4/*mmm* upon soft-chemical manipulation and are extremely air sensitive, behaving in a similar way to that described by Rutt et al., for a series of Mn-containing lithiated oxide sulfides, where on exposure to moist air, the ion exchange reaction is reversed (Li is deintercalated and the coinage metal re-enters the structure).[130]

Magnetic susceptibility data for these phases show broad transitions which are not very good at identifying the exact temperature at which transitions are occurring which is typical for layered compounds of this type. On cooling, it is typical for short-range magnetic ordering to occur before long-range order ensues which can be detected in magnetometry measurements as a transition at a higher temperature than would be observed in PND which looks at long-range ordering. However, these lithiated phases do not show any obvious signature of long-range antiferromagnetic ordering in their magnetic susceptibility.

As revealed by PND, all of the compounds in this chapter exhibit long-range antiferromagnetic order within the *ab*-plane. Their refined long-range ordered moments are shown below in Table 4.13.

At first glance, it seems surprising that the magnetic moments are above the value for spin-only Co^{2+} which is a d^7 cation and this has been attributed to a significant orbital contribution to the ordered moment.

Table 4.13 The refined magnetic moments of all the novel materials synthesised in this chapter.

Compound	Magnetic moment (μ_B)
$Sr_2CoO_2Cu_{1.214(8)}Li_{0.786(8)}S_2$	3.41(4)
$Sr_2CoO_2Cu_{1.24(6)}Li_{0.76(6)}Se_2$	3.21(7)
$Sr_2CoO_2Ag_{0.38(2)}Li_{1.62(2)}Se_2$	3.48(8)
$Ba_2CoO_2Ag_{0.48(2)}Li_{1.52(2)}Se_2$	3.55(6)

Figure 4.28 below shows the changes in the *d*-orbital energies on going from octahedral geometry to an axially elongated octahedra / pseudo square-planar environment.

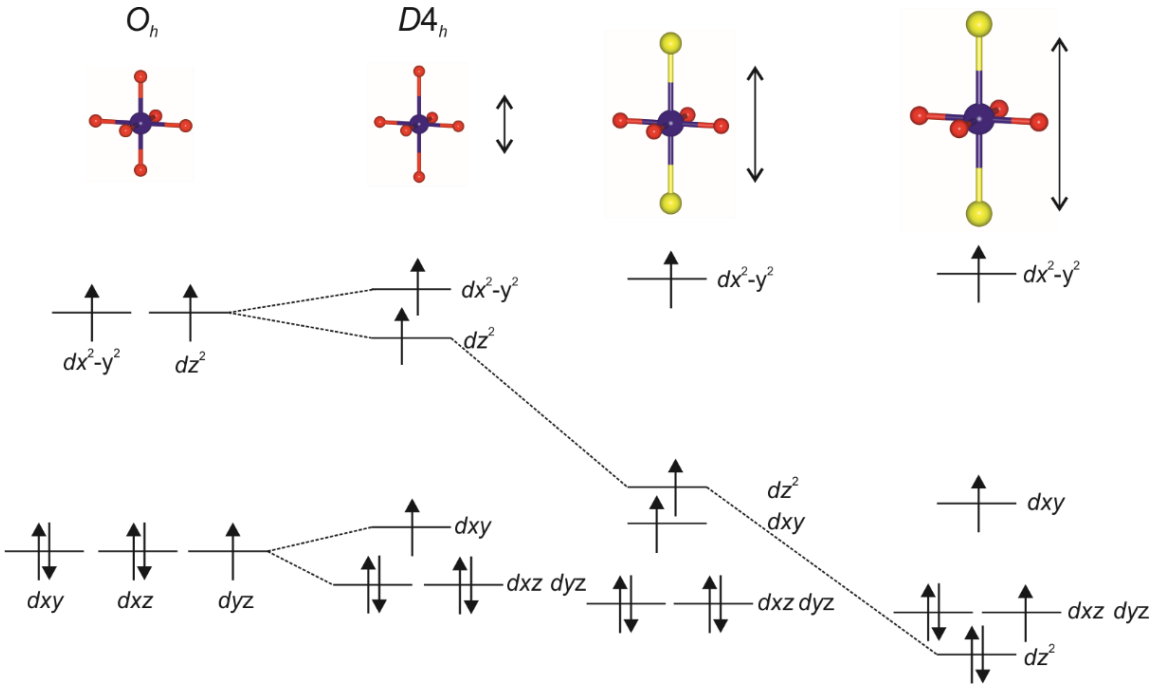


Figure 4.28 The changes in *d*-orbital energies as a function of the coordination environment for high-spin d^7 Co^{2+}.

The series of compounds $Ae_2CoO_2X_2Ch_2$ (*Ae* = Sr, Ba; *X* = Cu, Ag; *Ch* = S, Se) along with the series of lithiated compounds examined in this chapter are expected to reside within the orbital picture describe in the furthest right diagrams of Figure 4.28.

In the 3rd diagram, the ground state does not have an unevenly occupied, degenerate *d*-state and therefore requires the excitation of an electron from the *dxz*/*dyz* orbital into the *dxy*

orbital which would provide a 2nd order orbital moment from the 1st excited state of this configuration.

In contrast, a continued elongation of the CoO_4Ch_2 octahedra would in theory result in a configuration where dz^2 is lower in energy than the *dxz* / *dyz* orbitals (far right diagram) and this would result in an unevenly occupied degenerate *d*-state within the ground state and therefore a stronger, first order orbital contribution would be expected to add more to the spin contribution and result in a larger long-range ordered Co^{2+} moment.

This is seen experimentally in the solid solution $Sr_{2-x}Ba_xCoO_2Cu_2S_2$ which was investigated by Smura[21] where the less elongated Sr end member was hypothesised to have a 2nd order orbital contribution whereas the more elongated Ba end member had a 1st order contribution and a larger moment which matched experiment as shown in Figure 4.29. The *d*-orbital energies would need to be probed computationally as a function of the elongation ratio to confirm this theory.

As can be seen from the black data points below in Figure 4.29, it is actually very common for the magnetic moment of Co^{2+} to be larger than the expected spin-only moment and this resides in the behaviour of the *d*-orbitals as shown in Figure 4.28 whereby in CoO, the *dxy*, *dxz* and *dyz* orbitals, which are degenerate, unequally occupied and related by rotation about the principal axis of a cube (the 3-fold) give rise to an unquenched orbital moment which can mix with the spin moment via spin-orbit coupling.

For the case of axially elongated CoO_4X_2, the degeneracy of the t_{2g} and e_g orbitals are lifted as shown in Figure 4.28. Due to this phenomenon, any orbital with "*z*" contribution will be

stabilised with respect to the original energy whereas the orbitals with only "*x*" or "*y*" contribution will be destabilised.

This translates to a splitting of the $^4T_{1g}$ state into a non-degenerate $^4A_{2g}$ ground state and an excited ^4E_g state which can effectively mix into the ground state. This again corresponds to mixing of the *dxy*, *dxz* and *dyz* orbitals. However, as the structure becomes more distorted from octahedral then the difference in energies between *dxy* and that of *dxz* and *dyz* becomes progressively larger to the extent that it would be expected that the first order orbital contribution should be quenched (2nd and 3rd diagram in Figure 4.28).

The key to the magnitude of the magnetic moment of these compounds and related analogues thus lies within the dz^2 orbital and its energetic proximity to the *dxz* and *dyz* orbitals as well as the axial ligand whereby a larger moment in general is expected for a weaker ligand field such as what is observed for the two oxide halides $Sr_2CoO_2Br_2$ and $Sr_2CoO_2Cl_2$[107] as seen below in Figure 4.29.

The magnetic moments of the compounds within this chapter are somewhat supressed (red data points in Figure 4.29) when compared to the magnitude of the moment which would be predicted based on the coordination environment as displayed in Figure 4.29. It is possible that disorder between Li and coinage metal in these lithiated samples disrupts the long-range order sufficiently to cause a visible reduction in the long-range ordered moment which would be consistent with the glassy component to the magnetism observed in the magnetometry data in sections 4.2.4 and 4.3.3, although notably still enhanced moment from the predicted spin-only value, suggesting that the vast majority of Co^{2+} spins are still participating in long-range order.

In fact, it has already been observed that disorder within these systems can supress the long-range magnetic ordering as Blandy demonstrated by inducing disorder on the chalcogen site in $Sr_2CoO_2Cu_2Se_{1.6}S_{0.4}$[40] which as shown in Figure 4.29, supressed the long-range ordered moment well below what would be expected based on the Co coordination environment – similar to what is observed to the lithiated phases investigated in this chapter.

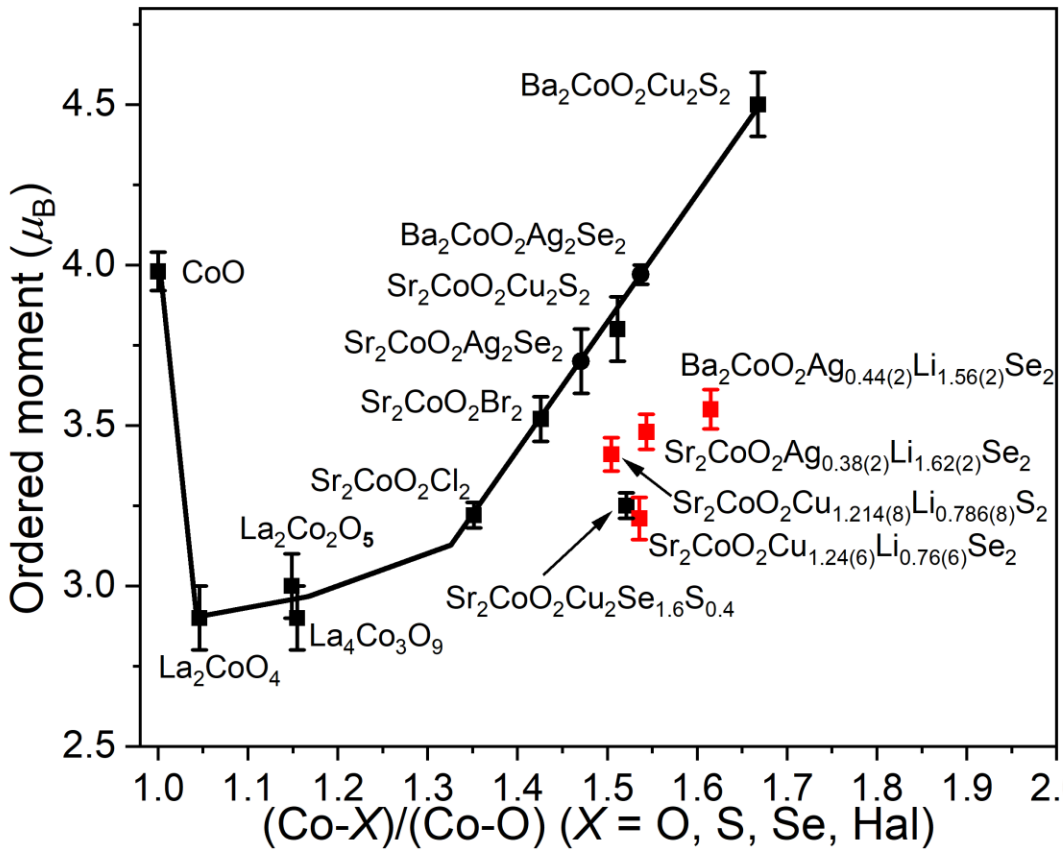


Figure 4.29 The relationship between the long-range ordered moment of Co^{2+} as a function of the coordination environment from the literature (black) and this work (red).

Despite the recent experimental evidence seemingly being conclusive that there is an orbital contribution leading to enhanced magnetic moments within these Co-containing oxide chalcogenides, recent literature has suggested an alternative picture. Initially, Whangbo et al., suggested from their calculations that there are no unevenly occupied degenerate *d*-states in systems similar to those investigated in this chapter with elongated CoO_4X_2 octahedra in contrary to CoO which has an unevenly degenerate t_{2g} state which provided an addition,

unquenched orbital moment of 1 μ_B to the total ordered moment[131] as can be seen visually in Figure 4.28. Calculations suggested that there should be no orbital moment in these systems.

Whangbo et al., then produced another piece of work[132] investigating the magnetic form factor used in the refinement of neutron diffraction data, arguing that the spin moment distribution around Co^{2+} deviates strongly from spherical symmetry and thus the metal-ion-sphere approximation is no longer valid and that its use in Rietveld refinement was producing strongly underestimated magnetic form factors which resulted in the large magnetic moments reported in Figure 4.29.

In the calculations performed by Whangbo, only a moderate elongation of the CoO_4X_2 octahedra is considered. What is proposed in this thesis is that the elongation is nearing the square-planar limit (and seemingly the high-low-spin boundary) whereby dz^2 is below *dxz* and *dxz* which results in the reinstatement of unevenly occupied, degenerate *d*-states which are the cause of the enhanced orbital moments observed in these systems.

There are plans in place outside of the timeframe of this thesis to work with collaborators at the ISIS neutron and muon source about implementing a modified magnetic form factor and revisiting the data for all the cobalt containing oxide chalcogenides of the form $Ae_2CoO_2X_2Ch_2$ (*Ae* = Sr, Ba; *X* = Cu, Ag; *Ch* = S, Se) synthesised within the group to determine whether a modified magnetic form factor is the key to aligning experiment and theory or whether there are aspects of the theory which need to be revised to account for the trends that are observed experimentally.

Chapter 5

5 Synthesis and characterisation of $Ae_{3x}Ae'_xFe_2O_5Cu_2Ch_2$ (*Ae*/Ae' = Ba, Sr, Ca; *Ch* = S, Se)

5.1 Introduction

$Sr_3Fe_2O_5Cu_2S_2$ was first reported in 1997 by Zhu and Hor.[11] With reference to the series of compounds shown in Figure 1.5, this is the $m = 2$, $n = 1$ structure and consists of anti-fluorite $[Cu_2S_2]^{2-}$ blocks and layers comprising of FeO_5 square pyramids fused by an apical oxide anion with *Ae* (*Ae* = Ba, Sr or Ca) cations in between the layers (Figure 5.1(a) and section 1.3.1.1) and crystallises in the *I*4/*mmm* space group. Extending this work, in 2005, Cario et al., synthesised the Se analogue, $Sr_3Fe_2O_5Cu_2Se_2$ and used Mössbauer spectroscopy to confirm the predicted oxidation state of Fe to be +3 and PND experiments revealed antiferromagnetic coupling within the basal plane with a $T_N \approx 490$ K.[29] Recently within the group, Sheath et al., in their attempted synthesis of $CaSrFeO_3CuSe$ (which has the Sr_2GaO_3CuS structure[12] shown in Figure 5.1(b)) noted that although they could not index the diffraction peaks to the target phase, it was noted that there was large amount of CaO impurity within the bulk sample. They discovered that what they had synthesised instead was the compound with the $m = 2$, $n = 1$ structure, $CaSr_2Fe_2O_5Cu_2Se_2$ according to equation 5.1.[14]

$$2\ CaSrFeO_3CuSe \rightarrow CaSr_2Fe_2O_5Cu_2Se_2 + CaO \qquad (5.1)$$

These materials were probed using PND and were found to order antiferromagnetically with a magnetic unit cell that could be indexed on a $\sqrt{2}a \times \sqrt{2}a \times c$ expansion of the nuclear cell containing Fe^{3+} moments tilted somewhat between the basal plane and the stacking direction. The favourability of the m = 2, n = 1 structure in this solid solution was attributed to the availability of two differently sized sites enabling the facile accommodation of two differently sized alkaline earth ions (i.e., Ca^{2+} and Sr^{2+}) via a high degree of cation ordering. Previously in 2008, Wilson was able to synthesise the Ba analogues resulting in the 2 novel compounds $Ba_3Fe_2O_5Cu_2S_2$ and $Ba_3Fe_2O_5Cu_2Se_2$[133] which suggested that the solid solution $Ba_{3-x}Sr_xFe_2O_5Cu_2Ch_2$ (x = 0, 1, 2; Ch = S, Se) should be achievable.

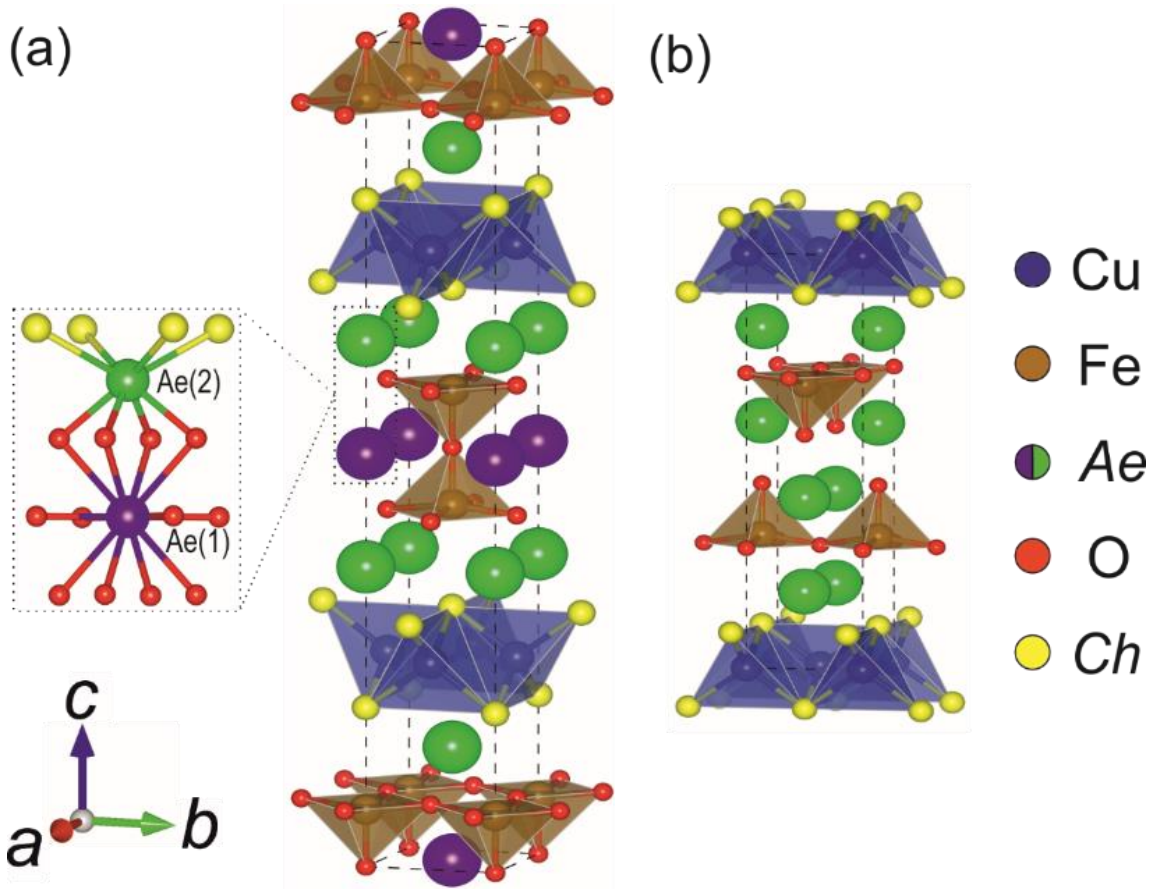


Figure 5.1(a) The $Ae_3Fe_2O_5Cu_2Ch_2$ structure showing the two distinct 12 and 8-coordinate alkaline earth cation sites in purple and green respectively. **(b)** The closely related Ae_2FeO_3CuCh structure with two more similar sites for the cations is shown for comparison; it is less favoured when two alkali cations of different radius are present.

Thus, this chapter reports the synthesis of the novel oxychalcogenides $Ba_{3-x}Sr_xFe_2O_5Cu_2Ch_2$ (x = 0, 1, 2; *Ch* = S, Se) along with $BaCa_2Fe_2O_5Cu_2S_2$. In line with what Sheath observed, these materials also show a high degree of cation ordering with Ba^{2+} preferring the 12-coordinate cubo-octahedron whereas the smaller Sr^{2+} and Ca^{2+} cations occupy the smaller 8-coordinate square anti-prismatic site.

The work carried out in this chapter has been published in the *Journal of Solid State Chemistry*.[134]

5.2 Synthesis

The synthesis of $Ba_{3-x}Sr_xFe_2O_5Cu_2Ch_2$ (x = 0, 1, 2; *Ch* = S, Se) along with $BaCa_2Fe_2O_5Cu_2S_2$ was achieved using a traditional, high-temperature ceramic approach.

These materials were synthesised by grinding together Fe (Alfa 99.998 %), CuO (Alfa 99.995 %) and S (Alfa 99.999 %) or Se (Alfa 99.999 %) along with the appropriate ratio of *Ae*O (Ae = Ba, Sr, Ca) (which themselves were synthesised as outlined in section 2.1.3.1) thoroughly in an agate mortar and pestle until homogeneous in an argon filled glovebox with O_2 typically below 1 ppm as outlined in section 2.1.1 and 2.1.2.

The lower synthesis temperature of 800 ℃ successfully used for $Ba_3Fe_2O_5Cu_2Ch_2$ (*Ch* = S, Se),[133] did not result in phase pure samples for the members of the solid solutions, so to increase the purity, a synthesis temperature of 950 ℃ was used for the Sr or Ca-containing samples. Neither the oxide selenide $BaCa_2Fe_2O_5Cu_2Se_2$ nor the more Ba-rich targets $Ba_2CaFe_2O_5Cu_2Ch_2$ (*Ch* = S, Se) could be prepared via this method. The attempts to synthesise the two selenides produced $BaCu_2Se_2$ and $Ca_2Fe_2O_5$ as the dominant phases, whereas attempts to synthesise $Ba_2CaFe_2O_5Cu_2S_2$ produced a phase with almost identical lattice parameters to $Ba_3Fe_2O_5Cu_2S_2$ along with CaO and various other impurities. It is possible that the alkaline earth ion size mismatch becomes so great in these attempted phases that they are not stable with respect to alternative products under ambient pressure conditions.

5.3 Results & Discussion

5.3.1 Room temperature PXRD / PND

Phase purity was initially assessed using in-house PXRD and resulting Rietveld refinement confirmed the samples to be of the same structure type as those described in the introduction, indexing in the tetragonal *I*4/*mmm* space group with Rietveld refinement performed using the structural model as in Table 5.1.

Rietveld refinements of all the materials discussed in this chapter are shown in Figures 5.2 - 6 confirming they have the $m = 2$, $n = 1$ structure as depicted in Figure 5.1(a), similar to the closely related structural analogues.[11,14,29,133]

The resulting refined structural parameters for these compounds can be seen in Table 5.2-4 and closely related analogues can be found in Table 5.5.

Table 5.1. Structural Model for $Ae_{3x}Ae'_xFe_2O_5Cu_2Ch_2$ (*Ae*/Ae' = Ba, Sr, Ca; *Ch* = S, Se).

Atom	Position	*x*	*y*	*z*
*Ae*1	2*b*	0	0	0.5
*Ae*1	2*b*	0	0	0.5
*Ae*2	4*e*	0	0	*z*Ae2
*Ae*2	4*e*	0	0	*z*Ae2
Cu1	4*d*	0	0.5	0.25
Fe1	4*e*	0	0	*z*Fe1
*Ch*1	4*e*	0	0	*z*Ch1
O1	8*g*	0	0.5	*z*O1
O2	2*a*	0	0	0
Space group = *I*4/*mmm*				

The ratio of the two alkaline earth metals was assumed to be equal to the synthesis ratio because the samples were of high purity and the cations are non-volatile and therefore it was assumed that both alkaline earth sites were fully occupied. Thus, a single parameter could be refined to describe the distribution of different alkaline earth metal cations over the available sites. These refined values are compared with the expectation based on a statistical distribution in section 5.3.2.

Table 5.2. Refined atomic coordinates for $Ae_{3x}Ae'_xFe_2O_5Cu_2Ch_2$ (*Ae*/Ae' = Ba, Sr, Ca; *Ch* = S, Se).

	*z*Ae2	*z*Fe1	*z*Ch1	*z*O1
$Ba_2SrFe_2O_5Cu_2S_2$	0.64301(3)	0.07026(6)	0.19600(9)	0.0822(1)
$Ba_2SrFe_2O_5Cu_2Se_2$	0.63894(4)	0.06881(8)	0.19565(6)	0.0762(2)
$BaSr_2Fe_2O_5Cu_2S_2$	0.64273(1)	0.07132(2)	0.19727(4)	0.08206(6)
$BaSr_2Fe_2O_5Cu_2Se_2$	0.63849(2)	0.06960(3)	0.19384(2)	0.07896(8)
$BaCa_2Fe_2O_5Cu_2S_2$	0.64194(3)	0.07569(3)	0.19443(5)	0.08672(8)

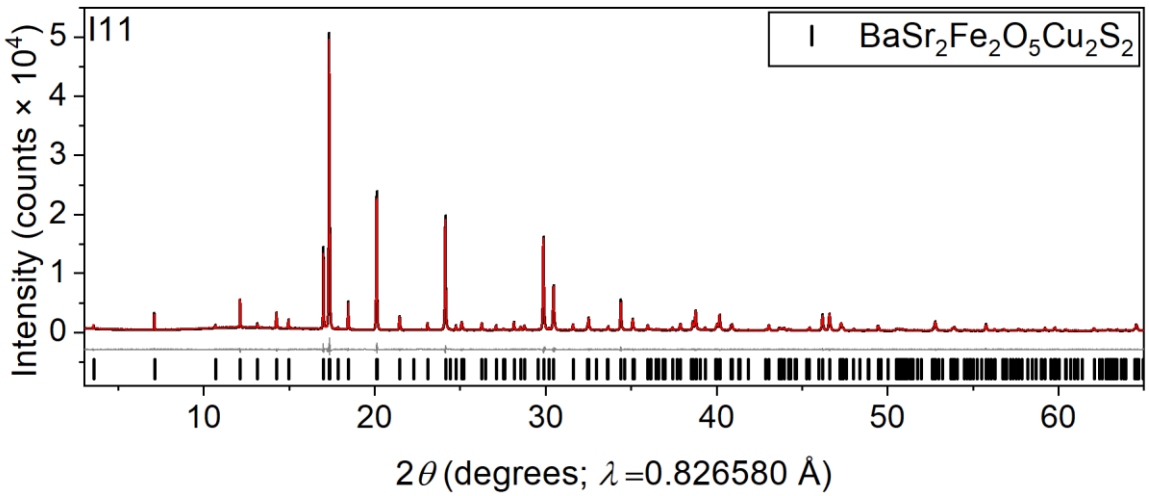


Figure 5.2 PXRD pattern of $BaSr_2Fe_2O_5Cu_2S_2$ (RDS006), measured on the MAC detector at I11 at room temperature, shown are data: black; fit: red; difference: grey Rwp: 5.660%.

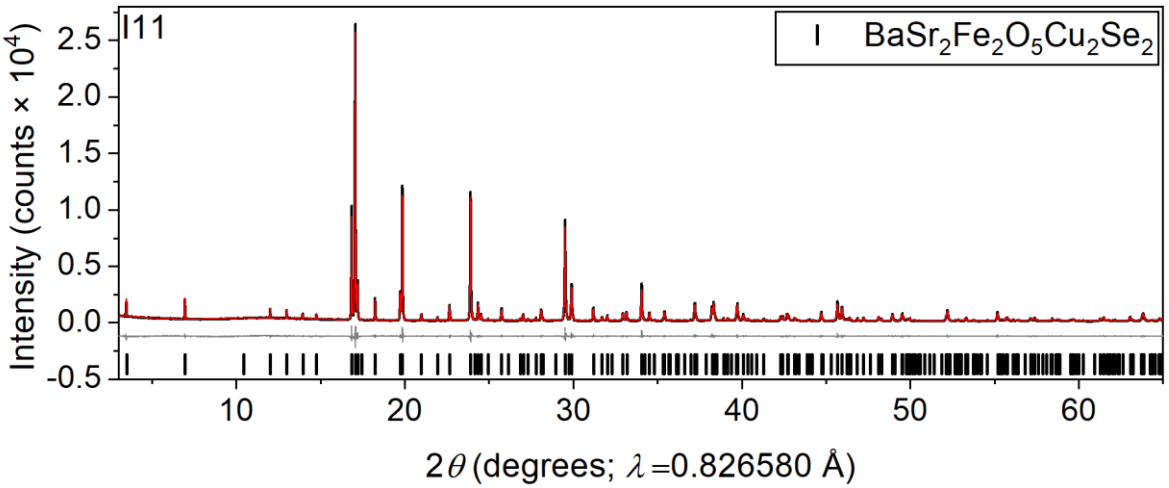


Figure 5.3 PXRD pattern of $BaSr_2Fe_2O_5Cu_2Se_2$, measured on the MAC detector at I11 at room temperature, shown are data: black; fit: red; difference: grey. R_{wp} 6.894 %.

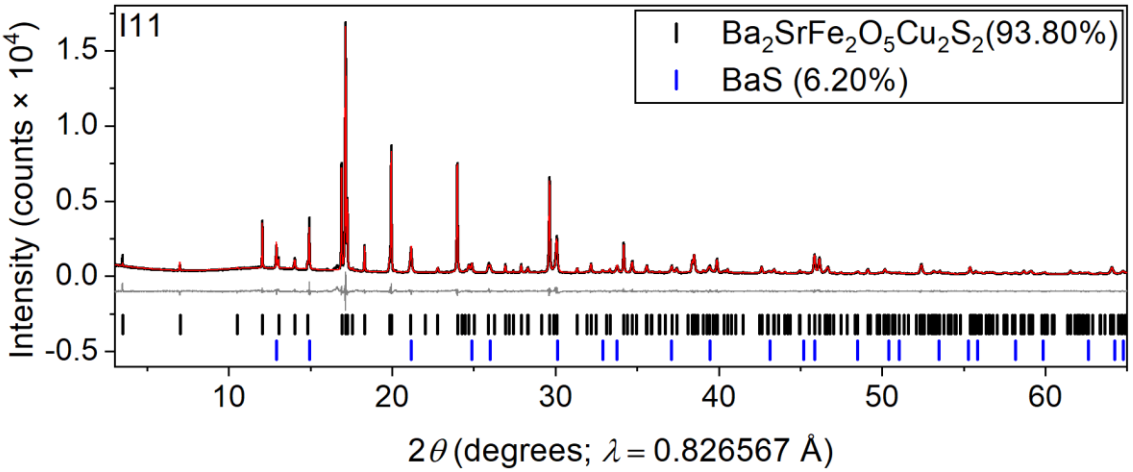


Figure 5.4 PXRD pattern of $Ba_2SrFe_2O_5Cu_2S_2$, measured on the MAC detector at I11 at room temperature, shown are data: black; fit: red; difference: grey. *Rwp* 6.971 %.

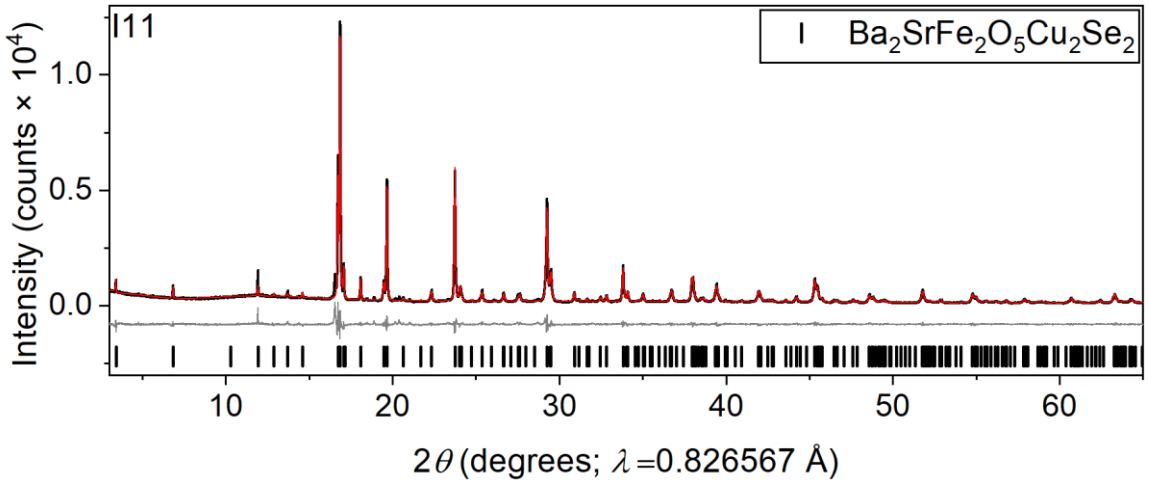


Figure 5.5 PXRD pattern of $Ba_2SrFe_2O_5Cu_2Se_2$, measured on the MAC detector at I11 at room temperature, shown are data: black; fit: red; difference: grey. *Rwp* 9.175 %.

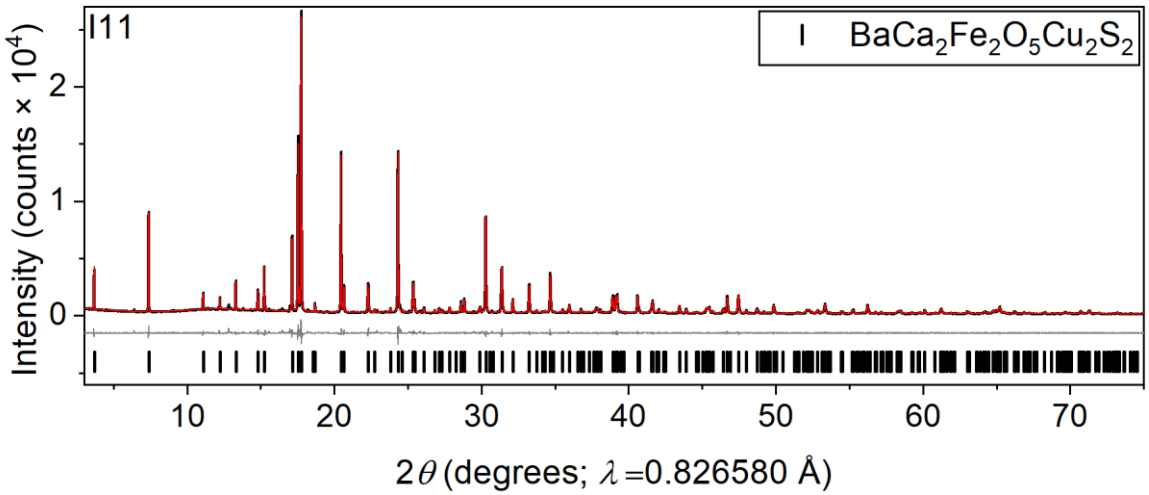


Figure 5.6 PXRD pattern of $BaCa_2Fe_2O_5Cu_2S_2$, measured on the MAC detector at I11 at room temperature, shown are data: black; fit: red; difference: grey. R_{wp} 6.939 %.

$BaCa_2Fe_2O_5Cu_2S_2$ and $BaSr_2Fe_2O_5Cu_2S_2$ were also measured as a function of temperature using PXRD from 100 K to 300 K using the cryostream on the I11 beamline. On close inspection of the diffraction patterns, it was clear that there were no extra peaks forming or peak splitting which would be indicative of a lowering of the cell symmetry or a cell expansion due to the formation of a superstructure via a distortion.

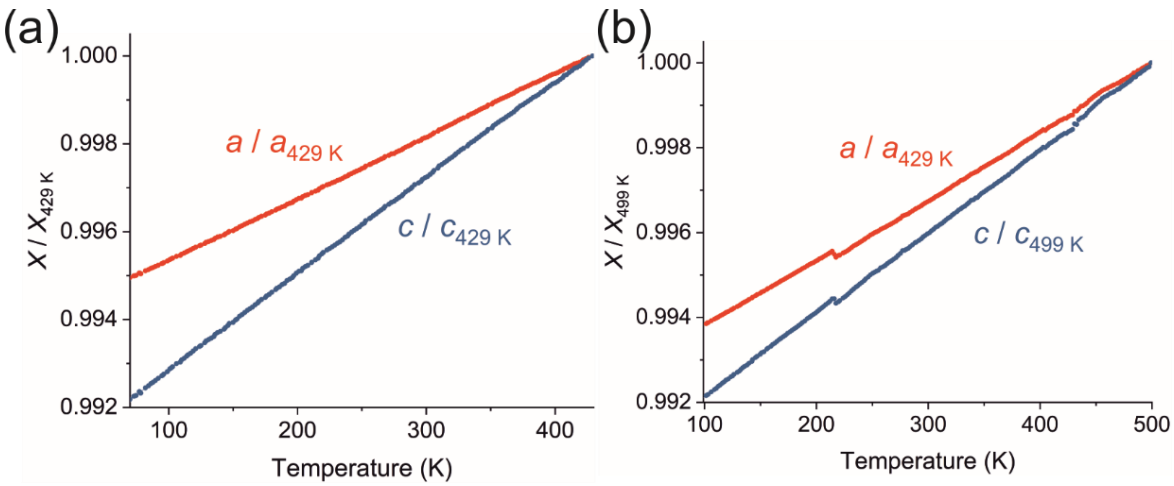


Figure 5.7 Variable temperature PXRD of **(a)** $BaCa_2Fe_2O_5Cu_2S_2$ and **(b)** $BaSr_2Fe_2O_5Cu_2S_2$, showing how the normalized lattice parameters vary with temperature, the kink around 220 K in (b) is presumably an artefact of the diffractometer or sample environment.

A plot of the lattice parameters against temperature showed a smooth trend, with the increases being attributed to the thermal expansion of the solid (see Figure 5.7) whereby the average coefficients of volume expansion over the temperatures $100 < T(K) < 429 / 499$ were 5.04 and 5.07 x 10^{-5} K^{-1} respectively for $BaCa_2Fe_2O_5Cu_2S_2$. and $BaSr_2Fe_2O_5Cu_2S_2$.

Table 5.3 shows the expected trends of the lattice parameters on cation and anion substitution whereby incorporation of larger radii ($r(Ba^{2+}) > r(Sr^{2+}) > r(Ca^{2+})$ and $r(Se^{2-}) > r(S^{2-})$)[9] results in larger refined cell parameters as would be expected. The more pronounced increase along *c* is a common characteristic of layered compounds and in this case, it is more pronounced due to the increase in the alkaline earth radius. The relative rigidity of the Fe-O(1) bonds which are close to being orientated within the *ab*-plane limits the amount of expansion within the basal *ab*-plane (≈ 1 %) with respect to the magnitude achievable within the stacking direction due to the weak interaction between the Fe ions and the chalcogenide ions and the flexibility of the Cu*Ch*$_4$ tetrahedra (≈ 10 %).

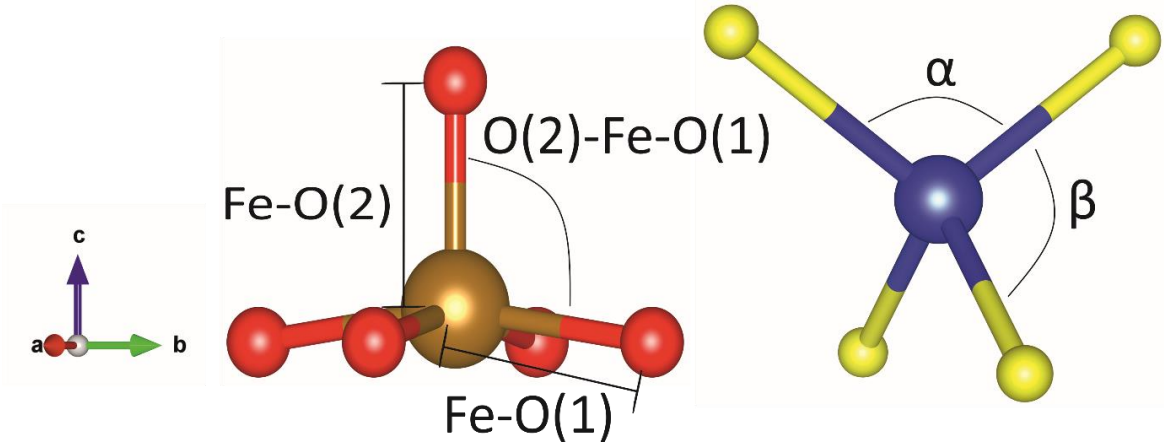


Figure 5.8 Defined bond lengths and angles from Table 5.4 showing the square pyramidal nature of the FeO_5 pyramid along with the anti-fluorite $[Cu_2Ch_2]^{2-}$ layer.

This expansion leads to 2 general trends which can be observed in Table 5.3. First, the expansion of the *ab*-plane of the unit cell when incorporating larger ions leads to an

expansion of the copper chalcogenide layer in the basal directions and a corresponding compression of the copper chalcogenide layer along the *c* direction, this leads to an increase in the *Ch*-*Cu*-*Ch* angle α defined in Figure 5.8 in Figure 5.9 on going from $Sr_3Fe_2O_5Cu_2Ch_2$ to $Ba_3Fe_2O_5Cu_2Ch_2$ for a given chalcogenide along with a corresponding decrease in β.

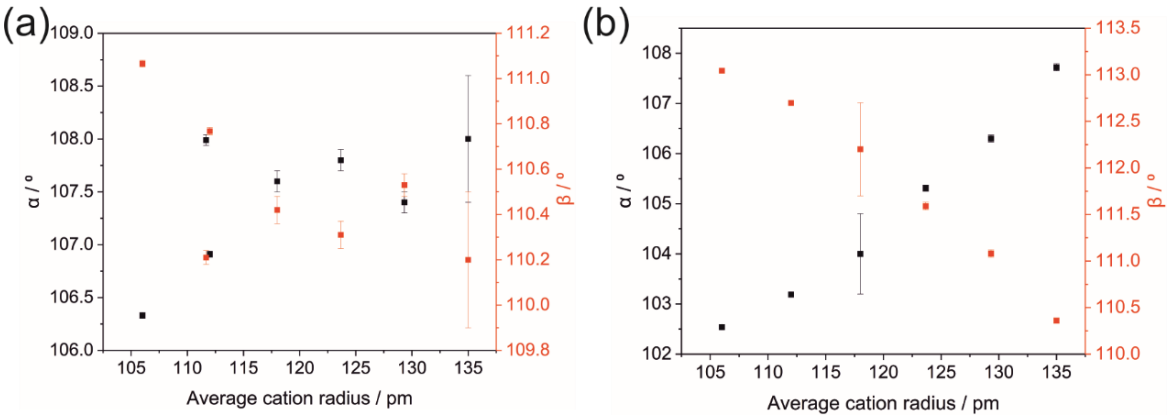


Figure 5.9 Behaviour of the α and β angle as defined in Figure 5.8 across the full family of $Ae_3Fe_2O_5Cu_2Ch_2$ (*Ae* = Ba, Sr, Ca) compounds for **(a)** Selenides and **(b)** Sulfides as a function of the average cation radius.

Another trend of note is the general behaviour of the FeO_5 pyramids across the series (also Figure 5.8). For example, the incorporation of successively larger, Ba^{2+} cations from $BaCa_2Fe_2O_5Cu_2S_2$ to $Ba_3Fe_2O_5Cu_2S_2$ results in an expansion of the unit cell in the *ab*-plane, which directly translates into an elongation of the Fe-(O)1 bonds along the base of the pyramid, which are almost parallel to the *ab*-plane. The Fe-O(2) bond length cannot contract sufficiently to compensate, especially when large Ba^{2+} cations are accommodated in the 12-coordinate sites in the oxide slabs because the O(2) ions are shared by two Fe cations. This is shown clearly in Figure 5.10 whereby there is a clearly positive correlation between the unit cell volume and the length of the Fe-O(1) bond length whereas the Fe-O(2) bond length is relatively invariant with cell volume for all the compounds except for $BaCa_2Fe_2O_5Cu_2S_2$ and $Ba_3Fe_2O_5Cu_2S_2$ which are somewhat anomalous. $Ba_3Fe_2O_5Cu_2S_2$ should be treated with caution as the sample was not phase pure and had refined parameters extracted from lab data

only. To verify this result, a purer sample would need to be synthesised and analysed using SPXRD to gauge the bond lengths within $Ba_3Fe_2O_5Cu_2S_2$ more accurately. The same cannot be said for $BaCa_2Fe_2O_5Cu_2S_2$. Multiple refinements to rule out a false minima concluded that the Fe-O(2) bond length does seem to be lengthened, however as can be seen in Figure 5.11, the bond valence sum is in line with closely related analogues. PND would be required to determine the magnetic moment of Fe^{3+} in $BaCa_2Fe_2O_5Cu_2S_2$ to confirm that it follows the trend in bond valence sum against moment as shown in 5.2.3.

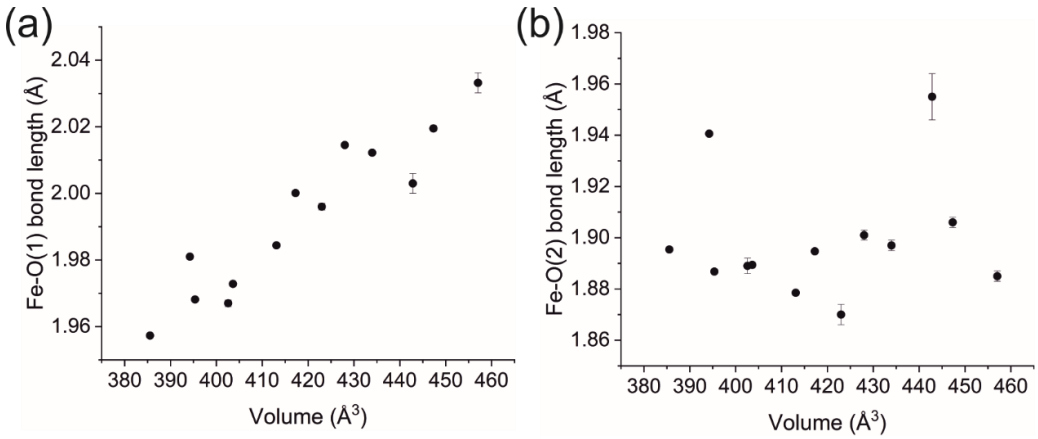


Figure 5.10 The behaviour of the **(a)** Fe-O(1) and **(b)** Fe-O(2) bond lengths in $Ae_3Fe_2O_5Cu_2Ch_2$. (*Ae* = Ba, Sr, Ca; *Ch* = S, Se).

Thus, the Fe bond valence sum (Table 5.3, Figure 5.11 and Figure 5.19) shows significant variation for these phases and is notably small in the Ba-rich phases. The implications of this for the magnetic ordering are discussed in section 5.3.3.

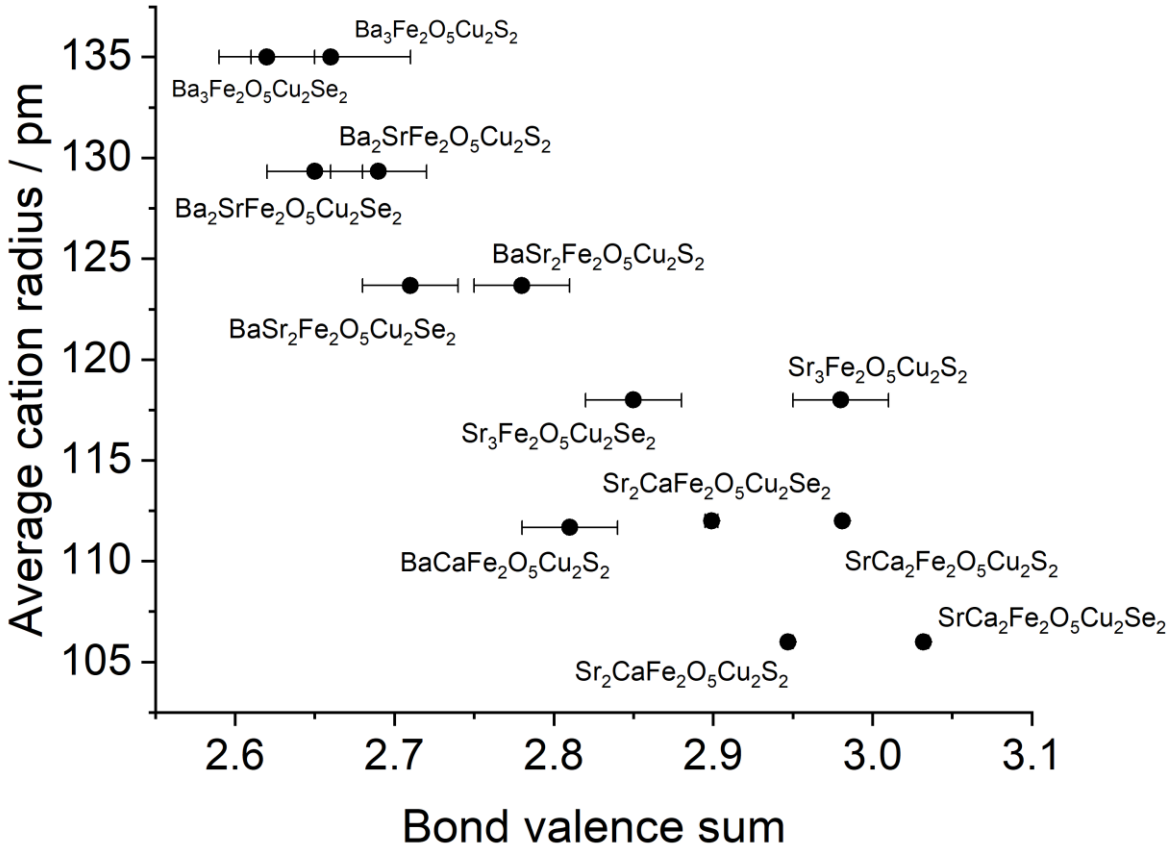


Figure 5.11 How the average cation radius correlates with the Fe bond valence sum across the full family of $Ae_3Fe_2O_5Cu_2Ch_2$ (*Ae* = Ba, Sr, Ca; *Ch* = S, Se) compounds.

3 g of $BaSr_2Fe_2O_5Cu_2Ch_2$ (*Ch* = S, Se) were also measured using PND on the WISH diffractometer[84] at the ISIS neutron and muon facility in Oxford, UK. Despite being primarily used for magnetic structure determination, WISH still provides more than adequate data in its high-resolution banks with good signal-to-noise to extract meaningful structural parameters. The room temperature Rietveld refinements are shown below in Figures 5.12 and 5.13.

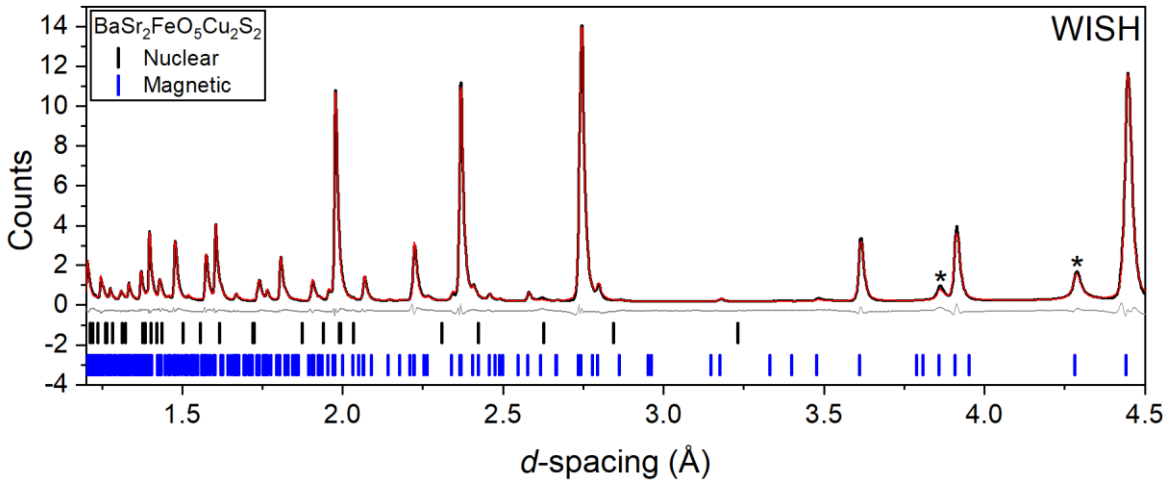


Figure 5.12 Rietveld refinement at RT of $BaSr_2Fe_2O_5Cu_2S_2$ against bank 5/6 of the WISH diffractometer at ISIS. R_{wp} = 3.790 %; χ^2 = 0.053.

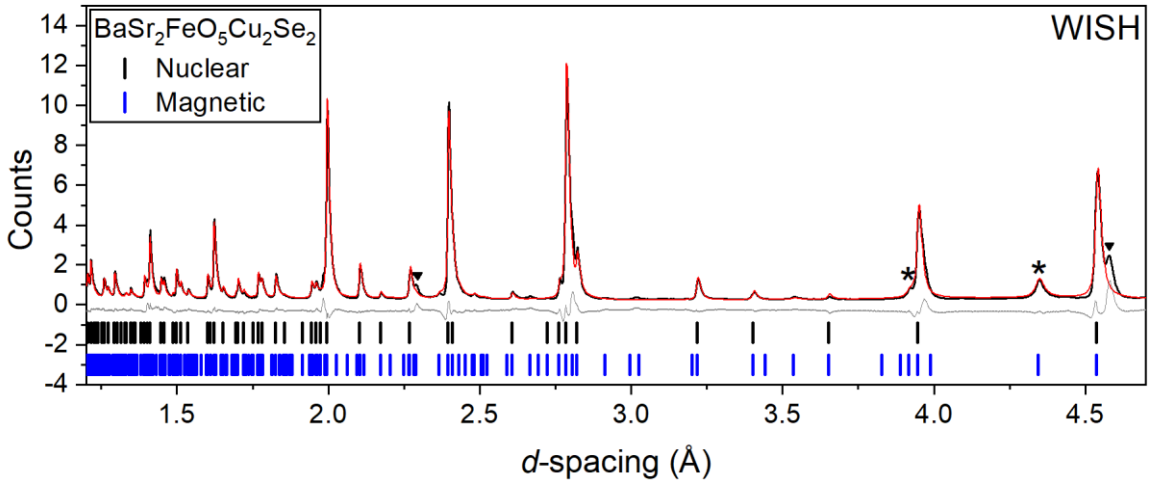


Figure 5.13 Rietveld refinement at RT of $BaSr_2Fe_2O_5Cu_2Se_2$ against bank 5/6 of the WISH diffractometer at ISIS. R_{wp} = 9.115 %; χ^2 = 0.114.

As is shown by the * in the refinements, there is already anti-ferromagnetic ordering of the Fe^{3+} cations at room temperature in both of these materials. The peak with an inverted triangle at approximately 4.5 Å aligns with the (111) reflection of FeO, however, FeO is not magnetically ordered at room temperature and therefore this remains an unidentified impurity which is surprising as the sample appeared phase pure as according to SPXRD. A more in-depth discussion of the magnetism at lower temperatures when the ordered Fe^{3+} moments have almost saturated can be found in section 5.3.3.

Table 5.3. Refined U_{iso} parameters for $Ae_{3x}Ae'_xFe_2O_5Cu_2Ch_2$ (Ae/Ae' = Ba, Sr, Ca; Ch = S, Se).

	Ba_2Sr / S_2	$BaSr_2 / S_2$	$BaCa_2 / S_2$	Ba_2Sr / Se_2	$BaSr_2 / Se_2$
$U_{iso}(Ae1)$ (Å^2)	0.0063(3)	0.0063(1)	0.0029(1)	0.0127(4)	0.0127(2)
$U_{iso}(Ae2)$ (Å^2)	0.0063(2)	0.0063(1)	0.0045(2)	0.0127(4)	0.0165(3)
U_{iso}(Cu1) (Å^2)	0.0380(4)	0.0161(2)	0.0181(2)	0.0241(5)	0.0066(2)
U_{iso}(Fe1) (Å^2)	0.0089(3)	0.0055(2)	0.0034(1)	0.0000(4)	0.0038(3)
U_{iso}(S1) (Å^2)	0.0096(6)	0.0070(3)	0.0073(2)	0.0032(4)	0.0114(2)
U_{iso}(O1) (Å^2)	0.0104(9)	0.0062(4)	0.0049(4)	0.000(1)	0.019(1)
U_{iso}(O2) (Å^2)	0.038(3)	0.0051(9)	0.005(1)	0.036(4)	0.020(2)

Table 5.4. Refined U_{11}, U_{22}, U_{33} parameters from PND at 300 K.

	$BaSr_2Fe_2O_5Cu_2S_2$	$BaSr_2Fe_2O_5Cu_2Se_2$
$U_{11}(Ae) = U_{22}(Ae)$ (Å^2)	0.0117(4)	0.0132(7)
$U_{33}(Ae)$ (Å^2)	0.022(1)	0.017(1)
U_{11}(Cu) = U_{22}(Cu) (Å^2)	0.0191(7)	0.052(2)
U_{33}(Cu) (Å^2)	0.0312(9)	0.009(2)
U_{11}(Fe) = U_{22}(Fe) (Å^2)	0.0121(3)	0.0062(6)
U_{33}(Fe) (Å^2)	0.0066(9)	0.022(2)
$U_{11}(Ch) = U_{22}(Ch)$ (Å^2)	0.015(2)	0.004(1)
$U_{33}(Ch)$ (Å^2)	0.015(2)	0.028(2)
U_{11}(O1) (Å^2)	0.0151(8)	0.000(1)
U_{22}(O1) (Å^2)	0.0202(6)	0.007(1)
U_{33}(O1) (Å^2)	0.0131(6)	0.014(1)
U_{11}(O2) = U_{22}(O2) (Å^2)	0.023(1)	0.018(2)
U_{33}(O2) (Å^2)	0.023(2)	0.016(3)

Table 5.5. Structural model for $Ba_{3-x}Sr_xFe_2O_5Cu_2Ch_2$ (x = 0, 1, 2, 3) (*Ch* = S, Se) and $BaCa_2Fe_2O_5Cu_2S_2$, along with selected bond distances and angles. All crystallographic data has been obtained from Rietveld refinement at room temperature. The magnetic moment, μ_B, has been obtained from Rietveld refinement at the lowest measured temperature from PND.

	Radiation	Diffractometer	a (Å)	c (Å)	Volume (Å^3)	Fe-O(1) [x4] (Å)	Fe-O(2) [x1] (Å)	α *Ch*-Cu-*Ch* [×2] (º)	β *Ch*-Cu-*Ch* [×4] (º)	O(1)-Fe-O(2) [×4] (º)	Fe BV Sum	μ_B
$Ba_3Fe_2O_5Cu_2S_2$[133]	X-Ray	X'Pert Pro	3.9988(2)	27.694(1)	442.84(4)	2.003(3)	1.955(9)	108.0(6)	110.2(3)	100.3922(3)	2.66(5)	-
$Ba_3Fe_2O_5Cu_2Se_2$[133]	PND	D2B[135]	4.02937(5)	28.1507(5)	457.05(1)	2.0332(3)	1.885(2)	107.72(7)	110.36(3)	97.74(6)	2.62(3)	5.22(5) / 5 K
$Sr_3Fe_2O_5Cu_2S_2$[11]	X-Ray	Rigaku Dmax	3.912(1)	26.313(7)	402.58(3)	1.967(1)	1.889(3)	107.6(1)	110.42(6)	96.1(3)	2.98(3)	-
$Sr_3Fe_2O_5Cu_2Se_2$[29]	PND	G4-1 2-axes	3.95770(4)	27.0045(4)	422.98(1)	1.996(1)	1.870(4)	105.0(8)	112.2(5)	97.4(3)	2.85(3)	3.6(2) / 2 K
$Ba_2SrFe_2O_5Cu_2S_2$	X-Ray	I11[83]	3.977(1)	27.061(7)	428.0(2)	2.0145(7)	1.901(2)	107.4(1)	110.53(5)	99.2(1)	2.69(3)	-
$Ba_2SrFe_2O_5Cu_2Se_2$	X-Ray	I11[83]	4.01827(3)	27.7036(4)	447.317(9)	2.0195(8)	1.906(2)	106.30(7)	111.08(4)	95.8(2)	2.65(3)	-
$BaSr_2Fe_2O_5Cu_2S_2$	PND	WISH[84]	3.95510(4)	26.6748(4)	417.27(1)	2.0001(2)	1.8947(8)	107.8(1)	110.31(6)	98.61(5)	2.78(3)	3.40(1) / 10 K
$BaSr_2Fe_2O_5Cu_2Se_2$	PND	WISH[84]	3.99126(7)	27.2421(7)	433.97(2)	2.0122(3)	1.897(2)	105.31(6)	111.59(4)	97.37(8)	2.71(3)	3.38(5) / 10 K
$BaCa_2Fe_2O_5Cu_2S_2$	X-Ray	I11[83]	3.9214(1)	25.638(1)	395.242(3)	1.9810(3)	1.9406(7)	107.99(5)	110.21(3)	98.21(7)	2.81(3)	

5.3.2 Cation ordering

The coherent neutron scattering lengths for Ca, Sr and Ba are 4.70(2), 7.02(2) and 5.07(3) fm respectively,[80] whereas for X-ray diffraction the scattering lengths are proportional to the atomic number (Z) of the element and hence since there is Ba (high Z) present in all the samples, it was appropriate to refine the occupancies from the SPXRD data which should provide a higher contrast between the alkaline earth metals and are not encumbered by magnetic Bragg scattering. As briefly mentioned in the section 5.3.1, within the refinement, one parameter was used to refine the distribution within each sample with the results displayed in Table 5.6.

Table 5.6. Ba^{2+} occupancies for $Ba_{3-x}Sr_xFe_2O_5Cu_2Ch_2$ (x = 1, 2; *Ch* = S, Se) and $BaCa_2Fe_2O_5Cu_2S_2$ on the larger 12-coordinate site and the smaller 8-coordinate site, for which the sites multiplicity and Wyckoff symbol are shown in brackets.

	Ba occupancy of 12-coordinate site (2*b*)		Ba occupancy of 8-coordinate site (4*e*)	
	Refined	Statistical	Refined	Statistical
$BaCa_2Fe_2O_5Cu_2S_2$	0.925(2)	0.333	0.038(1)	0.333
$BaSr_2Fe_2O_5Cu_2S_2$	0.656(2)	0.333	0.172(1)	0.333
$BaSr_2Fe_2O_5Cu_2Se_2$	0.717(2)	0.333	0.141(1)	0.333
$Ba_2SrFe_2O_5Cu_2S_2$	0.932(3)	0.667	0.534(1)	0.667
$Ba_2SrFe_2O_5Cu_2Se_2$	0.873(5)	0.667	0.563(3)	0.667

It is clear from Table 5.6 that the larger ions tend to occupy the larger 12-coordinate site and the smaller ions occupy the smaller 8-coordinate site. In the $Ae_3Fe_2O_5Cu_2Ch_2$ structure, there are half as many of the larger 12 coordinate sites (12 × O) as there are of the 8-coordinate sites (4 × O + 4 × *Ch*) and so one would expect when there are 2 smaller cations and one large, then there would be a large preference for most of the large cations to occupy the 12-coordinate site, and the majority of the small cations to occupy the 8-coordinate site. But when there are 2 large cations and one small, it would be expected that the majority of the

12-coordiante site would be occupied by the larger cation, and there would be an even distribution amongst the 8-coordiante site between the larger and smaller cations.

Analysis of compounds in which the ratio of the larger to smaller alkaline earth is 1:2 is shown in Figure 5.14. Looking at the *Ae* site variation it can also be seen from the average ionic radii ratios[9] (8 and 12 coordinate) that there is a larger site preference from $BaCa_2Fe_2O_5Cu_2S_2$ ($<r(Ba^{2+})/r(Ca^{2+})>$ = 1.20) as opposed to $BaSr_2Fe_2O_5Cu_2S_2/Se_2$ ($<r(Ba^{2+})/r(Sr^{2+})>$ = 1.11) and $SrCa_2Fe_2O_5Cu_2S_2/Se_2$ ($<r(Sr^{2+})/r(Ca^{2+})>$ = 1.08). The Sr/Ca compounds have a slightly greater preference for ordering than their Ba/Sr analogues which is in slight contradiction to the expectation based on the radius ratios. This is perhaps due to the small absolute value of the radius of the Ca^{2+} cation which has a very strong preference to be situated within a smaller coordination environment.

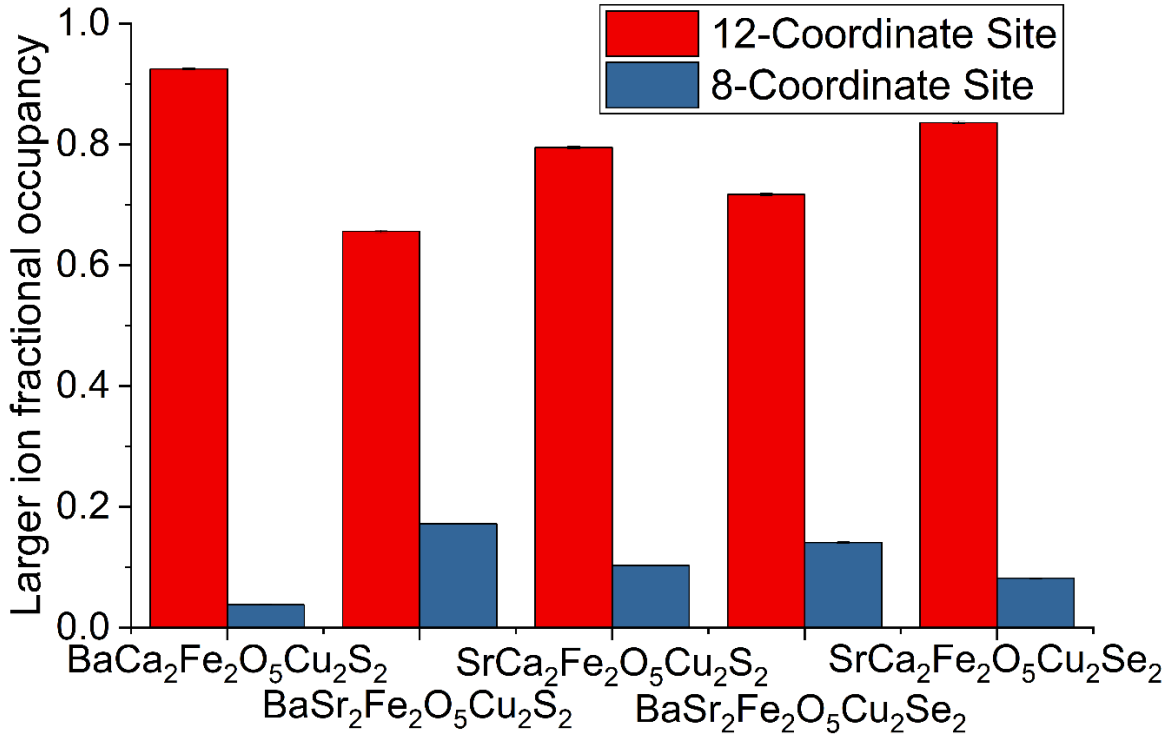


Figure 5.14 A graphical representation of the larger ion occupancies of the two available alkaline earth metal sites for $BaCa_2Fe_2O_5Cu_2S_2$, $BaSr_2Fe_2O_5Cu_2Ch_2$ (*Ch* = S, Se) along with $SrCa_2Fe_2O_5Cu_2Ch_2$ (*Ch* = S, Se).[14]

5.3.3 Low temperature PND to probe magnetic ordering

The $BaSr_2Fe_2O_5Cu_2Ch_2$ (*Ch* = S, Se) samples were measured at temperatures down to 10 K on the WISH diffractometer at the ISIS facility to measure the magnetic ordering. A representative Rietveld refinement is shown in Figure 5.15.

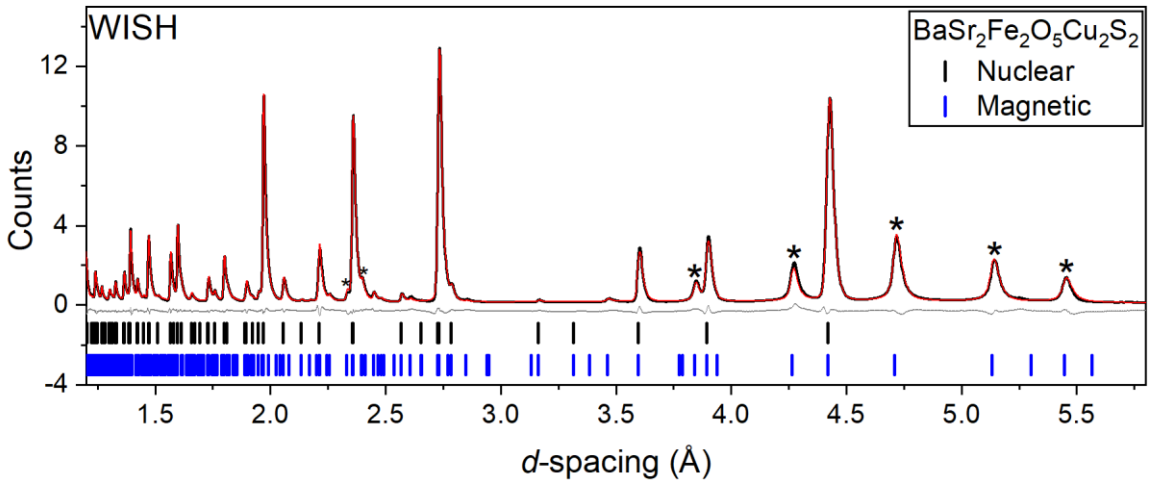


Figure 5.15 Rietveld plot of bank 3/8 of WISH for $BaSr_2Fe_2O_5Cu_2S_2$ (RDS063), measured at 10 K. The * indicate magnetic Bragg peaks and are discussed later for the magnetic structure. *Rwp* 3.395 %.

Additional peaks to those that could be accounted for using the nuclear model were evident at room temperature and these increased in intensity on cooling as shown in Figure 5.15.

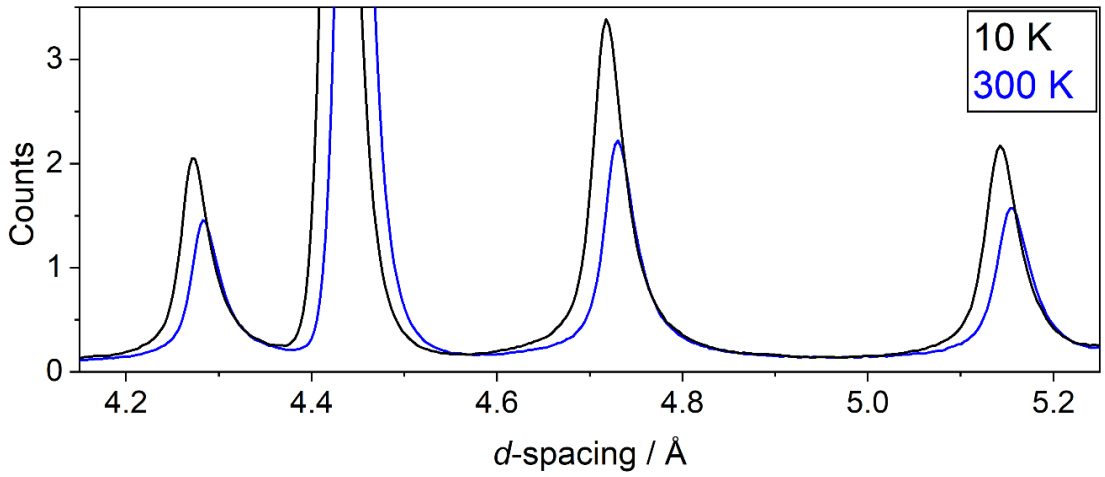


Figure 5.16 Zoomed in region of Figure 5.15 focusing on the peaks increasing in intensity on cooling in the high *d*-spacing regime and hence more likely to be magnetic in origin.

The additional reflections were limited to the larger *d*-spacing region and this and their evolution with temperature suggested that they were magnetic in origin. Measurements at higher temperatures would be needed to determine the Néel temperatures for these samples; the magnetic susceptibility data measured below room temperature in the magnetically ordered region were rather uninformative and often dominated by small amounts of impurity phases. The magnetic Bragg peaks were indexed on a $\sqrt{2}a \times \sqrt{2}a \times c$ expansion of the nuclear cell.

Symmetry-mode analysis was conducted using the ISODISTORT[124] software. The structures were initially analysed assuming *P*1 space group symmetry so that all possible modes could be considered. In conjunction with TOPAS V6, it was found that for the members of the solid solution, a model activating the mX1-(*a*,*b*) A2 mode along with the mX3- (*a*,*b*) E mode gave the best R_{wp} along with the best visually satisfactory fit, whereby the moments are tilted away from the *ab*-plane. This tilting is in contrast to the result when there is only one cation present such as in $Ba_3Fe_2O_5Cu_2Se_2$[133] or $Sr_3Fe_2O_5Cu_2Se_2$[29] where the Fe^{3+} moments couple antiferromagnetically in the basal plane as shown in Figure 5.17(a) but the observation of tilting is quantitatively similar (Table 5.7) to the results for other members of the isostructural series with a mixture of alkaline earth cations: $Sr_{3-x}Ca_xFe_2O_5Cu_2Ch_2$ (x = 1, 2) (*Ch* = S, Se) where the Fe^{3+} moments are still anti-ferromagnetically coupled but tilted away from the basal plane.

Table 5.7. The magnitude and tilt-angle of the Fe^{3+} moments for $Ba_3Fe_2O_5Cu_2Se_2$ at 5 K and for $Ba_{3-x}Sr_xFe_2O_5Cu_2Ch_2$ (x = 2; Ch = S, Se) at 10 K, compared with reported related compounds.

	Total ordered moment (μ_B)	Tilt angle from ab-plane (º)
$Ba_3Fe_2O_5Cu_2Se_2$[134]	5.22(5)	0
$BaSr_2Fe_2O_5Cu_2Se_2$	3.38(5)	59.7(7)
$BaSr_2Fe_2O_5Cu_2S_2$	3.40(1)	55.8(2)
$Sr_3Fe_2O_5Cu_2Se_2$[29]	3.6(2)	0
$Sr_2CaFe_2O_5Cu_2Se_2$[14]	3.376 (14)	57.7 (3)
$Sr_2CaFe_2O_5Cu_2S_2$[14]	3.068 (20)	58.8 (4)
$SrCa_2Fe_2O_5Cu_2Se_2$[14]	3.433 (15)	58.6 (3)
$SrCa_2Fe_2O_5Cu_2S_2$[14]	2.930 (16)	57.5 (3)

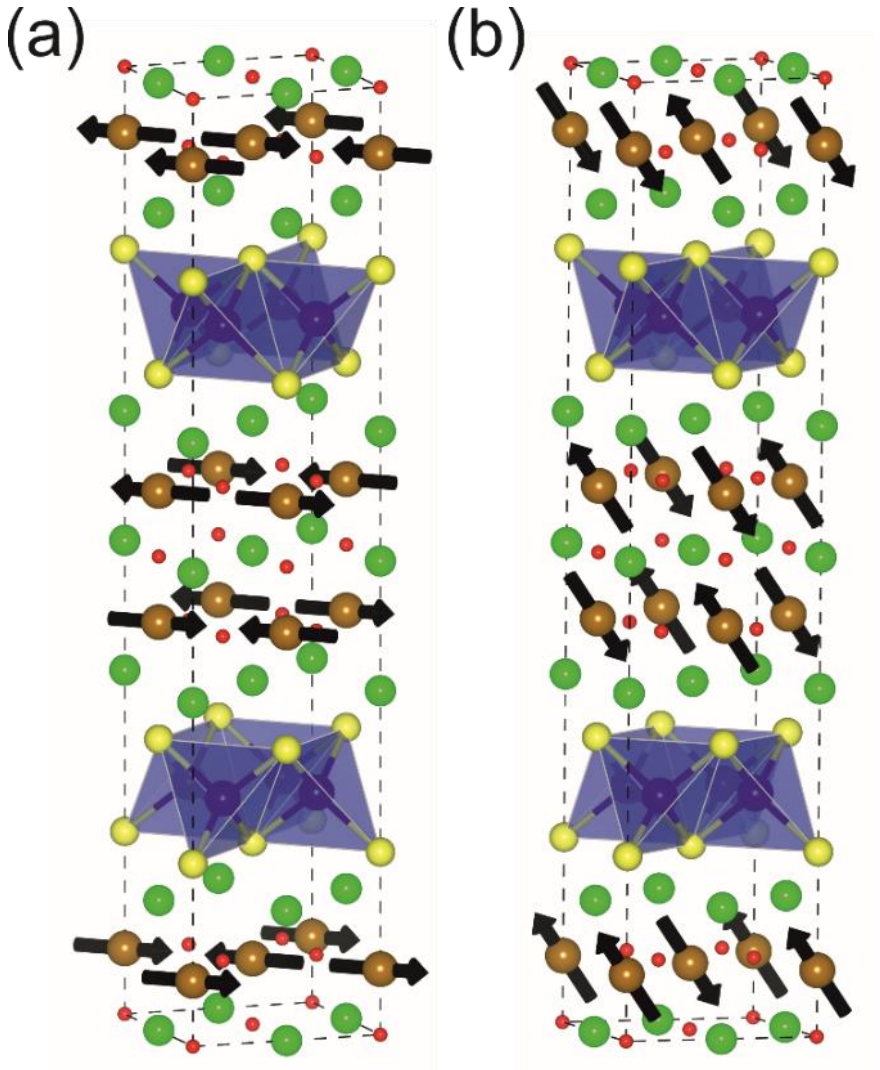


Figure 5.17(a) The magnetic structure of $Ba_3Fe_2O_5Cu_2Se_2$, with Fe^{3+} moments aligned in the *ab*-plane.[134] **(b)** The magnetic structure of $BaSr_2Fe_2O_5Cu_2S_2$ with Fe^{3+} moments tilted between the *ab*-plane and the *c*-axis.

There is a fairly good correlation between the size of the long range ordered moment and the Fe^{3+} bond valence sum (Figure 5.18). As the unit cell gets larger, the Fe-(O)1 bonds, which lie almost parallel to the *ab*-plane, are forced to elongate, and the Fe-O(2) bond cannot contract sufficiently to compensate because O(2) is shared by two Fe ions and the larger alkaline earth cations are accommodated in the oxide slabs. In general, as the alkaline earth cations increase in size and the unit cell increases in volume, the Fe bond valence decreases (Table 5.3). This slight under-bonding is expected to correspond to reduced covalency in the bonding and hence less of a reduction in the magnitude of the moment localised on the Fe centre. This is expected to result in a larger long range ordered moment for the larger cell volumes, which can be seen for $Ba_3Fe_2O_5Cu_2Se_2$, with its refined value of 4.22(5) μ_B being fairly close to the expected maximum value for a high spin d^5 ion of 5 μ_B. Figure 5.18 shows a strong negative correlation between the size of the refined long range ordered moment carried by Fe^{3+} and the Fe bond valence sum.

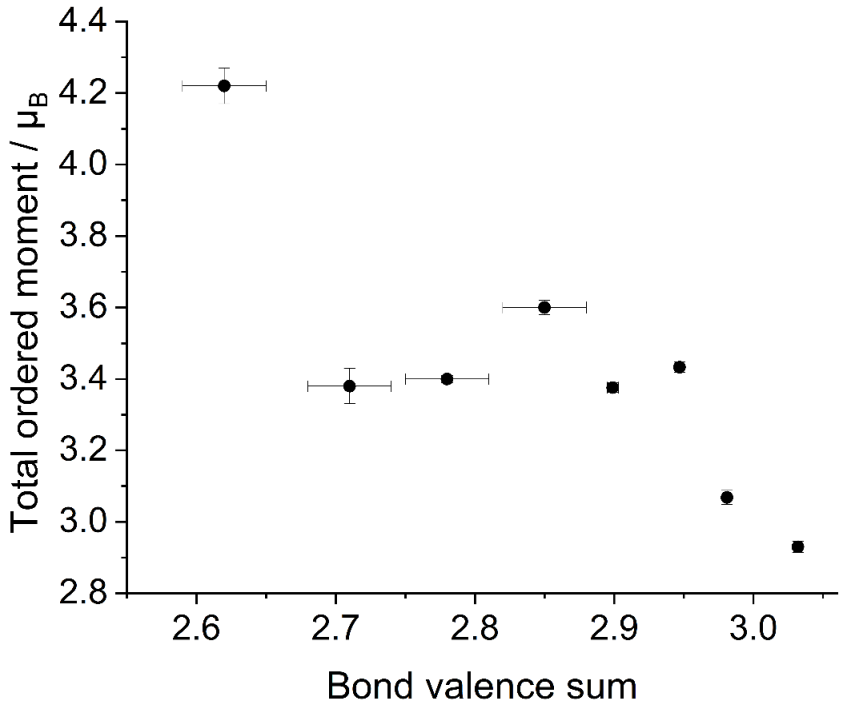


Figure 5.18 The negative correlation between the moment and the Fe bond valence sum across the full family of $Ae_3Fe_2O_5Cu_2Ch_2$ (*Ae* = Ba, Sr; *Ch* = S, Se) compounds.

With the Goodenough-Kanamori rules assisting in the prediction of superexchange interactions – it should also be possible to predict the alignment of the magnetic moments with respect to the basal plane in these transition metal systems relative to the ligand field and rationalised based on HOMO-LUMO interactions as discussed by Whangbo and co-workers.[136] The Fe^{3+} ions in the $Ae_3Fe_2O_5Cu_2Ch_2$ structure have C_{4v} symmetry leading to a $2(d\text{xz}, d\text{zy})^2 : 1(d\text{xy})^1 : 1\ (dz^2)^1 : 1\ (dx^2\text{-}y^2)^1$ orbital splitting. In these d^5 systems, the directional preference of the moments is weak because the HOMO and LUMO arise from different spin states as shown in Figure 5.19. The interaction between these 2 spin states results in $|\Delta L_z| = 1$ and therefore by Whangbo's arguments the Fe^{3+} moments should align parallel to the stacking direction. However, the high-spin configuration is much lower in energy than the low-spin configuration and thus there is little mixing with the ground state and so it would be expected that there would be a small / no preference for the spin orientation.

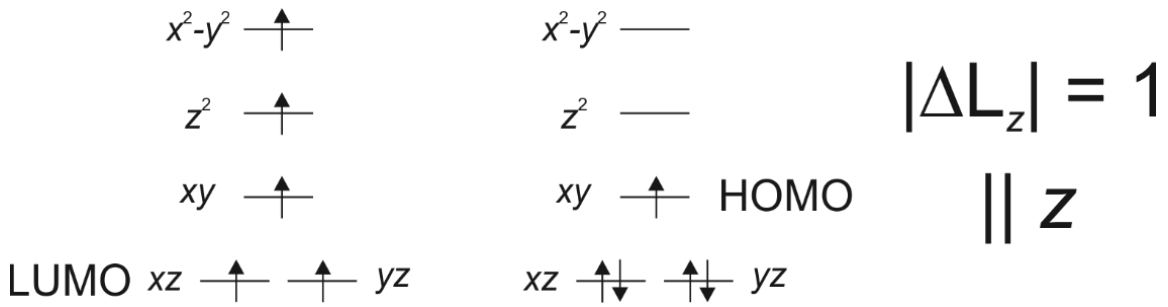


Figure 5.19 The HOMO-LUMO interaction present in the Fe^{3+} high spin d^5 cations, where this interaction must be with the low spin variant.

The observation is that the moments are oriented within the *ab*-plane when a single alkaline earth cation is present, but the introduction of disorder amongst the alkaline earth cations results in the moments tilting out of this plane, showing that for these d^5 species the directional preference is weak. There is no obvious correlation between the tilt angle and the degree of alkaline earth cation order.

5.3.4 Magnetometry

It was found that the *M vs H* isotherms for these samples were not linear at low fields which suggested small amounts of ferromagnetic impurities. The SQUID is much more sensitive than PXRD and hence can detect even trace amounts of such magnetic material. In this knowledge it was often the case that a 6 – 5 T subtraction was performed to obtain an accurate intrinsic measurement of the magnetic susceptibility using data for which the impurity was saturated. An example of such a correction is shown in Figure 5.20 for $BaSr_2Fe_2O_5Cu_2Se_2$ which has a sharp transition at ≈ 120 K. This is typical of the Verwey Transition indicating the presence of the mineral Fe_3O_4 in the sample.[137]

The magnetisation isotherms measured at 5 K for the samples have a small ferromagnetic component and are slightly asymmetric and displaced from the origin suggesting glassy behaviour but this is most likely dominated by the trace amount of impurity not detectable by PXRD but picked up in the SQUID.

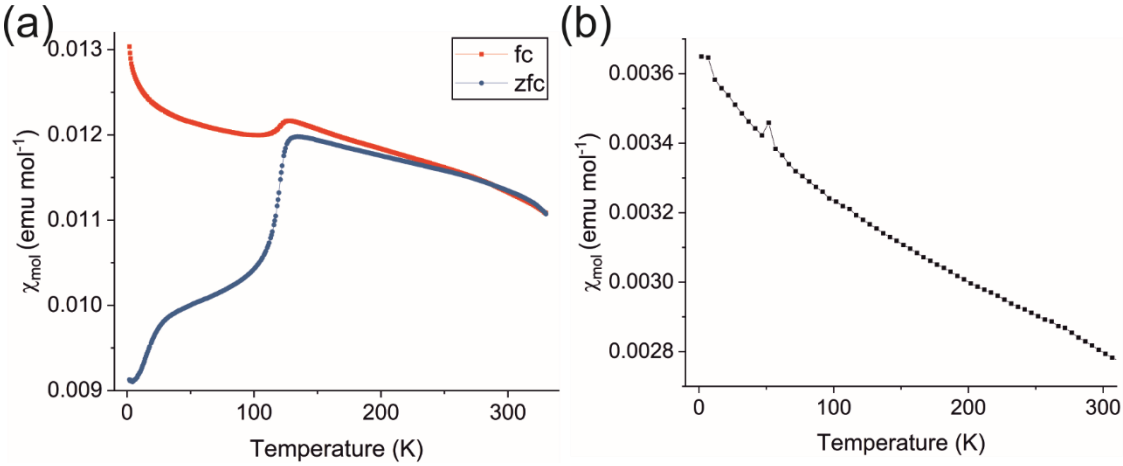


Figure 5.20 (a) ZFC / FC magnetic susceptibility (χ) of $BaSr_2Fe_2O_5Cu_2Se_2$ (RDS019) measured at 1000 Oe between 2K and 300 K and **(b)** measured using a 6 T – 5 T subtraction.

With the knowledge that the Néel temperature for the closely related Sr/Ca analogues is just under 600 K, high temperature magnetometry was also performed on some of the samples

in this chapter to see if there was any magnetic signal which would suggest a ballpark figure for the magnetic ordering transition – especially useful for compounds from which we were not able to perform a neutron study.

For these measurements, material was pressed into a 13 mm pellet, with a bar no wider than 5 mm or thicker than 2.5 mm cut using a scalpel. This bar was then attached to a temperature controller stick using Zicar cement. Heat loss was reduced by wrapping the sample in copper foil with the set-up kept under ultra-high vacuum to minimise heat transfer away from the sample via exchange gases. Measurements were then carried out as outlined in section 2.2.6.1.

The data for $BaCa_2Fe_2O_5Cu_2S_2$ and $BaSr_2Fe_2O_5Cu_2S_2$ are shown below in Figure 5.21. Despite high temperature PND results not being collected for $Sr_3Fe_2O_5Cu_2Ch_2$ (*Ch* = S, Se), calculations have been performed by Gordon to estimate the T_N to be around 500 K for these materials.[138] Furthermore, Sheath determined through PND that the T_N of $Ca_2SrFe_2O_5Cu_2Se_2$ was 568 K.[14] The T_N is directly influenced by the strength of the magnetic interactions between Fe^{3+} cations and hence a key structural parameter to determine the magnetic of the ordering temperature is the intra Fe-Fe bond distance within the iron oxide layers. This can most easily be seen between the Ae_2FeO_3Cu*Ch* structure and $Ae_3Fe_2O_5Cu_2Ch_2$ (section 1.3.1.1) whereby the fused square pyramids in the $Ae3Fe_2O_5Cu_2Ch_2$ structure enable a much closer Fe-Fe distance which leads to larger superexchange through the apical O, resulting in a larger T_N.

The novel materials from the $Ae_{3-x}Ae'_xFe_2O_5Cu_2Ch_2$ (*Ae/Ae'* = Ba, Sr, Ca; *Ch* = S, Se) series of compounds would be expected to have magnetic interactions of similar magnitude to that of Sheath's series of $Ae_{3-x}Ae'_xFe_2O_5Cu_2Ch_2$ (*Ae/Ae'* = Sr, Ca; *Ch* = S, Se) which seems to

be consistent with the high temperature magnetometry in Figure 5.21 with a broad maximum suggesting an approach towards anti-ferromagnetic ordering with Néel temperatures which are not well defined, but which appear to be around 700 K. High temperature PND would be needed to confirm this result or high temperature Mössbauer which Cario et al. also used in the characterisation of $Sr_3Fe_2O_5Cu_2Se_2$.

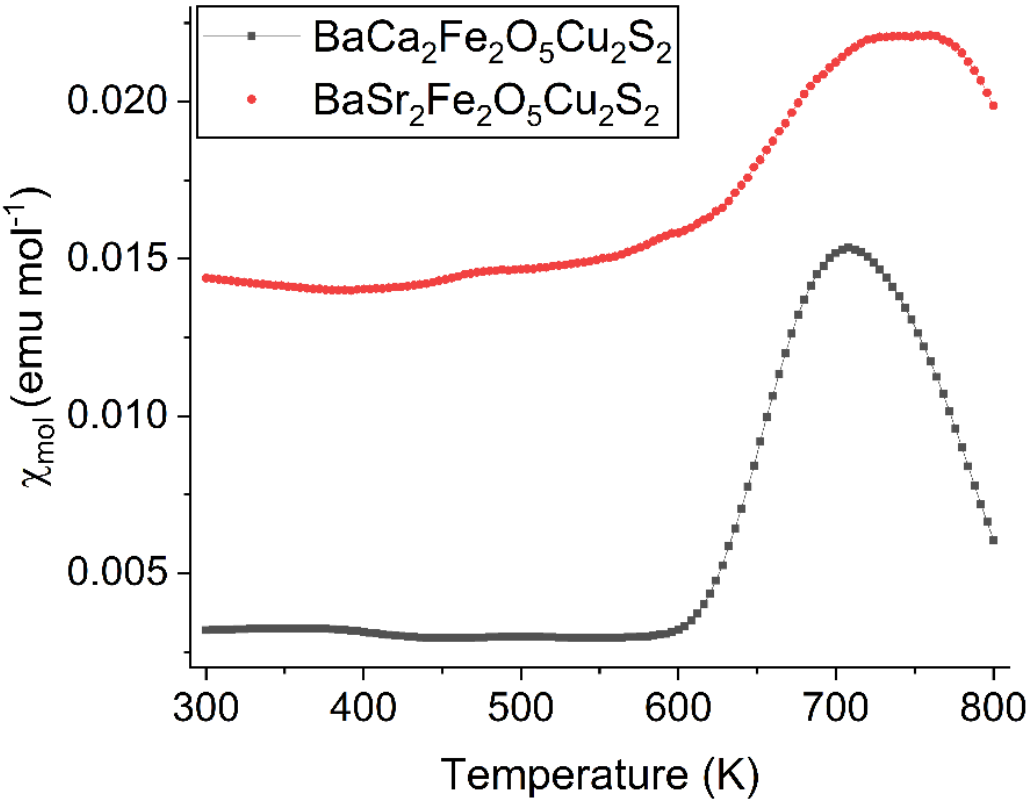


Figure 5.21 High temperature magnetometry results for $BaCa_2Fe_2O_5Cu_2S_2$ and $BaSr_2Fe_2O_5Cu_2S_2$ showing data from the "ZFC" measurement on warming in a field of 100 Oe.

5.4 Conclusion

In this chapter the novel compounds $Ba_{3-x}Sr_xFe_2O_5Cu_2Ch_2$ (x = 1, 2) (*Ch* = S, Se) as well as $BaCa_2Fe_2O_5Cu_2S_2$ have been synthesised for the first time. They are isostructural with the previously reported $Sr_3Fe_2O_5Cu_2S_2$.[11] For the solid solution $Ba_{3-x}Ae_xFe_2O_5Cu_2Ch_2$, there is a clear preference for Ba^{2+} to reside in the larger 12-coordinate site whereas smaller Sr^{2+} / Ca^{2+} prefer the smaller 8-coordinate site, similar to what Sheath *et al.* reported in the $Sr_{3-x}Ca_xFe_2O_5Cu_2Ch_2$ (x = 1, 2) (*Ch* = S, Se) family of compounds.[14]

Long range magnetic ordering can be indexed on a $\sqrt{2}a \times \sqrt{2}a \times c$ expansion of the nuclear cell for all the compounds with the saturated moments clearly showing a correlation with the bond valence sums for the Fe^{3+} ions, as such, the deviations from the spin only value of 5 μ_B across the series can be attributed to varying degrees of covalency which increases as the alkali metal ion mean radius decreases. For $Ba_3Fe_2O_5Cu_2Se_2$, similar to the Sr analogue, the magnetic moments align along the *ab*-plane,[29,134] whereas on the introduction of multiple alkaline earth metal cations, the moments tilt towards the *c* axis. This emphasises the point that once the orbital angular momentum is quenched and the spin-orbit coupling is small in magnitude as is the case for high spin Fe^{3+} ions, that the orientation of the moments is difficult to predict.

Chapter 6

6 Future work / conclusions

6.1 Future work

6.1.1 Introduction

A key concept within the scope of this thesis was the soft chemical concepts that were explored in chapter 4 with the Co-containing oxide chalcogenides. This has been followed up on with the investigation of the deintercalation of Ag from CeAgOSe which adopts the ZrSiCuAs structure which is shown in section 1.3.1.3 and which has similar coinage metal chalcogenide layers to the compounds discussed in the main body of this thesis. This preliminary work moves beyond control of the cation to control of the anion.

The first foray into lanthanide mixed-anion compounds with the ZrSiCuAs structure in section 1.3.1.3 was by Palazzi et al., with the fast ion conductor LaAgOS,[139,140] with the enhanced conducting properties facilitated by the increased cation mobility of coinage metal as confirmed by Wilmer et al.[141]

The Cu analogues were then duly discovered by Ueda et al.,[142] with the ultralow thermal conductivities of these solids recently reported for La*MOCh* (*M* = Cu, Ag; *Ch* = S, Se) by Ma et al.[143]

Since the discovery of these promising materials, within the group there has been a lot of interest for the cerium analogues Ce*MOCh* (*M* = Cu, Ag; *Ch* = S, Se) due to the facile

oxidation of Ce^{3+} ([Xe]4f^1) to Ce^{4+} which had the possibility of resulting in mixed-valence compounds.

Cassidy et al., showed that the high ionic mobility – particularly of Ag^+, allowed for soft chemical transformations[49] and that a metastable compound of nominal composition CeOS could be achieved with the oxidation state of Ce approaching +4.

Furthermore, they demonstrated that by reacting $CeAg_{0.8}SO$ with *n*-BuLi or performing electrochemical intercalation of Li on CeOS that the parent structure could be reformed with Li occupying the Ag sites as shown in Figure 6.1.

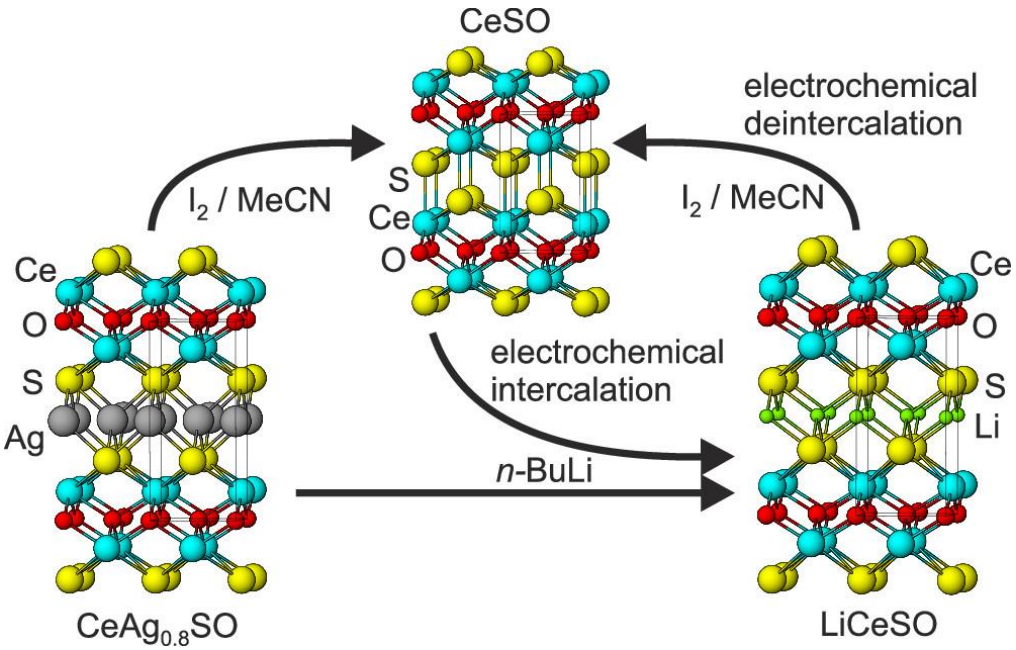


Figure 6.1 Schematic showing the topotactic and interchangeable reactions of $CeAg_{0.8}SO$.[49]

However, there was not full extrusion of the coinage metal with the diffraction data and TEM revealing stacking faults which were modelled as the sample having approximately 5 % residual Ag remaining. The presence of these faults was hypothesised to be due to the difficulty of stabilising the Ce^{4+} cations in the presence of sulfide which is a softer anion and tends to stabilise lower oxidation states.

The group has since done a lot of work investigating the selenide analogue with many masters students working on CeAgOSe and attempts to synthesis CeOSe.[144–147]

6.1.2 Synthesis of CeAgOSe and CeOSe

CeAgOSe was synthesised via the reaction of Ce (Alfa 99.9 %), CeO_2 (Alfa 99.99 %), Ag (99.99 %) and Se (Alfa 99.999 %). Due to the reactivity of the cerium ingot, it was imperative that the dull, outer layer was discarded in the solid waste as the glovebox does not have a perfect atmosphere and this thin outer coating was likely oxidised. Once complete, all reactants were stoichiometrically mixed and ground thoroughly as outlined in section 2.1.1.

The sealed silica ampoule containing the pellet in an alumina crucible was placed in a muffle furnace at 1000 ℃ for 6 days, before regrinding and X-raying to determine sample quality. If the sample was not deemed pure enough then the whole process was repeated. One reheat was usually sufficient to produce high quality samples of parent material in 1 – 2 g batches.

Soft chemical manipulations were carried out as outlines in section 2.1.4. For the samples in this thesis, an excess of both iodine (Alfa 99.99 %) and NaI (Alfa 99.9 %) was added to dry MeCN and transferred to a Schlenk tube using a cannula. I_2 has been shown to be a useful reagent in removal of ionically mobile coinage metal in mixed-anion materials, however, AgI is not soluble in MeCN and hence precipitates out and cannot be removed. Hence, the NaI is added to encourage the formation of AgI complexes such as [AgI_2^-] which are soluble and therefore can be filtered off.[69]

6.1.3 Room temperature powder X-ray diffraction

Once known to be of high purity, the samples were prepared for high resolution SPXRD as outlined in section 2.2.2. at the I11 beamline at Diamond Light Source Ltd. Rietveld refinement of the parent material, CeAgOSe is shown in Figure 6.2. This confirmed that it crystallises in the ZrSiCuAs structure in section 1.3.1.3.

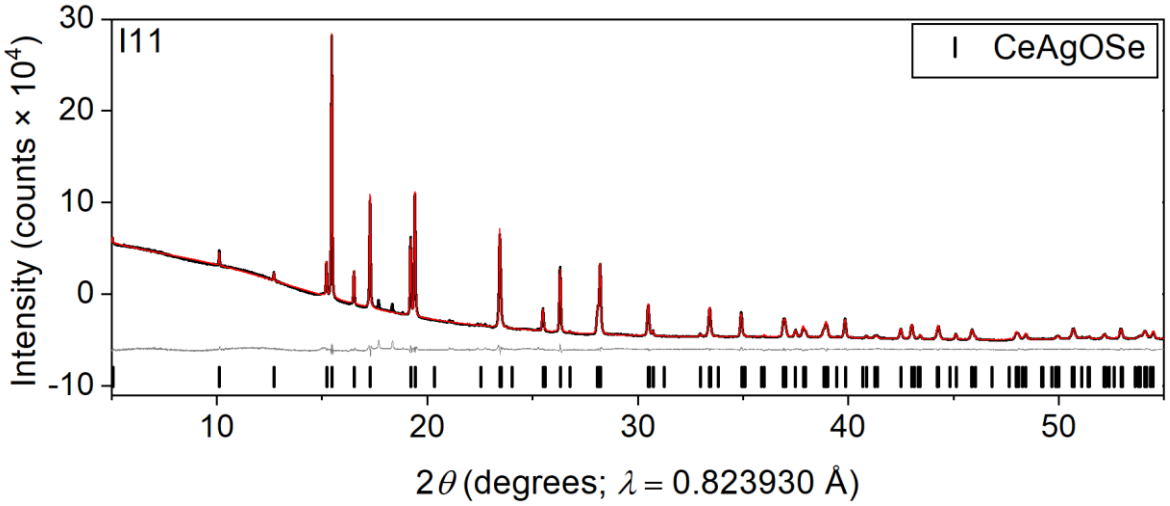


Figure 6.2 Rietveld refinement of CeAgOSe from data collected on the I11 beamline at Diamond Light Source Ltd. R_{wp} = 1.426 %; χ^2 = 3.305.

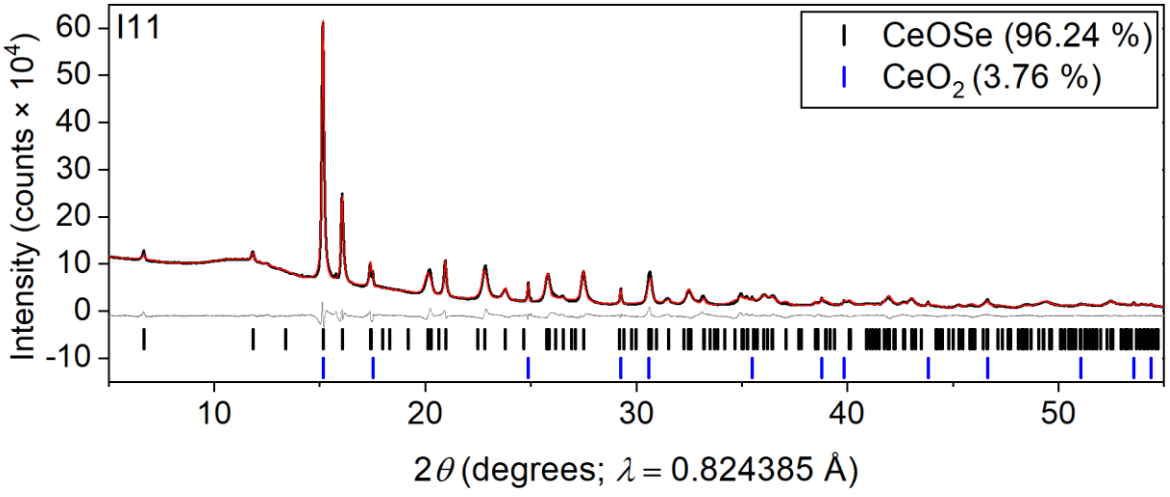


Figure 6.3 Rietveld refinement of CeOSe from data collected on the I11 beamline at Diamond Light Source Ltd using the *Cmca* model which can be seen visually in Figure 6.6. R_{wp} = 2.367 %; χ^2 = 5.897.

The current working hypothesis is that this material has the *Cmca* space group with Rietveld refinement of the data with this space group shown in Figure 6.3 and the structure shown in Figure 6.4.

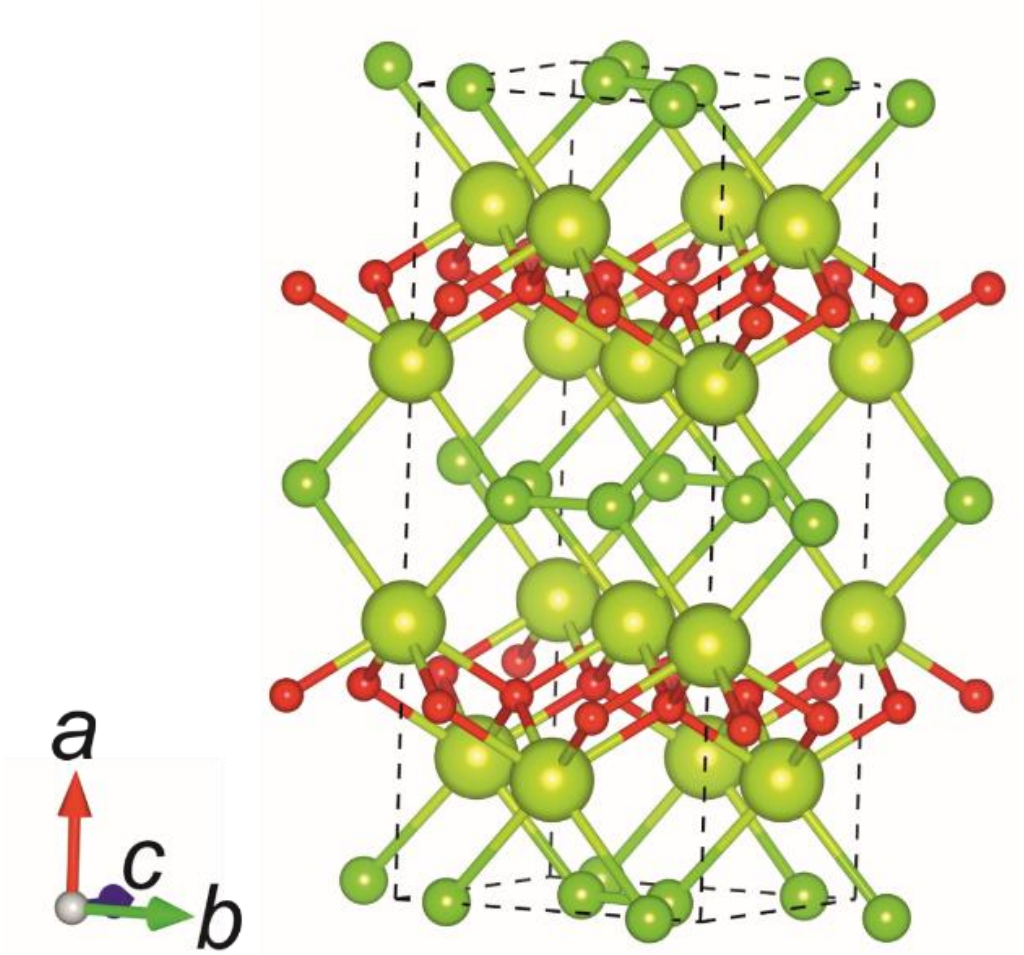


Figure 6.4 The possible structure of CeOSe in *Cmca*.

6.1.4 Raman spectroscopy

Raman spectroscopy measurements were carried out to determine the effect of the deintercalation on the Raman modes within the sample – particularly for Se-dimer modes which are well known to be Raman active and visible in compounds such as $MnSe_2$ with a

Se-Se bond length of 2.38 Å and a Raman active mode observed at 267cm^{-1}.[148] The results for CeAgOSe and CeOSe are shown below in Figure 6.5.

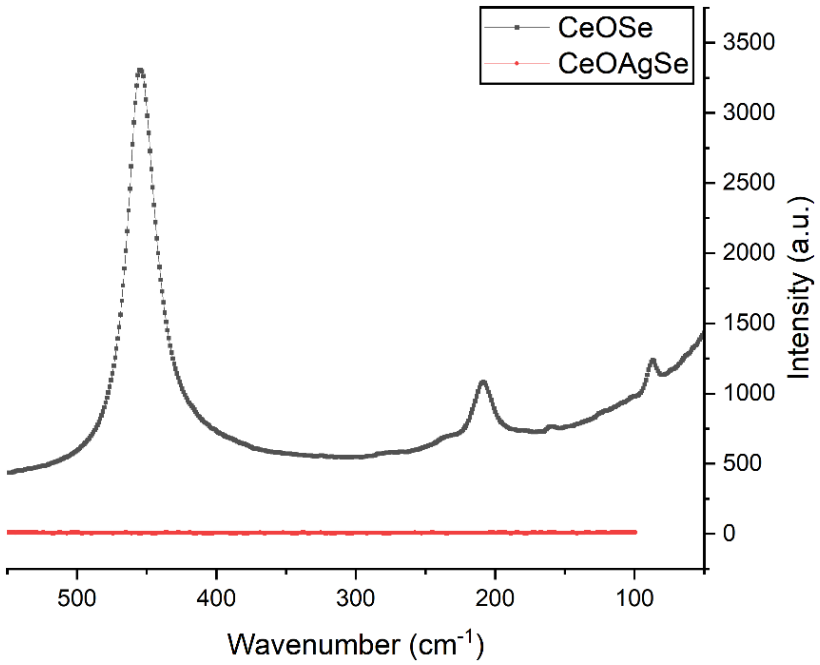


Figure 6.5. Raman spectra of CeOSe (black) and the CeAgOSe (red). The measurement was performed under air with excitation wavelength λ_{ex} = 532 nm.

It was found that the parent, CeAgOSe was not Raman active at all whereas the deintercalated daughter CeOSe had strong signals at 454, 210 as well as weaker signals at 160 and 87 cm^{-1}. It seems likely that the peak at 210 cm^{-1} corresponds to the formation of Se-Se bonds as it is in line with values previously reported. The strong peak at 454 cm^{-1} is unlikely to be Se-Se bonds and is unassigned but due to its intensity is likely to belong to some mode within the main CeOSe phase.

6.1.5 XANES

The oxidation state of both Ce and Se was probed using room temperature XANES on samples synthesised by Emily Townsend and William Arnold with the Se K-edge and Ce-

L3-edge using the B18 beamline at the Diamond Light Source with the resulting spectrum shown below in Figure 6.6.

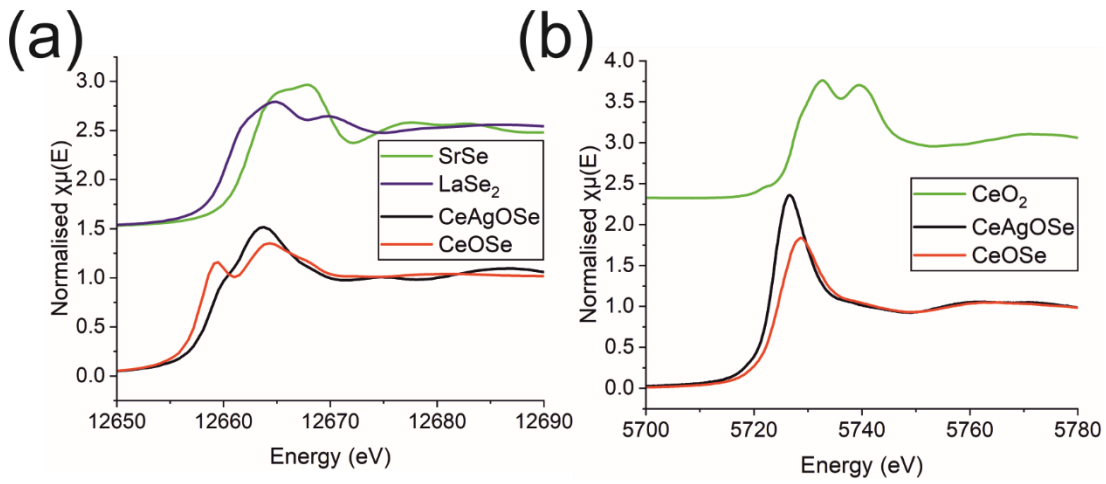


Figure 6.6 XANES of **(a)** Se K-edge and **(b)** Ce L3-edge of CeAgOSe, CeOSe and appropriate standards.

For the Se-K edge, there is a clear pre-edge peak at 12660 eV due to electrons that are excited to the antibonding σ* orbitals of the $[Se_2]^{2-}$ ions as well as the main peak at ≈ 12665 eV which is at a higher energy than the corresponding peak in CeAgOSe.

The shifting to higher energy in the Se K-edge verifies that it is oxidised but it is quantitively difficult to say to what extent due to the compared standards being SrSe [Se^{2-}] and $LaSe_2$ [$Se^{-1.5}$], a standard such as $MnSe_2$ would be required which is known to contain di-selenide units to make a better comparison.

Despite this, the Ce L3-edge data in Figure 6.6(b) confirm the oxidation of Se in this compound due to the presence of both peaks in CeAgOSe and CeOSe being at a lower energy and lacking in the double hump feature seen in CeO_2 which contains Ce^{4+} and therefore both CeAgOSe and CeOSe contain Ce^{3+} which is backed up by the magnetometry data.

6.1.6 EDX

To investigate the possibility of residual silver remaining in the compounds, EDX was performed on a sample of nominally "CeOSe" to determine an approximate composition.

The result is shown below in Figures 6.7 with the derived atomic percentage (at %) shown in Tables 6.1.

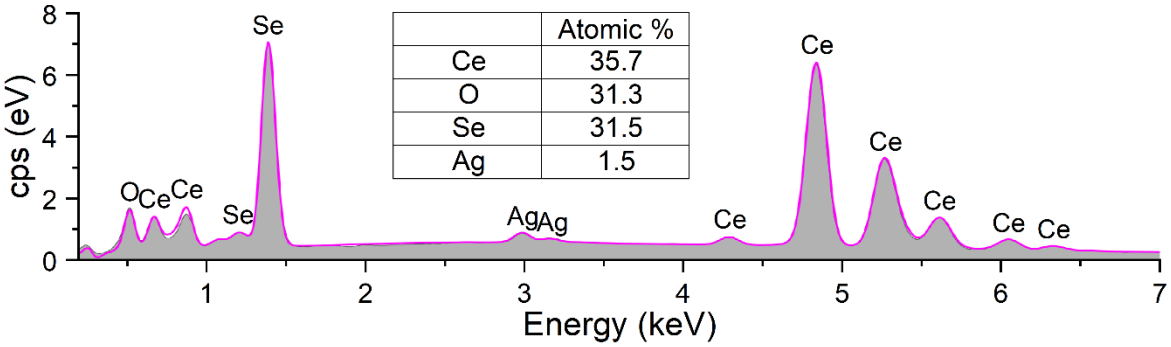


Figure 6.7 SEM-EDX elemental analysis results for one point in CeOSe.

Table 6.1 Average SEM-EDX elemental analysis results for CeOSe. Due to its low atomic mass, O content is an estimate.

Ce (at %)	Ag (at %)	O (at %)	Se (at %)
1.0(1)	0.0(1)	0.9(1)	0.9(1)

According to the point analysis of "CeOSe" the average composition is $Ce_{1.0(1)}Ag_{0.0(1)}O_{0.9(1)}Se_{0.9(1)}$ suggesting that nearly all the silver had been extruded from the compound.

Despite it being clear that Ag-free CeOSe is achievable using soft-chemistry, the structure has yet to be conclusively determined. Despite the *Cmca* structure shown in Figure 6.6 showing a good statistical and visual fit to the data, it is clear that this structure model needs to be improved upon. In compounds with known Se-Se dimers such as $BaSe_2$,[149] the Se-Se

distance is 2.330 Å whereas the extracted distance in Rietveld refinement in CeOSe with the *Cmca* structure model is 1.85(3) Å which is clearly unrealistically small. Presumably the X-ray diffraction technique which probes the average structure is not able to account for all the structural features.

As such, the next steps of this project involve using the current data collected as well as 3D-ED data recently collected using collaboration with the University of Antwerp, and which probes the structure on a shorter length scale to solve the structure of this complex oxide selenide. Pair Distribution Function and EXAFS measurements to probe the local structure will also likely be important.

6.2 Conclusion

This thesis has investigated the structure-property relationships in the series of mixed-anion solids $Ae_2MO_2X_2Ch_2$ (*Ae* = Sr, Ba; *M* = Co, Ni; *X* = Cu, Ag; *Ch* = S, Se), $Ae_{3-x}Ae'_xFe_2O_5Cu_2Ch_2$ (*Ch* = S, Se) as well as the characterisation of $Sr_2NiO_2Cl_2$ which was obtained through collaboration.

Chapter 3 investigated a series of Ni-containing oxide chalcogenides with a focus on the solid solution $Sr_2NiO_2Cu_2(Se_{1-x}S_x)$. Previous work by Smura[35] had determined that in $Sr_2NiO_2Cu_2S_2$, the central d^8 Ni^{2+} cation was in the low-spin, diamagnetic configuration. This work was followed up by Blandy[40], whom confirmed using PND that the Se analogue, $Sr_2NiO_2Cu_2Se_2$ was in the high-spin configuration.

Initially, it was thought that it would be possible to force $Sr_2NiO_2Cu_2Se_2$ using high pressure but unfortunately it was found that up to 7.3(1) Gpa, Ni^{2+} remains firmly in the high-spin regime.

Analysis of the solid solution $Sr_2NiO_2Cu_2(Se_{1-x}S_x)$ using PND allowed for the pinpointing of the spin-state crossover as a function of composition from high-spin $Sr_2NiO_2Cu_2Se_2$ to low-spin $Sr_2NiO_2Cu_2S_2$ going from fully 3-dimensional ordering with a magnetic structure similar to that of $Sr_2NiO_2Cu_2Se_2$[40] through a lower 2-dimensional ordered state in $Sr_2NiO_2Cu_2(Se_{0.656}S_{0.344})_2$ before loss of any sign of long-range magnetic order for more S-rich compositions. It was also noted that between these two magnetically ordered states there was a spin-reorientation towards the basal plane as the S content of the oxide chalcogenide was increased.

Computational calculations on these systems has reinforced that the structural and physical properties of these Ni-containing oxide chalcogenides are complex and it is possible that there is competition between spin-states and that a binary choice may be an oversimplification of the true state

A purer sample of $Sr_2NiO_2Cl_2$, obtained through collaboration channels, was fully characterised in this thesis with its magnetic structure determined for the first time. Magnetic peaks could be indexed on a $\sqrt{2}a \times \sqrt{2}a \times c$ expansion of the nuclear cell with localised Ni^{2+} moments with a magnitude of 1.57(7) μ_B at 1.5 K, which is consistent with calculation and with the closely related oxide chalcogenide analogue, $Sr_2NiO_2Cu_2Se_2$ with the difference in the magnetic structures laying within the $2c$ expansion of the magnetic structure of $Sr_2NiO_2Cu_2Se_2$.

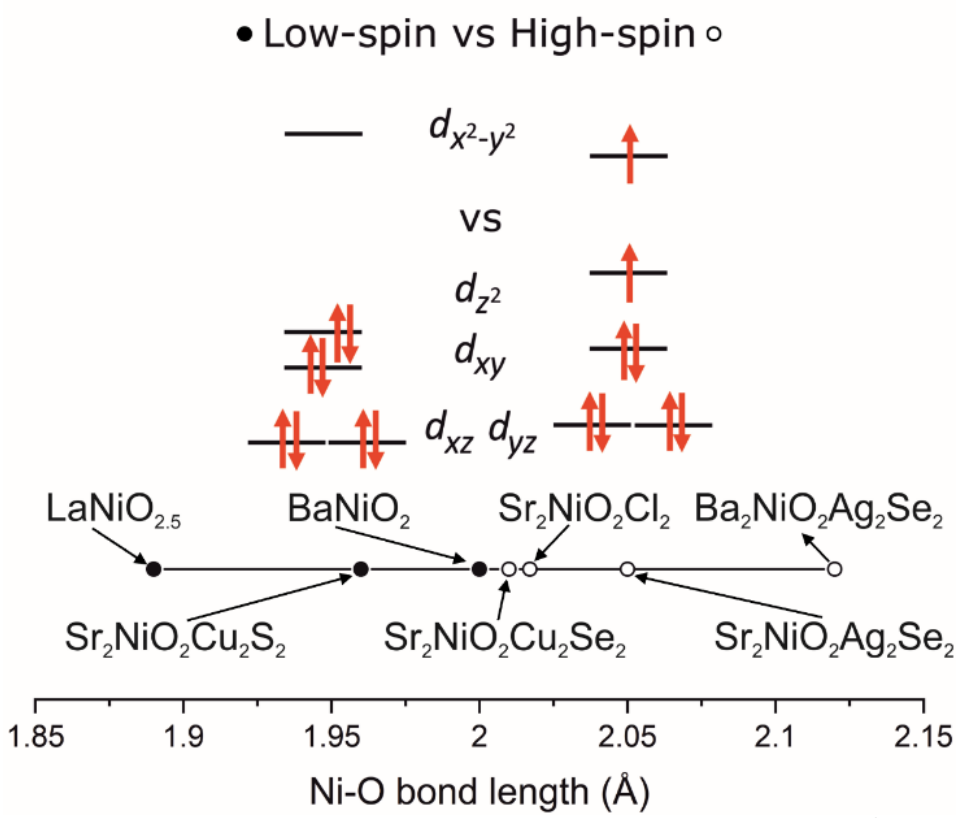


Figure 6.8 Ni-O bond length comparison and the spin-state for various Ni^{2+} containing solids.[7,33,38,127,128]

The Ni compounds investigated within this thesis have added to a vast amount of research on related systems and are consistent with previous findings that the Ni-O bond length in these systems seems to be deterministic in the spin-state.

Chapter 4 follows on from the oxidative deintercalation work previously performed by Blandy[40] on a series of Co-containing oxide chalcogenides.

A novel cycling technique, refined by Sasaki et al.,[70] allowed for the removal of more copper from $Sr_2CoO_2Cu_2Ch_2$ (*Ch* = S, Se) than was previously possible using only iodine. Unfortunately, the "collapsed phases" of $Sr_2CoO_2Ch_2$ (*Ch* = S, Se) were not attainable owing to the Cu containing $Sr_2CoO_2Cu_2Ch_2$ (*Ch* = S, Se) compounds being more resistant to the cycling technique than their Mn oxide chalcogenides counterparts.

An analogous technique could not be used on the Ag-containing compounds $Ae_2CoO_2Ag_2Se_2$ (*Ae* = Sr, Ba) as a suitable chelating agent could not be identified.

Thus, it was attempted to induce as much coinage metal / Li exchange as possible and investigate the effect on the structure and magnetic properties within these highly lithiated, novel phases.

As revealed by powder neutron diffraction, all of the compounds in this chapter exhibit long-range antiferromagnetic order within the *ab*-plane, similar to that reported for their parent materials with full occupancy of coinage metal.

A more startling discovery was that even with the introduction of cation disorder on the tetrahedral site, even though the moment was somewhat supressed from what had been

previously predicted using the Co^{2+} environment as a proxy, that the extracted value of the magnetic moments on Co were still higher than their spin-only value of 3 μ_B.

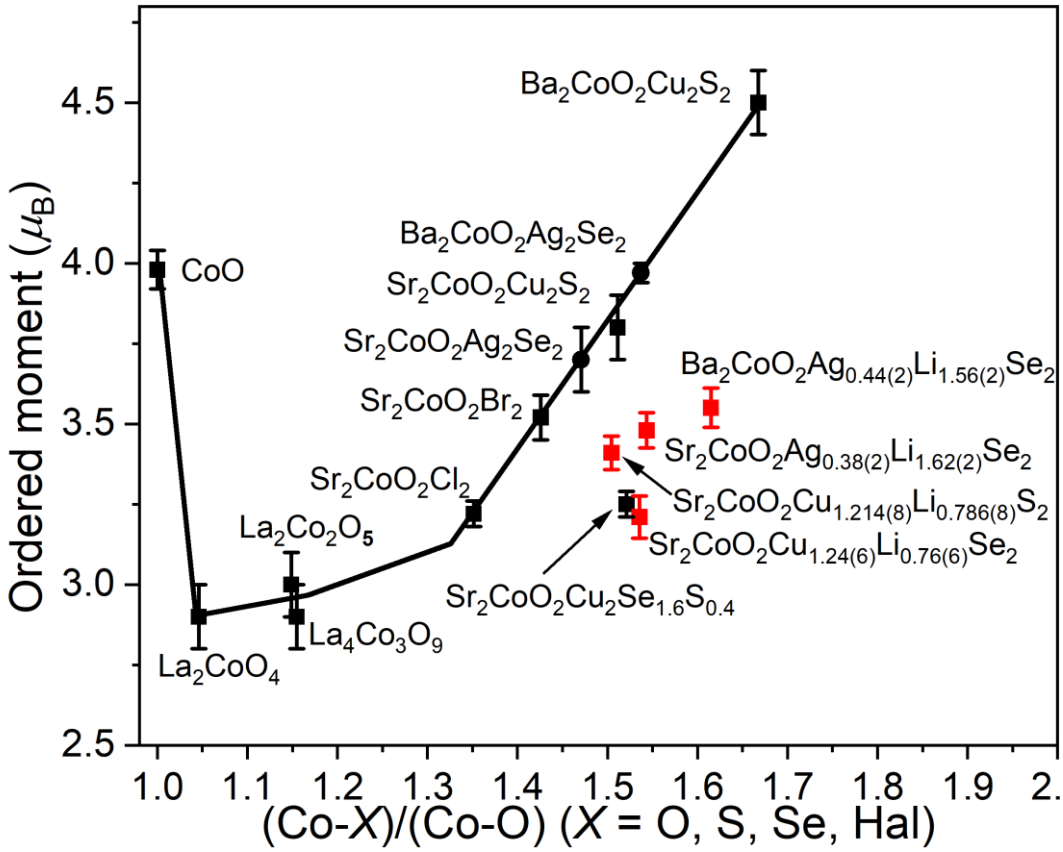


Figure 6.9 The relationship between the long-range ordered moment of Co^{2+} as a function of the coordination environment from the literature (black) and this work (red).

During the period of which this work was performed there have been computational reports,[131,132] suggesting that by not taking into account the anisotropic spin-distribution and by using the metal-ion-sphere approximation, that the magnetic form factor was strongly underestimated within the Rietveld refinements of the PND data.

The next logical step in this project on Co-containing oxide chalcogenides is to work through collaboration in incorporating a modified magnetic form factor within the refinement software to determine if the enhanced magnetic moments as found by experiment are in fact due to an orbital contribution to the moment or if it is quenched as found through calculation.

Chapter 5 reports the novel solid solution $Ba_{3-x}Sr_xFe_2O_5Cu_2Ch_2$ (x = 1, 2) (*Ch* = S, Se) as well as $BaCa_2Fe_2O_5Cu_2S_2$. The motivation for this work was following on from work performed by Sheath in the solid solution $Sr_{3-x}Ca_xFe_2O_5Cu_2Ch_2$ (x = 1, 2) (*Ch* = S, Se).[14]

It was clear from the SPXRD which has better contrast than the PND data for the *Ae (Ae* = Ba, Sr, Ca) sites that in all cases, Ba2+ preferentially occupied the larger 12-coordinate site and accordingly, the other ion in the smaller 8-coordinate site. It is not clear however which site is the driving force behind the segregation.

Long range magnetic ordering can be indexed on a $\sqrt{2}a \times \sqrt{2}a \times c$ expansion of the nuclear cell for all the compounds with the saturated moments clearly showing a correlation with the bond valence sums for the Fe^{3+} ions.

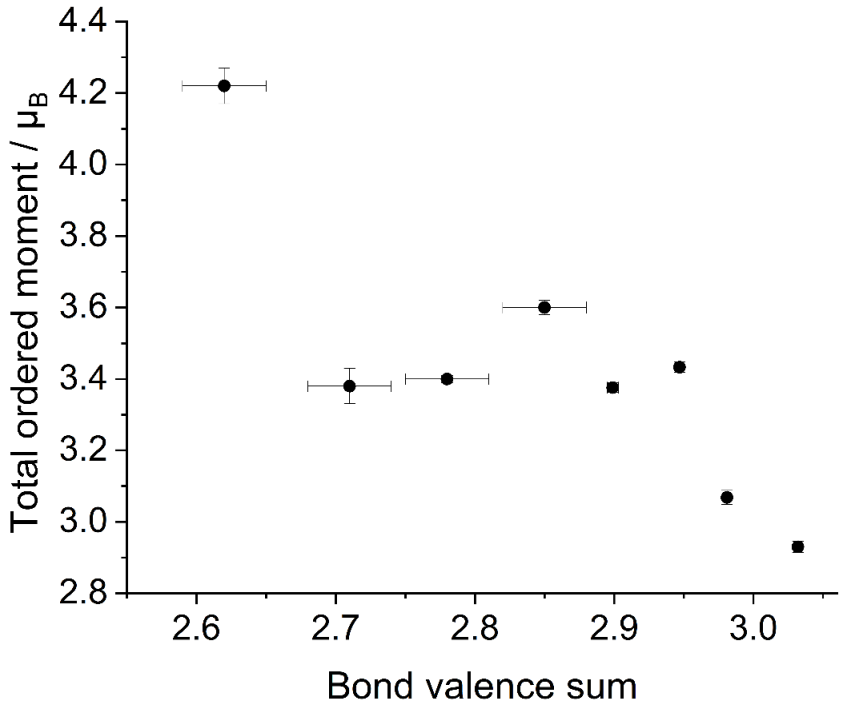


Figure 6.10 The negative correlation between the moment and the Fe bond valence sum across the full family of $Ae_3Fe_2O_5Cu_2Ch_2$ (*Ae* = Ba, Sr; *Ch* = S, Se) compounds.

However, the fact that the Fe^{3+} moments are orientated within the *ab*-plane whereas on the introduction of multiple alkaline earth metal cations, the moments tilt towards the *c*-axis

emphasising that once the orbital angular momentum is quenched and the spin-orbit coupling is small in magnitude as is the case for high spin Fe^{3+} ions, that the orientation of the moments is difficult to predict.[136]

This body of work emphasises how solid-state manipulations, whether that be through varying the ions within the structure or through topochemical modification using soft-chemical techniques can greatly change the properties of a material which emphasises the importance of structure-property relationships in solid-state materials. Of note is the use of low-temperature approaches to novel phases which are inaccessible through traditional, high-temperature solid-state synthesis.

The results presented in this thesis show that the detailed characterisation of the structure and transport properties of these functional materials is the essential to understanding structure-property relationships between different families of compounds and that the fundamental science underpinning this work is the key to building up our understanding of how functional materials work and the possibility of predicting which materials / structure types can have applicable properties to real life problems.

References

(1) Bragg, W. H.; Bragg, W. L. The Reflection of X-Rays by Crystals. *Proc. R. Soc. London. Ser. A* **1913**, *88* (605), 428–438. https://doi.org/10.1098/rspa.1913.0040.

(2) Madden, P.; Wilson, M. "Covalent" effects in "Ionic" systems. *Chem. Soc. Rev.* **1996**, *25*, 339–350. https://doi.org/10.1039/CS9962500339.

(3) Yamaguchi, M. High-Efficiency GaAs-Based Solar Cells. In *Post-Transition Metals*; IntechOpen, **2021**. https://doi.org/10.5772/intechopen.94365.

(4) Edmond, J.; Abare, A.; Bergman, M.; Bharathan, J.; Lee Bunker, K.; Emerson, D.; Haberern, K.; Ibbetson, J.; Leung, M.; Russel, P.; Slater, D. High Efficiency GaN-Based LEDs and Lasers on SiC. *J. Cryst. Growth* **2004**, *272* (1–4), 242–250. https://doi.org/10.1016/j.jcrysgro.2004.08.056.

(5) Bertora, L. MRI Magnets Based on MgB_2. *MgB_2 Superconducting Wires: Basics and Applications*; World Scientific Publishing Co., **2016**; pp 485–536. https://doi.org/10.1142/9789814725590_0018.

(6) Kageyama, H.; Hayashi, K.; Maeda, K.; Attfield, J. P.; Hiroi, Z.; Rondinelli, J. M.; Poeppelmeier, K. R. Expanding Frontiers in Materials Chemistry and Physics with Multiple Anions. *Nat. Commun.* **2018**, *9*, 772. https://doi.org/10.1038/s41467-018-02838-4.

(7) Clarke, S. J.; Adamson, P.; Herkelrath, S. J. C.; Rutt, O. J.; Parker, D. R.; Pitcher, M. J.; Smura, C. F. Structures, Physical Properties, and Chemistry of Layered Oxychalcogenides and Oxypnictides. *Inorg. Chem.* **2008**, *47* (19), 8473–8486. https://doi.org/10.1021/ic8009964.

(8) Pastrana-Fábregas, R.; Isasi-Marín, J.; Sáez-Puche, R. Synthesis and Characterization of Inorganic Pigments Based on Transition Metal Oxynitrides. *J. Mater. Res.* **2006**, *21* (9), 2255–2260. https://doi.org/10.1557/jmr.2006.0272.

(9) Shannon, R. D. Revised Effective Ionic Radii and Systematic Studies of Interatomic Distances in Halides and Chalcogenides. *Acta Crystallogr. Sect. A* **1976**, *32* (5), 751–767. https://doi.org/10.1107/S0567739476001551.

(10) Zhao, L. D.; He, J.; Berardan, D.; Lin, Y.; Li, J. F.; Nan, C. W.; Dragoe, N. BiCuSeO Oxyselenides: New Promising Thermoelectric Materials. *Energy and Environmental Science*. **2014**, pp 2900–2924. https://doi.org/10.1039/c4ee00997e.

(11) Zhu, W. J.; Hor, P. H. Crystal Structure of New Layered Oxysulfides: $Sr_3Cu_2Fe_2O_5S_2$ and $Sr_2Cu\mathit{M}O_3S$ (*M* = Cr, Fe, In). *J. Solid State Chem.* **1997**, *134* (1), 128–131. https://doi.org/10.1006/jssc.1997.7556.

(12) Zhu, W. J.; Hor, P. H. Sr_2CuGaO_3S, a Rare Example of Square Pyramidal Gallium. *Inorg. Chem.* **1997**, *36* (17), 3576–3577. https://doi.org/10.1021/ic970322c.

(13) Zhu, W. J.; Hor, P. H. Synthesis and Structure of Layered Manganese Oxychalcogenides: Sr_2CuMnO_3S and $Sr_4Cu_2Mn_3O_{7.5}Q_2$ (*Q* = S, Se). *J. Solid State Chem.* **2000**, *153* (1), 26–29. https://doi.org/10.1006/jssc.2000.8725.

(14) Sheath, B. C.; Cassidy, S. J.; Clarke, S. J. Cation Site Preferences in Layered Oxide Chalcogenides, Synthesis, Structures and Magnetic Ordering in $Sr_{3-x}Ca_xFe_2O_5Cu_2\mathit{Ch}_2$ (*Ch* = S, Se; *x* = 1, 2). *J. Solid State Chem.* **2021**, *293*, 121761. https://doi.org/10.1016/j.jssc.2020.121761.

(15) Otzschi, K.; Ogino, H.; Shimoyama, J. I.; Kishio, K. New Candidates for Superconductors; a Series of Layered Oxysulfides $(Cu_2S_2)(Sr_{n+1}MnO_{3n-1})$. *J. Low Temp. Phys.* **1999**, *117* (3–4), 729–733. https://doi.org/10.1023/A:1022545228168.

(16) Zhu, W. J.; Hor, P. H.; Jacobson, A. J.; Crisci, G.; Albright, T. A.; Wang, S.-H.; Vogt, T. $A_2Cu_2CoO_2S_2$ (*A* = Sr, Ba), A Novel Example of a Square-Planar CoO_2 Layer. *J. Am. Chem. Soc.* **1997**, *119* (50), 12398–12399. https://doi.org/10.1021/ja972542v.

(17) Zhu, W. J.; Hor, P. H. Unusual Layered Transition-Metal Oxysulfides: $Sr_2Cu_2\mathit{M}O_2S_2$ (*M* = Mn, Zn). *J. Solid State Chem.* **1997**, *130* (2), 319–321. https://doi.org/10.1006/jssc.1997.7299.

(18) Blandy, J. N.; Boskovic, J. C.; Clarke, S. J. Synthesis and Magnetic Structure of the Layered Manganese Oxide Selenide $Sr_2MnO_2Ag_{1.5}Se_2$. *J. Solid State Chem.* **2017**, *245*, 61–66. https://doi.org/10.1016/j.jssc.2016.10.010.

(19) Blandy, J. N.; Abakumov, A. M.; Christensen, K. E.; Hadermann, J.; Adamson, P.; Cassidy, S. J.; Ramos, S.; Free, D. G.; Cohen, H.; Woodruff, D. N.; Thompson, A. L.; Clarke, S. J. Soft Chemical Control of the Crystal and Magnetic Structure of a Layered Mixed Valent Manganite Oxide Sulfide. *APL Mater.* **2015**, *3* (4), 41520. https://doi.org/10.1063/1.4918973.

(20) Herkelrath, S. J. C.; Blandy, J. N.; Clarke, S. J. Magnetic Ordering in the Layered Oxyselenides

$Sr_2CoO_2Ag_2Se_2$ and $Ba_2CoO_2Ag_2Se_2$. *J. Solid State Chem.* **2018**, *264*, 119–123. https://doi.org/10.1016/j.jssc.2018.05.018.

(21) Smura, C. F.; Parker, D. R.; Zbiri, M.; Johnson, M. R.; Gál, Z. A.; Clarke, S. J. High-Spin Cobalt(II) Ions in Square Planar Coordination: Structures and Magnetism of the Oxysulfides $Sr_2CoO_2Cu_2S_2$ and $Ba_2CoO_2Cu_2S_2$ and their Solid Solution. *J. Am. Chem. Soc.* **2011**, *133* (8), 2691–2705. https://doi.org/10.1021/ja109553u.

(22) Brechtel, E.; Cordier, G.; Schäfer, H. Oxidpnictides: Preparation and Crystal Structure of $A_2Mn_3B_2O_2$ with *A* = Sr, Ba and *B* = As, Sb, Bi. *Zeitschrift für Naturforsch. B* **1979**, *34* (6), 777–780. https://doi.org/10.1515/znb-1979-0603.

(23) Blandy, J. N.; Liu, S.; Smura, C. F.; Cassidy, S. J.; Woodruff, D. N.; McGrady, J. E.; Clarke, S. J. Synthesis, Structure, and Properties of the Layered Oxide Chalcogenides $Sr_2CuO_2Cu_2S_2$ and $Sr_2CuO_2Cu_2Se_2$. *Inorg. Chem.* **2018**, *57* (24), 15379–15388. https://doi.org/10.1021/acs.inorgchem.8b02698.

(24) Xu, X.; Jones, M. A.; Cassidy, S. J.; Manuel, P.; Orlandi, F.; Batuk, M.; Hadermann, J.; Clarke, S. J. Magnetic Ordering in the Layered Cr(II) Oxide Arsenides $Sr_2CrO_2Cr_2As_2$ and $Ba_2CrO_2Cr_2As_2$. *Inorg. Chem.* **2020**, *59* (21), 15898–15912. https://doi.org/10.1021/acs.inorgchem.0c02415.

(25) Gál, Z. A.; Rutt, O. J.; Smura, C. F.; Overton, T. P.; Barrier, N.; Clarke, S. J.; Hadermann, J. Structural Chemistry and Metamagnetism of an Homologous Series of Layered Manganese Oxysulfides. *J. Am. Chem. Soc.* **2006**, *128* (26), 8530–8540. https://doi.org/10.1021/ja060892o.

(26) Blandy, J. N.; Parker, D. R.; Cassidy, S. J.; Woodruff, D. N.; Xu, X.; Clarke, S. J. Synthesis, Structure, and Compositional Tuning of the Layered Oxide Tellurides $Sr_2MnO_2Cu_{2-x}Te_2$ and $Sr_2CoO_2Cu_2Te_2$. *Inorg. Chem.* **2019**, *58* (12), 8140–8150. https://doi.org/10.1021/acs.inorgchem.9b00919.

(27) Adamson, P.; Hadermann, J.; Smura, C. F.; Rutt, O. J.; Hyett, G.; Free, D. G.; Clarke, S. J. Competing Magnetic Structures and the Evolution of Copper Ion/Vacancy Ordering with Composition in the Manganite Oxide Chalcogenides $Sr_2MnO_2Cu_{1.5}(S_{1-x}Se_x)_2$. *Chem. Mater.* **2012**, *24* (14), 2802–2816. https://doi.org/10.1021/cm301486v.

(28) Hyett, G.; Barrier, N.; Clarke, S. J.; Hadermann, J. Topotactic Oxidative and Reductive Control of the Structures and Properties of Layered Manganese Oxychalcogenides. *J. Am. Chem. Soc.* **2007**, *129* (36), 11192–11201. https://doi.org/10.1021/ja073048m.

(29) Cario, L.; Lafond, A.; Morvan, T.; Kabbour, H.; André, G.; Palvadeau, P. Design and Magnetic Properties of New Compounds Containing Iron 2D Building Blocks of the Perovskite Type. *Solid State Sci.* **2005**, *7* (8), 936–944. https://doi.org/https://doi.org/10.1016/j.solidstatesciences.2005.04.016.

(30) Zhang, H.; Jin, S.; Guo, L.; Shen, S.; Lin, Z.; Chen, X. Bandgap Narrowing in the Layered Oxysulfide Semiconductor $Ba_3Fe_2O_5Cu_2S_2$: Role of FeO_2 Layer. *Chinese Phys. B* **2016**, *25* (2), 26101. https://doi.org/10.1088/1674-1056/25/2/026101.

(31) Liu, M.-L.; Wu, L.-B.; Huang, F.-Q.; Chen, L.-D.; Chen, I.-W. I.-W. W. A Promising P-Type Transparent Conducting Material: Layered Oxysulfide $[Cu_2S_2][Sr_3Sc_2O_5]$. *J. Appl. Phys.* **2007**, *102* (11), 116108. https://doi.org/10.1063/1.2817643.

(32) Scanlon, D. O.; Watson, G. W. $(Cu_2S_2)(Sr_3Sc_2O_5)$−A Layered, Direct Band Gap, *p*-Type Transparent Conducting Oxychalcogenide: A Theoretical Analysis. *Chem. Mater.* **2009**, *21* (22), 5435–5442. https://doi.org/10.1021/cm902260b.

(33) Matsumoto, Y.; Yamamoto, T.; Nakano, K.; Takatsu, H.; Murakami, T.; Hongo, K.; Maezono, R.; Ogino, H.; Song, D.; Brown, C. M.; Tassel, C.; Kageyama, H. High-Pressure Synthesis of $A_2NiO_2Ag_2Se_2$ (*A* = Sr, Ba) with a High-Spin Ni^{2+} in Square-Planar Coordination. *Angew. Chemie - Int. Ed.* **2019**, *58* (3), 756–759. https://doi.org/10.1002/anie.201810161.

(34) Matsumoto, Y.; Nambu, Y.; Honda, T.; Ikeda, K.; Otomo, T.; Kageyama, H. High-Pressure Synthesis of $Ba_2CoO_2Ag_2Te_2$ with Extended CoO_2 Planes. *Inorg. Chem.* **2020**, *59* (12), 8121–8126. https://doi.org/10.1021/acs.inorgchem.0c00429.

(35) Smura, C. F. *DPhil. Thesis*, The synthesis, structures and properties of mixed-anion solids. University of Oxford. **2008**.

(36) Jin, S.; Chen, X.; Guo, J.; Lei, M.; Lin, J.; Xi, J.; Wang, W.; Wang, W. $Sr_2Mn_3Sb_2O_2$-type Oxyselenides: Structures, Magnetism, and Electronic Properties of $Sr_2AO_2M_2Se_2$ (*A* = Co, Mn; *M* = Cu, Ag). *Inorg. Chem.* **2012**, *51* (19), 10185–10192. https://doi.org/10.1021/ic301022g.

(37) Zhou, T.; Wang, Y.; Jin, S.; Li, D.; Lai, X.; Ying, T.; Zhang, H.; Shen, S.; Wang, W.; Chen, X. Structures and Physical Properties of Layered Oxyselenides $Ba_2MO_2Ag_2Se_2$ (*M* = Co, Mn). *Inorg. Chem.* **2014**, *53* (8), 4154–4160. https://doi.org/10.1021/ic500203k.

(38) Smyth, R. D.; Blandy, J. N.; Yu, Z.; Liu, S.; Topping, C. V.; Cassidy, S. J.; Smura, C. F.; Woodruff,

D. N.; Manuel, P.; Bull, C. L.; Funnell, N. P.; Ridley, C. J.; McGrady, J. E.; Clarke, S. J. High- versus Low-Spin Ni^{2+} in Elongated Octahedral Environments: $Sr_2NiO_2Cu_2Se_2$, $Sr_2NiO_2Cu_2S_2$, and $Sr_2NiO_2Cu_2(Se_{1-x}S_x)_2$. *Chem. Mater.* **2022**, *34* (21), 9503–9516. https://doi.org/10.1021/acs.chemmater.2c02002.

(39) Jin, S.; Chen, X.; Guo, J.; Lei, M.; Lin, J.; Xi, J.; Wang, W.; Wang, W. $Sr_2Mn_3Sb_2O_2$ Type Oxyselenides: Structures, Magnetism, and Electronic Properties of $Sr_2AO_2M_2Se_2$ (*A* = Co, Mn; *M* = Cu, Ag). *Inorg. Chem.* **2012**, *51* (19), 10185–10192. https://doi.org/10.1021/ic301022g.

(40) Blandy, J. N. *DPhil. Thesis*, Soft chemical control of layered oxychalcogenides. University of Oxford. **2017**.

(41) Broadley, S. *MChem. Thesis*, The synthesis, structures and properties of layered oxychalcogenides. University of Oxford. **2005**.

(42) Hirose, H.; Ueda, K.; Kawazoe, H.; Hosono, H. Electronic Structure of $Sr_2Cu_2ZnO_2S_2$ - Layered Oxysulfide with CuS Layers. *Chem. Mater.* **2002**, *14* (3), 1037–1041. https://doi.org/10.1021/cm0105864.

(43) Jiang, H.; Bao, J.-K.; Zhai, H.-F.; Tang, Z.-T.; Sun, Y.-L.; Liu, Y.; Wang, Z.-C.; Bai, H.; Xu, Z.-A.; Cao, G.-H. Physical Properties and Electronic Structure of $Sr_2Cr_3As_2O_2$ Containing CrO_2 and Cr_2As_2 Square-Planar Lattices. *Phys. Rev. B* **2015**, *92* (20), 205107. https://doi.org/10.1103/physrevb.92.205107.

(44) Xu, X. *DPhil. Thesis*, Synthesis and characterisation of layered oxypnictides and oxychalcogenides. University of Oxford. **2019**.

(45) Barrier, N.; Clarke, S. J. A Novel Layered Oxysulfide Intergrowth Compound $Sr_4Mn_2Cu_5O_4S_5$ Containing a Fragment of the α-Cu_2S Antifluorite Structure. *Chem. Commun.* **2003**, No. 1, 164–165. https://doi.org/10.1039/b209747h.

(46) Pöttgen, R.; Johrendt, D. Materials with ZrCuSiAs-Type Structure. *Zeitschrift fur Naturforsch. - Sect. B J. Chem. Sci.* **2008**, *63* (10), 1135–1148. https://doi.org/10.1515/znb-2008-1001.

(47) Johnson, V.; Jeitschko, W. ZrCuSiAs: A "Filled" PbFCl Type. *J. Solid State Chem.* **1974**, *11* (2), 161–166. https://doi.org/10.1016/0022-4596(74)90111-X.

(48) Kabbour, H.; Cario, L.; Boucher, F. Rational Design of New Inorganic Compounds with the ZrSiCuAs Structure Type Using 2D Building Blocks. *J. Mater. Chem.* **2005**, *15* (34), 3525–3531. https://doi.org/10.1039/b506031a.

(49) Cassidy, S. J.; Pitcher, M. J.; Lim, J. J. K.; Hadermann, J.; Allen, J. P.; Watson, G. W.; Britto, S.; Chong, E. J.; Free, D. G.; Grey, C. P.; Clarke, S. J. Layered CeSO and LiCeSO Oxide Chalcogenides Obtained via Topotactic Oxidative and Reductive Transformations. *Inorg. Chem.* **2019**, *58*, 3838–3850. https://doi.org/10.1021/acs.inorgchem.8b03485.

(50) Hiramatsu, H.; Yanagi, H.; Kamiya, T.; Ueda, K.; Hirano, M.; Hosono, H. Crystal Structures, Optoelectronic Properties, and Electronic Structures of Layered Oxychalcogenides *M*CuO*Ch* (*M* = Bi, La; *Ch* = S, Se, Te): Effects of Electronic Configurations of M^{3+} Ions. *Chem. Mater.* **2008**, *20* (1), 326–334. https://doi.org/10.1021/cm702303r.

(51) Kamihara, Y.; Watanabe, T.; Hirano, M.; Hosono, H. Iron-Based Layered Superconductor $La[O_{1-x}F_x]FeAs$ (x = 0.05 - 0.12) with T_c = 26 K. *J. Am. Chem. Soc.* **2008**, *130* (11), 3296–3297. https://doi.org/10.1021/ja800073m.

(52) Chen, X.; Ok, K. M. Metal Oxyhalides: An Emerging Family of Nonlinear Optical Materials. *Chemical Science*. **2022**, pp 3942–3956. https://doi.org/10.1039/d1sc07121a.

(53) House, R. A.; Jin, L.; Maitra, U.; Tsuruta, K.; Somerville, J. W.; Förstermann, D. P.; Massel, F.; Duda, L.; Roberts, M. R.; Bruce, P. G. Lithium Manganese Oxyfluoride as a New Cathode Material Exhibiting Oxygen Redox. *Energy Environ. Sci.* **2018**, *11* (4), 926–932. https://doi.org/10.1039/c7ee03195e.

(54) Anshukova, V, N.; Golovashkin, I, A.; Ivanova, I, L.; Rusakov, P, A. HTSCs with apical oxygen replaced by halogens. *Phys.-Usp.* **1997** *40* 843 https://doi.org/10.1070/pu1997v040n08abeh000274.

(55) Tsujimoto, Y.; Sathish, C. I.; Matsushita, Y.; Yamaura, K.; Uchikoshi, T. New Members of Layered Oxychloride Perovskites with Square Planar Coordination: $Sr_2MO_2Cl_2$ (*M* = Mn, Ni) and $Ba_2PdO_2Cl_2$. *Chem. Commun.* **2014**, *50* (44), 5915–5918. https://doi.org/10.1039/c4cc01422g.

(56) Tsujimoto, Y.; Yamaura, K.; Uchikoshi, T. Extended Ni(III) Oxyhalide Perovskite Derivatives: Sr_2NiO_3X (*X* = F, Cl). *Inorg. Chem.* **2013**, *52* (17), 10211–10216. https://doi.org/10.1021/ic402008n.

(57) Tsujimoto, Y.; Sugiyama, J.; Ochi, M.; Kuroki, K.; Manuel, P.; Khalyavin, D. D.; Umegaki, I.; Månsson, M.; Andreica, D.; Hara, S.; Sakurai, T.; Okubo, S.; Ohta, H.; Boothroyd, A.; Yamaura, K. Impact of Mixed Anion Ordered State on the Magnetic Ground States of S = 1/2 Square-Lattice

Quantum Spin Antiferromagnets, Sr_2NiO_3Cl and Sr_2NiO_3F. *Phys. Rev. Mater.* **2022**, *6* (11), 114404. https://doi.org/10.1103/PhysRevMaterials.6.114404.

(58) He, Y.; Gercsi, Z.; Zhang, R.; Kang, Y.; Skourski, Y.; Prendeville, L.; Larmour, O.; Besbas, J.; Felser, C.; Stamenov, P.; Coey, J. M. D. Au_4Mn: A Localized Ferromagnet with Strong Spin-Orbit Coupling, Long-Range Ferromagnetic Exchange, and High Curie Temperature. *Phys. Rev. B* **2022**, *106* (21), 214414. https://doi.org/10.1103/PhysRevB.106.214414.

(59) Hutchings, M. T.; Day, P.; Fair, M.; Gregson, A. K. Structure, Moment, and Magnetic Excitations of the Transparent Ferromagnet Rb_2CrCl_4. *AIP Conference Proceedings*; AIP Publishing, **2008**; Vol. 29, pp 263–263. https://doi.org/10.1063/1.30620.

(60) Meyer, A. J. P.; Taglang, P. Propriétés Magnétiques, Antiferromagnétisme et Ferromagnétisme de $MnAu_2$. *J. Phys. le Radium* **1956**, *17* (6), 457–465. https://doi.org/10.1051/jphysrad:01956001706045700.

(61) Kanamori, J. Superexchange Interaction and Symmetry Properties of Electron Orbitals. *J. Phys. Chem. Solids* **1959**, *10* (2–3), 87–98. https://doi.org/10.1016/0022-3697(59)90061-7.

(62) Goodenough, J. B. Theory of the role of covalence in the pervoskite-type manganites [La,*M*(II)]MnO_3. *Phys. Rev.* **1955**, 100, 564–573. https://doi.org/10.1103/PhysRev.100.564.

(63) Goodenough, J. B. An Interpretation of the Magnetic Properties of the Perovskite-Type Mixed Crystals $La_{1-x}Sr_xCoO_{3-\lambda}$. *J. Phys. Chem. Solids* **1958**, *6* (2–3), 287–297. https://doi.org/10.1016/0022-3697(58)90107-0.

(64) Mahendiran, R.; Tiwary, S.; Raychaudhuri, A.; Ramakrishnan, T.; Mahesh, R.; Rangavittal, N.; Rao, C. Structure, Electron-Transport Properties, and Giant Magnetoresistance of Hole-Doped Systems. *Phys. Rev. B - Condens. Matter Mater. Phys.* **1996**, *53* (6), 3348–3358. https://doi.org/10.1103/PhysRevB.53.3348.

(65) Whittingham, M. S. Intercalation Chemistry and Energy Storage. *J. Solid State Chem.* **1979**, *29* (3), 303–310. https://doi.org/10.1016/0022-4596(79)90187-7.

(66) Schirber, J. E.; Morosin, B.; Merrill, R. M.; Hlava, P. F.; Venturini, E. L.; Kwak, J. F.; Nigrey, P. J.; Baughman, R. J.; Ginley, D. S. Stoichiometry of Bulk Superconducting $La_2CuO_{4+\delta}$: A Superconducting Superoxide? *Phys. C Supercond. its Appl.* **1988**, *152* (1), 121–123. https://doi.org/10.1016/0921-4534(88)90081-0.

(67) Mizushima, K.; Jones, P. C.; Wiseman, P. J.; Goodenough, J. B. Li_xCoO_2 ($0 < x < 1$): A New Cathode Material for Batteries of High Energy Density. *Mater. Res. Bull.* **1980**, *15* (6), 783–789. https://doi.org/10.1016/0025-5408(80)90012-4.

(68) Lander, J. J. The Phase System BaO - $BaCO_3$. *J. Am. Chem. Soc.* **1951**, *12* (73), 5893–5894. https://doi.org/10.1021/ja01156a535.

(69) King, E. L.; Krall, H. J.; Pandow, L. M. Studies pertaining to soluble silver iodide species **1952**, *74* (14), 54. https://doi.org/10.1021/ja01134a012.

(70) Sasaki, S.; Giri, S.; Cassidy, S.; Dey, S.; Batuk, M.; Vandemeulebroucke, D.; Cibin, G.; Smith, R. I.; Holdship, P.; Grey, C.; Hadermann, J.; Clarke, S. Anion Redox as a Means to Derive Layered Manganese Oxychalcogenides with Exotic Intergrowth Structures. *Nat. Commun.* **2023**, *14* (1), 2917. https://doi.org/10.1038/s41467-023-38489-3.

(71) Eckert, M. Max von Laue and the Discovery of X-Ray Diffraction in 1912. *Annalen der Physik*. **2012**. https://doi.org/10.1002/andp.201200724.

(72) Patterson, A. L. A Fourier Series Method for the Determination of the Components of Interatomic Distances in Crystals. *Phys. Rev.* **1934**, *46* (5), 372–376. https://doi.org/10.1103/PhysRev.46.372.

(73) Karle, J.; Hauptman, H. The Phases and Magnitudes of the Structure Factors. *Acta Crystallogr.* **1950**, *3* (3), 181–187. https://doi.org/10.1107/s0365110x50000446.

(74) Sayre, D. The Squaring Method: A New Method for Phase Determination. *Acta Crystallogr.* **1952**, *5* (1), 60–65. https://doi.org/10.1107/s0365110x52000137.

(75) Oszlányi, G.; Süto̎, A. Ab Initio Structure Solution by Charge Flipping. *Acta Crystallogr. Sect. A Found. Crystallogr.* **2004**, *60* (2), 134–141. https://doi.org/10.1107/S0108767303027569.

(76) Hewat, A. W. D2B, A New High Resolution Neutron Powder Diffractormeter at Ill Grenboble. *Mater. Sci. Forum* **1986**, *9*, 69–80. https://doi.org/10.4028/WWW.SCIENTIFIC.NET/MSF.9.69.

(77) Institut Laue-Langevin. *ILL Neutrons for Society - Instrument layout*. https://www.ill.eu/users/instruments/instruments-list/d2b/description/instrument-layout.

(78) Caglioti, G.; Paoletti, A.; Ricci, F. P. Choice of Collimators for a Crystal Spectrometer for Neutron Diffraction. *Nucl. Instruments* **1958**, *3* (4), 223–228. https://doi.org/10.1016/0369-643X(58)90029-X.

(79) Ibberson, R. M. Design and Performance of the New Supermirror Guide on HRPD at ISIS. *Nucl.*

Instruments Methods Phys. Res. Sect. A Accel. Spectrometers, Detect. Assoc. Equip. **2009**, *600* (1), 47–49. https://doi.org/https://doi.org/10.1016/j.nima.2008.11.066.

(80) Sears, V. F. Neutron Scattering Lengths and Cross Sections. *Neutron News* **1992**, *3* (3), 26–37. https://doi.org/10.1080/10448639208218770.

(81) Bragg, W. H. Application of the Ionisation Spectrometer to the Determination of the Structure of Minute Crystals. *Proc. Phys. Soc. London* **1920**, *33* (1), 222–224. https://doi.org/10.1088/1478-7814/33/1/321.

(82) Brentano, J. C. M. Parafocusing Properties of Microcrystalline Powder Layers in X-Ray Diffraction Applied to the Design of X-Ray Goniometers. *J. Appl. Phys.* **1946**, *17* (6), 420–434. https://doi.org/10.1063/1.1707733.

(83) Thompson, S. P.; Parker, J. E.; Potter, J.; Hill, T. P.; Birt, A.; Cobb, T. M.; Yuan, F.; Tang, C. C. Beamline I11 at Diamond: A New Instrument for High Resolution Powder Diffraction. *Rev. Sci. Instrum.* **2009**, *80* (7), 075107. https://doi.org/10.1063/1.3167217.

(84) Chapon, L. C.; Manuel, P.; Radaelli, P. G.; Benson, C.; Perrott, L.; Ansell, S.; Rhodes, N. J.; Raspino, D.; Duxbury, D.; Spill, E.; Norris, J. WISH: The New Powder and Single Crystal Magnetic Diffractometer on the Second Target Station. *Neutron News*. 2011, pp 22–25. https://doi.org/10.1080/10448632.2011.569650.

(85) Bull, C. L.; Funnell, N. P.; Tucker, M. G.; Hull, S.; Francis, D. J.; Marshall, W. G. PEARL: The High Pressure Neutron Powder Diffractometer at ISIS. *High Press. Res.* **2016**, *36* (4), 493–511. https://doi.org/10.1080/08957959.2016.1214730.

(86) Marshall, W. G.; Francis, D. J. Attainment of Near-Hydrostatic Compression Conditions Using the Paris–Edinburgh Cell. *J. Appl. Crystallogr.* **2002**, *35* (1), 122–125. https://doi.org/10.1107/s0021889801018350.

(87) Klotz, S.; Chervin, J.-C.; Munsch, P.; Marchand, G. Hydrostatic Limits of 11 Pressure Transmitting Media. *J. Phys. D Appl. Phys* **2009**, *42* (7), 75413. https://doi.org/10.1088/0022-3727/42/7/075413.

(88) Fortes, A. D. *A Revised Equation of State for in Situ Pressure Determination Using Fcc-Pb (0 < P < 13 GPa, T > 100 K)*; RAL Technical Report TR–2019–002, **2019**.

(89) Khvostantsev, L. G. A Verkh-Niz (up-down) Toroid Device for Generation of High Pressure. *High Temp. High Press.* **1984**, *16* (2), 165–169.

(90) Besson, J. M.; Nelmes, R. J.; Hamel, G.; Loveday, J. S.; Weill, G.; Hull, S. Neutron Powder Diffraction above 10 GPa. *Phys. B Condens. Matter* **1992**, *180–181*, 907–910. https://doi.org/10.1016/0921-4526(92)90505-m.

(91) Arnold, O.; Bilheux, J. C.; Borreguero, J. M.; Buts, A.; Campbell, S. I.; Chapon, L.; Doucet, M.; Draper, N.; Ferraz Leal, R.; Gigg, M. A.; Lynch, V. E.; Markvardsen, A.; Mikkelson, D. J.; Mikkelson, R. L.; Miller, R.; Palmen, K.; Parker, P.; Passos, G.; Perring, T. G.; Peterson, P. F.; Ren, S.; Reuter, M. A.; Savici, A. T.; Taylor, J. W.; Taylor, R. J.; Tolchenov, R.; Zhou, W.; Zikovsky, J. Mantid—Data Analysis and Visualization Package for Neutron Scattering and μ SR Experiments. *Nucl. Instruments Methods Phys. Res. Sect. A Accel. Spectrometers, Detect. Assoc. Equip.* **2014**, *764*, 156–166. https://doi.org/10.1016/j.nima.2014.07.029.

(92) Williams, W. G.; Ibberson, R. M.; Day, P.; Enderby, J. E. GEM - General Materials Diffractometer at ISIS. *Phys. B Condens. Matter* **1997**, *241–243*, 234–236. https://doi.org/10.1016/S0921-4526(97)00561-9.

(93) *ISIS GEM **2014*** https://www.isis.stfc.ac.uk/Pages/gem.aspx.

(94) Pawley, G. S. Unit-Cell Refinement from Powder Diffraction Scans. *J. Appl. Crystallogr.* **1981**, *14* (6), 357–361. https://doi.org/10.1107/s0021889881009618.

(95) Coelho, A. A. TOPAS and TOPAS-Academic: An Optimization Program Integrating Computer Algebra and Crystallographic Objects Written in C++. *J. Appl. Crystallogr.* **2018**, *51* (Version 6), 210–218.

(96) Zagorac, D.; Muller, H.; Ruehl, S.; Zagorac, J.; Rehme, S. Recent Developments in the Inorganic Crystal Structure Database: Theoretical Crystal Structure Data and Related Features. *J. Appl. Crystallogr.* **2019**, *52*, 918–925. https://doi.org/10.1107/S160057671900997X.

(97) Zou, X.; Hovmoller, S.; Oleynikov, P. *Electron Crystallography. Electron Microscopy and Electron Diffraction* .; Oxford University Press, **2011**; Vol. 16. https://doi.org/10.1107/s1600576714002726.

(98) Zhao, J.; Liu, X. Electron Microscopic Methods (TEM, SEM and Energy Dispersal Spectroscopy). In *Reference Module in Earth Systems and Environmental Sciences*; Academic Press, **2022**; pp 575–588. https://doi.org/10.1016/b978-0-12-822974-3.00013-6.

(99) Yano, J.; Yachandra, V. K. X-Ray Absorption Spectroscopy. *Photosynthesis Research*. **2009**, pp 241–

254. https://doi.org/10.1007/s11120-009-9473-8.
(100) Dent, A. J.; Cibin, G.; Ramos, S.; Smith, A. D.; Scott, S. M.; Varandas, L.; Pearson, M. R.; Krumpa, N. A.; Jones, C. P.; Robbins, P. E. B18: A Core XAS Spectroscopy Beamline for Diamond. In *Journal of Physics: Conference Series*; **2009**; Vol. 190, p 12039. https://doi.org/10.1088/1742-6596/190/1/012039.
(101) Elliot, S. *The Physics and Chemistry of Solids*; Wiley and Sons: Chichester, **1998**. https://doi.org/10.1038/1781214b0.
(102) Dew-Hughes, D. The Critical Current of Superconductors: An Historical Review. *Low Temperature Physics*. AIP Publishing September 1, **2001**, pp 713–722. https://doi.org/10.1063/1.1401180.
(103) Cox, P. A. The Electronic Structure and Chemistry of Solids (Oxford Science Publications). *Oxford Univ. Press.* **1987**.
(104) Ferraro, J.; Nakamoto, K. *Introductory Raman Spectroscopy*; **1994**. https://doi.org/10.1016/c2009-0-21238-4.
(105) Brown, I. D.; Altermatt, D. Bond-valence Parameters Obtained from a Systematic Analysis of the Inorganic Crystal Structure Database. *Acta Crystallogr. Sect. B* **1985**, *41* (4), 244–247. https://doi.org/10.1107/S0108768185002063.
(106) Greven, M.; Birgeneau, R.; Kastner, M.; Matsuda, M.; Shirane, G. ZEITSCHRIFT FOR PHYSIK B Neutron Scattering Study of the Two-Dimensional Spin S = 1/2 Square-Lattice Heisenberg Antiferromagnet $Sr_2CuO_2Cl_2$. *Z. Phys. B* **1995**, *96*, 465477. https://doi.org/10.1007/BF01313844.
(107) Knee, C. S.; Weller, M. T. Neutron Diffraction Study of Crystal Structure and Antiferromagnetic Order in $Sr_2CoO_2X_2$ (X = Cl, Br). *Phys. Rev. B - Condens. Matter Mater. Phys.* **2004**, *70* (14), 144406. https://doi.org/10.1103/PhysRevB.70.144406.
(108) Zhou, W.; Li, S.; Wu, S. Magnetic and Electronic Properties of Layered $Sr_2NiO_2Cl_2$ with Square Planar Coordination. *J. Magn. Magn. Mater.* **2020**, *514*, 167195. https://doi.org/10.1016/j.jmmm.2020.167195.
(109) Smyth, R. D.; Khalyavin, D.; Tsujimoto, Y.; Yamaura, K.; Clarke, S. J. Magnetic Ordering in the Layered Oxyhalide $Sr_2NiO_2Cl_2$. *Solid State Sci.* **2023**, *144*, 1293–2558. https://doi.org/10.1016/j.solidstatesciences.2023.107297.
(110) Samuseva, R. G.; Plyushchev, V. E. Phase Diagram of Csl-Nal System. *Zh. Neorg. Khim.* **1961**, *6* (9), 2139–2140.
(111) Coles, B. R. The Lattice Spacings of Nickel-Copper and Palladium-Silver Alloys. *J Inst Met* **1956**, *84*, 346–348.
(112) Brock, S. L.; Raju, N. P.; Greedan, J. E.; Kauzlarich, S. M. The Magnetic Structures of the Mixed Layer Pnictide Oxide Compounds $Sr_2Mn_3Pn_2O_2$ (*Pn* = As, Sb). *J. Alloys Compd.* **1996**, *237* (1–2), 9–19. https://doi.org/10.1016/0925-8388(95)02066-7.
(113) Warren, B. E. X-Ray Diffraction in Random Layer Lattices. *Phys. Rev.* **1941**, *59* (9), 693–698. https://doi.org/10.1103/physrev.59.693.
(114) Warren, B. E.; Bodenstein, P. The Shape of Two-Dimensional Carbon Black Reflections. *Acta Crystallogr.* **1966**, *20* (5), 602–605. https://doi.org/10.1107/s0365110x66001464.
(115) Zhao, L. L.; Wu, S.; Wang, J. K.; Hodges, J. P.; Broholm, C.; Morosan, E. Quasi-Two-Dimensional Noncollinear Magnetism in the Mott Insulator $Sr_2F_2Fe_2OS_2$. *Phys. Rev. B* **2013**, *87* (2). https://doi.org/10.1103/physrevb.87.020406.
(116) Telling, M. T. F.; Andersen, K. H. Spectroscopic Characteristics of the OSIRIS Near-Backscattering Crystal Analyser Spectrometer on the ISIS Pulsed Neutron Source. *Phys. Chem. Chem. Phys.* **2005**, *7* (6), 1255–1261. https://doi.org/10.1039/b413934h.
(117) Hull, S.; Smith, R. I.; David, W. I. F.; Hannon, A. C.; Mayers, J.; Cywinski, R. The Polaris Powder Diffractometer at ISIS. *Phys. B Phys. Condens. Matter* **1992**, *180–181* (PART 2), 1000–1002. https://doi.org/10.1016/0921-4526(92)90533-X.
(118) Kresse, G.; Hafner, J. Ab Initiomolecular Dynamics for Liquid Metals. *Phys. Rev. B* **1993**, *47* (1), 558–561. https://doi.org/10.1103/physrevb.47.558.
(119) Kresse, G.; Furthmüller, J. Efficient Iterative Schemes for Ab Initio Total-Energy Calculations Using a Plane-Wave Basis Set, *Phys. Rev. B*, Vol. 54, Pp. 11169-11186. **1996**.
(120) Perdew, J. P.; Burke, K.; Wang, Y. Generalized Gradient Approximation for the Exchange-Correlation Hole of a Many-Electron System. *Phys. Rev. B* **1996**, *54* (23), 16533–16539. https://doi.org/10.1103/physrevb.54.16533.
(121) Birch, F. Finite Elastic Strain of Cubic Crystals. *Phys. Rev.* **1947**, *71* (11), 809–824. https://doi.org/10.1103/physrev.71.809.

(122) Gonzalez-Platas, J.; Alvaro, M.; Nestola, F.; Angel, R. EosFit7-GUI: A New Graphical User Interface for Equation of State Calculations, Analyses and Teaching. *J. Appl. Crystallogr.* **2016**, *49* (4), 1377–1382. https://doi.org/10.1107/s1600576716008050.

(123) Roth, W. L. Magnetic Structures of MnO, FeO, CoO, and NiO. *Phys. Rev.* **1958**, *110* (6), 1333–1341. https://doi.org/https://doi.org/10.1103/PhysRev.110.1333.

(124) Campbell, B. J.; Stokes, H. T.; Tanner, D. E.; Hatch, D. M. ISODISPLACE: A Web-Based Tool for Exploring Structural Distortions. *J. Appl. Crystallogr.* **2006**, *39* (4), 607–614. https://doi.org/10.1107/S0021889806014075.

(125) Litvin, D. B. Magnetic Group Tables: 1-, 2- and 3-Dimensional Magnetic Subperiodic Groups and Magnetic Space Groups. *Int. Union Crystallogr.* **2013**. https://doi.org/10.1107/9780955360220001.

(126) Ueda, K.; Hosono, H. Band Gap Engineering, Band Edge Emission, and p-Type Conductivity in Wide-Gap $LaCuOS_{1-x}Se_x$ Oxychalcogenides. *J. Appl. Phys.* **2002**, *91* (7), 4768–4770. https://doi.org/10.1063/1.1456240.

(127) Alonso, J. A.; Martínez-Lope, M. J.; García-Muñoz, J. L.; Fernández, M. T. Crystal Structure and Magnetism in the Defect Perovskite $LaNiO_{2.5}$. *Phys. B Condens. Matter* **1997**, *234–236*, 18–19. https://doi.org/10.1016/S0921-4526(96)00863-0.

(128) Matsuda, M.; Katsumata, K.; Zheludev, A.; Shapiro, S. M.; Shirane, G. Neutron Scattering Study in $BaNiO_2$. *J. Phys. Chem. Solids* **1999**, *60* (8), 1121–1123. https://doi.org/10.1016/S0022-3697(99)00070-0.

(129) Harris, L. *MChem. Thesis*. The chemistry of layered oxychalcogenides. University of Oxford. **2011**.

(130) Rutt, O. J.; Williams, G. R.; Clarke, S. J. Reversible Lithium Insertion and Copper Extrusion in Layered Oxysulfides. *Chem. Commun.* **2006**, *0* (27), 2869–2871. https://doi.org/10.1039/b605105g.

(131) Koo, H.-J.; Kremer, R. K.; Whangbo, M.-H. Orbital Magnetic Moments of the High-Spin Co Ions at Axially-Elongated Octahedral Sites: Unquenched as Reported from Experiment or Quenched as Predicted by Theory? *Cite This Inorg. Chem* **2020**, *59*, 18319–18324. https://doi.org/10.1021/acs.inorgchem.0c02929.

(132) Whangbo, M.-H.; Kremer, R. K.; Koo, H.-J. Unusually High Magnetic Moments Reported for the High-Spin Co^{2+} Ions at Axially Elongated CoO_4X_2 (*X* = Cl, Br, S, Se) Octahedral Sites: Overestimated Magnetic Moments Caused by Underestimated Magnetic Form Factors. *J. Phys. Chem. C* **2022**, *2022*, 16563–16567. https://doi.org/10.1021/acs.jpcc.2c05586.

(133) Wilson, J. *MChem. Thesis*. Synthesis, structure and properties of layered oxychalcogenides. University of Oxford, **2008**.

(134) Smyth, R. D.; Wilson, J. A. D.; Manuel, P.; Clarke, S. J. Synthesis, Structure, Magnetism and Cation Ordering in $Ba_{3-x}Sr_xFe_2O_5Cu_2Ch_2$ (*x* = 0, 1, 2; *Ch* = S, Se) and $BaCa_2Fe_2O_5Cu_2S_2$. *J. Solid State Chem.* **2022**, *307*, 122841. https://doi.org/10.1016/J.JSSC.2021.122841.

(135) Suard, E.; Hewat, A. The Super-D2B Project at the ILL. *Neutron News* **2001**, *12* (4), 30–33. https://doi.org/10.1080/10448630108245006.

(136) Whangbo, M. H.; Gordon, E. E.; Xiang, H.; Koo, H. J.; Lee, C. Prediction of Spin Orientations in Terms of HOMO-LUMO Interactions Using Spin-Orbit Coupling as Perturbation. *Acc. Chem. Res.* **2015**, *48* (12), 3080–3087. https://doi.org/10.1021/acs.accounts.5b00408.

(137) Verwey, E. J. W. Electronic Conduction of Magnetite (Fe_3O_4) and Its Transition Point at Low Temperatures. *Nature*. Nature Publishing Group **1939**, pp 327–328. https://doi.org/10.1038/144327b0.

(138) Gordon, E. E. Analysis of the Properties of Magnetic Solids by Density Functional Theory (DFT) Calculations., **2018**.

(139) Palazzi, M.; Carcaly, C.; Flahaut, J. Un Nouveau Conducteur Ionique (LaO)AgS. *J. Solid State Chem.* **1980**, *35* (2), 150–155. https://doi.org/10.1016/0022-4596(80)90487-9.

(140) Palazzi, M.; Jaulmes, S. Structure Du Conducteur Ionique (LaO)AgS. *Acta Crystallogr. Sect. B Struct. Crystallogr. Cryst. Chem.* **1981**, *37* (7), 1337–1339. https://doi.org/10.1107/s0567740881005876.

(141) Wilmer, D.; Jorgensen, J. D.; Wuensch, B. J. Two-Dimensional Silver Fast-Ion Conduction in (LaO)AgS. *Solid State Ionics* **2000**, *136–137*, 961–966. https://doi.org/10.1016/S0167-2738(00)00512-9.

(142) Ueda, K.; Hosono, H. Crystal Structure of $LaCuOS_{1-x}Se_x$ Oxychalcogenides. *Thin Solid Films* **2002**, *411*, 115–118. https://doi.org/10.1016/S0040-6090(02)00198-0.

(143) Ma, J.-J.; Liu, Q.-Y.; Liu, P.-F.; Zhang, P.; Sanyal, B.; Ouyang, T.; Wang, B.-T. Ultralow Thermal Conductivity and Anisotropic Thermoelectric Performance in Layered Materials La*MOCh* (*M* = Cu, Ag; *Ch* = S, Se). *Phys. Chem. Chem. Phys.* **2022**, *24* (35), 21261–21269. https://doi.org/10.1039/D2CP02067J.

(144) Arnold, W. *MChem. Thesis*. The synthesis and properties of the cerium oxide chalcogenides. University of Oxford. **2021**.
(145) Prascher, A. *MChem. Thesis*. The chemsitry of cerium oxide chalcogenides. University of Oxford. **2013**.
(146) Lim, J. *MChem. Thesis*. The chemsitry of cerium oxide chalcogenides. University of Oxford. **2012**.
(147) Townsend, E. *MChem. Thesis*. Intercalation and deintercalation chemistry of lanthanide oxide chalcogenides. University of Oxford. **2022**.
(148) Müller, B.; Lutz, H. D. Raman Spectra of $MnSe_2$, $MnTe_2$, $RuTe_2$, and $OsTe_2$. *Solid State Commun.* **1991**, *78* (5), 469–471. https://doi.org/10.1016/0038-1098(91)90706-2.
(149) Hulliger, F.; Siegrist, T. The Crystal Structures of $BaSe_2$ and $BaSe_3$. *Zeitschrift fur Naturforsch. - Sect. B J. Chem. Sci.* **1981**, *36* (1), 14–15. https://doi.org/10.1515/znb-1981-0104.

Appendices

Appendix A Computation of $Sr_2MO_2Cu_2Ch_2$ (*M* = Co, Ni, Cu, Zn; *Ch* = S, Se)

A.1 Full computational procedure

DFT calculations on the series $Sr_2MO_2Cu_2Ch_2$ (*M* = Co, Ni, Cu, Zn; *Ch* = S, Se) were carried out using the VASP software package,[1,2] version 6.2.1, with the PBE functional[3] and a plane-wave cut-off of 850 eV. A $\sqrt{2}a \times \sqrt{2}a \times c$ expansion of the unit cell containing two M^{2+} centres per layer was used throughout, and the tetragonal Brillouin zone was sampled on a 4 × 4 × 2 Γ-centred grid.[4] A finer 10 × 10 × 1 Γ-centred grid was used to generate the DOS. The effect of the core electrons was incorporated using projector augmented wave (PAW) potentials,[5] and a Hubbard U_{eff} value[6] of 2 eV was applied to the transition metal cations in the oxide layer. The DFT-D3 method was introduced for the van der Waals forces correction.[7,8] The results are shown in Figure 3.20.

Both lattice parameters and atomic positions were optimised for a tetragonal unit cell, where a Hubbard *U* value of 2.0 eV was applied to all open-shell transition metal ions (Co, Ni, Cu). The lattice parameters, *M*-O and *M*-*Ch* bonds, *M*-*Ch* / *M*-O ratio and the magnetic moment on the transition metal ion are collected in Table 3.5 for *M* = Ni and Table A.1.1 for *M* = Co/Cu combinations with S and Se.

Table A.1.1 Structural data by experiment and calculation for $Sr_2MO_2Cu_2Ch_2$ (*M* = Co, Cu; *Ch* = S, Se).

	$Sr_2CoO_2Cu_2S_2$		$Sr_2CoO_2Cu_2Se_2$	
	exp	DFT	exp	DFT
a / Å	5.643	5.617	5.720	5.705
c / Å	17.720	17.460	18.357	18.102
Co-O / Å	1.986	1.986	2.024	2.017
Co-E / Å	3.008	3.007	3.0827	3.041
Co-E/Co-O	1.515	1.514	1.523	1.507
μ(Co)		2.60		2.60

	$Sr_2CuO_2Cu_2S_2$		$Sr_2CuO_2Cu_2Se_2$	
	exp	DFT	exp	DFT
a / Å	5.544	5.509	5.616	5.610
c / Å	18.20	18.034	18.820	18.604
Cu-O / Å	1.96	1.948	1.986	1.984
Cu-E / Å	3.11	3.115	3.169	3.143
Cu-E/Cu-O	1.587	1.599	1.596	1.584
μ(Cu)		0.90		0.90

In all cases where the transition metal is one of Co, Cu or Zn, the correspondence between the computed structural parameters and the experimental structural data is extremely good.

The results are more complicated for Ni, where there are two quite distinct states of similar energy, one where the Ni^{2+} ions are in local high-spin configurations ($\mu / \mu_B = 1.6$), the other where they are low-spin. For both Ni systems (S and Se), the properties of both high-spin (HS) and low-spin (LS) configurations are shown in Table 3.5 For the selenide, the high-spin configuration is the more stable of the two, lying at 0.26 eV (per unit cell) lower in energy than the corresponding low-spin state. The high-spin configuration also offers the best match to the measured structural parameters (the dashed line in Figure 3.20), particularly in the *ab*-plane where the Ni-O bonds are within 0.01 Å of the experimental values. In contrast to the success in replicating *a*, the computed value of *c* is underestimated by 0.55 Å, a far greater deviation from experiment than was observed in any of the Co / Cu / Zn systems where the error was consistently of the order of 0.25 Å as seen in Table A.1.1.

As a result, the Ni-Se / Ni-O ratio is also underestimated, the computed value being 1.481 vs a measured value of 1.536. The alternative low-spin configuration (dotted line in Figure 3.20), in addition to being higher in energy, also affords a much worse match with experiment: the lattice is compressed in the *ab*-plane, and the computed *c* parameter is 0.85 Å greater than experiment (note that the value of *c* is always underestimated, not overestimated, in the Co / Cu / Zn systems, so such a large deviation appears entirely out of line with the general behaviour of this class of compounds).

Turning to the sulfide system, the situation is even more complex. Both high- and low-spin configurations were located, and this time it is the latter that is more stable, lying 0.27 eV below the high-spin alternative for $U_{Ni} = 2$ eV . However, the high-spin / low-spin separation is well known to be sensitive to the chosen value of *U*, and indeed if the calculation is repeated with $U_{Ni} = 4$ eV, it is found that the energies are reversed and the high-spin

configuration is the more stable by 0.87 eV. Given this uncertainty, there is not much emphasis placed on the computed energies other than to note that for a given value of U_{Ni} (2.0 eV in Table 3.5), the low-spin configuration is relatively stabilised in the sulfide compared to the selenide, consistent with the absence of additional Bragg peaks in $Sr_2NiO_2Cu_2S_2$. Tables A.2.1 and A.2.2 show the sensitivity of the sensitivity of the spin density to both the value of U_{Ni} and the coordination environment.

The computed lattice parameters also present a rather ambiguous picture, with neither high-spin (dashed line) or low-spin (dotted line) forms offering convincing agreement with experiment (see Figure 3.20). All the experimentally measured bond lengths and lattice parameters, along with the Ni-S / Ni-O elongation ratio, sit almost exactly between the limiting values of the high- and low-spin forms.

In absolute terms, the high-spin value for *c* in $Sr_2NiO_2Cu_2S_2$ is underestimated by 0.85 Å, even more than the selenide case. The low-spin value for *c* in $Sr_2NiO_2Cu_2S_2$ is closer to experiment (0.33 Å higher), but note again that this value is consistently underestimated, not overestimated, by the calculations for Co / Cu / Zn where the spin-state is unambiguous. If the Ni-S values are corrected for this 0.25 Å underestimation, it is seen again that the experimental value of *c* lies almost exactly midway between the computed high- and low-spin values. This observation prompted an investigation into locally stable configurations with mixed high-spin and low-spin configurations.

The 'mixed' entry in Table 3.5 and Figure 3.20 corresponds to one ordered example where high-spin and low-spin Ni^{2+} ions are arranged within each layer in a checkerboard arrangement. This was achieved by first imposing different values of U_{Ni} (2 eV for low-spin Ni^{2+}, 4 eV for high spin Ni^{2+}) and then using the converged geometry and density to initialise

a calculation where U_{Ni} = 2 eV was imposed for all metal centres. This mixed configuration offers remarkably good agreement with experiment – *c* is now underestimated by 0.21 Å and *a* by 0.03 Å, replicating precisely the behaviour of the Co/Cu/Zn systems. The Ni-O and the Ni-S distances now differ, with the high-spin (Ni-O 1.99 Å, Ni-S 3.04 Å) and low-spin values (Ni-O 1.90 Å, Ni-S 3.14 Å) values close to those computed for the all-high or all-low configurations, respectively. The Ni-S / Ni-O ratio computed using the average of the two Ni-O and the two Ni-S distances is in remarkable agreement with the experimental value (widely spaced dashed line in Figure 3.20). It is, of course, possible that other, less ordered, arrangements of high-spin / low-spin Ni^{2+} ions would afford similar structural parameters, or indeed that the agreement between experiment and theory for the mixed state is coincidental.

A.2 Sensitivity of the spin-state to *U*

Table A.2.1 Calculation data of $Sr_2NiO_2Cu_2Se_2$ using different U values for Ni.

U = Ni^{2+}		Energy / eV	ΔE / eV	Spin density	d-orbital configuration	M-O / Å	M-Se / Å	*a* / Å	*c* / Å
	Exp					2.01	3.08	4.02	18.39
4	Cal	-171.60	-1.70	1.608,-1.608,1.608, -1.608	Octahedral	2.03	3.05	4.05	18.17
4	Cal	-169.90		-0.005,-0.005,0.005, 0.005	Square-planar	1.97	3.22	3.94	18.98
3	Cal	-173.02	-0.90	1.548,-1.548,1.548, -1.548	Octahedral	2.03	3.05	4.05	18.18
3	Cal	-172.12		0.363,0.363,-0.363, -0.363	Square-planar	1.97	3.24	3.95	19.03
2	Cal	-174.58	-0.32	1.471,-1.471,1.471, -1.471	Octahedral	2.02	3.05	4.05	18.17
2	Cal	-174.26		-0.352,-0.352,0.352, 0.352	Square-planar	1.97	3.24	3.95	19.03
1	Cal	-176.53		0.534,0.536,-0.534, -0.536	Square-planar	1.97	3.23	3.95	19.03
1	Cal	-176.54		0.546, 0.546, 0.546, 0.546	Square-planar	1.98	3.21	3.96	18.89
0	Cal	-179.03		0.508,0.508,0.508, 0.508	Square-planar	1.97	3.22	3.95	18.98
0	Cal	-178.98		-0.504,0.504,0.504, 0.504	Square-planar	1.98	3.21	3.96	18.91

$\Delta E = E_{oct} - E_{squ}$

Table A.2.2 Computational data for $Sr_2NiO_2Cu_2S_2$ using different U values for Ni.

U = Ni^{2+}		Energy / eV	ΔE / eV	Spin density	d-orbital configuration	M-O / Å	M-S / Å	*a* / Å	*c* / Å
	Exp					1.96	3.11	3.92	18.12
4	Cal	-177.67	-0.97	1.61,-1.61,1.61,-1.61	Octahedral	1.99	3.03	3.98	17.60
4	Cal	-176.69		0,0,0,0	Square-planar	1.93	3.21	3.86	18.52
3	Cal	-179.07	-0.36	1.55,-1.55,1.55,-1.55	Octahedral	1.99	3.03	3.98	17.61
3	Cal	-178.71		0,0,0,0	Square-planar	1.93	3.22	3.85	18.58
2	Cal	-180.69	0.14	1.47,-1.47,1.47,-1.47	Octahedral	1.99	3.01	3.99	17.49
2	Cal	-180.86		0.37,0.37,0.37,0.37	Square-planar	1.94	3.21	3.87	18.44
1	Cal	-183.09		0,0,0,0	Square-planar	1.93	3.21	3.86	18.47
0	Cal	-185.71		-0.51,-0.51,-0.51,-0.51	Square-planar	1.93	3.20	3.87	18.44

$\Delta E = E_{oct} - E_{squ}$

Appendix B Ni-*Ch* / Ni-O ratio as a function of temperature in $Sr_2NiO_2Cu_2Ch_2$ (*Ch* = S, Se)

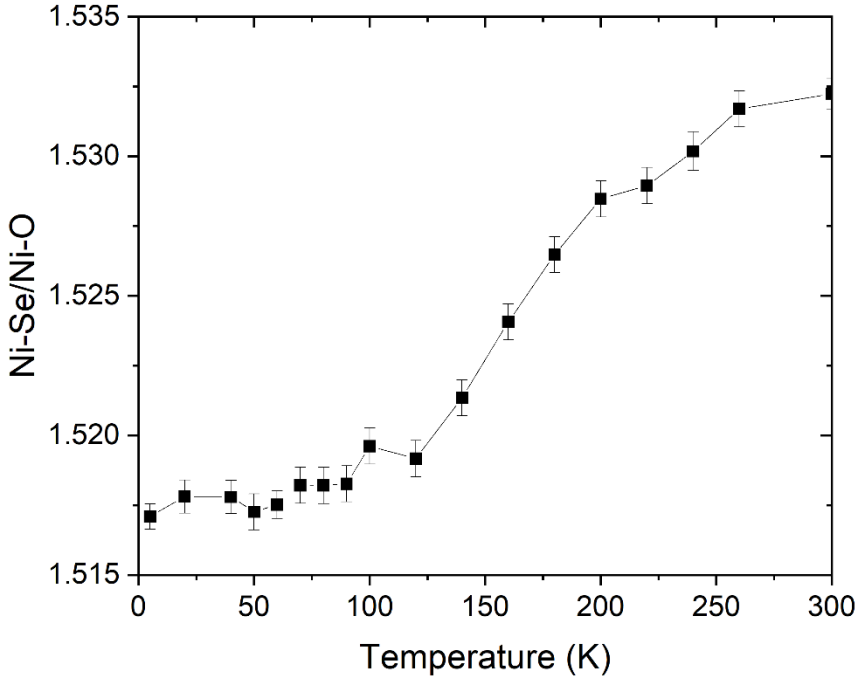


Figure B.1 The Ni-Se / Ni-O ratio as a function of temperature for $Sr_2NiO_2Cu_2Se_2$.

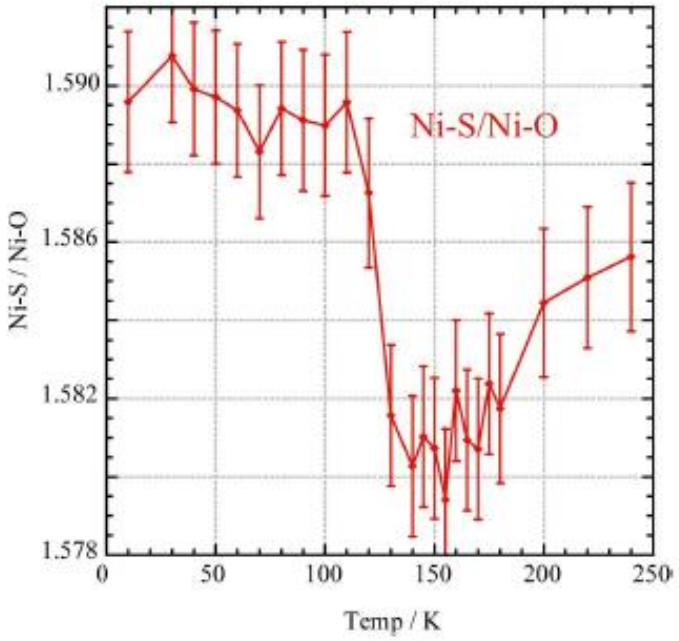


Figure B.2 The Ni-S / Ni-O ratio as a function of temperature for $Sr_2NiO_2Cu_2S_2$.

Appendix C Previous report of $Sr_2NiO_2Cl_2$

C.1 Comparison of structural parameters

Table C.1.1 Difference in lattice parameters between $Sr_2NiO_2Cl_2$ synthesised using NiO and Ni powder.

Beamline	I11	BL15XU
Ni source	NiO	Ni
Reference	This work	Ref.[9]
a (Å)	4.03417(2)	4.03896(4)
c (Å)	15.1058(1)	15.09293(16)
Ni–O (Å) [4]	2.01708(1)	2.01948(3)
Ni–Cl (Å) [2]	2.7076(9)	2.716(3)

C.2 Comparison of magnetometry

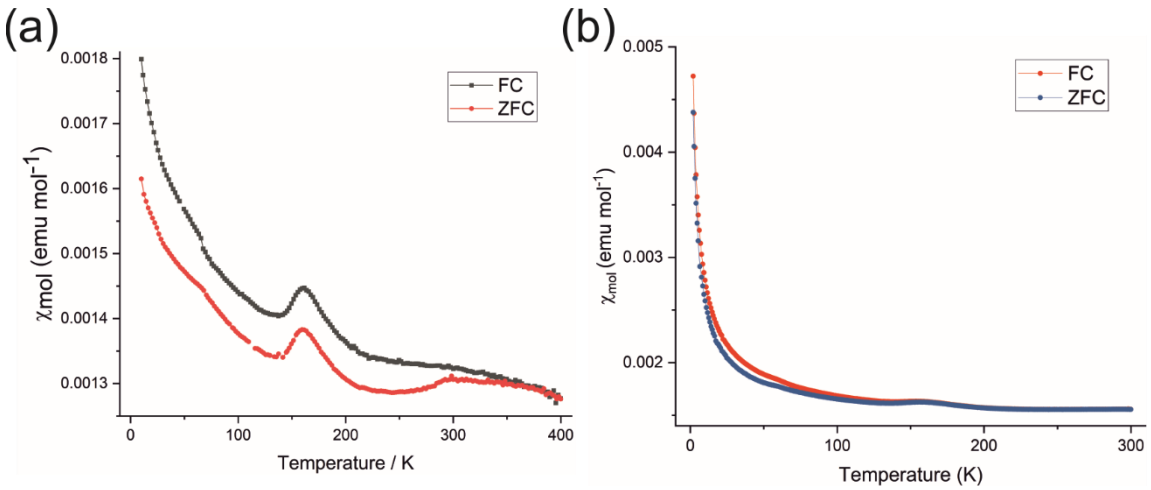


Figure C.2.1 The ZFC / FC plots of "$Sr_2NiO_2Cl_2$" synthesised with **(a)** Ni and **(b)** NiO as a Ni source.

Appendix D Reactivity of $Sr_2CoO_2Cu_2Te_2$ to *n*-BuLi

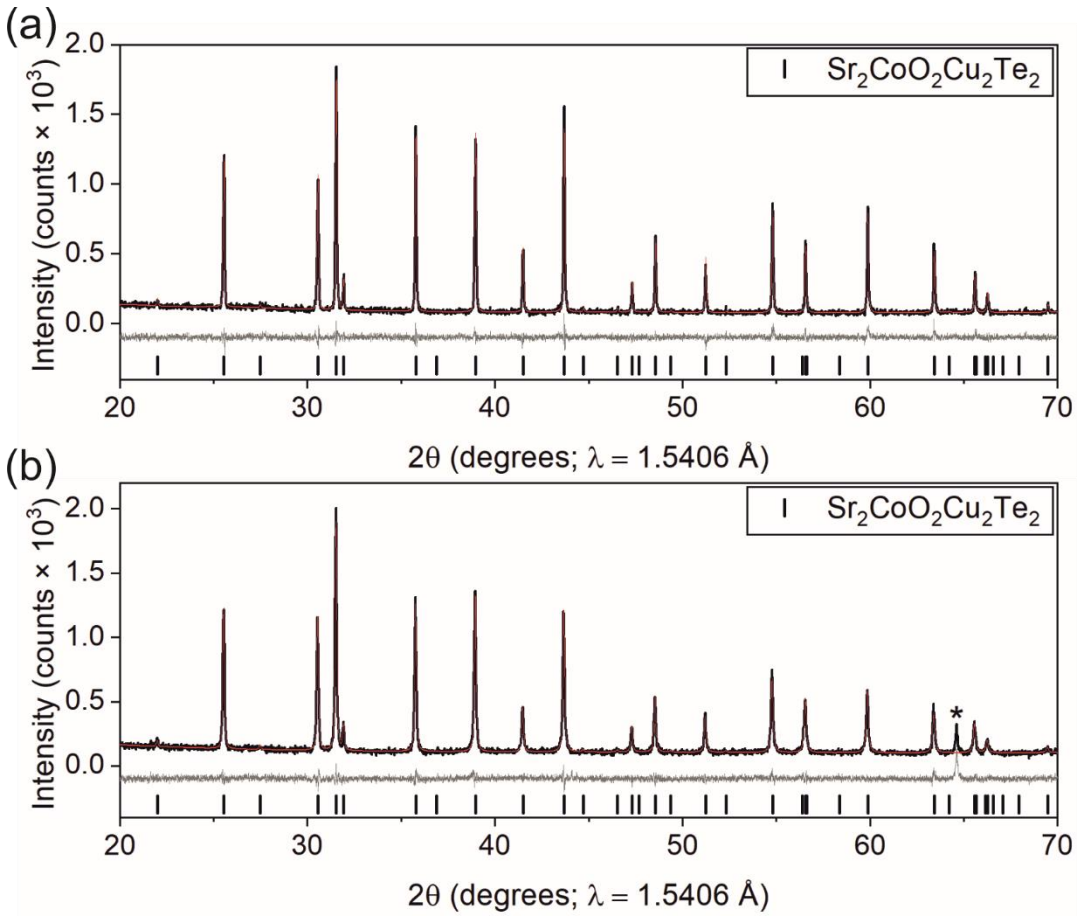


Figure D.1.1 Comparison of Rietveld refinement of **(a)** $Sr_2CoO_2Cu_2Te_2$ as synthesised and **(b)** $Sr_2CoO_2Cu_2Te_2$ reacted with n-BuLi for 3 days at 50 °C. The * is an unidentified impurity.

From chapter 4, it can be seen that reaction of the Co-containing oxide chalcogenides which contain Cu that a successful reaction with *n*-BuLi (and hence underwent Cu / Li exchange) had with in an associated change in peak shape where the peak shape become a lot broader. Figure D.1 above thus shows that there is no reaction with n-BuLi which is backed up by the refinement whereby the parent, $Sr_2CoO_2Cu_2Te_2$, can refine the data with a refined Cu occupancy of 1.98(3) i.e., fully occupied.

Appendix E Further magnetometry of $Ae_2CoO_2X_2Ch_2$

E.1 *M* vs *T* plots

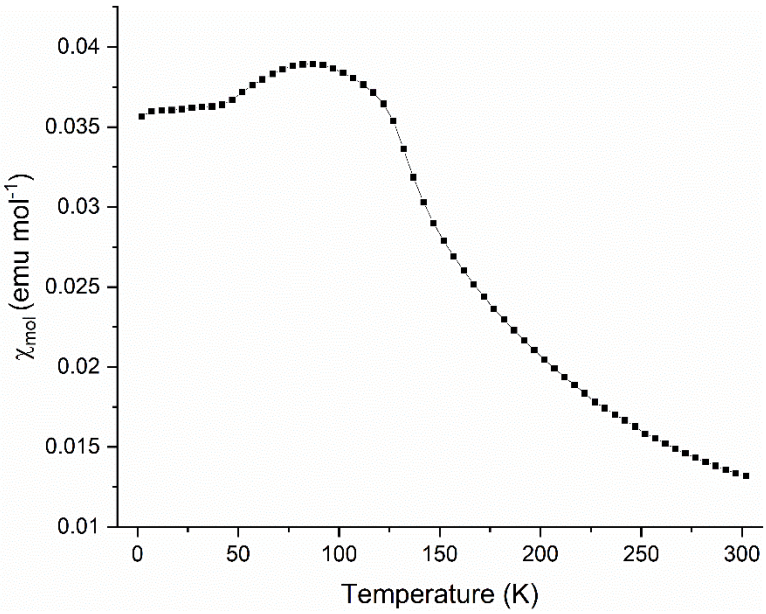


Figure E.1.1 Field-cooled magnetic susceptibility of $Sr_2CoO_2Cu_{2-x}Li_xS_2$, measured using a 6 – 5 T subtraction (as described in section 2.2.7.1).

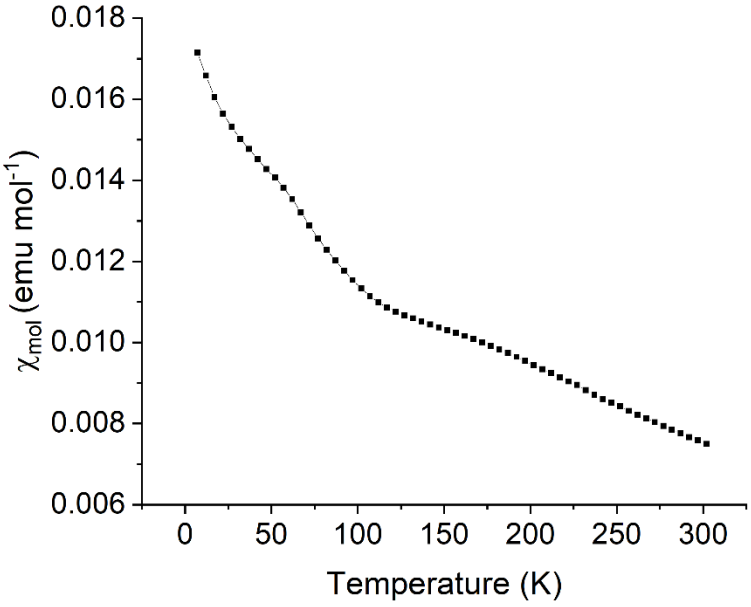


Figure E.1.2 Field-cooled magnetic susceptibility of $Sr_2CoO_2Cu_{2-x}Li_xSe_2$, measured using a 6 – 5 T subtraction (as described in section 2.2.7.1).

E.2 *M* vs *H* plots

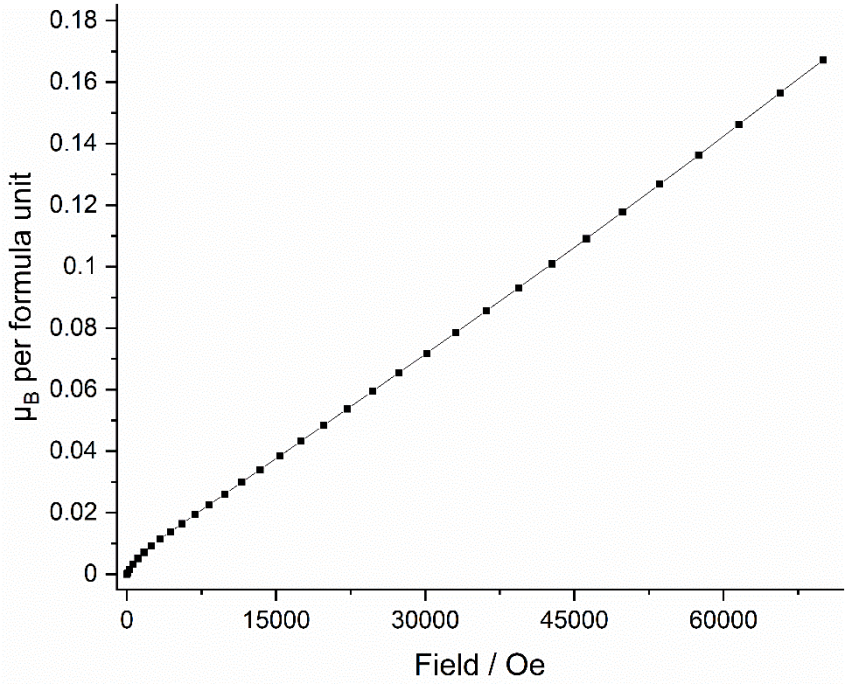


Figure E.2.1 *M vs H* plot for $Sr_2CoO_2Cu_{2-x}Li_xS_2$.

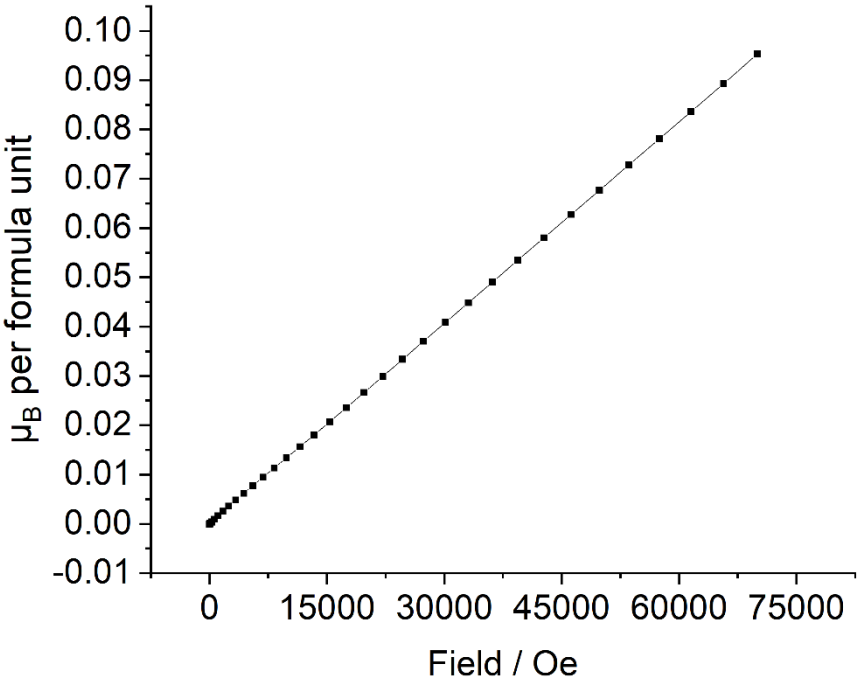


Figure E.2.2 *M vs H* plot for $Sr_2CoO_2Cu_{2-x}Li_xSe_2$.

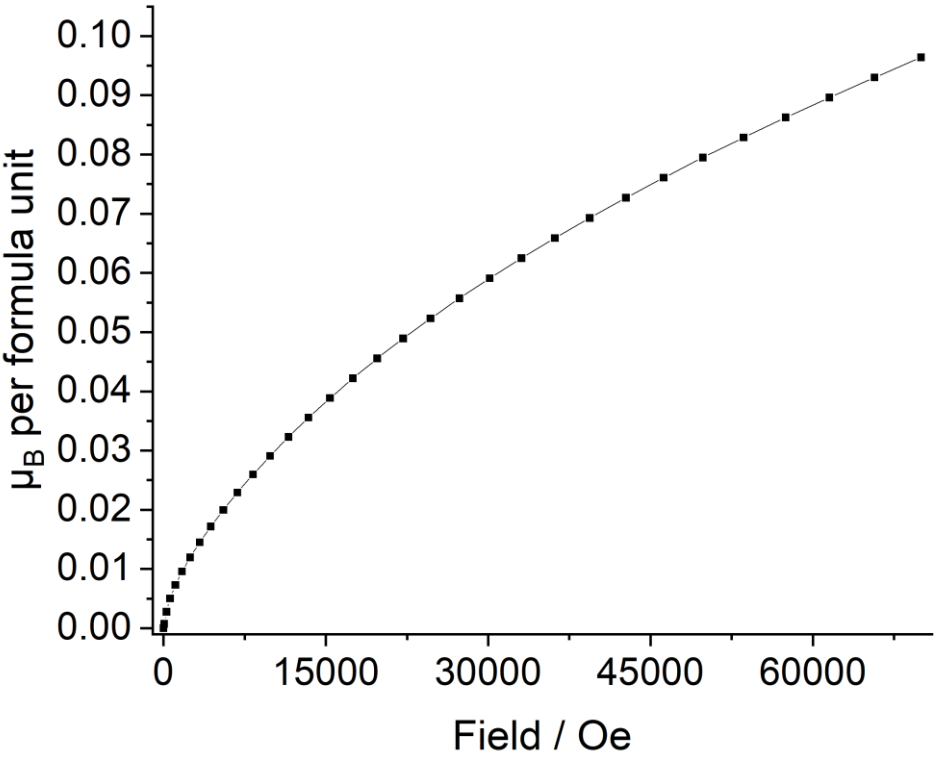


Figure E.2.3 *M vs H* plot for $Sr_2CoO_2Ag_{2-x}Li_xSe_2$.

A high-field subtraction could not be performed on $Sr_2CoO_2Ag_{2-x}Li_xSe$ due the non-linearity of the *M vs H* above in Figure E.2.3. Typically when there is a small amount of ferromagnetic impurity within a sample, it will saturate at low fields and the *M vs H* will be linear in the high-field region. It may be that there is a ferromagnetic impurity in the sample which does not saturate even up to 7 T or another explanation may be that there is superparamagnetic impurity which would require further investigation to distinguish the root cause of this behaviour.

References

(1) Kresse, G.; Hafner, J. Ab Initiomolecular Dynamics for Liquid Metals. *Phys. Rev. B* **1993**, *47* (1), 558–561. https://doi.org/10.1103/physrevb.47.558.

(2) Kresse, G.; Furthmüller, J. "Efficient Iterative Schemes for Ab Initio Total-Energy Calculations Using a Plane-Wave Basis Set," Phys. Rev. B, Vol. 54, Pp. 11169-11186. **1996**.

(3) Perdew, J. P.; Burke, K.; Wang, Y. Generalized Gradient Approximation for the Exchange-Correlation Hole of a Many-Electron System. *Phys. Rev. B* **1996**, *54* (23), 16533–16539. https://doi.org/10.1103/physrevb.54.16533.

(4) Monkhorst, H. J.; Pack, J. D. Special Points for Brillouin-Zone Integrations. *Phys. Rev. B* **1976**, *13* (12), 5188–5192. https://doi.org/10.1103/physrevb.13.5188.

(5) Blöchl, P. E. Projector Augmented-Wave Method. *Phys. Rev. B* **1994**, *50* (24), 17953–17979. https://doi.org/10.1103/physrevb.50.17953.

(6) Dudarev, S. L.; Botton, G. A.; Savrasov, S. Y.; Humphreys, C. J.; Sutton, A. P. Electron-Energy-Loss Spectra and the Structural Stability of Nickel Oxide: An LSDA+U Study. *Phys. Rev. B* **1998**, *57* (3), 1505–1509. https://doi.org/10.1103/physrevb.57.1505.

(7) Grimme, S.; Antony, J.; Ehrlich, S.; Krieg, H. A Consistent and Accurate Ab Initio Parametrization of Density Functional Dispersion Correction (DFT-D) for the 94 Elements H-Pu. *J. Chem. Phys.* **2010**, *132* (15), 154104. https://doi.org/10.1063/1.3382344.

(8) Grimme, S.; Ehrlich, S.; Goerigk, L. Effect of the Damping Function in Dispersion Corrected Density Functional Theory. *J. Comput. Chem.* **2011**, *32* (7), 1456–1465. https://doi.org/10.1002/JCC.21759.

(9) Tsujimoto, Y.; Sathish, C. I.; Matsushita, Y.; Yamaura, K.; Uchikoshi, T. New Members of Layered Oxychloride Perovskites with Square Planar Coordination: $Sr_2MO_2Cl_2$ (M = Mn, Ni) and $Ba_2PdO_2Cl_2$. *Chem. Commun.* **2014**, *50* (44), 5915–5918. https://doi.org/10.1039/c4cc01422g.